Optimisation multidisciplinaire de pales d'hélice d'avion

Benoît Marinus

Nb ECL: 2011-33
Nb VKI: 2011-00

ROYAL MILITARY ACADEMY
Polytechnical Faculty
Department of Mechanical Engineering

VON KARMAN INSTITUTE
Department of Turbomachinery and Propulsion

CENTRALE LYON - UNIVERSITY LYON I
Doctoral School of Mechanics, Energetics, Civil Engineering and Acoustics
Laboratorium for Fluid Mechanics and Acoustics

Manuscript for the degree of
Doctor in Applied Sciences (RMA) - Doctor in Acoustics (ECL)

Multidisciplinary Optimization of Aircraft Propeller Blades

Benoît G. MARINUS

Keywords: propeller, multidisciplinary, optimization, aeroacoustic, aerodynamic, aeroelastic, transonic, aircraft

publicly defended on the 8^{th} of November 2011 in front of the jury composed of

MM *W. Bosschaerts*, Prof. Dr. Ir., Royal Military Academy
Co-director
K. Brentner, Prof. Dr., Pennsylvania State University
Reviewer and President of the jury
D. Casalino, Dr., Italian Research Center for Aeronautics
Reviewer and Member of the jury
L. Rabet, Prof. Dr. Ir., Royal Military Academy
Member of the jury
M. Roger, Prof. Dr., Centrale Lyon
Co-director
R. Van den Braembussche, Prof. Ir., von Karman Institute
Co-director
T. Verstraete, Dr. Ir., von Karman Institute
Member of the jury

UNIVERSITÉ DE LYON

Great ideas, it has been said, come into the world as quietly as doves. Perhaps then, if we listen attentively we shall hear, among the uproar of empires and nations, the faint fluttering of wings, the gentle stirrings of life and hope. Some will say this hope lies in a nation; others in a man. I believe rather that it is awakened, revived, nourished by millions of solitary individuals whose deeds and works every day negate frontiers and the crudest implications of history. Each and every one, on the foundations of their own suffering and joy builds for all.
– Albert Camus

Anyone who believes exponential growth can go on forever in a finite world is either a madman or an economist.
– Kenneth Boulding

Acknowledgment

Academia has its roots with $\varphi\iota\lambda o\sigma o\varphi\iota\alpha$ (philosophia) in ancient Greece. Since its origins, and probably even before, when the concept was not as clearly embodied, it pursuits in depth knowledge, for the sake of wisdom. This quest explores an infinity of fields and is in progress over many centuries thanks to the major or minor contributions from known or unknown individuals, or groups, from every region and culture of our planet. This endeavour is all around us both in time and space. Along my tiny steps on this path, I owe my personal development, my feeling of happiness, and my bewilderment of the immenseness of the physical and spiritual world that surrounds us, to every bit of hope, joy, questioning, in depth discussion, calling into question, or even argument and despair, I had, have and will have the opportunity to share with so many people.

It is henceforth very restricting to write some names on a sheet of paper as most people I met are outstanding. Nevertheless, I would like to acknowledge Professor René Van den Braembussche, Professor Michel Roger and Professor Walter Bosschaerts for sharing that many thoughts and giving me so much of their time. They gave me the taste for learning. I would also like to record and thank some very special contributors to my everyday life: Anou, Babs, Bart, Cha, Elise, Fabio, Fred, Geo, uncle Jean, Maman, Memo, Nico, Romane, Sven, Tom, Vasilis, Virginie and many others. They carved deeply into my soul the living truth that dialogue is paramount; whether it is about the practical things of life or over the fundamental differences that strengthen us.

About the past, I just have to say that I profoundly miss my papa. About the future, I just hope for our daughter, Victoire, to feel much warmth from the people around her and to discover many of the marvels our world has to offer. I'll do my best to take a few steps with her, on her path in that direction. About the present, I feel happy to have a place called home where Eloïse, my love and wife, succeeds in delicately spicing up the flavour of things, instants and people.

Abstract

Open rotors are known to have significant advantages in terms of propulsive efficiency. These advantages translate directly in reduced fuel burn so that they nowadays benefit from a surge of interest. At the same time, recent advances in numerical simulations make the application of multidisciplinary optimization for the demanding design of transonic propeller blades, an affordable option. Therefore, an optimization method in which the performance objectives of aerodynamics, aeroacoustics and aeroelasticity compete against each other, is developed and applied for the design of high-speed single-rotation propellers.

The optimization is based on Multi-Objective Differential Evolution (MODE). This technique is a particular kind of evolutionary algorithm that mimics the natural evolution of populations by relying on the selection, recombination and eventually mutation of blade designs, each of them being represented by a vector of design variables (e.g. chord width, tip sweep, etc). MODE has the advantage of dealing concurrently with all the objectives in the selection of potentially promising designs among a population. In order to keep the computational cost within reasonable margins, the assessment of the performance of proposed designs is done in a two-level approach. A metamodel provides performance estimates for each proposed design at extremely low computational effort while high-fidelity analysis codes provide accurate performance values on some promising designs at much higher cost. To safeguard the accuracy of the estimates, the metamodel is initially trained on a population that is specifically assembled for that purpose. The training is repeated from time to time with the high-fidelity performance values of promising designs. Different high-fidelity tools have been developed and used for the assessment of performance.

The CFD-tool performs steady RANS simulations of a single blade passage of the isolated propeller in free air under zero angle of attack. These simulations provide the aerodynamic performance values. The full propeller is modelled thanks to cyclic boundary conditions. The $k - \varepsilon$ turbulence model is used in combination with wall treatment. Adiabatic no-slip wall conditions are imposed on the spinner and blade surfaces whereas the test-section radial boundary is reproducing the effects of a pressure far-field. This approach has proven its robustness and, above all, its accuracy as satisfactory agreement with experimental results has been found for different operating conditions over a wide range of blade shapes, as well as sufficient grid independency.

In the post-processing of the aerodynamic results, the Sound Pressure Level (SPL) is computed for tonal noise at various observer locations by the aeroacoustic solver (CHA). Formulation 1A from Farassat is used for this purpose. This formulation is related to the inhomogeneous wave equation derived from Lighthill's acoustic analogy by Ffowcs Williams and Hawkings (FW-H). It benefits from the partial decoupling of the acoustic and aerodynamic aspects and is particularly suited to compute the noise from propellers. The thickness noise and loading noise are expressed by separate equations in the time-domain whereas the quadrupole source term is dropped from the original FW-H equation. The blade surface is chosen as integration surface and a newly developed truncation technique is applied to circumvent the mathematical sin-

gularity arising when parts of the blade reach sonic conditions in terms of kinematics with respect to the observer. This approach delivers accurate values at acceptable computational cost.

Besides, CSM-computations make use of a finite elements solver to compute the total mass of the blade as well as the stresses resulting from the centrifugal and aerodynamic forces. Considering the numerous possibilities to tailor the blade structure so that it properly takes on the stresses, only a simplified blade model is implemented. The simplified blade is a monocoque design. The shell is composed of several layers of braided composite and the core is filled with foam. Additionally, the aeroelastic problem is decoupled from the aerodynamic one as the analysis is performed solely on the 'cold' blade shape. Hence the CSM computations provide a convenient, yet rudimentary, sanity check from a structural point of view. Nonetheless, the optimization tends to minimize the mass and stresses; to some respect, this should also benefit a tailored structure analyzed with full coupling.

A first optimization is performed by integrating the CFD and CHA tools in the optimizer. It uses a broad set of design variables controlling the spanwise variations of chord, thickness, sweep and twist of the blade as well as the airfoil shape. The propellers are assessed under different operating conditions corresponding to cruise ($M_\infty = 0.75$) and take-off/landing ($M_\infty = 0.2$), each time at various rpm so that off-design performance is also taken into account. The objectives aim at increasing the efficiency while reducing the noise in and out of the propeller plane. This optimization delivered a small number of optimized blades (28). All of them satisfy an extensive set of operational constraints. Moreover, it pointed out the weaknesses and deficiencies of the way the optimization method and high-fidelity tools have been implemented. A few specific blade designs are analyzed in more detail to better understand the potential of the set of design variables. These designs have peculiar geometrical features and offer only small improvement in terms of efficiency but a substantial one in terms of noise.

A second optimization is performed with complete integration of the CFD, CHA and CSM tools. The design variables allow again complete control of the blade shape. Propellers are assessed under both operating conditions, though this time cruise is at $M_\infty = 0.7$. One objective is defined to improve the aerodynamic efficiency, another to minimize noise emissions and a last one to decrease blade mass and stress levels. The optimization provided a set of 61 optimized designs that are fully compliant with operational as well as structural constraints. Specific designs are once more subject to a thorough analysis. These designs also have innovative geometrical features. They come with a substantial increase in efficiency but a moderate decrease of the emitted noise. Their geometrical features do not cause unacceptable levels of stresses.

Both optimizations illustrate the feasibility and the capabilities of the method. It is proficient in exploring the search space and delivering designs with features that are worth further investigation. One of them is the humps on the blade obtained by smoothly increasing the chord of a specific region of the blade. Finally, general conclusions are drawn and improvements to the method are proposed.

Résumé

Les hélices sont connues pour leur avantage significatif en termes de rendement propulsif. Ces avantages se traduisent directement par une réduction de la consommation de carburant de sorte qu'elles connaissent aujourd'hui un regain d'intérêt. Actuellement, les avancées récentes en simulations numériques rendent possible d'appliquer l'optimisation multidisciplinaire au cas exigeant du design de pales d'hélice transsonique. Pour ces raisons, une méthode d'optimisation est développée, dans laquelle les objectifs de performance aérodynamique, aéroacoustique et aéroélastique sont en concurrence. Cette méthode est appliquée au design de pales d'hélice à haute vitesse et à simple rotation.

L'optimisation s'appuie sur l'Evolution Différentielle Multi-Objectifs (Multi-Objective Differential Evolution - MODE). Cette technique est une des formes d'algorithme évolutionnaire qui mimique l'évolution naturelle des populations par le concours de la sélection, de la recombinaison et de l'éventuelle mutation de formes de pales, chacune d'elles étant représentée par un vecteur de variables (corde, angle de flèche, etc...). MODE offre l'avantage de considérer tous les objectifs en concurrence lors de la sélection des designs prometteurs au sein d'une population. Afin de garder le coût computationnel dans des limites acceptables, l'évaluation des performances des designs proposés est faite par une approche à deux niveaux. Un meta-modèle fournit les estimations de performance pour chaque design à un coût computationnel extrêmement faible alors que des codes d'analyse à haute fidélité calculent les performances précises à un coût nettement plus élevé. Pour préserver la précision des estimations, le meta-modèle est initialement entraîné sur une population composée à cet effet. L'entraînement est ensuite répété de temps à autres avec les performances haute fidélité de designs prometteurs. Différents outils à haute fidélité ont été développés et utilisés dans ce cadre.

L'outil CFD exécute la simulation RANS stationnaire d'un seul passage d'entrepales pour une hélice isolée sans angle d'attaque dans un écoulement libre. Ces simulations délivrent les valeurs de performance aérodynamique. L'hélice complète est modélisée grâce à des conditions aux limites cycliques. Le modèle de turbulence $k-\varepsilon$ est utilisé en combinaison avec un traitement adapté près des murs. Des conditions adiabatiques et sans glissement sont imposées sur le carénage et la surface de la pale tandis que la limite radiale de la section d'essais reproduit les effets d'un champ de pression lointain. Cette approche a prouvé sa robustesse et, par-dessus tout, sa précision puisque une correspondance acceptable avec des résultats expérimentaux est obtenue pour différentes conditions d'utilisation et un large éventail de formes de pales. De plus, l'indépendance par rapport au maillage est satisfaisante.

Lors de l'analyse a posteriori des résultats aérodynamiques, le Sound Pressure Level (SPL) est calculé par l'outil aéroacoustique (CHA) pour le bruit tonal en différentes positions. La formulation 1A de Farassat est utilisée à cette fin. Cette formulation découle de l'équation non-homogène d'onde dérivée de l'analogie acoustique de Lighthill par Ffowcs Williams et Hawkings (FW-H). Elle bénéficie du découplage partiel des aspects aérodynamiques et aéroacoustiques en plus d'être particulièrement adaptée pour le calcul du bruit d'hélice. Le bruit d'épaisseur et le bruit de charge sont

exprimés par des termes séparés dans le domaine temporel tandis que les quadripôles de l'équation de FW-H sont négligés. La surface de la pale est utilisée comme surface d'intégration et une nouvelle technique de troncation a été développée et appliquée pour circonvenir la singularité mathématique qui apparaît lorsque des parties de la pale ont des conditions soniques en termes de cinématique par rapport à l'observateur. Cette approche délivre des résultats fiables à un coût acceptable.

En outre, l'outil CSM utilise un programme d'éléments finis pour calculer la masse de la pale ainsi que les contraintes qui résultent des forces centrifuges et aérodynamiques. Considérant les nombreuses possibilités pour adapter la structure de la pale afin de reprendre les efforts au mieux, seul un modèle simplifié est implémenté. La pale simplifiée a une structure monocoque dont la peau se compose de plusieurs couches de composite tressé et le cœur est rempli de mousse. De plus, le problème aéroélastique est découplé du problème aérodynamique puisque l'analyse est effectuée sur la forme non-déformée de la pale seulement. De ce fait les calculs CSM fournissent un moyen commode, même si rudimentaire, de réaliser une vérification d'intégrité structurelle. Néanmoins, l'optimisation tend à réduire la masse et les contraintes, ce qui devrait profiter aussi à une structure plus sur mesure qui serait analysée avec un couplage total des problèmes.

Une première optimisation intégre les outils CFD et CHA. Un ensemble extensif de variables contrôle la distribution radiale de la corde, de l'épaisseur, de l'angle de flèche et de l'angle de torsion de la pale ainsi que la forme du profil. Les hélices sont considérées sous différentes conditions correspondant au vol de croisière ($M_\infty = 0.75$) et au décollage/atterrissage ($M_\infty = 0.2$), à chaque fois pour différents régimes de sorte que la performance hors design soit aussi prise en compte. Les objectifs visent à augmenter le rendement tout en réduisant le bruit dans et en-dehors du plan de l'hélice. Cette optimisation aboutit sur un petit nombre de pales (28). Toutes satisfont un ensemble extensif de contraintes opérationnelles. De plus, elle permet d'identifier les faiblesses et les défauts de la façon dont l'optimisation et les outils haute fidélité ont été implémentés. Quelques designs particuliers sont analysés plus en détails pour mieux comprendre le potentiel des variables de design. Ces designs ont des caractéristiques géométriques originales et n'offrent qu'une faible amélioration du rendement mais bien une amélioration substantielle en termes de bruit.

Une seconde optimisation est effectuée avec l'intégration complète des outils CFD, CHA et CSM. Les variables permettent encore un contrôle complet de la forme de la pale. Les hélices sont considérées sous les deux conditions de vol bien que cette fois le vol de croisière soit à $M_\infty = 0.7$. Un objectif est défini pour améliorer le rendement, un autre pour minimiser les émissions de bruit et un dernier pour réduire la masse et les contraintes. Cette optimisation fournit un ensemble de 61 designs qui obéissent à des contraintes opérationnelles et structurelles. Des designs spécifiques sont une fois de plus analysés en profondeur. Ces designs ont aussi des caractéristiques géométriques innovatrices. Ils offrent une augmentation confortable en rendement mais seulement une amélioration modeste par rapport au bruit. Leur forme ne cause pas de niveau inacceptable de contraintes.

Les deux optimisations illustrent la faisabilité et les capacités de la méthode. Elle est efficace pour l'exploration de l'espace de design et pour délivrer des formes avec des attributs qui méritent de plus amples d'investigations. Parmi eux sont les bosses sur la pale, obtenues par une augmentation locale de la corde. Finalement, des conclusions plus générales sont tirées et des améliorations à la méthode sont proposées.

Samenvatting

Propellers staan bekend om hun voordelen met betrekking tot het propulsierendement. Die voordelen geven aanleiding tot een gereduceerd brandstofverbruik en dit is ook de reden voor de huidige vlaag van interesse. Tegelijkertijd, zorgen recente ontwikkelingen in numerieke simulaties ervoor dat het toepassen van multidisciplinaire optimalisatie voor het veeleisende design van transsone propellerschoepen, een te veroorloven optie wordt. Om die reden, wordt een optimalisatiemethode ontwikkeld, in dewelke de prestatiedoelstellingen van aerodynamica, aero-akoestiek en aeroelasticiteit in concurrentie zijn. Deze wordt toegepast voor het ontwerp van hoge snelheid, enkelroterende propellers.

De optimalisatie baseert zich op Multi-Objectieven Differentiële Evolutie (MODE). Het is een type evolutionair algoritme dat de natuurlijke evolutie van populaties nabootst door selectie, recombinatie en eventueel mutatie van schoepontwerpen, elk bestaande uit een vector van designvariabelen (bv. koordlengte, pijlhoek, enz...). MODE heeft het voordeel dat het alle objectieven concurrerend behandelt bij de selectie van veelbelovende designs onder een populatie. Om de rekenkost te begrenzen, gebeurt de beoordeling van de prestatiekenmerken van de voorgestelde designs op twee niveaus. Een metamodel levert de geschatte prestatie van de voorgestelde ontwerpen met een zeer lage computationele kost, terwijl analysecodes met hoge nauwkeurigheid het precieze prestatiekenmerk berekenen voor veelbelovende schoepen, maar tegen een hogere kost. Om de nauwkeurigheid van de geschatte waarden te garanderen, wordt het metamodel aanvankelijk getraind op een populatie die daarvoor specifiek samengesteld is. De training wordt nadien van tijd tot tijd herhaald met de hoog nauwkeurige waarden van veelbelovende designs. Verscheidene rekencodes met hoge nauwkeurigheid worden daarvoor gebruikt.

De CFD-code voert stationaire RANS-berekeningen uit voor een bladkanaal van een geïsoleerde propeller in vrije lucht en zonder aanvalshoek. Deze simulaties geven de aerodynamische prestatiekenmerken weer. De volledige propeller wordt door middel van cyclische grensvoorwaarden gemodelleerd. Het $k - \varepsilon$ turbulentiemodel wordt gebruikt in combinatie met gepaste behandeling bij de wanden. De spinner en het bladoppervlak worden adiabaat en zonder verschuivingen verondersteld, daar waar de radiale grens van het domein de effecten van een ver drukveld nabootst. Deze aanpak heeft zijn robuustheid aangetoond en, bovenal, zijn nauwkeurigheid, daar een bevredigende overeenstemming bekomen wordt voor meerdere werkingspunten en bladvormen, alsook voldoende gridonafhankelijkheid.

In de postprocessing van de aerodynamische resultaten, wordt de Sound Pressure Level (SPL) berekend door de aero-akoestische solver (CHA) voor toongeluid bij een aantal locaties. Formulering $1A$ van Farassat wordt daarvoor gebruikt. Het is gerelateerd aan de niet-homogene golfvergelijking die door Ffowcs Williams en Hawkings (FW-H) afgeleid werd uit de akoestische analogie van Lighthill. Ze haalt voordelen uit de partiële ontkoppeling van de akoestische en aerodynamische aspecten en is bijzonder geschikt voor het geluid van propellers. Het dikte- en belastingsgeluiden worden door afzonderlijke vergelijkingen in het tijdsdomein weergegeven, terwijl de

quadripool-term van de originele FW-H vergelijking wordt verwaarloosd. Het bladoppervlak wordt als integratieoppervlak gebruikt en een nieuwe aftoppingstechniek wordt op punt gesteld om de wiskundige singulariteit te omzeilen, die ontstaat wanneer er delen van het blad in sonische toestand verkeren in termen van kinematica ten opzichte de waarnemer.

Daarbij gebruikt de CSM-code een eindige elementen solver om de totale massa en de spanningen die ontstaan door de aerodynamische en centrifugale krachten, te berekenen. Gezien er tal van mogelijkheden bestaan om de structuur van het blad aan te passen, zodat het de spanningen beter opneemt, wordt slechts een vereenvoudigd model geïmplementeerd. Het is een monocoque design. De schaal bestaat uit meerdere lagen van gebreide composieten met een kern uit schuim. Bovendien, wordt het aero-elastisch probleem ontkoppeld van het aerodynamisch probleem gezien enkel het niet-vervormde blad wordt beschouwd. Om die redenen levert de CSM-code een handige, doch rudimentaire, controle van de structurele integriteit. Desalniettemin, probeert de optimalisatie de massa en de spanningen te verminderen, wat ook voordelig zou moeten zijn voor een verfijnde structuur, gemodelleerd met volledige koppeling.

Een eerste optimalisatie wordt uitgevoerd met CFD- en CHA-codes. Men beschouwt een uitgebreide set van ontwerpvariabelen die de radiale verdeling controleert van koorde, dikte, pijlhoek en draaiing, alsook de vorm van de vleugelprofielen. De propellers worden beoordeeld in kruis ($M_\infty = 0.75$) en bij het opstijgen/landen ($M_\infty = 0.2$), telkens bij meerdere omwentelingsnelheden zodat off-design prestaties ook in rekening worden gebracht. De doelstelling is de efficiëntie te verhogen terwijl het geluid in en uit het propellervlak gereduceerd wordt. Deze optimalisatie levert een klein aantal geoptimaliseerde schoepen (28) die allemaal een veelomvattende set operationele beperkingen naleven. Tevens laat deze toe de zwakheden en deficiënties van de manier waarop de optimalisatiemethode en hoge nauwkeurigheid codes geïmplementeerd werden, te identificeren. Enkele bijzondere designs worden meer in detail onderzocht om het potentieel van de gekozen variabelen beter te vatten. Deze designs hebben bijzondere geometrische kenmerken en bieden maar een kleine verbetering van het rendement, maar een substantiële verbetering voor het geluid.

Een tweede optimalisatie met volledige integratie van de CFD-, CHA- en CSM-codes wordt uitgevoerd. De designvariabelen laten alweer een totale controle toe van de vorm van de schoep. De propellers worden nogmaals bij beide vluchtomstandigheden beoordeeld, doch deze keer in kruis bij $M_\infty = 0.7$. Een objectief wordt gedefinieerd om de aerodynamische efficiëntie te verhogen, een ander om het geluid te minimaliseren en een laatste om de massa en de spanningen te verminderen. De optimalisatie resulteert in 61 ontwerpen die aan alle operationele en structurele eisen voldoen. Enkele designs worden grondig onderzocht. Deze hebben ook innoverende geometrische kenmerken en bieden een aanzienlijke toename van het rendement met een gematigde afname van het geluid. Deze geometrische kenmerken veroorzaken geen onaanvaardbare spanningen.

Beide optimalisaties illustreren de haalbaarheid en de mogelijkheden van de methode. Ze is uitermate geschikt voor de verkenning van het zoekdomein en voor het leveren van designs met kenmerken die verder onderzoek verdienen. Een ervan zijn de bulten door een zachte, lokale verbreding van de koorde. Tot slot worden besluiten en voorstellen tot verbetering geformuleerd.

Contents

List of Symbols

$\mathbf{M}$	Mach number vector expressed in a frame fixed to the undisturbed medium	
$\mathbf{r}$	Radiation vector	$\mathbf{r} = \mathbf{x} - \mathbf{y}$
$\mathbf{x}$	Observer position vector	
$\mathbf{y}$	Source position vector	
$\mathcal{Q}$, $\tilde{\mathcal{Q}}$, $\check{\mathcal{Q}}$	Generic functions	
b	Blade chord	
$B_{n,i}(.)$	Bernstein polynomial	
c	Speed of sound	$c = \sqrt{\gamma r T}$
$C(.)$	Curve coordinate vector	
C_P	Propeller power coefficient	$C_P = P/(\rho_\infty.n^3.D^5)$
C_p	Pressure coefficient	$C_p = (2/(\gamma M^2)).(p/p_\infty - 1)$
C_T	Propeller thrust coefficient	$C_T = T/(\rho_\infty.n^2.D^4)$
C_{PTFel}	Elemental PTF coefficient	$C_{PTFel}(r) = \frac{PTF_{el}(r)}{1/2\rho_\infty u(r)^2 b_{ref}}$
C_{Tel}	Elemental thrust coefficient	$C_{Tel}(r) = \frac{T_{el}(r)}{1/2\rho_\infty u(r)^2 b_{ref}}$
$C_{Tq,z}$	Moment coefficient around the pitch change axis $C_{Tq,z} = Tq_z/(\rho_\infty.n^2.D^5)$	
D	Propeller diameter	
E	Young's modulus	
e_a	Approximate relative error	
e_r	Relative error	
e_{ext}	Extrapolated relative error	
f	Blade surface's mathematical representation	$f = 0$, $f > 0$ outwards
$F_{i,q}(.)$	Basis function	
G	Shear modulus	
h	Cell size parameter	
$H(f)$	Heaviside function	
J	Advance ratio	$J = u_\infty/(n.D)$
l_i	Local force intensity components acting on the fluid	
M	Mach number	
m	blade mass	
M_n	Mach number projected in the normal direction	$M_n = \mathbf{M}.\hat{\mathbf{n}}$
M_r	Mach number projected in the radiation direction	$M_r = \mathbf{M}.\hat{\mathbf{r}}$
M_{tip}	Tip Mach number	$\sqrt{M_\infty^2 + (\omega R/c_\infty)^2}$
n	Propeller rotational velocity (in rounds per second - rps)	
$N_{i,q}(.)$	B-spline basis function	
P	Propeller net power	
p	Pressure	
p'	Acoustic pressure	$p' = c_\infty^2 \rho'$
PTF	Propeller Torque Force	
R	Blade tip radius	
Re	Reynolds number	
S	Surface	

LIST OF SYMBOLS

Sw	Blade sweep at 1/4 chord line	
T	Propeller net thrust, Temperature	contextual
t	Time, Observer time , Blade section thickness	contextual
T_{ij}	Lighthill's stress tensor	$T_{ij} = \rho u_i u_j - \sigma_{ij} + (p' - c_\infty^2 \rho')\delta_{ij}$
Tq	Torque	
Tw	Blade twist	
u	Velocity, Displacement	contextual
V	Volume	
v_n	Normal velocity magnitude of blade surface	
w	Weighting factor	
x	Design variable	
X, Y	Coordinates	
β_{ref}	Blade angle at 75% radius	
$\delta(f)$	Dirac delta function	
δ_{ij}	Kronecker delta	
η	Propeller net efficiency	$\eta = T.u_\infty / P = J.C_T / C_P$
γ	Isentropic coefficient	
Γ, Φ	Constraint function	
κ	Half-truncation interval	
λ	Wavelength	
ν	Poisson's ratio, Frequency	contextual
Ω	Objective function	
ω	Propeller rotational velocity (in rad per second - rad/s)	
ϕ'	Generic acoustic pressure	
ρ	Volumic mass	
ρ'	Perturbation density	
σ	Stress	
σ_{ij}	Stress tensor, Viscous stress tensor	contextual
τ_e	Retarded time	
θ	Angle between normal and radiation vectors	
ε	Strain	
$\zeta_.$	Stress criteria value	
$\bar{(.)}$	Vector, Mean value	contextual
$\dot{(.)}$	Time derivative with respect to source time	$\partial / \partial \tau$
$\hat{(.)}$	Unit vector, Normalized value based on high-fidelity analysis	contextual
$\tilde{(.)}$	Normalized value based on metamodel	contextual
$\cdot^i$	i^{th}-Iteration	
$\cdot_0$	Total quantity	
$\cdot_{TW}$	Tsai - Wu	
$\cdot_{VM}$	von Mises	
$\cdot_C$	Compressive	
$\cdot_i$	Component of a vector, Member of a population	contextual
$\cdot_L$	Loading	
$\cdot_{,0}$	Reference value	
$\cdot_\infty$	Freestream quantity	
$\cdot_{el}$	Elemental	
$\cdot_T$	Tensile, Thickness	contextual
$1D$	One-dimensional	
$2D$	Two-dimensional	
$3D$	Three-dimensional	
ANN	Artificial Neural Network	
ATM	Aerodynamic Twisting Moment	
BPF	Blade Passing Frequency	
BPH	Blade Passing Harmonic	
CFD	Computational Fluid Dynamics	
CSM	Computational Structure Mechanics	
CTM	Centrifugal Twisting Moment	
DoE	Design of Experiments	

DoF	Degree of Freedom	
EA	Evolutionary Algorithm	
GCI	Grid Convergence Index	
LE	Leading Edge	
$MODE$	Multi-Objective Differential Evolution	
NS	Navier-Stokes	
PS	Pressure Side	
PTF	Propeller Torque Force	
$RANS$	Reynolds Averaged Navier-Stokes	
RBF	Radial Basis Functions	
SPL	Sound Pressure Level	$p_{ref} = 20\mu Pa$
SS	Suction Side	
TE	Trailing Edge	
FW-H	Ffowcs Williams and Hawkings	

Chapter 1

Introduction

1.1 Interest of propellers

1.1.1 The past

On December the 17^{th} 1903 history changed. What started as the ancestral fascination for joining birds in their freedom to exploit the vertical dimension and latter evolved into the quest of having man actually making a sustained and self-controlled flight, became reality when the Wright brothers took off at Kitty Hawk with their propeller-driven aircraft for a 12 seconds flight. Their aircraft was propelled by a wooden propeller with an astonishing peak efficiency of just over 70%. Wilbur Wright was then the first person to recognize that a propeller is nothing more than a rotating twisted wing [19] whose primary function is to convert shaft power into propulsive thrust at the highest possible efficiency.

Since this major event, propellers were first the only propulsion system for aircraft but became merely an alternative when the turbojet and latter the turbofan appeared. It is only in the late $1970's$ and early $1980's$, under the pressure of high fuel prices, that new concepts such as the single- or counter-rotation propfan were developed. These concept promised interesting efficiencies though they required additional development to keep vibration and noise levels within reasonable limits. The low and reasonably stable fuel prices at the end of the $1980's$ led to the end of these programs before they reached the necessary level of maturity to convince a rather conservative industry.

Despite this demise, turboprops were still flourishing in the regional aircraft market and so it seemed logical to increase the flight speed of turboprops to deliver interesting economics on longer routes. But the introduction of the regional jet broke that line of effort. Strong barriers in operator and passenger perception appeared as is wonderfully illustrated by news articles such as [209] which is just one manifestation of the 'prop avoidance factor' [148].

1.1.2 The present and the future

Nowadays, the economical pressure is augmented with the environmental one so that a new deal is set up. Under this deal, propellers seem to offer at least part of the

answer and the perception barriers might be overcome. High-speed turboprops or other advanced open-rotor concepts are in for a resurgence. This supports the view of D. Edgerton [87] that old ideas are worth being periodically investigated instead of just being dismissed. Innovation is not always disruptive, sometimes new problems require 'old' answers. At present, propellers represent a growing market share in civil aviation, a significant one in military aviation and enjoy an undiscussed leap in general aviation.

Military use of propellers is driven by some breaching advantages, these include:

- their robustness for badly prepared terrain,
- their short take-off and landing performance,
- their good low speed performance,
- they are relatively easy to fly,
- and they have a high to very high efficiency.

This insures that propellers will still be widely used for those specific applications that correspond to these advantages, e.g.: training and advanced training of pilots, tactical transport, surveillance and counter-insurgency among others. For the training purpose, the trend is to higher flight speeds in order to match the performance of fighter-jets as closely as possible with a reasonable cost when compared to jet-trainers [38, 238]. Tactical transport applications have traditionally seen extremely successful use of turboprops. The recent development of the Lockheed-Martin C-130J or the impressive Airbus A-400M are interesting examples of the drive for higher flight Mach numbers whilst delivering better efficiency. Future contracts such as the Future Cargo Aircraft (FCA) for the US Air Force and US Army, rely solely on turboprops. For surveillance purposes, turboprops are considered for the Aerial Common Sensor (ACS) program [11]. Use of propellers for Unmanned Aerial Vehicles (UAV's) is also quite frequent these days and advanced propellers should bring improvements with regard to both endurance and noise generation. Recent developments even include a fast, stealthy, turboprop equipped UAV [300], the solar-electric-powered Solar Eagle or the hydrogen-powered Phantom Eye, both from Boeing. For counter-insurgency purposes, the advantages of turboprop aircraft such as those extensively used in the Vietnam war, are sought after in future requirements [12].

In civil aviation, propeller aircraft are used in impressive numbers for sub-regional and regional transport (both for freight and passengers). For these markets, the high subsonic speed domain is quite interesting but the noise generation is still a major item of concern. The high fuel efficiency of propellers is the main factor for companies to select propeller driven aircraft for this particular market. Moreover, their ability to accelerate a large amount of air at low speeds, which translates in shorter take-off length and climbing time, makes them attractive for airliners that operate on small airports with shorter runways or with stringent noise abatement procedures. Advanced propellers have brought new potentials as their reduced noise emissions allow for less cabin insulation, their high performance allow to compete with turbofan aircraft while flying at higher speeds and their modern manufacture concepts together with high fuel efficiency have helped reducing the operating costs. Turboprop equipped aircraft face a brilliant perspective if judged by the considerable amount of statements made in this direction [148,169,198,58,227,3,73,161,170,2,146,195]. Part of this move is sustained by the 'greener' perception of turboprops [184,6,4] and led to

an increase from 15% to 40% of the anticipated total demand in the regional aircraft market [31].

For general aviation, most aircraft are equipped with a piston-engine and propeller. In this case, propellers represent the low cost solution by excellence, both for investment and in-service cost.

Recent works have underlined the potential advantage of turboprops in civil aviation. Whereas turboprops were typically confined to routes shorter than $550km$, [252] and [269] show the potential benefits of advanced propellers for routes up to $2750km$. Taking into account that close to 95% of the flights in the European airspace have a direct distance less than $1000km$ [155], one should indeed give propellers a second chance and relieve them of their status of anathema.

Recent development of high speed propellers has extended the flight domain to high subsonic speeds (thereby increasing the need for ideally optimized blades) along with an increased efficiency. As of today, concern is rising fast on environmental issues; the desperate search for reduced pollutant emissions is dramatically requiring enhanced performance. Also, the scarcity of fuel resources requires a parsimonious use of it. These two reasons along with the fact that propellers achieve better fuel efficiency when compared to a technologically equivalent turbofan, are a solid motivation to continue research for advanced propellers. As a matter of fact, the recent release of the four reports in the framework of NASA's study for a 2030-era aircraft, gives a strong boost for advanced open-rotor concepts. Indeed, the recurring themes of those reports are [26, 114]:

- Slower cruising at about Mach 0.7 and at higher altitudes, to save fuel.
- Engines requiring less power during take-off, for quieter flight.
- Shorter runways to increase operating capacity and efficiency.
- Smaller aircraft flying shorter and more direct routes, for cost-efficiency.
- Reliance on future advancements in Air Traffic Management for merging and spacing enroute, during climbs and during descents.

These conclusions led two of the four teams to favour aircraft equipped with propellers. Hence turboprops or, more generally, innovative single- and counter-rotation open-rotor concepts, associated with advanced engine concepts, should have a bright future. The main features of these modern-age propellers include:

- they are multi-bladed,
- they are potentially used in dual-rotation,
- they have high loading,
- they have high twist and sweep,
- they have thin airfoil sections at the tip,
- they have wide chord airfoils,
- they have advanced planform shapes,
- and they are tailored to the use of progressive materials.

1.2 Literature survey

Though the purpose of this section is not to deliver a complete literature survey, this is done more appropriately in the subsequent chapters, it is necessary to locate the present dissertation among the works on multidisciplinary optimization applied on aircraft propeller blades. The path to a true multidisciplinary approach of propeller design, with the disciplines acting in a concurrent way rather than the traditional approach where disciplines were pursued in an independent or serial way, has probably been laid by the end of the $1990's$ by the work of M. Dunn and F. Farassat [81]. They presented an integrated procedure to retrieve the aerodynamic, aeroacoustic and aeroelastic performance of a given blade geometry. The work is rather focused on the precise assessment of the aeroacoustics with inclusion of the effects of blade deformations and so it lacks the coupling to a search engine capable of generating new geometries based on the acquired knowledge. Later on, multidisciplinary design procedures were proposed such as in [59] though it relies on rather simple models such as 2D approximations, or as in [61] but with a limited set of design parameters.

At present, multidisciplinary design has become the standard and this is reflected in the amount of works published. In [61], an optimization of propeller blades for low-speed applications is proposed. In [134, 133], O. Gur and A. Rosen proposed a fairly complete optimization procedure for propellers aiming at the UAV segment; hence their work is limited to low speed aircraft. They use deterministic optimization methods where the amount of individuals (i.e. blade designs), thus also of computations, is limited. A. Pagano, in [219], presents a multi-objective optimization applied for a pusher propeller installed on medium-speed aircraft. It uses genetic optimization methods involving more individuals but with a limited set of design parameters.

To the author's knowledge, noise generation from propellers for high-speed transport aircraft is rarely blended into multi-disciplinary design based on Evolutionary Algorithms. The high computational cost of aerodynamic and aeroacoustic computations in the transonic domain on top of the cost of structural computations are the main reasons for this. Moreover, the rare multidisciplinary optimizations that have been performed over the last decades are proprietary information of a few industrial concerns and have not been cleared for public release to this date.

1.3 Thesis objective

Current propellers have been selected on a wide spectrum of characteristics: low fuel consumption, high trust generation under different conditions, long lifetime, low cost, high mechanical integrity, high environmental friendliness (including cabin and outbound noise) and other potential requirements that are specific to the intended use. Modern propellers explore new fields by increasing the number of blades, increasing the tip speed and introducing new planform shapes and section profiles; all of that to optimize one or more of the selection criteria. The latest advances in computing capabilities made a large range of reliable tools available to the scientific community. Until recently, many of the benefits of computational methods (applied to aerodynamics, aeroacoustics, stress, vibrations and many other fields) could only be yielded with limited extent because of the large computational cost involved. But nowadays computers and software improvements allow for far more reaching applications. Time has come for multidisciplinary optimization.

Optimization according to one design criterion may lead to a blade design that is not optimal in terms of other disciplines or violates constraints. So, multidisciplinary optimization is needed. It consists of finding a geometry that is optimal/acceptable according to the different disciplines. In this work, the fields of aerodynamics and aeroacoustics are considered to some extent, along with the issue of aeroelasticity. The objective is to propose an integrated, multidisciplinary and multi-objective design procedure that autonomously searches for optimal blade shapes that satisfy specific constraints. The procedure should be applied with innovative design parameters in order to explore new possibilities.

The core of the proposed optimization tool consists of a robust and inexpensive algorithm to find one or several candidates close to optimality. Wrapped around the optimizer are the following discipline related prediction tools that help in the correct assessment of the value of a given blade design:

- a tool for aerodynamic performance prediction,
- a tool for the prediction of the noise emitted by a blade design in specific conditions,
- and a tool for the prediction of the structural status of the blade,

These tools need to be developed for the present purpose and given the possibilities of the institutions involved. They also require validation to make sure they work properly. As they are still quite expensive in computational terms, their use should be reduced by means of a fast optimization based on approximation tools and embedded within the global optimization. However, the accuracy of the overall method should be safeguarded by a recurrent but limited use of the aforementioned prediction tools. This assures that inaccuracies in the approximations do not lead to false optima. The different tools should run in parallel in order to save time. Such a two level optimization process should be less expensive (finding the optimum with a minimum of computational effort) and highly effective(finding solutions near the true optimum).

In a nutshell, one might say the ultimate objective is about shortening and improving the design cycle of propeller blades with increased efficiency, and reduced noise emissions while complying with mechanical characteristics and potentially proposing innovative shapes. This should be done with maximum use of already available design expertise in a modular and automatic system at a minimum cost.

1.4 Preliminary remarks

A first point that immediately arises, is the integrated nature of the work. It translates more into a 'network' structure rather than a serial account of the path that is followed. So this dissertation is written in this sense and tries to respect that nature though it still pretends to deliver a scientific explanation of the tools, their results and how they interact.

The focus of this dissertation is on 'improvement' rather than finding a true, possibly non-existing, global optimum. And this quest is deliberately done without strong restrictions on the blade geometry. The net result is a very wide search-space out of which the author hopes to retrieve interesting features that are worth blending into future designs. It should be clear that these designs will for sure need refinements

and should be subject to analysis with much more details before maturity. So the present dissertation is purposely placed at the earliest design stage.

As often as possible, the analysis tools used in the present work, have been assessed by comparison to published results on known propeller configurations. Unfortunately, propellers have long fallen in the industrial realm so that exploitable data (and that implies mainly the precise knowledge of the blade shape) are scarce. One is either restricted to the NACA-era or the $1980's$ propfans studied under a NASA-effort. This is even more crucial when structural data are sought after as only 'old' propeller structures are available.

1.5 Thesis outline

This dissertation is articulated around three parts. In the next chapter, basic propeller principles are discussed in order to sketch the problem of optimizing a propeller blade in a multidisciplinary environment. In part I, composed of chapters 3 to 7, the optimizer is described along with the various analysis tools around it. In each case, a perspective is given and the chosen approach is described into all necessary details. Part II (chapters 8 to 10) is dedicated to an aerodynamic and aeroelastic optimization that served as a first test case. The specific details of the optimization, resting upon the tools of part I, are first discussed before analyzing and commenting the results. The conclusions of that part serve as springboard for the next optimization. This second optimization is dealt with in part III (chapters 11 to 13). It includes all three disciplines. Here again, the optimization set-up is first described before jumping to the analysis and synthesis of the results. Finally, general conclusions are drawn together with possible points for improvement. The dissertation ends with the list of figures, tables and references.

Chapter 2

Basic propeller theory

Prior to the detailed discussion of the elements assembled in the present optimizations, this chapter provides some basic insight into the forces and loads active on a propeller blade as well as the origins of the sound emitted by a running propeller.

2.1 Aerodynamic forces, flow and efficiency

The purpose of a propeller is to generate thrust which is the force in the flight direction. But when decomposing the overall aerodynamic force produced by a single blade, one obtains two components: thrust $\overline{T}$ and a Propeller Torque Force (PTF) $\overline{PTF}$. The last is responsible for the torque $\overline{Tq}$ that is usually overcome by an air-breathing engine, a turboshaft or an electric drive. The forces and the torque are illustrated in Fig. 2.1. Basically, a propeller blade may be seen as a series of radial elements having an airfoil shape and subject to a velocity depending on the radial position. Such an element is illustrated in Fig. 2.2 together with the traditional decomposition of the aerodynamic force in elemental lift $\overline{L}_{el}$ and drag $\overline{D}_{el}$ or in elemental thrust $\overline{T}_{el}$ and PTF $\overline{PTF}_{el}$. In Fig. 2.2, $\overline{u}_\infty$ is the free-stream velocity, $\overline{u}_i$ the induced velocity, $\overline{\omega r}$ the local tangential velocity resulting from rotation and $\overline{u}_b$ the velocity relative to the blade section. The angle β is the local blade angle and α_b is the angle of attack for that particular section. The angles ε_b and ε_i are the advance and induced angles respectively.

Depending on the radial location of the section $A - A'$, the angles vary and so do the forces too. In general, the inner part of the blade, close to the root, does not contribute significantly to the generation of thrust [213, 32, 29] whereas the outer part, from 50% radius on, is responsible for most of it. Hence the pressure loads are significantly different.

The flow around a blade is essentially 3D because of the presence of the spinner that induces radial displacement of the incoming fluid, but also because of the local pressure distributions along the radius. In transonic flow, a shock on the suction side of the outer part of the blade is a common feature. Possibly, in harsher conditions, this shock spans the whole blade passage but this corresponds to a rather inefficient situation. Sometimes, a shock is present at the root part of the blade due

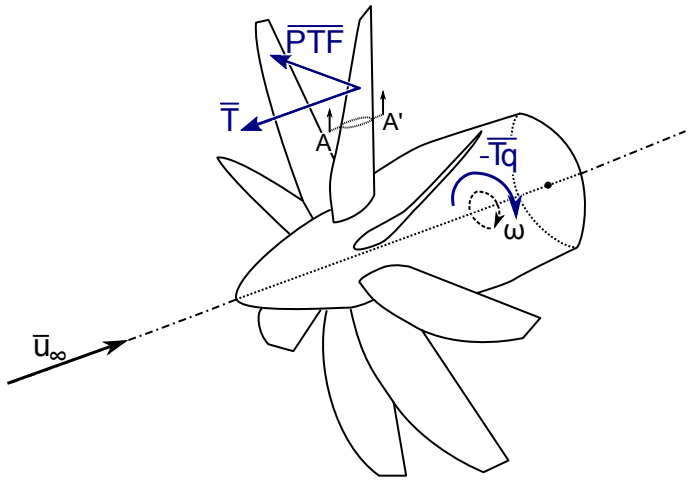

Figure 2.1: Aerodynamic forces applied on a blade at its center of pressure. The propeller is placed in uniform inflow at zero angle of attack.

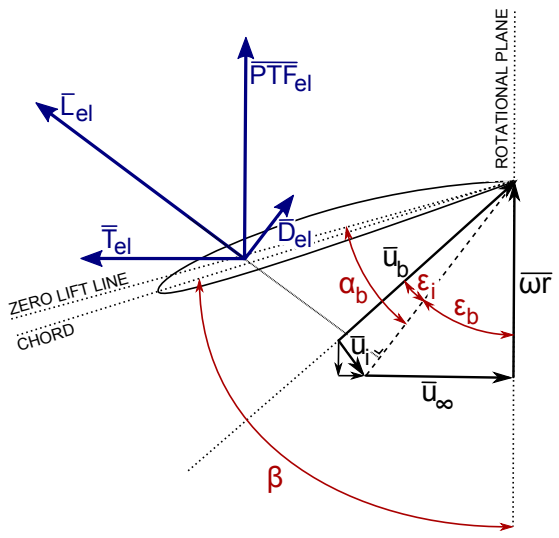

Figure 2.2: Elemental forces and velocities on section $A-A'$ of Fig. 2.1. Forces are applied at the local center of pressure.

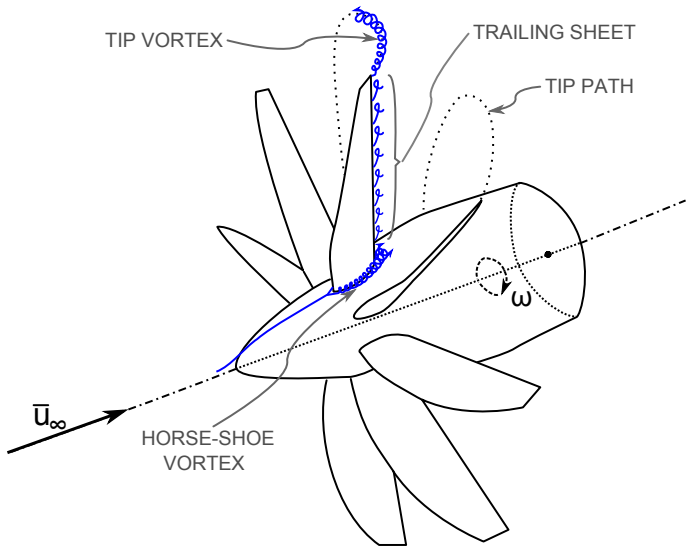

Figure 2.3: Main flow features around a propeller blade.

to blockage effects but again this situation should be avoided [274]. Concerning vortical structures, there are essentially three regions of intense vorticity: the tip vortex, the horse-shoe vortex at the root and a sheet of trailing vorticity. These structures are illustrated in Fig. 2.3. The tip vortex follows the helical path of the tip and has a strong intensity. Its core extension, measured to the point of maximum circumferential velocity, is typically of the order of 5 to 10% of the blade chord [159] and tends to increase with decreasing blade tip thickness [292]. The horse-shoe vortex in comparison has a much smaller spatial extent [190]. The wake of the blade contains a sheet of trailing vorticity that usually vanishes within one chord length. Additionaly, a leading-edge vortex as well as shock-induced vorticity due to baroclinic effects are often encountered [190].

Typical installed efficiencies for propellers are given in Fig. 2.4 from [158, 275]. The figure is related to the installed efficiency:

$$\eta_{installed} = \frac{u_\infty T_{installed}}{P_{installed}} \tag{2.1}$$

with $T_{installed}$ and $P_{installed}$ referring respectively to the thrust and power of the installed propeller. This efficiency is, for tractor configurations at least, somewhat higher than the net efficiency of the propeller (η) because the wings usually act as swirl recovery vanes. The installed efficiency of conventional propellers drops for free-stream Mach numbers (M_∞) higher than 0.6, and this is the reason why most turboprop equipped aircraft do not fly at higher speeds. But modern blade and airfoil shapes allow for better efficiencies at Mach numbers of the order of $0.7 - 0.75$ as is proven by recent developments in military transport aircraft. High efficiencies at high free-stream Mach numbers are obtained with high-speed propellers whose tip travels at Mach numbers well above unity. For these open-rotors, counter-rotation

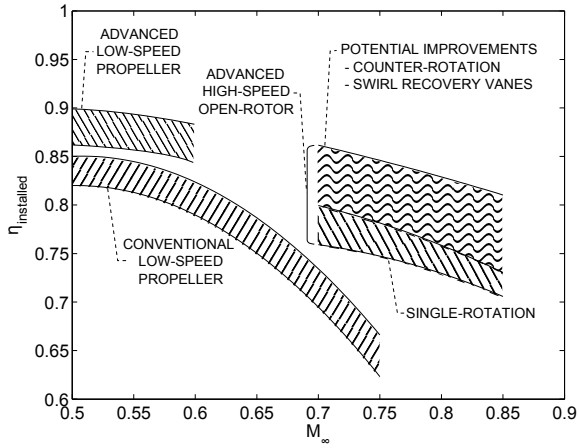

Figure 2.4: Typical installed efficiency of open-rotors in general ([158, 275]).

and swirl recovery vanes could offer substantial improvement and are currently being investigated by different research teams. The drawback are the aeroacoustic issues related to such high tip speeds as will appear in chapter 6.

2.2 Structural loads

A single blade is essentially a rotating cantilever beam subjected to both steady and vibratory loads. The steady loads, in unaccelerated rectilinear flight, are composed of (see also Fig. 2.5):

- the centrifugal load due to rotation,
- the torque and thrust loads resulting from the aerodynamic forces (pressure and viscous),

The centrifugal load results in tension on the blade but also in a powerful twisting moment. This Centrifugal Twisting Moment (CTM) results from the twist in the blade and the resulting presence of blade material away from the pitch change axis. This is illustrated in Fig. 2.6. The torque and thrust loads are responsible not only for local shear, because of their radial distribution, but also for considerable bending moments and the Aerodynamic Twisting Moment (ATM) which is a similar mechanism as the CTM though the cause is the local distribution of pressure around the section. The ATM, which mostly tends to increase the blade angle, is usually negligible with respect to the CTM that tends to decrease the blade angle. For most operating conditions, the centrifugal loads are dominant with respect to the aerodynamic loads [213, 81].

In the present early-design optimization, vibratory loads are not considered.

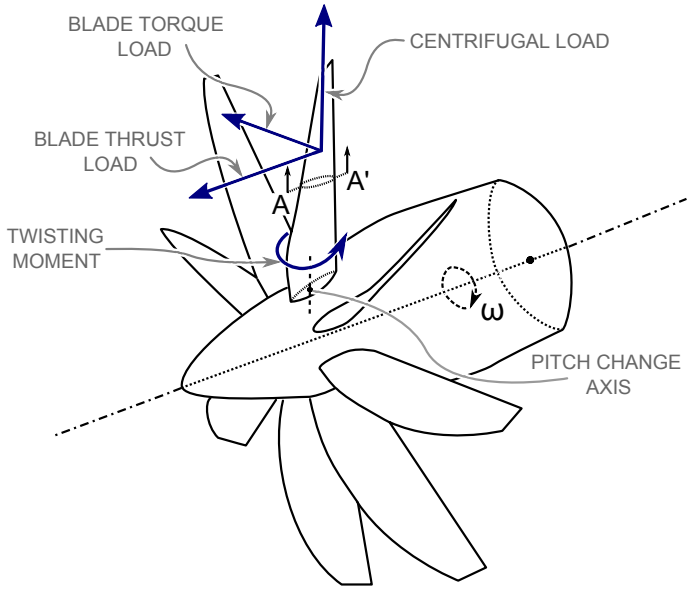

Figure 2.5: Main steady loads.

2.3 Origins of noise

Sound is related to density fluctuations and is thus associated with compressibility. The motion induced by an acoustic source (like the motion of a blade for example) is locally balanced by reciprocal motion of the fluid particles around it. However, inertial effects prevent this local motion from entirely compensating the motion induced by the source; hence local compressibility perturbations arise and are transmitted to adjacent particles. The local motion and the local compressibility perturbations have different properties and only the latter propagate at large distances from the source and are called sound. The pressure fluctuations associated with the local motion are called pseudo-sound and decay very rapidly with the distance from the source.

Several distinct noise mechanisms contribute to the emission of propeller noise. A typical spectrum is given in Fig. 2.7 and reveals the main classification into discrete-frequency (or tonal) noise and broadband noise. Both classes are further subdivided depending on the physical origin of noise:

- Tonal noise:
  - Steady aerodynamic noise, also called rotor-locked noise: is related to the aerodynamics and kinematics of the blade in uniform flow. It usually increases with the rotational velocity and is further divided into:
    - Thickness noise: is due to the displacement of the fluid by the blade and is related to the linear aerodynamic theory. Thickness noise has a monopole-type directivity pattern as illustrated in Fig. 2.8(a).
    - Loading noise: is caused by the accelerating force applied on the fluid

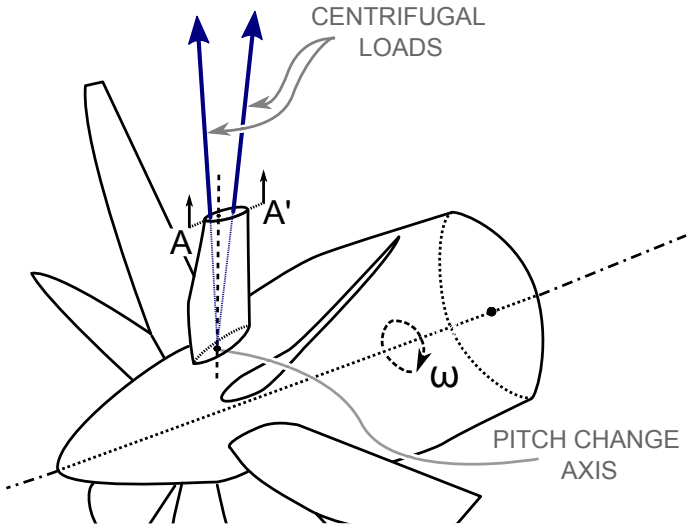

(a) Centrifugal loads of a blade element $A - A'$ considered as two concentrated masses.

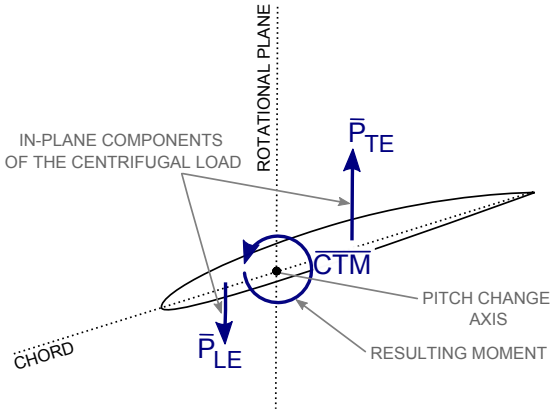

(b) In-plane components of the centrifugal loads and resulting twisting moment.

Figure 2.6: Centrifugal Twisting Moment (CTM).

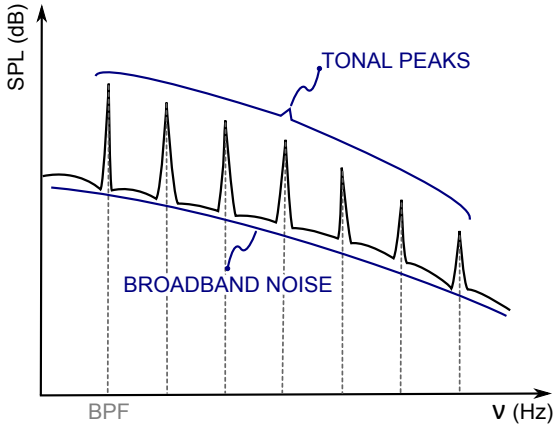

Figure 2.7: Typical envelope of a propeller noise spectrum.

by the motion of the blade surface and is also a direct consequence of the linear aerodynamic theory. Its directivity is of the dipole-type as shown in Fig. 2.8(b).

* Quadrupole noise: has various origins and is essentially accounting for non-linearities (see section 6.2.1.1).

– Noise from stationary distortion of inflow: This phenomenon induces periodic variations of the flow-field around the blade. These periodic variations distort the previous contributions and generally feed the nearest harmonics of the Blade Passing Frequency (BPF).
– Noise from ingestion of stretched turbulence: The chopping of large stretched eddies by the blades produces nearly tonal components due to the periodic interaction of the blades with those eddies.

- Broadband noise:
  – Leading Edge (LE) noise: is due to the ingestion of upstream turbulence and the consequent modification of vortices passing the LE. In general, this noise becomes dominant for highly turbulent flows but it is partly decreased by increasing the LE radius.
  – Trailing Edge (TE) and wake noise: is generated as the inertia of vortical structures is modified at the TE or in the wake. This noise is highly correlated with the boundary-layer or wake thicknesses.
  – Blade-tip vortex and laminar vortex shedding are other possible contributors as any change of inertia of these structures would radiate noise.
  – Self-noise sources: are related to phenomena occurring on the blade itself like turbulence for example, or unsteady loading.

A more complete explanation of these phenomena can be found in [43, 182, 183, 256, 257].

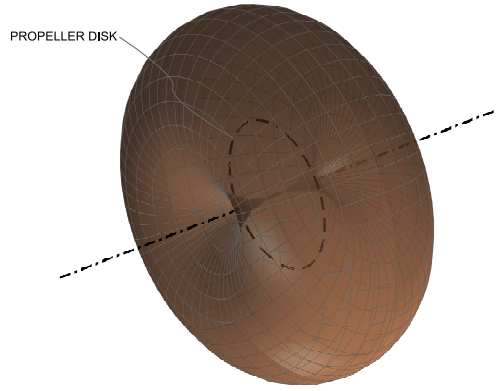

(a) Rotating monopole-type directivity typical of thickness noise.

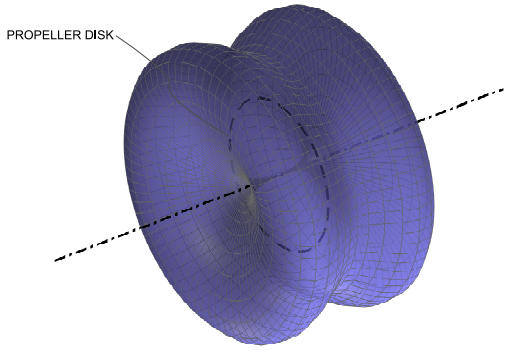

(b) Rotating dipole-type directivity typical of loading noise.

Figure 2.8: Thickness and loading noise directivities.

Part I

Of the Tools

Chapter 3

Optimization method

The term "optimization" refers to finding one or more solutions satisfying one or more constraints and corresponding to extreme values of one or more objectives. At its simplest, a design team could carry out an analysis of a single design to assess its performance. At the next level, it may wish to analyze a small number of competitive designs to determine which best suits the requirements. The next step would be to carry out a local optimization with a few variables against a single objective and a few constraints. At the end of the scale are wide-ranging searches with multiple constraints and competing objectives. Beyond this, multiple operating conditions could be considered so as to correspond as closely as possible to the in-service life and it could be required to address various disciplines simultaneously so that the whole scope of requirements (such as cost, weight, performance, manufacturability, supportability, environmental impact and ultimate disposal) is included early in the design stage.

Nowadays, the advent of parallelized computing power combined with more robust, reliable and faster codes offer the design team the possibility to conduct wide-ranging searches in a multi-point and multidisciplinary environment. This challenge has a strong potential for improvements and even innovation while respecting the demand for products with a better performance versus cost ratio and with increased quality, in a ceaselessly decreasing design-cycle time. The work-load of the design team is then shifted from making design changes to a true search for better and more-balanced designs, within a global trade-off of desirable characteristics.

Optimization algorithms have been developed to help the design team in this quest. They drive the optimization by making autonomous modifications of the variables. As such, they assist the team in conducting the search as efficiently as possible, over the multi-dimensional domain delimited by acceptable values of all design variables. For that purpose, one requirement of such algorithms is to be highly automated in order to reduce the high costs associated with manpower but also to reduce the design-cycle time. Another requirement is to provide those algorithms with information about the relationships between the design-parameters and their effect on constraints and objectives. Specific computational tools intend to provide those relationships at a relatively low computational cost in order to alleviate part of the "curse of dimensionality" [28] (i.e. the exponential increase in volume associated by adding

dimensions to a search space).

This chapter will give an overview of optimization algorithms and metamodeling techniques. Its purpose is not to give a detailed account of each of the existing methods but rather to locate the ones that are used in the present work, within their respective landscape. More details are also given for the tools used in the present arrangement which is an improved version of the procedure used and developed by S. Pierret [229] and T. Verstraete [297] at the von Karman Institute.

3.1 Optimization methods

3.1.1 Formulation of the problem

Consider a set of N design variables such as blade thickness, chord length, blade diameter, constitutive material, etc. A particular design, i.e. a particular blade shape, is represented by its vector of design variables:

$$\bar{x} = \begin{bmatrix} x_1 \\ x_2 \\ x_3 \\ \vdots \\ x_N \end{bmatrix} \tag{3.1}$$

Throughout this dissertation, the terms *solution* and *individual* will be interchangeably used to refer to a vector of design variables $\bar{x}$. The multi-objective optimization problem involving L objectives is mathematically formulated as:

$$\text{Minimize/Maximize:} \quad \Omega_i(\bar{x}, ...) \qquad i = 1..L \tag{3.2}$$

$$\text{Subject to:} \quad \Gamma_j(\bar{x}, ...) \leq 0 \qquad j = 1..M \tag{3.3}$$

$$\Phi_k(\bar{x}, ...) = 0 \qquad k = 1..P \tag{3.4}$$

$$x_p^l \leq x_p \leq x_p^u \qquad p = 1..N \tag{3.5}$$

where the functions $\Omega_i(\bar{x}, ...)$ are the objective functions, $\Gamma_j(\bar{x}, ...)$ the inequality constraint functions and $\Phi_k(\bar{x}, ...)$ the equality constraint functions. Each objective function depends on the design variables $\bar{x}$ but also on external parameters defining, for example, a particular operating condition of the propeller (rpm, flight velocity, ...) or a particular material of the blade (yield strength, Youngs' modulus,...). The objective functions correspond to some engineering performance such as efficiency, blade mass, strength, emitted noise, etc, or even a combination of them. Henceforth they require the use of dedicated analysis tools such as Computational Fluid Dynamics (CFD) or Computational Structural Mechanics (CSM). Owing to the duality principle [71], a maximization problem can be converted into a minimization problem and reversely. This enables the treatment of mixed types of objectives as minimization problems as done in the present work. In the development of multi-objective methods, one key requirement is that at least two, but preferably all, objectives are competing against each other.

Inequalities such as Eqn. 3.3 correspond to constraints that must be satisfied, in this category fall a minimum strength that needs to be guaranteed or a minimum thrust that needs to be achieved, etc. Eqn. 3.4 refers to equality constraints that give a relationship, often in explicit manner, between design variables (e.g. a relationship between variables to obtain a prescribed value for the volume of the blade). This kind of constraints are extremely difficult to satisfy and can generally be eliminated by careful selection of a reduced set of design variables owing to the information from $\Phi_k(\bar{x})$ or transformed into relaxed inequality constraints with some loss of accuracy. Both equality and inequality constraints might require dedicated analysis so they generally depend on external parameters also. For the sake of clarity, this dependence is dropped from the shorthand notations $\Omega_i(\bar{x})$, $\Gamma_j(\bar{x})$ and $\Phi_k(\bar{x})$ though it is formally an important aspect of these functions.

The last set of constraints stands for the bounds of the design variables, restricting each design variable x_p to take a value within the interval defined by the lower x_p^l and upper x_p^u bounds. These bounds define a search space of N dimensions ($\mathbb{D}^N$). Within this space, a solution is called *infeasible* if it has properties that prohibit its realization or its representation with a computer model. A blade with a negative thickness or a chord of zero length would fall into that category. One that is feasible and satisfies the *M+P* constraints is called a *compliant* solution.

By applying the functions $\Omega_i(\bar{x})$ to all individuals of the feasible regions of the search space $\mathbb{D}^N$, one in fact realizes a unique mapping of the N-dimensional search space onto the L-dimensional objective space $\mathbb{O}^L$, i.e. for each solution $\bar{x}$, a point $\bar{\Omega}(\bar{x}) = [\Omega_1(\bar{x}), \Omega_2(\bar{x}), ..., \Omega_L(\bar{x})]^T$ exists in the objective space as illustrated on Fig. 3.1. This mapping is often non-linear and the properties of these two spaces are not likely similar. For example, proximity of two solutions in the search space might result in considerable distance in the objective space. These two spaces and their relationship are of considerable importance for the optimization problem as the search among elements of $\mathbb{D}^N$ is based on decisions relying on the corresponding elements of $\mathbb{O}^L$.

3.1.2 Objectives and constraints

3.1.2.1 Pareto-front

The essence of multidisciplinary optimization is to find a set of compliant solutions that offers the best potential in terms of more than one objective and to make that set as diverse as possible. The first goal is common to all optimizations but the second is specific to multi-objective optimization as it requires a good set of trade-offs. To sort individuals with respect to competing objectives, the concept of *domination* is defined in $\mathbb{O}^L$ as:

Definition 1 *Given two compliant individuals $\overline{x_a}$ and $\overline{x_b}$ from $\mathbb{D}$, $\overline{x_a}$ is said to* ***dominate*** *$\overline{x_b}$ if and only if:*

1. $\Omega_i(\overline{x_a}) \leq \Omega_i(\overline{x_b})\ \forall i \in [1, L]$,
   and
2. $\exists i'\ :\ \Omega_{i'}(\overline{x_a}) < \Omega_{i'}(\overline{x_b})$.

This relation can be shown to be not reflexive, not symmetric, not antisymmetric but well transitive. As it is at least transitive, it qualifies as an ordering relation [71].

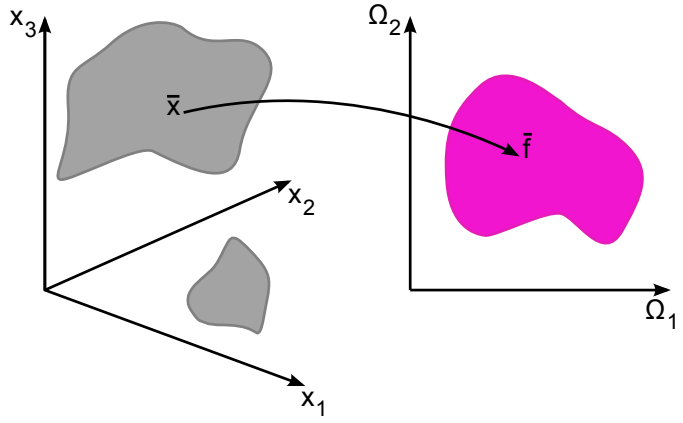

Figure 3.1: Feasible regions of a 3-dimensional search space $\mathbb{D}^3$ mapped to the corresponding 2-dimensional objective space $\mathbb{O}^2$.

Fig. 3.2 illustrates the concept of dominance; point X corresponds to a solution that dominates the one corresponding to point Y as at least one objective value of point X is strictly smaller than the one of point Y. On this figure, points X and Y correspond to solutions that *dominate strongly* the solution behind point Z as they have lower objective values for all objectives simultaneously.

Given a finite set of individuals, often referred to as *population*, one could identify a subset of individuals which have the property of dominating all other solutions which do not belong to this subset. This subset is defined as the non-dominated set:

Definition 2 *Among a set of compliant solutions $\mathcal{P}$, the* ***non-dominated set*** *of solutions $\mathcal{P}'$ are those that are not dominated by any member of the set $\mathcal{P}$.*

From there, the *globally Pareto-optimal set* is defined by

Definition 3 *The non-dominated set of the entire compliant search space is the* ***globally Pareto-optimal set.***

This definition is illustrated in Fig. 3.2 by the so called *Pareto-front* which is the locus of the globally Pareto-optimal set in the objective space (points A to F). By extension, the concept of global Pareto-optimality can be applied in the neighborhood of a solution to define a local Pareto-optimal set. At this point, it is important to note that if the objectives are not competing, the cardinality of the Pareto-optimal set becomes one. This means that the minimum solution corresponding to any objective is the same.

In the past, and at times in the present, single objective optimization is used despite most real-world engineering problems being multi-objective in essence. In this case, L=1 and most single-objective optimizations have the single goal of finding one, preferably global, optimum. Hence the goal of having a diverse set as is the

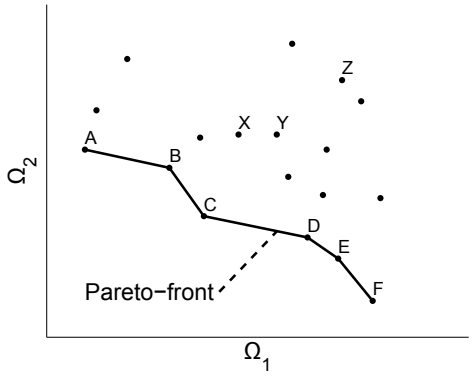

Figure 3.2: Concepts of dominance and Pareto-front in a 2-dimensional objective space $\mathbb{O}^2$ (Ω_1 and Ω_2).

case with multi-objective optimization, vanishes. Moreover, only the search space is considered in single-objective optimization and solutions are assessed directly on their objective value, hence there is no need for the concept of dominance. The last difference for such methods is that they require artificial fix-ups to blend different disciplines and/or different performance for a discipline, into one single objective. Many methods exist, such as the weighted sum and ε-constraint approaches [71], to create a composite objective but the major drawback is that optimization results depend on the chosen weights or constraint limits. This is also the reason for choosing a multi-objective approach in this work.

3.1.2.2 Constraints handling

Various methods exist to handle the inequalities of Eqn. 3.3 [251,204,160,68,226,71]. An approach that immediately comes to mind is to ignore non-compliant solutions. Any solution that violates at least one constraint is irremediably ignored. This approach is simple to implement but real-world problems require the precious information obtained by evaluating the values of the constraint functions $\Gamma_j(\bar{x})$ for non-compliant solutions to drive the search toward the compliant region.

Among indirect methods to handle constraints, the use of penalty functions is very popular. It is known that penalty functions based on the distance from feasibility outperform those based on the number of violated constraints [251,160]. So generally, they consist in replacing the objective functions $\Omega_i(\bar{x})$ by a pseudo-objective functions $\tilde{\Omega}_i(\bar{x})$ that needs to be minimized:

$$\tilde{\Omega}_i(\bar{x}) = \Omega_i(\bar{x}) + \sum_{j=1}^{M} R_{ij}\delta_j \left|\Gamma_j(\bar{x})\right| \tag{3.6}$$

$$\text{where} \quad \begin{cases} \delta_j = 0 & \text{if } \Gamma_j(\bar{x}) \leq 0 \\ \delta_j = 1 & \text{if } \Gamma_j(\bar{x}) > 0 \end{cases}$$

Hence for compliant solutions, the pseudo-objective function is equal to the objective function. In Eqn. 3.6, the penalty parameter R_{ij} is zero if one does not want the j^{th}-constraint to influence the i^{th}-objective and otherwise chosen such that both terms of the right-hand side have the same order of magnitude. Different strategies coexist to determine R_{ij} either in a static way by a choice made before starting the optimization, which is the most common, or a dynamic approach where R_{ij} is continuously updated along the optimization process. In some cases, R_{ij} is made dependent of each constraint, resulting in a R_{ij}-term within the summation. In any case, R_{ij} does not influence the Pareto-optimal set (as $\delta_j = 0$ for that set) but it does influence strongly how the optimization algorithm reaches the compliant region of the search space in case feasible solutions exist. High values of the penalty parameter might result in the pseudo-penalty functions to become ill-conditioned. Consequently, R_{ij} should be chosen with great care to balance the preservation of the algorithm against the pressure for compliance. In any way, the usage of penalty functions results in noisy pseudo-objective functions that might be detrimental to some optimization algorithms.

A common direct approach, especially in multi-objective problems, is to treat the constraints as objectives to be minimized though this transforms slightly the problem as true constraints should be just satisfied and not minimized. From this perspective, various schemes exist to stop the "constraints-optimization procedure" once compliant solutions are found.

Finally, other direct approaches exist in which the inequalities of Eqn. 3.3 are treated simultaneously with the objectives stated in Eqn. 3.2. These techniques rely on specific logic and definitions to compare individuals among a set by considering objectives and constraints. The details of such a technique are given in section 3.2.

3.1.3 Overview of optimization methods

Many of the analysis tools used to estimate or to compute $\Omega_i(\bar{x})$ and $\Gamma_j(\bar{x})$, are time consuming to run. Therefore, it is important to speed-up the search method. A common, yet not always applicable, way to do this is to work with population based methods. In contrary to their single-point counterpart, population based methods consider multiple design points in the search space, in parallel. Despite being computationally more intensive, they have become extremely popular thanks to the availability of clustered computing facilities and because they reduce considerably the design-cycle time. It goes without saying that such methods must be developed so that they can deploy their activities over the available computing facilities in an appropriate fashion thereby preventing analysis issues to form a bottleneck.

A detailed overview of common optimization methods for problems involving multiple design variables, can be found in [294, 164] or [229, 297]. Nevertheless, a brief recap is given here in order to situate the method used in this work in the global framework. This recap is by no means a complete account of all existing methods nor a thorough description of the ones presented. Additionally, most of the methods hereunder where developed for single-objective problems so that their implementation for population-based searches is impractical. Optimization algorithms differ in the way they update the Q design vectors $\bar{x_q}^t$ of a population ($q \in [1, Q]$) at the t-th iteration, into the Q design vectors at iteration $t+1$: $\bar{x_q}^{t+1}$. In general, the update

can be represented by:

$$\bar{x_q}^{t+1} = \bar{x_q}^{t} + \alpha_t \bar{s_q}^{t} \tag{3.7}$$

where $\bar{s_q}^{t}$ is the vector defining the search direction and α_t is a scalar relaxation factor. Optimization methods are classically grouped depending upon the order of the derivatives of $\bar{\Omega}(\bar{x})$ they require to determine $\bar{s_q^t}$ and α_t.

3.1.3.1 0^{th}-order methods

Only the function values are used in these search methods; hence they do not require any higher-level information than $\Omega_i(\bar{x})$ and the constraint values. Among these methods, a distinction is made between stochastic methods (purely random) and heuristic methods (that obey a rule). In most cases, these methods are non-deterministic in that successive searches, starting from identical sets of individuals, will not follow the same path toward the optimum.

- Random search
  This very simple search algorithm works by selecting randomly candidate vectors $\bar{x_q}^{t}$ at each iteration and evaluating $\bar{\Omega}(\bar{x_q}^{t})$. This inefficient search requires extremely large population sizes to be successful and avoid being trapped into local extrema. Constraints can be dealt with in direct or indirect ways.
- Walk search or Random walk
  This kind of search starts from a population $\bar{x_q}^{t}$ and perturbs those vectors by $\bar{s_q}^{t}$ in a specific direction. The direction can be fixed (walk search) or obtained randomly (random walk). The relaxation factor is usually fixed. In this case, a new vector $\bar{x_q}^{t+1}$ will replace the current one $\bar{x_q}^{t}$ if it is a better design. Direct constraint handling is very familiar with this type of search.
- Simulated Annealing (SA)
  SA is inspired by the process whereby crystalline structures take up minimum energy configurations if cooled sufficiently slowly from some high temperature. It relies usually on a random scheme to perturb design vectors $\bar{x_q}^{t}$ by the quantity $\bar{s_q}^{t}$. A new design $\bar{x_q}^{t+1}$ replaces $\bar{x_q}^{t}$ at once if it is better. If it is worse, it will replace $\bar{x_q}^{t}$ with a given probability. This probability obeys a so-called Boltzmann probability distribution and is based on the difference in performance between both designs (virtual energy) and an ever decreasing number (virtual temperature). Constraints are often enforced by indirect methods in this case.
- Particle Swarm Optimization (PSO)
  PSO is inspired by the dynamics of bird flocks. For the Q individuals (particles) of a population (swarm), the direction $\bar{s_q}^{t}$ is determined for each individual by its best previous position in the search space as well as the relative position between the individual and the entire swarm's best known individuals. Doing so, the swarm is expected to move globally toward better solutions. This method is relatively new [165, 266] and is becoming increasingly popular.
- Evolutionary algorithms (EA)
  EA's mimic Darwinian evolutionary principles. This means that a population of design vectors $\bar{x_q}^{t}$ "evolves to" iteration $t+1$ by survival of the fittest after selection, crossover and mutation among the members of the population.

Selection is always performed in the objective space while new solutions are created in the search space by exchange of partial information among solutions from the selected pool and by perturbing them in their neighbourhood. The introduction of those principles in optimization algorithms has been done by J. Holland [149] and I. Rechenberg [243]. The obvious advantage of such methods is that they are intrinsically population-based.

– *Genetic Algorithm (GA)*: This particular class of EA is also the one that is the closest to the human-evolution process. The most well known work about GAs is that by D. Goldberg [126]. As GAs are the most convenient place to explain the basic principles of EAs, a more detailed description is given.
First, each of the Q individuals $\bar{x_q}^t$ of the population at the t^{th}-iteration are coded in a string as illustrated on Fig. 3.3. For convenience, binary coding was used first in analogy with the coding of our chromosomes, but real-coded variants exist to circumvent the limitations in accuracy related to the number of bits. The obtained code is the *genotype* of the individuals.
Then the population evolves when two different individuals (two parents) from t^{th}-population mate and generate two offspring. Doing so, the population size is kept constant but variants exist.
Selection of the parents is based on the idea that matting two individuals with desirable characteristics will result in an offspring having also favourable characteristics and preferably better ones. Selection is classically performed by either the tournament or roulette-wheel rules. In either cases, selection is performed on the *phenotype* of the individuals which are its observable characteristics such as $\bar{\Omega}(\bar{x_q}^t)$. In a tournament selection, s individuals are chosen randomly from the population and only the best is kept as parent. The second parent is selected the same way. The tournament size s enables a switch between elitist selection (high values of s) and diversity-preserving selection (low values of s). Usually, strong elitism (down to $s = 2$) is very effective. In a roulette-wheel selection, the probability for an individual to be selected is proportional to its share in the total fitness of the population (i.e. the sum of the fitness of all individuals). D. Goldberg and K. Deb [127] have shown that tournament selection, though less elaborate, has better or equivalent convergence and complexity than any other selection operator.
Consequently after selection, reproduction can now occur. The cross-over operator used for that purpose is schematically shown in Fig. 3.4 where the cross-over location is chosen randomly. To preserve diversity, a probability between 70% to 90% is assigned to the cross-over operation so that parents have a chance to pass directly in the next generation without reproduction. Additionally, mutation could occur. This operator changes one or more random bits of the offspring (see Fig. 3.5) with a probability of occurrence of the order of 0.1 to 0.8%. The purpose of mutation is to create new individuals and avoid too high similarity between genotypes of successive generations. This way, the algorithm avoids being cornered into local optima. After these operations, the offspring replace the parents in the new generation.

$$\bar{x_q}^t = [x^t_{q,1}, x^t_{q,2}, x^t_{q,3}, ..., x^t_{q,N}]^T$$

$$\Downarrow$$

$$\overbrace{10110100}^{x^t_{q,1}}\overbrace{11010101}^{x^t_{q,2}}...\overbrace{00110101}^{x^t_{q,N}}$$

Figure 3.3: Coding of a solution into a binary string.

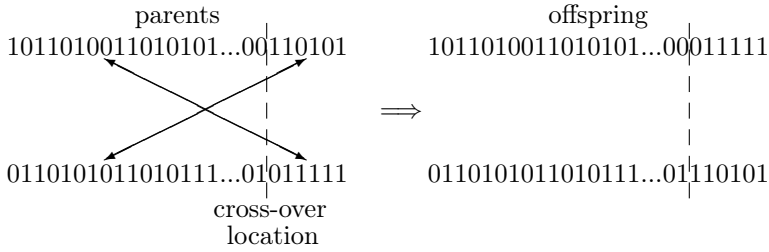

Figure 3.4: Cross-over operator applied to two parents to create two offspring.

Given their long existence, GAs exist with many variants in how the operators work. Commonly encountered features include augmentation of the elitism strategy by unaltered passing of the best individual of a generation to the next one so that the loss of valuable information is prevented.
GAs were originally developed for single-objective problems. For this reason, pseudo-objective functions have often been used to deal with constraints [126, 251, 160, 71] but other techniques were also used like the "death penalty"[1]. In the choice of penalty functions, care should be given to the preservation of information which is the counterpart of diversity.
Despite their single-objective origins, GAs have successfully evolved in the multi-objective environment first by the weighted sum of objectives, then through Pareto-optimality. The various Pareto-optimality approaches [71] are more complex to implement but do not suffer from the sensitivity and bias introduced by the values of the weights [63, 71].
A golden rule in the development and use of GAs is to maintain a proper balance between the extent of exploration, obtained by the cross-over and mutation operators, and the extent of exploitation by the selection operator. This is achieved by parameters such as the population size Q, the tournament size s, the degree of elitism, and various probabilities.

– *Differential Evolution (DE)*: DE has been developed by K. Price and

[1] Rejection of non-compliant individuals.

1011010$\boxed{0}$11010101...0$\boxed{0}$011111

$\Downarrow$

1011010$\boxed{1}$11010101...0$\boxed{1}$011111

Figure 3.5: Mutation operator applied to one offspring of Fig. 3.4 on randomly chosen bits.

R. Storn [277] and use selection, mutation and cross-over operators like GAs. The difference lies in the fact that cross-over is done by exchange of complete design variables rather than parts of the string representing a variable. DE will be fully described in section 3.2.

- *Evolution Strategies (ES)*: ESs were developed at the same time as GAs but differ by the absence of a cross-over like operator and the manipulation of real (uncoded) parameter values. Hence ESs rely solely on the selection and mutation operators applied to each $\bar{x_q}^t$ to form $\bar{x_q}^{t+1}$. The main parameters are the strength and distribution of mutations.
- *Evolutionary Programming (EP)*: EP is a mutation-based algorithm. It uses a stochastic selection process to decide the next parents from the combined set of parents and children at the t^{th}-iteration. Mutation is related to the value of the objective function so that successful ideas are mutated less.

The previous algorithms are built with very simple operators such as selection, cross-over and mutation, and provide numerous variants depending on how these operations are combined and on what kind of information they act. EAs get their power from the structured, yet randomized, exchange of information between individuals from one generation to create the next one. They result from the formal analogy with the striking, albeit undeniable and inescapable, conclusions of biology and anthropology. Further development of EAs continue to be inspired by these sciences and see the apparition of *distributed EAs* which subdivide the population into "islands". The sub-populations evolve in isolation and exchange some individuals on regular basis. The net result of such an algorithm is to reduce the number of objective-function evaluations needed to reach the optimum [122].

EAs have as common threads that:

1. they evolve from one population into another and usually start with a random set,
2. they include some finite probability for mutation,
3. they include mechanisms to avoid loss or deterioration of the best individuals,
4. they use operators based on stochastic principles and do not involve derivatives of any kind.

These features give them the following abilities by nature:

1. they can capture multiple optima of multi-modal problems in one single run but require large amounts of function evaluations,
2. they explore all parts of the search space, even if it is composed of disjoint regions, and are keen not to be trapped in local optima,
3. they exploit promising ideas but do not guarantee ultimate convergence and are slow at resolving precise optima,
4. they do not assume any particular property, like continuity or smoothness, of the problem to be solved since they do not use deterministic rules; hence they deal seamlessly with noisy objective functions.

3.1.3.2 1^{st}-order methods

1^{st}-order methods require evaluation of the first order derivatives of $\Omega_i(\bar{x})$. The gradient $\nabla\Omega(\bar{x_q}^t)$ in single-objective problems or the Jacobian matrix $J_{\bar{\Omega}}$ $(L \times N)$ for multi-objective problems is used to determine the search direction $\bar{s_q}^t$. These methods involve a high computational cost to compute the gradient possibly for all individuals of a population. On top of this, strict assumptions are needed with respect to continuity of the objective function and they perform poorly in presence of discontinuities of the first derivative and noise.

Once the gradient is known, the first method that comes to mind is the steepest descent due to A. Cauchy. For a single-objective problem, the search direction is opposed to the strongest gradient:

$$\bar{s_q}^t = -\nabla\Omega(\bar{x_q}^t) \tag{3.8}$$

and the relaxation factor α_t (see Eqn. 3.7) is chosen with care to avoid overshooting the minimum. Extensions to multi-objective problems are based on combinations of the gradient vectors contained in the Jacobian matrix.

Other methods use the information from one or more previous iterations to increase convergence. This is because the local steepest descent rarely points toward the desired optimum [164]. These methods fall within:

$$\bar{s_q}^t = -\nabla\Omega(\bar{x_q}^t) + \beta_t \sum_i \bar{s_q}^{t-i} \tag{3.9}$$

Evaluating $J_{\bar{\Omega}}$ is a computationally demanding task. Among the available methods one finds:

- Finite-difference method:
  Truncating the Taylor series expansion of each $\Omega_i(\bar{x_q}^t)$ $(i = 1, ...L)$ to the first order terms corresponds to evaluating $\Omega_i(x^t_{q,n})$ $(n = 1, ...N)$ with a small perturbation of the design variable x_n:

  $$\frac{\partial\Omega_i(\bar{x_q}^t)}{\partial x_n} \approx \frac{\Omega_i(\bar{x_q}^t + \varepsilon_n\hat{u}_n) - \Omega_i(\bar{x_q}^t)}{\varepsilon_n} + \mathcal{O}(\varepsilon_n) \tag{3.10}$$

  Hence this method is a first order approximate and requires $(N + 1)$ computations.

- Algorithmic Differentiation or Automatic Differentiation:
  This method requires the constraint- and objective-functions to be preferably

written in a high-level programming language such as C or C++. The complete source code (including all libraries) is decomposed into a long sequence of a limited set of elementary arithmetic operations (+,−,.,...) and intrinsic functions (sin,exp,...). The chain rule of differential calculus is then applied to the original source code to create a new code capable of exactly computing the derivatives of the objective- and constraint-functions with respect to the design variables. The implementation is thus at the programming level, and might prove to be cumbersome. Nevertheless, it results in high accuracy yet the computation speed is dependent on N.

- Adjoint methods:
  For problems were the number of design variables N is greater than the number of outputs $L + M + P$, the adjoint formulation has the advantage of a reduced computational cost when compared to the previous methods. Its first application within the framework of design is the work of O. Pironneau [230]. The idea is to use the Lagrange multipliers to transform key differential equations of the analysis (used to compute the objectives and constraints) into their respective adjoint equation. The cost of solving the adjoint and original equations next to each other is twice the cost of solving the original equation solely. The adjoint solutions are then used to compute the gradient.
  In the continuous version of the adjoint method, the adjoint equations are found analytically from the governing equation, and are then discretized whereas in the discrete version, the governing equation is first discretized and the discrete adjoint equations immediately follow.
  Because of their low computational cost, adjoint formulations are very popular in design [230, 153, 245, 154, 220, 207]. However, the main drawback is the difficulty to formulate the differential equations relevant for the problem and translate them into the adjoint problem; a step that might end up taking some man-months. This implies that changes to the objective functions (due to changes in the analysis tools or reflecting changes in strategy from the design team thanks to information gained along the design process) are difficult to implement.

3.1.3.3 2^{nd}-order methods

The first known second order method is I. Newton's method [294]. It requires knowledge of the Hessian matrices H_{Ω_i} containing all second order derivatives everywhere. The elements h^i_{jk} of $H_{\bar{\Omega}}$ for particular objective Ω_i are given by:

$$h^i_{jk} = \frac{\partial^2 \Omega_i(x^t_{q,n})}{\partial x_j \partial x_k} \tag{3.11}$$

These matrices are used to compute the search direction $\bar{s_q}^t$ and the factor α_t. The move is done at each step in the direction of the minimum of the approximating quadratic form. For a quadratic function, the first step completes the search but for non-quadratic functions (like most real-world problems), additional iterations are needed but convergence is faster than any first order method.

The disadvantage of 2^{nd}-order methods is that they rely on the availability of the Hessian. In most practical applications, the Hessian is not directly available,

expensive to compute and prone to difficulties due to its sensitivity to noise. To circumvent this, methods have been developed relying on higher order truncation of $\Omega_i(\bar{x_q}^t)$. These terms are included in Eqn. 3.9 to form quasi-quadratic search directions. These methods are usually qualified as "quasi-Newton's" method.

3.2 Multi-Objective Differential Evolution

As previously mentioned, DE is a particular class of EA. The extension of DE into Multi-Objective Differential Evolution (MODE) is the result of various works [16,25]. MODE has proven to offer an acceptable trade-off between convergence rate (number of iteration needed to locate optima) and robustness (ability not to miss the global optima). It even proved to perform better than advanced GAs by rendering a Pareto-front with better diversity [25]. MODE uses real-coding of the design variables. The process starts with a random population comprising Q individuals $\overline{x_0}$. At the t-th generation, an individual q of the population ($q \in [1, Q]$) is represented by

$$\overline{x}_q^t = [x_{q,1}^t, x_{q,2}^t, ..., x_{q,N}^t]^T \tag{3.12}$$

To evolve $\overline{x}_q^t$ toward the next generation, three other vectors $\overline{a}$, $\overline{b}$ and $\overline{c}$ are randomly picked within the population such that $\overline{x}_q^t \neq \overline{a} \neq \overline{b} \neq \overline{c}$. Then, a trial vector $\overline{y}^t$ is defined with

$$y_i^t = a_i + F.(b_i - c_i) \qquad \text{for } i = 1...N \tag{3.13}$$

in which F ($F \in]0, 1.2[$), the weighting factor, is arbitrarily chosen by the user . K. Price and R. Storn determined the upper limit empirically [236] and advise to use values in the range $[0.4, 1.0]$. A value of 0.8 is recommended [8]. Next, recombination is performed to form the candidate vector $\overline{z}^t$ by

$$z_i^t = \begin{cases} y_i^t & \text{if} \quad r_i \leq C \\ x_{q,i}^t & \text{if} \quad r_i > C \end{cases} \qquad \text{for } i = 1...N \tag{3.14}$$

In this step, C, the cross-over constant, is an arbitrary evolutionary constant chosen by the user ($C \in]0, 1[$) and r_i is a uniformly distributed variable chosen randomly such that $r_i \in [0, 1[$. DE is much more sensitive to the choice of F than it is to C which is more like a fine-tuning constant [8].

The previous steps coalesce the mutation and recombination operators; the last relates to the cross-over operator discussed in section 3.1.3.1 and is responsible for the exchange of information between individuals among the parent population. The random mutation is induced by Eqn. 3.14.

Now $2Q$ individuals coexist and prior to the next iteration, the population size is restored to Q by a set of selection rules. There exists various sets of selection rules for single- and multi-objective problems [16, 185, 239, 24].

In the present approach, multi-objective selection is performed by a method similar to the elitist Non-dominated Sorting Genetic Algorithm (NSGA-II) proposed by Deb et al.. [72]. For the population consisting of the parents and offspring that entirely satisfy all constraints (i.e. $\Gamma_j(\overline{x}_q^t) \leq 0 \ \forall j \in [1, M]$), the ranking relies on the concept of domination (see definition 1). The sorting first selects all the non-dominated individuals, assigns them the rank 0 and removes them temporarily from the population.

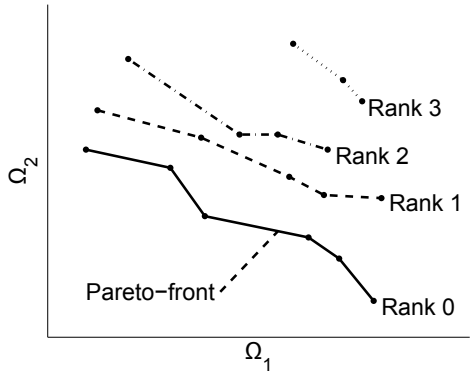

Figure 3.6: Pareto-ranking of the population from Fig. 3.2 according to two objectives Ω_1 and Ω_2.

Next, all non-dominated individuals of the remaining compliant population are assigned the rank 1 and this algorithm is repeated until the complete set is ranked as shown in Fig. 3.6, where the rank 0 individuals form the so called Pareto front. Once this population is ranked, the new parent-population $(t+1)$ is filled by the individuals from the rank 0 front, then the rank 1 ones and those of the consecutive fronts until it comprises Q individuals. If a front cannot be accommodated entirely, the individuals required to attain the Q individuals in the new population, are selected with the intervention of a distance metric so that diversity is maintained. The distance metric used here is the geometrical distance between the points in the objective space $\mathcal{O}$ though other metrics such as the crowding distance [72, 239] exist but are more complex to implement.

In case less than Q individuals of the $2Q$ population composed of parents and offspring, comply with all constraints; then the remaining slots in the $t+1$ parent-population are filled with individuals that do not satisfy the constraints. That selection of those individuals treats the constraints as objectives and applies a similar ranking (i.e. the best ranked individuals are those that are the closest to satisfy the constraints). The required number of best ranked individuals are passed and in case two individuals have the same rank with respect to the constraints, the one with the best rank in the objective space is selected.

3.3 Metamodelling

As discussed previously, evolutionary methods have the disadvantage of involving large populations and numerous generations. Consequently, these methods tend to be computationally expensive as real-world problems often involve numerical simulations that may well be measured in hours or even days. Moreover, having all the individuals of a population assessed in parallel would result in prohibitive costs for software

licenses. This often results in some sequentiality in the computational process and thus increases the computational time and cost.

One of the measures taken to reduce the number of expensive function evaluations is the implementation of *hierarchical EAs* [264,122]. These algorithms use low fidelity analysis tools as accelerators. This means that the objective functions of some individuals are computed by using tools that are computationally less expensive, but are also less accurate. For example, this could be achieved by using larger discretization steps in the spatial and/or temporal discretization of the characteristic equations of the problem or by using a reduced set of characteristic equations (e.g. by using the Euler equations instead of the Navier-Stokes equations for a fluid dynamics problem). When hierarchical EAs are used, promising individuals evaluated by the low fidelity analysis need to be reassessed by the high fidelity analysis. Many implementations of hierarchical EAs are build upon distributed EAs.

The next step in reducing the computational burden of EAs is to work with a *metamodel assisted EA*. The high or medium fidelity tools, based on the physical model, are replaced by interpolators that are trained on a limited set of individuals analyzed with the high fidelity tools. These interpolators are developed to be computationally inexpensive and as accurate as possible though the accuracy drops in general when evaluating points that lie far from the sample points or even out of the sample domain (in the case of extrapolation). The interpolators are "models for the model", literally *metamodel* but the terms *surrogate model* are also used. Only those metamodelling techniques that are currently popular in the literature will be discussed into more details but an overview can be found in [268, 115].

Metamodels are defined mathematically by:

Definition 4 *Suppose the analysis of a particular design $\overline{x}$ can be written as a function f:*

$$\overline{p} = f(\overline{x}), \quad f : \mathbb{R}^N \mapsto \mathbb{R}^R$$

where $\overline{p}$ is a vector of R performance variables. A ***metamodel*** *is a function $\tilde{f} : \mathbb{R}^N \mapsto \mathbb{R}^R$ with a much lower computational cost than f and such that*

$$\|\tilde{f}(\overline{x}) - f(\overline{x})\| < \varepsilon$$

where $\|.\|$ is an appropriate $\mathcal{L}_p$ norm and ε is sufficiently small when compared to $f(\overline{x})$ so that $\overline{p}$ is approximated by $\tilde{p} = \tilde{f}(\overline{x})$.

Due to their reduced accuracy, metamodels used in optimization are often, but not always, accompanied by scarce calls to the high fidelity analysis. The purpose of these calls is to somewhat maintain or increase the accuracy of the optimal solutions found. One way is to use the metamodel only in the direct vicinity of known designs and increase the probability to use the high fidelity analysis with the distance those designs [122]. The obvious weakness of such approaches is that proximity in the search space does not necessarily result in proximity in the objective space. A second technique consists in using the metamodel systematically on all individuals and high fidelity analysis on the most promising ones at each generation. *On-line training* is used to refer to this implementation. A third procedure is to use the metamodel during several generations, stop the evolutionary process temporarily and then recur to training of the metamodel on a set composed of high fidelity analysis of the initial individuals

augmented by those of the current generation before starting the evolutionary process again. This is *off-line training* as used in [229, 297].

Constructing a metamodel involves three steps: choosing an experimental design to generate data (section 3.3.1), choosing a mathematical model to represent the data, and finally fitting the model to the observed data. The last two steps differ strongly depending upon the mathematical background of the model and some are described in the subsequent sections. Once these steps are accomplished, the metamodel is ready for use.

3.3.1 Design of Experiments (DoE)

Since metamodels require a set of solutions to be trained, care should be given on how this set is chosen in the search space $\mathbb{D}$ so that the metamodel represents all possible solutions with maximum fidelity yet at moderate computational cost. DoE is used with a twofold set of conflicting objectives: to decide on a set of points (where high fidelity analysis should be conducted) so as to maximize the predictive capability of the metamodel, and to minimize the number of points so as to keep the computational cost of evaluating them within reasonable limits. Given the ranges from Eqn. 3.5, the search space $\mathbb{D}$ is often represented as an hypercube of N dimensions. Depending on the problem to be modelled, on the class of surface to fit and on the number of sampling points one can afford, one of the following tools may be best suited:

1. Monte Carlo technique: This pure random sampling technique is the only completely unbiased one. It fills the search space $\mathbb{D}$ with randomly chosen points, as illustrated in Fig. 3.7(a) and requires usually large amounts of samples to be safe. This technique could end up in regions of the search space left completely unexplored and fails to exploit the fact that limited curvature of the response surface is expected since physical problems are modelled [164].
2. Latin Hypercube sampling: For this technique, the range of each design variable x_p is divided into S bins of equal probability, hence a total of S^N bins in $\mathbb{D}$. Subsequently, S samples are generated such that for each design variable, no two values should be in the same bin. In other words, there is one single sample in each bin as in Fig. 3.7(b). Various approaches exist to make sure that the latin hypercube keeps good space-filling characteristics by avoiding concatenation of samples in neighbouring bins. Latin hypercube sampling has good coverage but require many samples to do so.
3. Full factorial design: Here, the range of each variable is divided into S levels. Sampling of $\mathbb{D}$ is achieved by evaluating all the corners of the hypercube and possibly some interior points. This means S^N points so that this kind of sampling is usually far too expensive. Moreover, it tends to focus on the exterior points. Variants, illustrated in Fig. 3.7(c), involve restricted ranges such as $x_p^l + 0.15(x_p^u - x_p^l) \leq x_p \leq x_p^u - 0.15(x_p^u - x_p^l)$ instead of $x_p^l \leq x_p \leq x_p^u$. In case only the minimum and maximum design variable values are used, one speaks of a 2^N factorial.
4. Fractional factorial design: This sampling only considers a fraction $1/2^F$ of the full factorial design. Thus it requires only 2^{N-F} evaluations at the cost of accuracy. These samplings are based on the assumption that the system is dominated by main effects that must be sampled and low order interactions

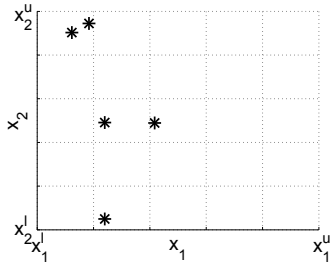

(a) Monte Carlo sampling with 5 samples.

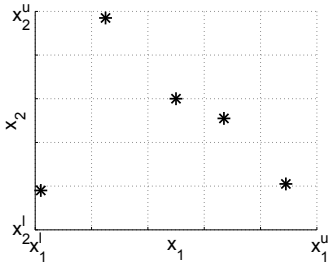

(b) Latin hypercube sampling with 5 bins ($S = 5$).

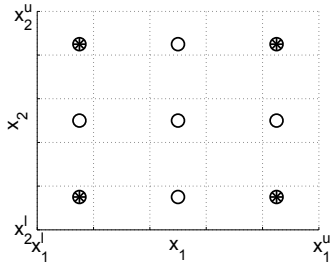

(c) Full factorial design with 2 ($*$, $S = 2$) and 3 ($\circ$, $S = 3$) levels.

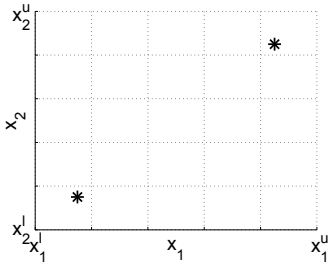

(d) Partial factorial design with 2 samples.

Figure 3.7: Common DoE sampling technique applied on a 2D search space (N=2).

that can be neglected during the sampling [268]. Fractional factorial sampling is illustrated in Fig. 3.7(d).

3.3.2 Response Surface Model (RSM)

RSM uses polynomials of different orders to represent $\tilde{f}$ [211, 115]. For a vector $\overline{x} = [x_1, x_2, ..., x_N]^T$, the quadratic approximate of the i^{th}-component of $f(\overline{x})$ is given by

$$\tilde{f}_i(\overline{x}) = \beta_{i0} + \sum_{1 \leq j \leq N} \beta_{i,j} x_j + \sum_{1 \leq j \leq N} \sum_{j < k \leq N} \beta_{i,(N-1)+j+k} x_j x_k \tag{3.15}$$

in which the β-coefficients are determined through least squares regression applied on the set of sampling vectors $\overline{x}_1, \overline{x}_2, ..., \overline{x}_S$ to minimize $\|\tilde{f}(\overline{x}) - f(\overline{x})\|$. This implies that S should be larger than or equal to N to avoid under-determination of the coefficients. This is problematic as the number of unknown coefficients for regression of the B^{th}-order is given by $(N + B)!/(N!.2B)$ so it is recommended to use RSM for problems involving say 10 variables [164]. In some cases, splines assembled in patchwork to cover the design space are also used but they require some form of smoothness between patches and thus are cumbersome to implement.

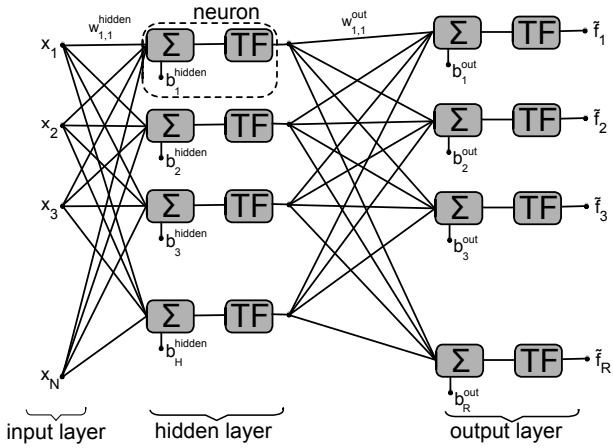

Figure 3.8: ANN network with a single hidden layer.

This interpolation technique has difficulties to cope with noisy, multi-modal or even discontinuous data. Still it is popular because derivation of the approximate function $\tilde{f}(\overline{x})$ is easy. Therefore, RSM are often combined with Newtonian search methods and off-line training.

3.3.3 Artificial Neural Network (ANN)

Neural networks are inspired by certain brain functions and have proven to be powerful interpolators [179, 304, 305, 62] as well as extrapolators [268] which is a rare property. They have seen numerous applications in fields such as signal processing, control theory or even prediction of financial markets. For a vector $\overline{x} = [x_1, x_2, ..., x_N]^T$, the approximate of the vector $f(\overline{x})$ is constructed according to Fig. 3.8. This figure illustrates how elementary processing units called *neurons* or *nodes* are arranged in successive layers (one hidden layer containing H neurons in the present example but more hidden layers are possible). These layers are connected by *connection weights* w_{ij} with an input layer consisting of the N components of $\overline{x}$ and an output layer containing the R components of the vector $\tilde{f}(\overline{x})$. Additional hidden layers would be interconnected with the neighbouring ones. A network architecture such as the one illustrated on Fig. 3.8 results in a feed forward ANN as the output of a layer is directed in one way to the next layer.

Any neuron j is performing two operations in the present case:

1. it sums up all weighted input values and a bias b_j:

$$in_j = \sum_{i=1}^{N} w_{i,j} x_i + b_j \tag{3.16}$$

2. it processes the resulting value in_j through a transfer function $TF(in_j)$:

$$out_j = TF(in_j) \tag{3.17}$$

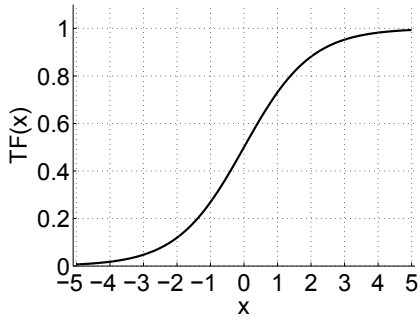

Figure 3.9: Sigmoid function.

Though a variety of transfer functions exists, the sigmoid function (see Fig. 3.9) is used in most cases, hence:

$$TF(in_j) = \frac{1}{1 + e^{-in_j}} \tag{3.18}$$

An important property of ANNs is their ability to match any continuous function from $\mathbb{R}^N$ to $\mathbb{R}^R$ by a three layers feed-forward neural network with $(2N + 1)$ neurons in the hidden layer. This property is known as one of Kolmogorov's theorems [305] and holds without any assumption on the relation between inputs and outputs. It is a pure consequence of the topology of the network combined with the implicit use of power series by the non-linear transfer function.

Once the step of choosing a topology is made, one is left with the determination of the connection weights $w_{i,j}$ and the biases b_h so that the $\mathcal{L}_p$-norm of definition 4 is minimized. With the topology of Fig. 3.8, the number of network parameters amounts to $N_{param} = H.(N+1)+R.(H+1)$. In the case of a DoE sampling involving N_{sample}, $R.N_{sample}$ equations are available. If one wants the system to be at least determined, the number of neurons in the hidden layer should obey [304]:

$$H \leq H_{crit} = \frac{(N_{sample} - 1)R}{N + R + 1} \tag{3.19}$$

In most cases, where low values of N_{sample} due to cost considerations would result in extremely low values of H, the number of neurons H is chosen greater than the critical number H_{crit}. The system is thus under-determined and connection weights are not uniquely defined. This multiplicity is taken as an advantage by splitting the set of samples into a training set used to compute the parameters and a validation set used to select that set of parameters that minimizes the error on the validation set.

Training of the network, also called "learning" by analogy to human brains, is itself an optimization problem. There exists numerous techniques in the literature [143,304,62,233,268,239]. These techniques range from gradient based methods to the use of EAs. However, the most common method is the error back-propagation [143] that consists in an iterative modification of the parameters to minimize the error $\|\tilde{f}(\overline{x}) - f(\overline{x})\|$ for each sample. Modification of the parameters ($w_{i,j}$ and b_h) is based on the difference between $\tilde{f}(\overline{x})$ and $f(\overline{x})$ hence the crucial requirement for infinitesimally

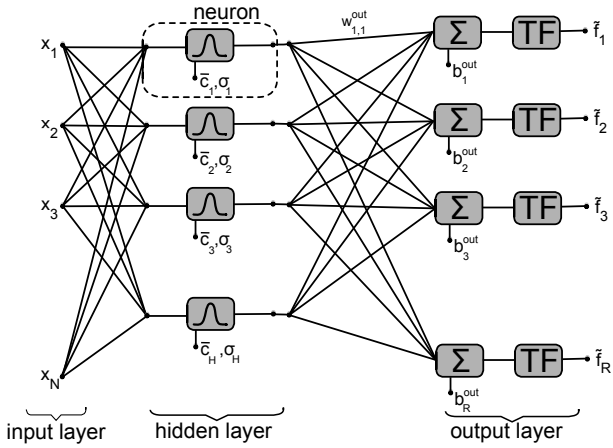

Figure 3.10: RBF network.

small step sizes in the iterative procedure to guarantee convergence [233]. Sometimes, early stopping is used. This requires to split the samples set into a training set (used to determine the parameters), a testing set (used to test the ability of the ANN to predict points different from the training set) and a validation set (used for eventual disambiguation). Early stopping refers to a premature interruption of the learning procedure when the error on the testing set is minimum instead of waiting for absolute convergence of the error on the training set. The purpose of early stopping is to avoid the ANN to become too complex so that it overfits the data by fitting the noise as well. If this would occur, the training error falls but the metamodel becomes less general as it fails to predict safely for points that are not in the training set.

3.3.4 Radial Basis Function (RBF)

RBF networks [85, 187, 164, 115] belong to the same class of generalized linear models as ANNs but differ in the composition of neurons. As for ANNs, suitable RBF networks can approximate any function to an arbitrary degree of accuracy. Evidence exists that RBF networks are effective extrapolators [164], though some care should be taken as is usual with extrapolating data. They are sometimes preferred to ANNs because they are easier to understand and interpret. The major differences lie in the fact that the input of the neurons in the hidden layer (see Fig. 3.10) is the vector $\overline{x}$ itself and that neuron j of the hidden layer applies a non-linear function $g : \mathbb{R}^N \mapsto \mathbb{R}$ with radial basis $(\overline{x} - \overline{c}_j)$. So the one-dimensional output of those neurons is given by

$$g_j(\|\overline{x} - \overline{c}_j\|)$$

Typical choices for the RBF include but are not limited to linear splines, cubic splines, multiquadrics and Gaussian functions [164] as is the case in the present implementation. The Gaussian function is given by

$$G(\|\overline{x} - \overline{c}_j\|) = \exp\left(-\frac{\|\overline{x} - \overline{c}_j\|^2}{\sigma_j^2}\right) \tag{3.20}$$

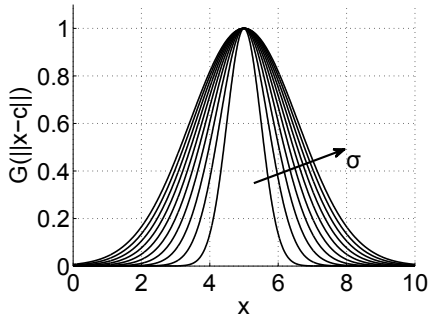

Figure 3.11: Gaussian function with $c = 5$.

where σ_j is a shape parameter used to control the domain of influence of G, centered around $\overline{c}_j$ as illustrated in Fig. 3.11. Following this, the output of the hidden layer depends directly on the nearest centers as is illustrated in Fig. 3.12. The output of the network is then computed by the weighted sum of all responses from the hidden layer though in some cases as illustrated in Fig. 3.10, an additional transfer function is applied:

$$\tilde{f}_i = TF\left(\sum_{h=1}^{H} w_{i,h}^{out} \exp\left(-\frac{\|\overline{x} - \overline{c}_h\|^2}{\sigma_h^2}\right) + b_i^{out}\right) \tag{3.21}$$

Determination of the network parameters like the centers, the shape parameters, the biases and the weights is done with the same techniques as for the ANN described in section 3.3.3.

3.3.5 Kriging

Kriging refers to a statistically rigorous approach to compose a metamodel for the deterministic results of computer analyses. Kriging is based on Gaussian stochastic process models and its origins are traced back to D.G. Krige [173, 260], a South African mining engineer who used statistical techniques to predict gold grades at the Witwatersrand complex. One of the key ideas behind Kriging is that the function values at the training points are purely deterministic and not prone to errors; hence the uncertainty derived from residuals in the least-squares sense, have no obvious reason to be. It is in fact desirable that the observed data (i.e. the training set) are matched perfectly (i.e. $\tilde{f}(\overline{x}) = \overline{f}(\overline{x})$). For this reason, some statisticians [260, 172] have proposed to approximate a relationship of the type $p = f_i(\overline{x})$ of one component of $\overline{f}(\overline{x})$ by a combination of a polynomial model, $R_i(\overline{x})$ in Eqn. 3.22 plus departures, $Z_i(\overline{x})$:

$$\tilde{f}_i(\overline{x}) = R_i(\overline{x}) + Z_i(\overline{x}) \quad (i \in [1, ...R]) \tag{3.22}$$

where $R_i(\overline{x})$ is a known polynomial function and $Z_i(\overline{x})$ is the realization of a Gaussian stochastic process with zero mean. The purpose of $R_i(\overline{x})$ is to "globally" approximate the main trend of $f_i(\overline{x})$. This polynomial could be the result of an RSM approach but many authors [268,164,157] use a simple constant. So $Z_i(\overline{x})$ is supposed to create

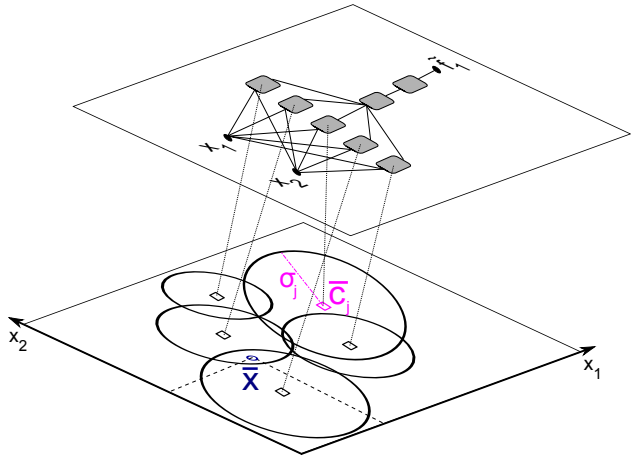

Figure 3.12: Interpretation of a 2D RBF interpolation showing the correspondence between the network layout (above) and the domain of activation of the neurons (below) determined by their center $\overline{c}_j$ and shape parameter σ_j.

"localized" deviations to allow the model to fit the sampled data points. The main assumptions are made on the covariance of $Z_i(\overline{x})$ that is written as

$$Cov(Z_i(\overline{x}), Z_i(\overline{x}')) = \sigma_Z^2 S(Z_i(\overline{x}), Z_i(\overline{x}')) \tag{3.23}$$

where σ_Z^2 is the so-called process variance and $S(Z_i(\overline{x}), Z_i(\overline{x}'))$ is a parameterized correlation function. This function is specified by the user while considering some specific assumptions [164]. Sacks, et al.. [260] and Koehler and Owen [172] give several possible correlation functions though a Gaussian function is often used. In this case, the covariance of $Z_i(\overline{x})$ is depending on a set of hyperparameters θ_k:

$$S(Z_i(\overline{x}), Z_i(\overline{x}')) = \prod_{k=1}^{Q} exp\left(-\theta_k \left|\overline{x}_k - \overline{x}'_k\right|^2\right) \tag{3.24}$$

where Q is the number of samples in the training set.

The hyperparameters θ_k are determined from the training set and control the non-linearity of the model. They are usually determined by minimizing the mean square error

$$E\left[\left(\tilde{f}(\overline{x}) - f(\overline{x})\right)^2\right]$$

with a strong unbiasedness constraint stating that the mean error of the approximation should be zero:

$$E\left[\tilde{f}(\overline{x}) - f(\overline{x})\right] = 0$$

The implementation of a kriging metamodel is delicate, complex and computationally expensive (though usually less than the original model) [164]. The core

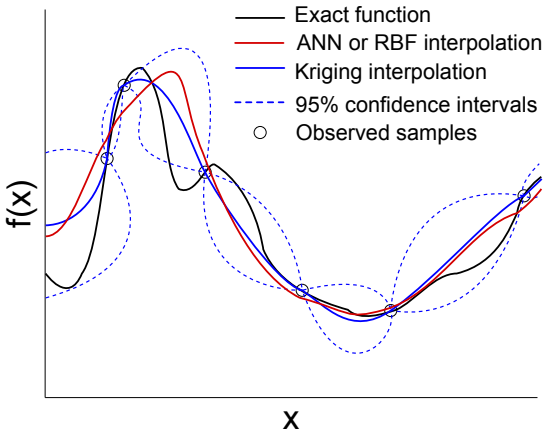

Figure 3.13: Illustration of 1D kriging interpolation. Observed samples are reproduced without bias contrary to ANN or RBF interpolation. Additionally, confidence intervals are directly available.

assumption that observations are the result of a Gaussian process is often not valid for results obtained by computer models [192]. This explains why many authors report computational problems and workarounds [276, 164, 193]. Another drawback of kriging is that it is has seldom been applied to problems involving many dimensions of the search space (say > 20) though recent works involved as many as 40 design variables. On the other hand, a kriging model, like ANN- or RBF-models but unlike RSM-models, becomes more accurate the more sample points are added and always reproduces the observed data exactly [164].

Despite these disadvantages, kriging offers two exceptional advantages. First, there is no error on the prediction of sample points. Second, the model provides an estimate for the error of the prediction in addition to the prediction itself. This is illustrated in Fig. 3.13. This valuable information could be used in the optimization process as discussed in [297]. A new individual located in a region of high uncertainty of the metamodel would trigger a high fidelity evaluation even if it would otherwise be rejected.

3.4 VKI Optimization code

The optimization code developed at the von Karman Institute has its roots in the work of S. Pierret [229] who implemented a GA-based search algorithm combined with a metamodel for 2D and hybrid 2D/3D optimization of axial turbomachinery blades. At that time, 20 design variables were used. This code was later extended and refined for use with full 3D multi-point applications for radial compressors and turbines. T. Verstraete evolved the code to a true multidisciplinary environment by adding structural integrity requirements and heat transfer considerations [297]. On

top of this, he refined the code even further by various enhancements with respect to workflow, metamodelling capabilities and parameterization. Later, he implemented a modular version of the code offering not only MODE (see section 3.2) but also single objective DE, both in a two-level (with the combined use of metamodelling and high fidelity analysis) or single-level approach (high fidelity analysis or metamodelling only). Moreover, various possibilities exist for the metamodel such as ANN (see section 3.3.3) trained either by backward propagation or EA, RBF (see section 3.3.4) or even kriging (see section 3.3.5). The decision to use an evolutionary approach for this code is the direct consequence of the advantages listed in section 3.1.3.1 and in particular for the robustness of such methods with respect to the shape of the objective functions.

The layout of the code as used in the present work is given in Fig. 3.14. The two-level approach has been chosen since this results in a direct reduction of the computational cost, hopefully at a not too big expense of accuracy. The use of a metamodel requires the analysis of a database at the start of the process and it is obtained by conducting a DoE based on partial factorial sampling augmented with random interior samples as this seems to be a good compromise between computational burden and coverage of the search space. Once this process is completed, the *generation* loop is initiated with a random population. The evolutionary process is then driven by the metamodel estimates of the performance for typically 1000 generations with a population size of 50. At this point, part of the last population is submitted to the high-fidelity analysis tools and the accurate performance is then fed back to the database. This off-line training safeguards the accuracy of the metamodel as it is regularly trained with individuals from the newest regions of the search space. The augmented database is used to update the metamodel for the next *iteration* before starting the generation loop again. The number of iterations should best be based on some convergence criteria but could also result from pure time- or cost-related concerns.

The VKI optimization code has interesting peculiarities that come at hand in the current optimization. First, it allows building one metamodel for each respective performance parameter (such as efficiency at a given working condition for example) instead of modelling directly the objectives (such as, e.g., the weighted sum of efficiencies at different working conditions) and constraints. Doing so, the metamodel has to stick more to the physics of the phenomena to be modelled and the interpretation of the outcome is eased. Second, the off-line training of the metamodel is a good compromise between accuracy and computational cost. The computational cost of conducting only high-fidelity analyses over the amount of individuals necessary to have an comprehensive search, would quickly prove to be prohibitive even by current standards. Last, it can be easily coupled to any standard solver as it does not require any kind of derivation.

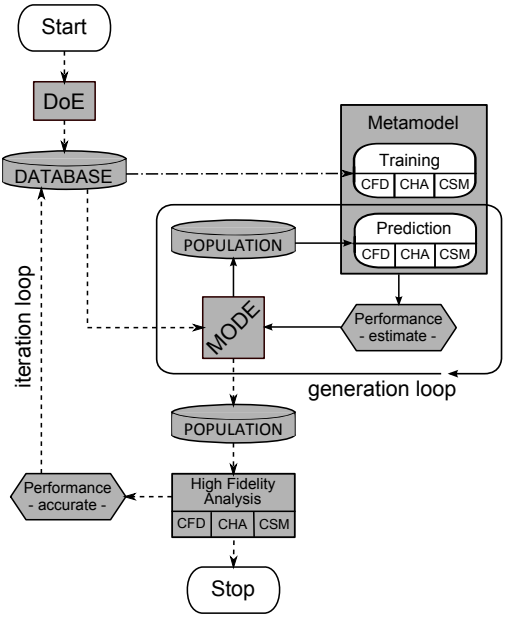

Figure 3.14: Layout of the VKI optimization code.

Chapter 4

Blade parameterization and mesh generation

The key role in transforming the engineering problem of optimizing a propeller blade in a mathematical problem lies within the mathematical representation of the blade shape. Hence one requirement of a successful optimization is to provide the optimization algorithm with an adequate set of design variables. This choice should not be made light handedly and must take many considerations into account. Is this set practical to implement? Is it feasible to generate a computerized 3D model of the blade from this set? Is this set suited for metamodelling? Is this set likely to generate shapes that are both consistent and relevant? Is this set likely to include the yet unknown optima? Is this set prone to interactions between design variables? Etc... Bearing in mind that the set should have the lowest possible cardinality!

At one extreme, one could foresee the direct use of the coordinate points on the blade surface as design variables, for example those points that lie at the nodes of the geometrical discretization of the blade. This is applied by A. Jameson [151, 152] and R. Campbell [51] for airfoils but results in extremely large sets of design variables and requires additional techniques to ensure the smoothness of the shape. It is often used in combination with adjoint- or gradient-based optimization algorithms. This very compact model spans virtually all possible blade shapes as the feasible region of the search space is not staked out by the capabilities of the blade model but would result in an unacceptable number of dimensions for the search space. It is also less suited than other parameterizations to take feasibility and manufacturability[1] into account. Next on the scale would be to use a polynomial representation of the blade surface but this would result in tremendous mathematical complexity to accurately represent this kind of closed surface. This is why most optimizations rely on some form of interpolation so that the 3D model of the blade is build from a limited set of design variables.

This chapter describes how the 3D model of the blade is constructed from the design variables and how this model is discretized in space to allow its use with

[1] A design is said to be *manufacturable* if its geometrical features are such that it can effectively be manufactured given the limitations of nowadays manufacturing equipment.

high-fidelity numerical analysis software.

4.1 Airfoil parameterization

As for many objects in aerodynamic design, propeller blades consist of a 3D assembly of airfoil sections. So the first thing to parameterize is the airfoil itself. The mathematical representation of an airfoil should have adequate flexibility in order not to limit the search space but should be robust in order to inherently generate relevant airfoil shapes. Moreover, it should have a low number of parameters and these parameters should control those important features of the design that are relevant for the considered optimization problem. The low number of parameters is here specifically important as a considerable amount of parameters is reserved for the modelling of the 3D blade. Another nice feature of a particular parameterization is its predictability i.e. the relationship between the parameters and the shape should be as obvious as possible. For the airfoil purpose, numerous techniques have been developed:

- *Zhukovsky and extended Zhukovsky tranformations*: consist the mathematical transform of a circle in the complex plane, into an airfoil shape. These transformations are limited in the shapes they can represent and must be seen in an historical perspective as the potential flow around such airfoils can be solved analytically.
- *Polynomials*: are used to model directly the shape of either the upper and lower sides of the airfoil, or the camberline and thickness distributions. This is the way traditional NACA airfoils are described [17]. These polynomials suffer from the relatively large amount of parameters (i.e. the coefficient and possibly the degree of the terms) and the unpredictable behaviour they could have which might result in non-smooth shapes.
- *PARSEC* [270]: is aimed at effectively controlling important features relative to the aerodynamics but mainly relative to manufacturability as well. The upper and lower airfoil surfaces are represented by polynomials whose coefficients are determined from basic geometric parameters such as leading-edge radius, crest location, maximum thickness and trailing-edge ordinate, thickness, direction and wedge angle. The PARSEC method is very tentative for airfoil parameterization as it allows representation of a wide range of shapes with direct inclusion of geometrical constraints while the design parameters control directly the aerodynamic properties. But this method suffers from the large number of parameters needed.
- *Orthogonal shape functions*: are an extension of polynomials. They rely on the linear combination of a basis function and a set of perturbation functions defined either analytically [144, 57] or numerically [253]. In the case of Hicks-Henne shape functions, the functions consist of 'bumps' of the type $Y = \sin^3(X^\beta)$ with β used to control the chord-wise position of the bump. These methods have great flexibility but usually lack robustness and require extended sets of parameters to be efficient.
- *Bézier or b-spline curves*: use a limited set of control points to define the shape of a curve by interpolation. The parameters are the coordinates of a set of $n+1$

control points $\overline{X_0}$, $\overline{X_1}$,...,$\overline{X_n}$ and the expression of the curve $\overline{C}(u)$ is given in both cases by:

$$\overline{C}(u) = \sum_{i=0}^{n} F_{i,q}(u)\overline{X_i} \tag{4.1}$$

over the interval $u \in [0,1]$ with q computed from the required degree of the curve in order to achieve the desired continuity properties. Bézier and b-spline curves differ by the basis functions used to compute the $F_{i,q}(u)$ coefficients. Bézier curves with $n+1$ control points are of degree $q = n$ whereas b-spline curves require a more complex theory with more information (i.e. the degree of the curve q must be chosen and a knot vector comprising $n+q+1$ elements must be defined over the same interval). The curve $\overline{C}(u)$ can represent either the suction and pressure sides directly or a camberline and a thickness distribution. The last one is more often used as it is more robust [271,189] and is closer to the basic phenomena in the flow (i.e. curvature versus loading and thickness versus blockage). In some cases, the parameters are not directly the coordinates of the control points but some distances and directions between them [297]. These types of curves are very popular because of their robustness and flexibility as well as their strong relation to computerized models. They also offer great modularity as they can be build with few or many parameters.

Most works involving airfoil optimization, from pure aerodynamic airfoil design to multidisciplinary optimization for turbomachinery applications or wings, rely on spline parameterization [80, 150, 175, 242, 176, 214, 163, 208] or Bézier parameterization [206, 232, 285, 224, 225, 89, 181] with typically 10 to 50 parameters. For Bézier parameterization, the curve of order $q = n$ is defined by

$$\overline{C}(u) = \sum_{i=0}^{n} B_{n,i}(u)\overline{X_i} \tag{4.2}$$

where the coefficients $B_{n,i}(u)$ are determined by Bernstein polynomials

$$B_{n,i}(u) = \frac{n!}{i!(n-i)!} u^i (1-u)^{n-i} \tag{4.3}$$

B-spline parameterization uses $n+1$ control points and the knot vector $\overline{U} = [u_0, u_1, ..., u_m]^T$ defined over $[0,1]$ with the order $q = m - n - 1$. The $q+1$ first and last knots are defined with multiplicity to ensure the curve is clamped [265]. The curve is given by

$$\overline{C}(u) = \sum_{i=0}^{n} N_{i,q}(u)\overline{X_i} \tag{4.4}$$

where the $N_{i,q}(u)$ coefficients are computed recursively using the Cox-de Boor recursion formula:

$$N_{i,0}(u) = \begin{cases} 1 & \text{if } u_i \leq u < u_{i+1} \\ 0 & \text{otherwise} \end{cases} \tag{4.5}$$

$$N_{i,q}(u) = \frac{u-u_i}{u_{i+q}-u_i} N_{i,q-1}(u) + \frac{u_{i+q+1}-u}{u_{i+q+1}-u_{i+1}} N_{i+1,q-1}(u) \tag{4.6}$$

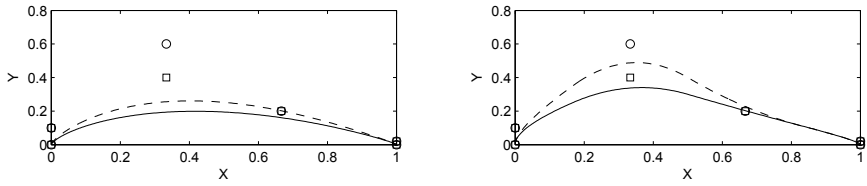

(a) Bï¿½zier parameterization. (b) B-spline parameterization.

Figure 4.1: Local modification property of b-splines, illustrated with two sets of control points (□ and — or ○ and −−) differing only in the ordinate of the 3^{rd} control point.

As apparent from Eqn. 4.4, the recursive formulation of the basis function requires additional computational effort through implementation of de Casteljeau's algorithm. This disadvantage for the b-spline curves is compensated by the fact that b-splines have the local modification property together with all important properties of Bézier curves. These include the convex hull property (i.e. the curve is enclosed within the convex perimeter set by the control points) and at least $\mathcal{G}^2$-continuity if the number of control points $n+1$ is chosen accordingly. The local modification property implies that changing a control point does not globally change the shape of the curve but allows a more localized shape control. It stems from the influence of the knot vector $\overline{U}$ in the definition of the basis functions $N_{i,q}(u)$ in Eqs.4.5 and 4.6. This interesting property [271] is illustrated on Fig. 4.1 where curves for both representations are drawn for two sets of control points differing only in the Y-coordinate of a single point. Irrespectively of the difference in shape due to the particular formulation, the local character of the modification for the b-spline is clearly illustrated by the negligible impact of the change of a single parameter on the trailing part of the curve.

Woefully, few papers compare the parameterization techniques [217,261,311,271], in particular b-spline versus Bézier curves and whether these curves should describe directly the upper and lower sides or the camberline and thickness distribution. Generally speaking, the parameterization of a camberline and thickness distribution, as illustrated in Fig. 4.2, has more ability to deliver airfoil-like shapes and has demonstrated its efficiency [217, 164]. In particular, the investigations done in [189] show that b-spline interpolation of a camberline and a thickness distribution with a scarce set of parameters, is more likely to lead to a successful optimization. It makes the parameter set prone to have less interactions because of the more direct relationship underlying input (the parameters) and output (the shape); and allows it to represent those important features of the design problem that are relevant to the forces on the airfoil. In this way, the design space is searched more efficiently, hence a better convergence, at some expense of the freedom to generate radically new shapes [271].

As is often the case for propellers, the blades consist of two airfoils. Airfoil I is used from the blade root to 35% radius and airfoil $I\!I$ from 45% radius to the tip. Between these two intermediate radii, both airfoils are blended into one by interpolation so that no abrupt geometry variation is encountered. Each airfoil is obtained by b-

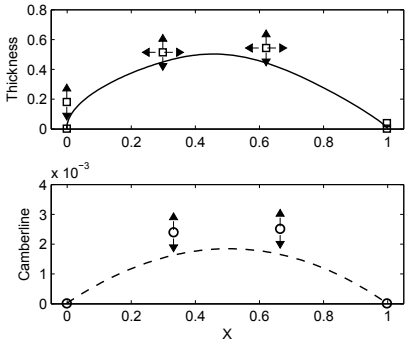

(a) Thickness and camberline distributions with control points and their respective degrees of freedom.

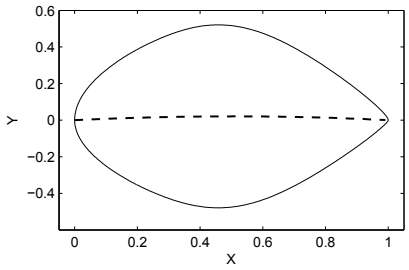

(b) Airfoil shape and camberline.

Figure 4.2: Airfoil parameterization and degrees of freedom for the control points.

spline interpolation between 6 control points for the thickness distribution and 4 for the camberline. The coordinates of the end-points are fixed at this stage because the adequate chord length and airfoil thickness are governed by separate design variables. For the thickness, the abscissa of the 2^{nd} and 5^{th} control points are kept at 0 and 1 respectively to enforce at least $\mathcal{G}^2$-continuity at the leading- and trailing-edges. The ordinate of the 2^{nd} point is effectively controlling the leading-edge radius. The trailing-edge radius is fixed to save design variables. For the camberline, only the ordinate of the two central points are allowed to fluctuate. For airfoil I, only one central point is used.

4.2 Blade parameterization

Since the appearance of propellers, different ways have been used to describe their planform. One method is to work with projected views but this is rather cumbersome for interpretation and manufacturing. Another method in particular is widely used since the early $1930's$ [124, 250, 213, 32]. This is the method chosen by the former NACA to describe planform shapes [246, 90, 247, 167]. NASA opted for the same method in the $1980's$ for its propfan designs [132]. The planform description is based on the radial distributions of chord length b, blade thickness t, twist angle Tw and finally sweep angle Sw. An example of such distributions is given in Fig. 4.3 with the chord and thickness distributions non-dimensionalized by the diameter D and chord b respectively. When given airfoil families are used, as is the case for NACA and NASA blades, the radial distribution of the design lift coefficient for the airfoils, is also given. The advantage of radial distributions is to present the major geometrical characteristics of the blade decoupled from each other.

Because the radial distributions have such widespread usage and because they allow easy interpretation of the major factors determining aerodynamic, aeroacoustic

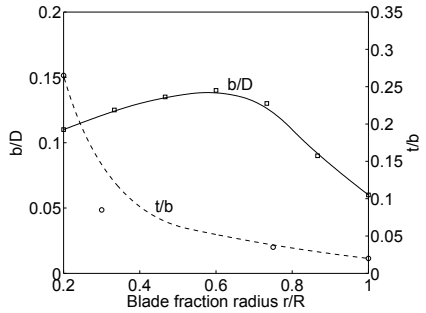

(a) Chord (b/D) and thickness (t/b) distributions.

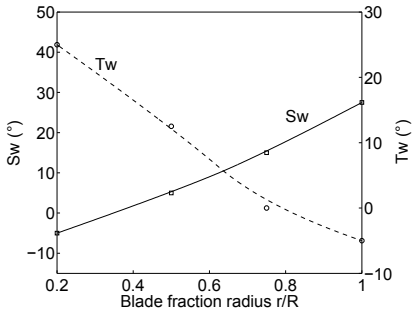

(b) Geometrical sweep (Sw) and twist (Tw) distributions.

Figure 4.3: Planform definition of an hypothetical blade with the corresponding control points for b-spline interpolation (○,□).

and to some extent aeroelastic performance; it is this method that has been retained in the present work. Parameterization of the curves is done by using b-spline interpolation between sets of control points, as illustrated in Fig. 4.3. This way, localized variations of the distributions are allowed by moving a single control point.

Once the airfoils and radial distributions are known, shape can be given to the blade by following the same procedure as in [30]. The first step is to scale the airfoil sections according to the chord and thickness definitions given in Fig. 4.3(a). The consequent stacked view is given in Fig. 4.4(a) where sections are stacked along the locus of their respective center of gravity. Next, sections are oriented to the proper twist, specified in Fig. 4.3(b)) as in Fig. 4.4(b). At this point, in compliance with Fig. 4.3(b), the only section aligned with the rotational axis is the 75%-radius section. Hence its blade angle β_{ref} is for now equal to 0°. Then the sections are swept back along their extended chord line resulting in Fig. 4.4(c). Therefore, the word 'sweep' refers here to geometrical sweep[2]. The final step is to rotate the blade around the pitch change axis to the desired blade angle β_{ref} at 75%-radius, as is shown in Fig. 4.4(d).

4.3 Spatial discretization

Gambit version v2.4.6 [5] is used as an integrated geometry/meshing package to perform the spatial discretization of the blade for the high-fidelity solvers. Gambit relies on a hierarchical geometry definition and meshing sequence. The geometry relies on an $ACIS$ kernel. The structured/unstructured mesher allows for different meshing schemes ranging from quadrilaterals or triangles for surface meshing, to hexahedrons, tetrahedrons, pyramids or wedges for volume meshing, with size-functions that allow local control of the mesh properties.

[2]Geometrical sweep is defined as the angle between the pitch axis of the blade and the locus of the 1/4-chord of its sections. In contrast, leading-edge sweep is defined as the angle between the pitch axis and the leading-edge line.

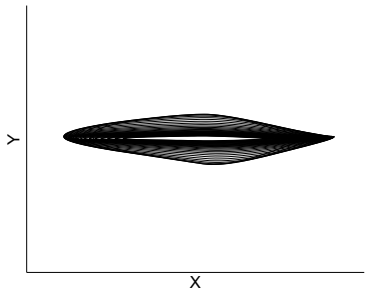

(a) Chord and thickness scaling.

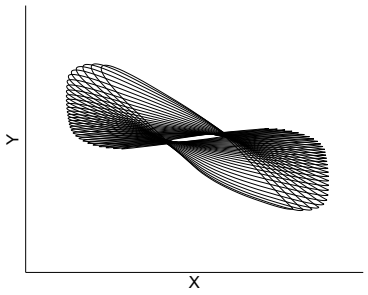

(b) Twisting. Note at this point that $\beta_{ref} = 0°$

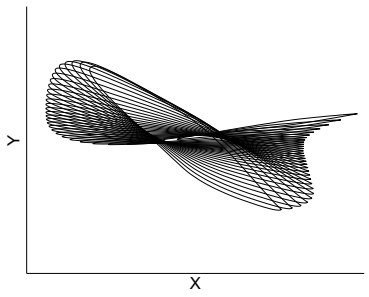

(c) Sweeping of the quarter-chord line.

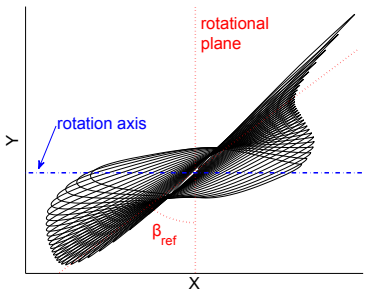

(d) Blade rotation to the desired β_{ref}.

Figure 4.4: Stacked views of a blade at various stages of the shape-giving procedure and definition of β_{ref} (blade angle at 75%-radius).

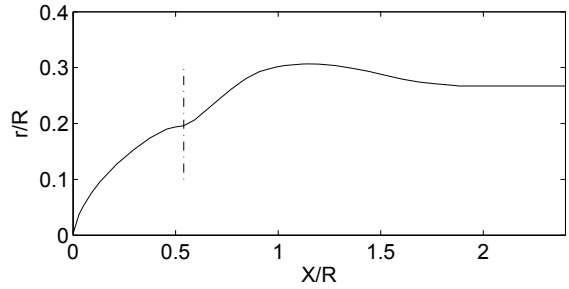

Figure 4.5: Spinner contour with indication of the pitch change axis $(-\cdot)$.

Once the vertices are imported, edges are created by b-spline interpolation to create a skeleton corresponding to Fig. 4.4(d). Surfaces are then made using the skin technique. Each blade segment between two stations is consecutively transformed into a volume by surfaces stitching. The tip consists of the last airfoil section so it is flat and parallel to the axis, no round off is applied. At this stage, the computerized representation of the active part of the blade is completed.

4.3.1 Mesh for aerodynamic and aeroacoustic solvers

Mesh details

For the aerodynamic and aeroacoustic analysis, a scaled model of the blade is subsequently mounted onto a spinner. The scale is chosen such that the compactness criterion (cfr *infra*) is satisfied with a reasonable number of mesh elements. Appropriate scaling laws are then used to compute the aerodynamic and aeroacoustic results of the full-scale propeller from the scaled model. Figure 4.5 gives the non-dimensionalized spinner contour along the rotational axis (X-axis) and the spinner volume is obtained by axial revolution. It is a 27.5° half-angle cone that blends into a nacelle with a maximum diameter equal to 26.72% of the propeller diameter. The blade is placed with its pitch change axis aligned with the position marked on Fig. 4.5 and this part of the spinner features area-ruling to help alleviate transonic effects particularly in the inboard blade passages. The extent of area-ruling is based on the area of a mean blade. The shape of the spinner is not subject to optimization in the subsequent chapters as this would increase the number of design variables. Moreover, the present blade-spinner model does not represent with high-fidelity the mechanisms present at the blade root for a real propeller.

Blade and spinner are subtracted from a pie-shaped domain to create the flow domain as is shown in Fig. 4.6. The angular extent of the domain is only $\pi/4$ as a single blade passage of the 8-bladed propellers, is considered with special periodic conditions valid because the propeller is considered isolated from any other aircraft part and at zero angle of attack with respect to the flow. This simplification is important as the different designs cannot be truly tested for robustness in yawed flow or installed conditions. The axial and radial extent of the domain are $2.5D$ in length and $2D$ in radius. These values are the result of a parametric study to

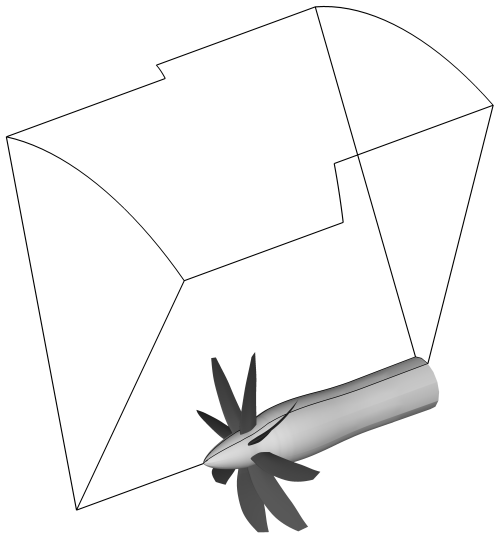

Figure 4.6: Flow channel, spinner and blade.

maintain accuracy of the aerodynamic analysis while driving down the numerical cost by reducing the spatial extent of the domain [188].

The next step is to realize the surface mesh on all boundaries. The scheme starts with a quadrangular mesh applied to the blade surface consisting of approximatively 40000 elements. This mesh is locally adapted to both the leading edge curvature and the expected pressure gradient along the pressure and suction sides. The typical chordwise dimension of the elements ranges from $0.0005D$ to $0.002D$ by $0.002D$ in the radial direction, with D the diameter of the scale model. Doing so, this mesh verifies the compactness criterion for aeroacoustic purposes (see section 6.2.1.3):

$$L << \lambda_m(1 - M_r) \tag{4.7}$$

where L is the cell elongation (the maximum cell dimension), λ_m is the wave length associated with the highest sound frequency to be resolved (here, $4000Hz$) and M_r is the local Mach number of a point on the blade surface, projected on the radiation direction (i.e. the direction to the receiver). Note that M_r depends purely upon the kinematics of the helical movement of the blade with respect to the receiver's position and that, strictly speaking, when $M_r = 1$, there is no mesh that would satisfy Eqn. 4.7. The mesh size is kept within reasonable limits by scaling the blade by a factor 2/9.

All remaining surfaces are meshed with triangles. As Gambit can not handle suitable meshes for boundary layers on arbitrarily curved surfaces, it has been necessary to restrict the use of Gambit to the 2D meshing of all surfaces which are then exported to TGrid v5.0.6 [7]. In TGrid, the quadrilateral surface mesh is extruded perpendicularly to the blade surface to generate an O-type boundary-layer mesh as illustrated in Fig. 4.7. 12-layers are built with the cell height satisfying wall treatment requirements. Indeed, $y+$-values range typically from 50 to 200. After this operation,

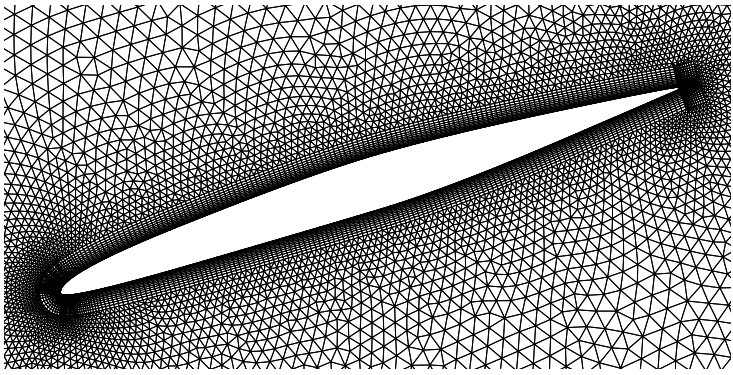

Figure 4.7: Cut made at 50%-radius revealing the section of the O-type boundary-layer mesh and the projection of the faces of the flow channel mesh.

the remaining of the domain is meshed with tetrahedrons starting from a conformal interface obtained by splitting the quadrangular elements from the last layer of the boundary-layer mesh. As pointed out by Boyle [35], fine and accurate propeller blade meshing is a tricky task. Difficulties for good blade meshes are due mainly to three factors:

- the strong variation of the leading edge curvature radius (in each blade section plane) between the hub and the tip due to large variations of the radial thickness distribution,
- the variation of the blade leading edge curvature along the radial direction related to the radial distribution of chord length, the introduction of sweep and the selected stacking procedure,
- and the strong blade twist that distorts the blade leading edge around the blade axis.

The combination of these three elements required the development of a specific automatic meshing scheme in order to capture correctly complex geometries with a minimum risk for degenerated cells and without loss of fidelity due to strong geometric approximations.

During the previous operations, Gambit and TGrid attribute to each newly created entity (vertex, edge, surface, nodes,...) a label and a number. The label can be controlled by the user by modifying the default settings for labels. But the number is attributed sequentially in the family of the considered entity. At this stage, the position of the entity also plays a role. This could give rise to major difficulties when applying the same geometry/meshing procedure to different propellers as one entity name might not refer to the same entity for another propeller. To circumvent these difficulties and be able to apply the same journal file to different propellers, a rigorous series of labelling operations based on entity location, had to be developed in order to automate completely the meshing process with the highest chances of successful meshing.

Grid convergence analysis

Though the results of the CFD- and CHA-solvers will be validated against experimental results in sections 5.4 and 6.3 respectively, a grid independence analysis has been conducted a posteriori on selected designs from part II. The purpose is to check whether significant departures from traditional blade geometries, combined with relatively coarse meshes so that the computational time is kept to a minimum, result in difficulties related to the correct computation of aerodynamic and aeroacoustic performance. Table 4.1 gives an overview of this analysis. The reader is referred to chapters 5 and 6 for the explanation of the computed quantities. The method used for the convergence analysis, is the one prescribed by the Journal of Fluids Engineering [56]. Four propellers have been analyzed in the design cruise and take-off/landing conditions ($J_{CR,2}$ and $J_{TO,2}$) for C_T, C_P and the SPL in the propeller plane. In all cases, the Grid Convergence Index (GCI) between the finest and the regular mesh is below 2.7% which is a satisfactory result. The maximum approximate relative error e_a between the finest and the regular mesh is usually far below 3.3% while the extrapolated relative error e_{ext} is kept under 2.2%. This analysis proves that the computed performance values are not depending onto spatial discretization issues when evaluated on the "regular" mesh as it is the case in the subsequent chapters.

4.3.2 Mesh for aeroelastic solver

Mesh details

For the aeroelastic analysis, a full-scale model of the blade is used to avoid the difficulty of correct scaling with respect to material specific volume and aeroelastic properties. It includes part of the shank assembly connecting the blade to the hub as illustrated in Fig. 4.8. The necessity to avoid kinks in the placement of the composite material composing the blade surface, makes a transition zone necessary. This zone is designed to ensure a progressive shape conversion from airfoil shaped sections to a circular shank. In the current model, this zone has a 10.67% radial extent and the shank diameter is 8.89% of the propeller tip radius R. The transition zone is obtained by b-spline interpolation of 4 curves between the airfoil at 30.67%-radius and the shank at 20%-radius. These curves define the frame of the transition region. Throughout this process, $\mathcal{G}^2$-continuity is maintained between the transition zone, the shank and the outboard part of the blade. The spaces between the aerodynamic shape and the composite structure are supposedly filled with foam cuffs that are not modeled in the present approach.

The structural model shown in Fig. 4.8 is first surface meshed with triangles having a typical side length of $0.0044D$. Proper grading is applied down to side lengths of $0.0018D$ to guarantee the geometrical fidelity of the mesh in regions of high curvature as well as correct estimation of the stresses in regions of high gradients. This surface mesh is exported to Samcef v13.1-02 [10]. In Samcef, the GHS3D mesher [121] is used to mesh the inner volume of the blade without alteration of the surface mesh so that the nodes remain collocated. The last requirement is crucial since the surface mesh, used to model the composite shell, will be used in conjunction with the volume mesh used to model the foam core (see chapter 7). Both the volume and surface mesh consist of linear elements to keep the computational time within acceptable limits in the framework of multidisciplinary optimization. Quadratic elements have not been

		PROPELLER A			PROPELLER D			CENTRAL INDIVIDUAL			BENCHMARK		
		Coarse mesh	Regular mesh	Fine mesh	Coarse mesh	Regular mesh	Fine mesh	Coarse mesh	Regular mesh	Fine mesh	Coarse mesh	Regular mesh	Fine mesh
Cells N		9.12e05	1.71e06	3.84e06	9.62e05	1.25e06	3.70e06	8.43e05	1.23e06	4.08e06	9.35e05	1.53e06	9.36e06
h		0.0127	0.0104	0.0079	0.0125	0.0115	0.0080	0.0132	0.0116	0.0078	0.0126	0.0107	0.0059
C_T		0.3399	0.3642	0.3588	0.3552	0.3627	0.3632	0.3182	0.3333	0.3353	0.3237	0.3258	0.3256
C_P		1.7719	1.8240	1.8027	1.8212	1.8378	1.8391	1.6636	1.6928	1.7009	1.6075	1.6108	1.6113
$SPL^{rec\,3}$		119.78	120.28	120.47	113.46	114.30	114.53	120.53	120.74	120.56	129.70	131.02	131.45
C_T	GCI (%)	8.67	2.65		5.22	0.26		0.77	0.00		0.68	0.00	
	e_a (%)	6.69	3.25		2.03	0.97		4.53	0.01		0.65	0.06	
	e_{ext} (%)	6.49	2.17		4.01	0.21		0.61	0.00		0.07	0.00	
C_P	GCI (%)	2.86	0.72		0.09	0.00		0.60	0.00		0.04	0.05	
	e_a (%)	2.85	1.18		0.90	0.07		1.73	0.47		0.20	0.03	
	e_{ext} (%)	2.23	0.58		0.00	0.07		0.48	0.00		0.08	0.00	
$SPL^{rec\,3}$	GCI (%)	0.25	0.05		0.08	0.00		2.65	0.68		0.46	0.00	
	e_a (%)	0.42	0.15		1.01	0.06		0.17	0.15		1.01	0.37	
	e_{ext} (%)	0.20	0.04		0.07	0.00		2.07	0.55		0.37	0.01	
Cells N		9.62e05	1.34e06	3.92e06	9.86e05	1.46e06	4.07e06	9.91e05	1.35e06	4.69e06	8.73e05	1.53e06	4.27e06
h		0.0125	0.0112	0.0078	0.0124	0.0109	0.0077	0.0124	0.0112	0.0074	0.0129	0.0107	0.0076
C_T		0.3153	0.3080	0.3102	0.3134	0.3299	0.3202	0.3361	0.2996	0.3002	0.2814	0.2716	0.2689
C_P		0.5564	0.5636	0.5607	0.6353	0.6092	0.6117	0.5002	0.5285	0.5367	0.4854	0.4737	0.4785
$SPL^{rec\,3}$		101.2	100.3	100.8	100.6	102.4	103.0	105.1	106.3	107.1	103.2	104.1	104.5
C_T	GCI (%)	2.00	0.04		15.84	2.61		0.26	0.00		1.33	0.08	
	e_a (%)	2.37	0.71		5.00	3.03		1.18	0.20		3.61	1.00	
	e_{ext} (%)	1.62	0.04		11.24	2.13		0.21	0.00		1.08	0.08	
C_P	GCI (%)	1.94	0.10		0.63	0.00		1.94	0.00		2.89	0.46	
	e_a (%)	1.28	0.52		4.28	0.41		5.35	1.53		2.45	1.00	
	e_{ext} (%)	1.52	0.08		0.63	0.00		1.53	0.00		2.36	0.36	
$SPL^{rec\,3}$	GCI (%)	0.91	0.01		0.76	0.02		0.97	0.02		0.57	0.07	
	e_a (%)	1.79	0.71		1.76	0.59		1.13	0.75		0.86	0.38	
	e_{ext} (%)	0.72	0.01		0.61	0.02		0.77	0.02		0.44	0.06	

Table 4.1: Grid independence for aerodynamic and aeroacoustic results at $J_{CR,2}$, (top) and $J_{TO,2}$, (bottom). See chapter 10 for details about the geometry of the blades.

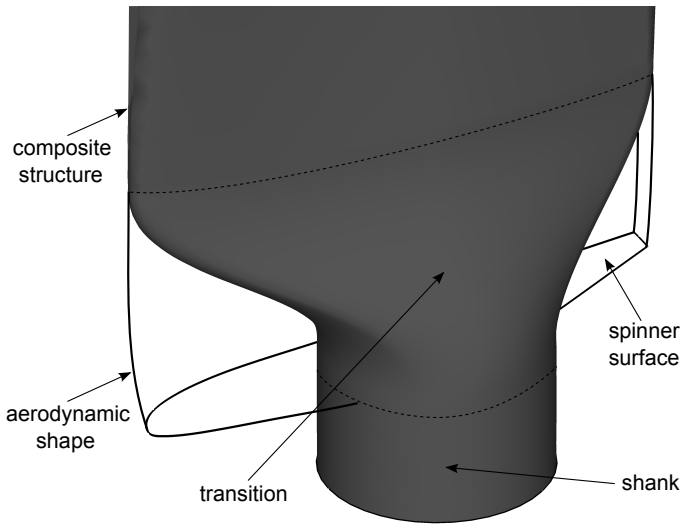

Figure 4.8: Detail of the blade root showing the difference between the aerodynamic shape and the blade structure.

used because of specific restrictions pertaining to the solver and hypotheses in Samcef v13.1-02.

Grid convergence analysis

Unfortunately, no comparison to experiments could be made due to the lack of available experimental data about the aeroelastic properties and performance of modern blades. Nevertheless, a grid independence analysis has been conducted a posteriori on the same designs as in section 4.3.1. The reader is referred to chapter 7 for the explanation of the computed quantities. The fine and coarse mesh differ from the regular one by a factor 1.3 in terms of typical mesh dimension h. The relative error between the different meshes on those values that are significant in the present framework, are given in table 4.2 and suggest that satisfactory grid convergence is obtained on the regular mesh.

	PROPELLER A			PROPELLER D			CENTRAL INDIVIDUAL			BENCHMARK		
	Coarse mesh	Regular mesh	Fine mesh	Coarse mesh	Regular mesh	Fine mesh	Coarse mesh	Regular mesh	Fine mesh	Coarse mesh	Regular mesh	Fine mesh
Elements N	81.3e03	106.4e03	138.8e03	74.2e03	96.9e03	125.1e03	95.8e03	124.6e03	158.8e03	73.9e03	93.9e03	122.0e03
DoF	43.1e03	56.3e03	73.3e03	39.6e03	51.4e03	66.9e03	50.4e03	65.4e03	83.6e03	39.2e03	49.3e03	64.3e03
m (kg)	42.078	42.081	42.083	39.470	39.487	39.492	47.872	47.890	47.900	35.784	35.780	35.802
ζ_{TW}	0.291	0.293	0.293	0.140	0.137	0.138	0.204	0.205	0.205	0.067	0.069	0.068
ζ_{VM}	0.616	0.619	0.620	0.360	0.360	0.362	0.598	0.597	0.598	0.265	0.266	0.266
e_r on m (%)		−0.01	0.01		−0.04	0.01		−0.03	0.02		0.01	0.06
e_r on ζ_{TW} (%)		−0.7	0.0		2.2	0.7		−0.5	0.0		2.8	−1.4
e_r on ζ_{VM} (%)		−0.5	0.2		0.0	0.6		0.2	0.2		−0.4	0.0
Elements N	76.6e03	102.4e03	130.2e03	74.1e03	96.8e03	125.8e03	94.7e03	123.2e03	162.2e03	72.8e03	95.4e03	124.0e03
DoF	40.5e03	54.3e03	69.1e03	40.5e03	51.3e03	66.7e03	49.8e03	64.7e03	85.1e03	38.3e03	50.0e03	65.8e03
ζ_{TW}	0.464	0.462	0.470	0.339	0.334	0.330	0.314	0.322	0.324	0.085	0.090	0.089
ζ_{VM}	0.897	0.913	0.920	0.512	0.491	0.490	0.662	0.676	0.678	0.317	0.325	0.324
e_r on ζ_{TW} (%)		0.4	1.7		1.5	−1.8		−2.5	0.6		−5.5	−1.1
e_r on ζ_{VM} (%)		−1.7	0.8		4.3	−0.2		−2.0	0.3		−2.5	−0.3

Table 4.2: Grid independence for aeroelastic results at $J_{CR,2}$, and $J_{TO,2}$,. See chapter 10 for details about the geometry of the blades.

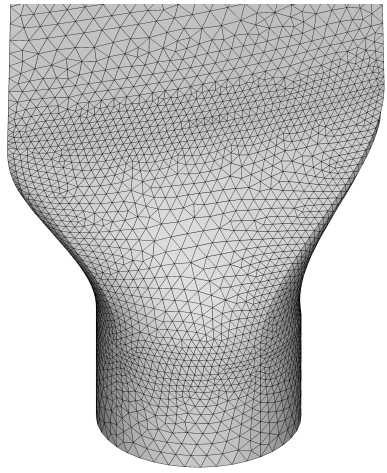

Figure 4.9: Surface mesh of the blade structure.

Chapter 5

Aerodynamic solver

Among the high-fidelity analysis tools used in the optimization procedure, the aerodynamic solver plays an important role. It provides an accurate estimate (as opposed to the metamodel approximate) of the propeller performance, and it feeds the aeroacoustic solver with the necessary flow details or the aeroelastic solver with the pressure distribution on the blade surface.

This chapter gives an overview of the available methods for the Computational Fluid Dynamics tool (CFD), and argues the choices made for the present optimization. A more detailed account is given of the chosen solver together with the set of boundary conditions and the performance parameters computed at the end of the numerical simulation. Finally, comparisons are made between computations and experiments for some performance values in order to assess the validity of the current approach.

5.1 Available numerical methods

5.1.1 Legacy methods

Legacy methods have their origins in the need to predict the performance of propellers for marine applications. The first and most simple method is the axial momentum theory developed by W. Rankine [241]. This theory considers a propeller disk consisting of an infinite number of blades (actuator disk) in incompressible inviscid flow and neglects the rotation induced in the slipstream by the rotating disk (also called swirl). Basically, it computes propellers performance from the difference in pressure and velocity up- and down-stream of the propeller by application of the conservation laws. The first improvement to this method was made by R. Froude [119] who introduced the general momentum theory which takes the effects of slipstream rotation into account. Over the years, improvements included the introduction of friction losses and compressibility corrections [298].

Even though the momentum theory has quite recently been extended to account for non-uniform radial distribution of the load [64] as well as heavy loading of the disk [65], it suffers from the negligence of real-world phenomena such as the finite number of blades or viscous flow. Hence these methods are usually good at predicting

overall performance parameters such as thrust (C_T) and power coefficients (C_P) or efficiency (η) but they fail at predicting accurate details of the flow up- and downstream of the propeller disk let alone in the disk itself.

As an alternative to the momentum theory, the blade element theory was developed in parallel by R. Froude [118]. This theory recognizes that the airfoil section at each station along the span, meets the flow at different angle and speed. A blade is decomposed into elements of finite span for which 2D airfoil coefficients are used to compute the forces and if necessary the pressure distribution from the local chord and velocities. Hence the blade element method gives more details about the flow on the finite number of blades. This first implementation falls short of taking the influence of the wake into account and this triggered the combination of the momentum and blade element theory by H. Glauert [123]. But both theories are only valid for lightly loaded propellers (thus small slipstream contractions) and ignore the radial components of the flow as well as tip losses. Because these methods do not predict detailed flow features, they would not be appropriate for the present work.

5.1.2 Lifting-line, lifting-surface and panel methods

For incompressible inviscid flows, the lifting-line theory was onset by F. Lanchester and published by L. Prandtl [234] working with A. Betz and M. Munk. It models the blade by a single bound vortex line of strength Γ located at the quarter chord position and having vorticity shed downstream at both extremities to satisfy the Helmholtz theorem. The unknown circulation Γ is obtained by using the Biot-Savart law with the boundary condition $\overline{u}.\overline{n} = 0$ at a given control point on the blade surface with $\overline{n}$ the vector normal to the surface (tangency condition stating that there is no flow normal to the wall surface). Once Γ is known, the induced velocity can be obtained together with the lift from the Kutta-Zhukovsky theorem.

In a more elaborate approach, the vortex strength reduces spanwise by shedding a vortex-sheet from the trailing edge, rather than just at the tips. In this case, the coefficients of the radial distribution of $\Gamma(r)$ are determined by using the appropriate number of control points. Some extensions of this method have been developed to incorporate curvature of the lifting-line [33].

To take more intricate geometries than a straight blade into account, the lifting-line theory has been extended to the lifting-surface theory by placing a series of lifting-line at different chordwise positions. Doing so, vortex strength dependency is gained in the radial and chordwise directions. Applying the Biot-Savart law and the tangency condition on a convenient set of control points allow for the determination of the individual vortex strengths. This is the major difficulty of such methods as the individual circulations are mutually dependent. The most common numerical method to solve the system of bound horseshoe vortices is the *Vortex Lattice Method* [92].

Several improvements exist to consider compressibility, viscous losses, the effect of thickness of the blades (better accounted for in panel methods by using sources and doublets for example) [33, 263] or the presence of the spinner [263]. Most lifting surface methods suffer from the ignorance of thickness effects hence are limited to thin blades of arbitrary shape up to mild transonic conditions [274, 33, 263]. These methods are also extremely popular for low speed cases with low loading such as in [49].

Panel methods, use sources, sinks and doublets distributed over a surface to model the flow over the blade. These potential flow methods are limited, in their uncorrected form, to inviscid incompressible flow and are therefore rejected for the present optimization despite their extremely low computational cost. This low cost is the reason why such methods are still used for optimization purposes [49] or for industrial assessment by propeller manufacturers.

5.1.3 Lattice Boltzmann Methods (LBM)

LBM is a simulation technique developed from the late $1980's$ and is increasingly attracting researchers in computational physics. Traditional CFD methods solve the conservation equations of macroscopic properties (i.e. mass, momentum, and energy) numerically. Unlike these methods, LBM models the fluid by fictive particles that consecutively propagate and collide over a discrete lattice mesh. LBM methods evolved from the first Lattice Gas Automata (LGA) with proven Navier-Stokes dynamics [116, 309]. In LGA, at a particular step, either 1 or 0 particle is present at each node of the lattice moving in the direction of one neighbouring node. After a time interval, each particle moves to the neighbouring node according to its direction (propagation). At the next step, if more than one particle arrives at a particular node from different directions, they collide and change direction (collision). The governing equations for the collision and propagation are beyond the scope of this section but are such that mass, momentum and energy are conserved locally. Henceforth some kind of localized continuity is obeyed unlike the Navier-Stokes equations which are continuous forms of the conservation equations. The drawback of LGA was its rather noisy nature and this is removed by replacing the propagation operator by its ensemble average (leading to a lattice Boltzmann equation) and the discrete collision rule by a continuous collision operator celebrating the molecular chaos assumption of Boltzmann. The last replacements are the spine of the LBM method.

Owing to its particulate nature and local dynamics, LBM has several advantages over conventional CFD methods [180]:

- they have intrinsic parallelism,
- they can handle complex boundaries without compromising the computational speed,
- they allow easy incorporation of microscopic interactions.

These are the reason for the recent successes obtained with LBMs in various flow applications of external and internal dynamics of turbulent flows even if difficulties are encountered for high Mach number flows. As such, LBMs are a reliable candidate for the current application [48] but have been discarded in favor of a RANS approach.

5.1.4 Euler and RANS methods

These methods tend to solve numerically the continuous conservation equations for mass, momentum and energy:

$$\frac{\partial \rho}{\partial t} + \frac{\partial \left(\rho u_j\right)}{\partial x_j} = 0 \tag{5.1}$$

$$\frac{\partial(\rho u_i)}{\partial t} + \frac{\partial(\rho u_i u_j)}{\partial x_j} = \frac{\partial}{\partial x_j}\left[-p\delta_{ij} + \tau_{ij}\right] + f_i, \quad i = 1, 2, 3 \tag{5.2}$$

$$\frac{\partial(\rho e_0)}{\partial t} + \frac{\partial(\rho u_j e_0)}{\partial x_j} = \frac{\partial}{\partial x_j}\left[-u_j p + u_i \tau_{ij} + q_j\right] - f_i u_i + \dot{q} \tag{5.3}$$

in which δ_{ij} is the Kronecker symbol, τ_{ji} is the deviatoric stress tensor, f_i is the i^{th}-component of the body forces, e_0 is the total energy ($e_0 = e + 1/2.\rho.u^2$), q_j is the j^{th}-component of the heat transfer by conduction and $\dot{q}$ is the time rate of volumetric heat addition per unit mass. In propeller applications, the heat terms and body forces terms (in an absolute frame of reference) are often left aside.

Euler methods consider Eqs. 5.1 and 5.2 but without the influence of the deviatoric stress tensor for the last equation. So, they model inviscid adiabatic flow. Such methods became popular with the advent of computers and remove the hypothesis of small perturbation usually associated with the methods of sections 5.1.1 and 5.1.2. Euler methods are able to compute non-linear phenomena, such as shocks occurring in the blade passage, quite accurately but at the price of a considerable increase in computational cost when compared to legacy, lifting-surface and panel methods. In the time where numerical solutions of the Navier-Stokes equations were still not affordable, numerous papers used a numerical solution of the Euler equations in the case of propellers [274, 33, 307, 212, 273, 37, 36, 34, 125]. In some cases as in [307, 273, 34], remarkable agreement with experimental results was obtained but this probably comes from the weakness of viscous effects when compared to pressure loads at such high Reynolds numbers, and hides the mutual influence of some effects not accounted for in the computations such as the deformation of the blade during the experiments [34].

Navier-Stokes methods solve the complete system of Eqs. 5.1, 5.2 and 5.3 with some additional hypotheses for turbulence closure that will be discussed in the next section. These methods became extremely popular at the beginning of the $1990's$ and are widely applied for the computation of propeller flow [194, 34, 295, 35, 279, 302, 313].

5.2 RANS-solver

Fluent v12.0.16 [9] is used for the high-fidelity aerodynamic analysis with periodicity allowing to limit the domain to the channel described in section 4.3.1. The RANS-solver used in Fluent will here be briefly described along with the main theory. This way the choices made for the application to propellers are given adequate light even though the contribution of the authors is limited to these choices. Note that, for now, a RANS-approach is the most detailed way to compute the flow field around a propeller as the requirements for Large Eddy Simulation or Direct Numerical Simulation would make it prohibitive, if not just impossible, to run on current generation computers; let al.one for optimization in the foreseeable future.

5.2.1 Governing equations

The governing equations for the fluid dynamics problem are Eqs. 5.1, 5.2 and 5.3. In the presence of turbulent flows, as is the case for propellers, small scale flow structures exist and evolve with time. A computationally inexpensive and popular option is to average the governing equations statistically before solving them (hence the RANS

term standing for Reynolds Averaged Navier-Stokes) though this comes with some limitations with respect to the accuracy of the description of the flow.

Two averaging approaches are combined to form the set of RANS equations: Reynolds and Favre averaging. Reynolds averaging consists in splitting a scalar quantity $\rho(x,t)$ in the sum of its mean part $\bar{\rho}(x,t)$ and a fluctuating part $\rho'(x,t)$ so that:

$$\rho(x,t) = \bar{\rho}(x,t) + \rho'(x,t)$$

with

$$\bar{\rho}(x,t) = \frac{1}{T}\int_t^{t+T} \rho(x,t)dt$$

where T is an arbitrary, yet sufficiently long time interval. Similarly, Favre averaging splits the instantaneous velocity component $u_i(x,t)$, for example, by

$$u_i(x,t) = \tilde{u}_i(x,t) + u_i''(x,t)$$

with

$$\tilde{u}_i(x,t) = \frac{1}{\bar{\rho}T}\int_t^{t+T} \rho(x,t)u_i(x,t)dt$$

The average form of the NS equations is then obtained by using Reynolds averaging for ρ and p, Favre averaging for all other quantities and the fact that the mean of fluctuating parts is zero. This leads to a new set of equations:

$$\frac{\partial \bar{\rho}}{\partial t} + \frac{\partial\left(\bar{\rho}\tilde{u}_j\right)}{\partial x_j} = 0 \tag{5.4}$$

$$\frac{\partial\left(\bar{\rho}\tilde{u}_i\right)}{\partial t} + \frac{\partial\left(\bar{\rho}\tilde{u}_i\tilde{u}_j\right)}{\partial x_j} = -\frac{\partial\left(\overline{\rho u_i'' u_j''}\right)}{\partial x_j} - \frac{\partial \bar{p}}{\partial x_i} + \frac{\partial \overline{\tau_{ij}}}{\partial x_j}, \quad i = 1,2,3 \tag{5.5}$$

$$\begin{aligned}\frac{\partial\left(\bar{\rho}\tilde{e}_0\right)}{\partial t} + \frac{\partial\left(\bar{\rho}\tilde{u}_j\tilde{e}_0\right)}{\partial x_j} &= \frac{\partial}{\partial x_j}\left[-\tilde{u}_j\bar{p} - \overline{\rho u_j'' h''} + \overline{\tau_{ij}'' u_i''} - \overline{1/2\rho u_j'' u_i'' u_i''}\right] \\ &\quad + \frac{\partial}{\partial x_j}\left[\tilde{u}_i(\bar{\tau}_{ij} - \overline{\rho u_i'' u_j''})\right]\end{aligned} \tag{5.6}$$

where h is the enthalpy. These equations define the transport of mean quantities. Although the continuity equation (Eqn. 5.4) does not contain any additional term, the momentum equation (Eqn. 5.5) has the additional Reynolds-stresses term $-\overline{\rho u_i'' u_j''}$ and the energy equation has been augmented with the turbulent heat flux vector $\overline{\rho u_j'' h''} - \overline{\tau_{ij}'' u_i''} + \overline{1/2\rho u_j'' u_i'' u_i''}$. These terms lie at the origin of the closure problem as additional equations are needed for the six components of the Reynolds-stress tensor and the three components of the turbulent heat flux vector in order to solve the RANS system.

5.2.2 Closure of the RANS-equations and wall behaviour

5.2.2.1 Exact Reynolds-stress transport equation

The exact transport equation for the Reynolds-stresses can be obtained by subtracting Eqs. 5.4-5.6 from the original Navier-Stokes equations expressed in terms of $\tilde{u} + u''$ and multiplying the difference by a fluctuating quantity. The resulting equation yields

$$\frac{\partial \overline{\rho u_i'' u_j''}}{\partial t} + \frac{\partial \overline{\rho u_i'' u_j''} \tilde{u}_k}{\partial x_k} = P_{ij} - \bar{\rho}\varepsilon_{ij} - \frac{\partial J_{ijk}}{\partial x_k} + \Pi_{ij} - \overline{u_j''}\frac{\partial \bar{p}}{\partial x_i} - \overline{u_i''}\frac{\partial \bar{p}}{\partial x_j} \tag{5.7}$$

where the terms in the right hand-side are:

- P_{ij}: this accounts for the production of turbulent stresses by deformation at the expense of the mean flow energy. This term does not require closure.
- J_{ij}: the transport term accounting for turbulent diffusion (transport through velocity fluctuations), pressure transport and molecular diffusion. The first two parts require closure.
- Π_{ij}: the pressure-strain term accounting for the redistribution of turbulent stresses among components to make turbulence more isotropic. This term needs closure.
- ε_{ij}: the stress dissipation term occurring at the smallest scales.

5.2.2.2 Eddy viscosity assumption

This assumption results from Boussinesq's hypothesis which relies on a turbulent viscosity μ_t, depending on flow features, to connect the Reynolds-stress components to the strain rate. This hypothesis is quite similar to Newton's law for molecular viscosity. It can be written as

$$\tau_{ij}^{Reynolds} = -\overline{\rho u_i'' u_j''} = 2\mu_t(\tilde{S}_{ij} - 1/3\delta_{ij}\tilde{S}_{kk}) - 2/3\rho k\delta_{ij} \tag{5.8}$$

where $S_{ij} - 1/3\delta_{ij}S_{kk}$ is the shear tensor so that the deviatoric stress tensor is $\tau_{ij} = 2\mu\left(S_{ij} - 1/3\delta_{ij}S_{kk}\right)$. In Eqn. 5.8, k is the Turbulent Kinetic Energy (TKE) defined as

$$k = \frac{1}{2}\frac{\overline{-\rho u_i'' u_i''}}{\bar{\rho}} \tag{5.9}$$

5.2.2.3 Turbulent kinetic energy equation

Starting from the Reynolds-stress equations, an exact form for the TKE equation can be derived:

$$\frac{1}{2}\frac{\partial\left(\overline{\rho u_i'' u_i''}\right)}{\partial t} + \frac{\partial}{\partial x_k}\left[1/2\overline{\rho u_i'' u_i''}\tilde{u}_k\right] = \bar{\rho}P_k - \bar{\rho}\varepsilon - \frac{\partial J_k}{\partial x_k} + \Pi - \overline{u_i''}\frac{\partial \bar{p}}{\partial x_i} \tag{5.10}$$

with P_k a production term for TKE and $\bar{\rho}\varepsilon$ a dissipation term. The pressure strain term (Π) is often neglected and the remaining diffusion terms are modelled with a gradient hypothesis consistent with the Boussinesq assumption, so that

$$\frac{\partial \bar{\rho}k}{\partial t} + \frac{\partial \bar{\rho}k\tilde{u}_k}{\partial x_k} = \bar{\rho}P_k - \bar{\rho}\varepsilon + \frac{\partial}{\partial x_i}\left[(\mu + \frac{\mu_t}{\sigma_k})\frac{\partial k}{\partial x_i}\right] \tag{5.11}$$

where σ_k is a Prandtl number. At this stage, the production term does not need further modelling as it is $P_k = 2\mu_t\tilde{S}_{ij}\tilde{S}_{ij}/\bar{\rho}$.

5.2.2.4 Energy cascade

Turbulent motion is the result of the instability of large vortical structures that break down into smaller and smaller scales. These large structures have a size characteristic of the shear flow that creates them and the break-up process transfers kinetic energy from those large structures to smaller ones. The large structures have a length scale L_0, a velocity fluctuation u_0 and as their Reynolds number $Re_0 = u_0 L_0/\nu$ is large (and is a significant portion of Re_{flow}), they are not affected by molecular viscosity. This means that they transfer kinetic energy to smaller scales without significant dissipation and account for the production term P_k. At the smaller scales L_η, kinetic energy is dissipated into heat by the effects of molecular viscosity. For those scales, $Re_\eta \approx 1$ and they account for the dissipation term ε. The scales between L_0 and L_η account for the transfer of TKE only and are called the inertial range of the energy cascade shown on Fig. 5.1. This cascade gives the energy spectrum $E(\kappa)$ as a function of the wave number $\kappa = 2\pi/L$ corresponding to scale L. In ideal flows, $P_k = \varepsilon$.

From Richardson's concept, one can build a relation between a length scale L, the corresponding velocity fluctuation scale u_L and ε in the inertial range:

$$\frac{u_L^2}{\tau_L} \sim \varepsilon \qquad \text{with } \tau_L = \frac{L}{u_L} \qquad \text{so } \frac{u_L^3}{L} \sim \varepsilon \tag{5.12}$$

Supposing that equilibrium occurs at the inertial range, one has $\varepsilon = T$ with T the energy transfer rate. And if Kolmogorov's hypothesis is accepted, i.e. within the inertial range, the statistics of the motions at scale L have a universal form uniquely determined by ε and independent of ν, then

$$\frac{k_L^{3/2}}{\tau_L} \sim \varepsilon \tag{5.13}$$

where k_L is the TKE in the range from small to L. So the energy spectrum can only be:

$$E(\kappa) = C_K \varepsilon^{2/3} \kappa^{-5/3} \tag{5.14}$$

C_K is the Kolmogorov constant. From this point, it is even possible to determine the scale at which dissipation occurs:

$$L_\eta = \frac{\nu^{3/4}}{\varepsilon^{1/4}} \qquad \text{with } \tau_\eta = \frac{\nu^{1/2}}{\varepsilon^{1/2}} \qquad \text{and } u_\eta = \nu^{1/4}\varepsilon^{1/4} \tag{5.15}$$

5.2.2.5 Eddy viscosity expression

With the eddy viscosity assumption of section 5.2.2.2, some scales are filtered away and the effect of these scales on the remaining motion is replaced by an increased viscosity. On Fig. 5.1, if scales smaller than a cut-off length L_c corresponding to some κ_c are filtered away, the spectrum that is filtered away is characterized by ε and L_c so that the length L_c can be replaced with the kinetic energy in the spectrum that is filtered: k_c. One can derive then

$$\nu_t \sim \varepsilon^{1/3} L_c^{4/3} \qquad \text{and } k_c \sim \varepsilon^{2/3} L_c^{2/3} \tag{5.16}$$

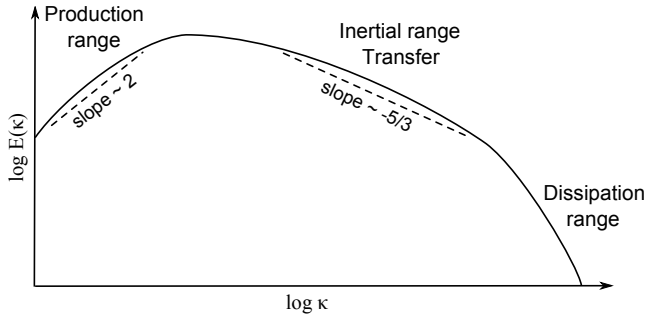

Figure 5.1: Energy cascade.

For this hypothesis to hold, L_c must be far away from L_η so that molecular viscosity has no influence at that scale. This implies that Re_{flow} must be sufficiently big. This further leads to

$$\nu_t = c_\mu \frac{k^2}{\varepsilon} \tag{5.17}$$

with c_μ a constant yet to be determined and k the TKE of the whole spectrum.

5.2.2.6 Scale-determining equation

In Eqn. 5.17, k is required and can be obtained from Eqn. 5.11. The next ingredient is the dissipation rate ε that will determine the overall length scale of the turbulent motion. From k and ε, a time scale $\tau = \varepsilon/k$ can be formed and the TKE-equation (Eqn. 5.11) can be transformed into

$$\frac{\partial \bar{\rho}\varepsilon}{\partial t} + \frac{\partial \bar{\rho}\varepsilon\tilde{u}_k}{\partial x_k} = c_{\varepsilon 1}\bar{\rho}\frac{\varepsilon}{k}P_k - c_{\varepsilon 2}\bar{\rho}\frac{\varepsilon}{k}\varepsilon + \frac{\partial}{\partial x_i}\left[(\mu + \frac{\mu_t}{\sigma_\varepsilon})\frac{\partial \varepsilon}{\partial x_i}\right] \tag{5.18}$$

where the constants $c_{\varepsilon 1}$ and $c_{\varepsilon 2}$ have been introduced together with the Prandtl number σ_ε.

This intuitive approach is further confirmed by the ReNormalization Group theory (RNG) consisting in a spectral methodology over the scale range. This theory also delivers estimates for the constants c_μ, σ_k, σ_ε, $c_{\varepsilon 1}$ and $c_{\varepsilon 2}$.

5.2.2.7 The law of the wall

Models based on the eddy viscosity concept are constructed to be consistent with the law of the wall i.e. the expression of the velocity profile in the logarithmic part of the boundary layer (see Fig. 5.2). One defines the friction velocity $u_\tau = \sqrt{\tau_w/\rho}$, $u^+ = u/u_\tau$ and the non-dimensional wall coordinate $y^+ = yu_\tau/\nu$ with the Y-axis normal to the wall. Derivation of the NS equations in the boundary layer close to the wall, where the viscous stresses are dominant, leads to

$$u^+ = y^+ \tag{5.19}$$

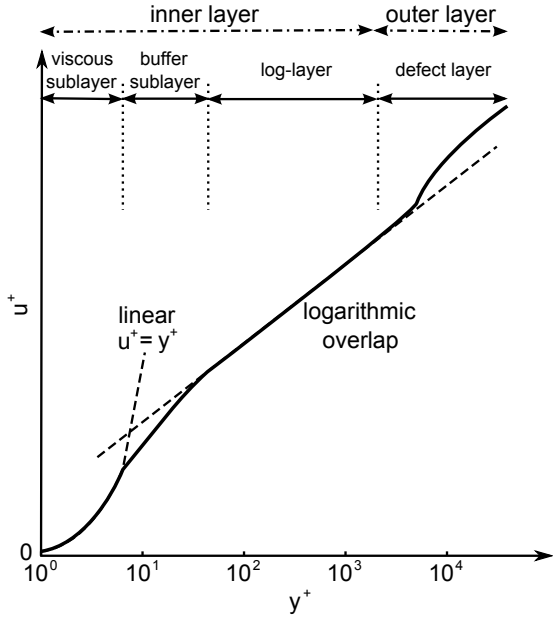

Figure 5.2: Schematic velocity profile near the wall in a turbulent boundary layer.

In this viscous sub-layer, one can show that the dissipation at the wall is non-zero and a limiting value for ε can be computed: $\varepsilon = 2\nu k/y^2$ for $y \to 0$.

Furthermore, if one admits that close to the wall but not extremely close, there is a region where the velocity profile is determined by the turbulent shear stress but not by the shear stress due to molecular viscosity, one can show

$$u^+ = \frac{1}{\kappa} \ln y^+ + B \tag{5.20}$$

where κ is the von Karman constant and B another constant. This law is valid in the logarithmic layer and expresses that in this layer, the Reynolds stresses are dominant on viscous stresses. Different experimental results tend to confirm this hypothesis and the validity of the law of the wall (logarithmic profile). Generally, the law of the wall applies from $y^+ = 30$ to $y/\delta \approx 0.1$ with δ the boundary layer thickness.

5.2.3 Turbulence modelling

Many models exist to close the RANS equations given certain assumptions. In this section, the chosen model is discussed in more details so that the reasons for this choice but also its the limitations it implies, come to light.

5.2.3.1 Standard $k-\varepsilon$ model

Developed by Jones and Launder in 1972 [162], this model uses the RANS-equations together with the TKE-equation (Eqn.5.11), the ε-equation (Eqn. 5.18), and the eddy-viscosity (Eqn. 5.17). Standard values for the constants c_μ, σ_k, σ_ε, $c_{\varepsilon 1}$ and $c_{\varepsilon 2}$ have been obtained from simple flows. The constant c_μ comes from the observation of thin shear flows with an approximate balance between production and dissipation, the constant $c_{\varepsilon 2}$ from the decay of homogeneous turbulence and the constant $c_{\varepsilon 1}$ from homogeneous shear flow experiments. The Prandtl number σ_k is a priori taken as unity since it governs the turbulent diffusion of the TKE by the turbulent motion itself. The Prandtl number σ_ε comes from consideration of the diffusion of ε in the logarithmic layer. For that Prandtl number, it is imperative to satisfy

$$\sigma_\varepsilon = \frac{\kappa^2}{(c_{\varepsilon 2} - c_{\varepsilon 1})\sqrt{c_\mu}}$$

so that the law of the wall can be predicted correctly. The set of equations for this model is:

$$\begin{cases} \dfrac{\partial k}{\partial t} + \dfrac{\partial k u_i}{\partial x_i} = P_k - \beta^* \omega k + \dfrac{\partial}{\partial x_i}\left[(\nu + \sigma^* \nu_t)\dfrac{\partial k}{\partial x_i}\right] \\ \dfrac{\partial \bar{\rho}\varepsilon}{\partial t} + \dfrac{\partial \bar{\rho}\varepsilon u_i}{\partial x_i} = c_{\varepsilon 1}\bar{\rho}\dfrac{\varepsilon}{k}P_k - c_{\varepsilon 2}\bar{\rho}\dfrac{\varepsilon}{k}\varepsilon + \dfrac{\partial}{\partial x_i}\left[(\mu + \dfrac{\mu_t}{\sigma_\varepsilon})\dfrac{\partial \varepsilon}{\partial x_i}\right] \end{cases} \tag{5.21}$$

This model is the simplest of two-equations models and is known to be very robust.

5.2.3.2 Wall functions

When low-Reynolds modelling is used (i.e. when the $k-\varepsilon$ model is used up to the wall), the near-wall behaviour of turbulent quantities must be carefully modelled. Indeed, close to the wall, turbulence is damped and the turbulent Reynolds number $Re_t = k^2/(\nu\varepsilon)$ becomes small. To achieve this, damping functions are introduced into Eqn. 5.21.

As with low Reynolds modelling the first grid point should be at $y^+ \approx 1$, the numerical cost is elevated because around 50 grid points are necessary in the boundary-layer. However, in many applications, the precise description near the walls is not needed and high Reynolds modelling can be used. In high Reynolds modelling, the first grid point A is typically so that $y^+ \in [30, 100]$. At this point, special boundary conditions are imposed:

$$\tau_A = \tau_w \qquad k_A = \frac{u_\tau^2}{\sqrt{c_\mu}} \qquad \varepsilon_A = \frac{u_\tau^3}{\kappa y} \tag{5.22}$$

where u_τ is determined from

$$\frac{u}{u_\tau} = \frac{1}{\kappa}\ln\left(\frac{B_2 y u_\tau}{\nu}\right)$$

with u from the previous iteration, $\kappa = 0.41$ and $B_2 = 7.768$. The drawback of this method is that it corresponds to impose a constant value of k at the first grid point in

the logarithmic-layer although in reality, the TKE has a pronounced maximum in the buffer-layer so there is no zone of constant TKE between the first grid point and the wall. The TKE-equation (Eqn. 5.11) can be solved at the first grid point by imposing $P_k = \tau_A \partial u/\partial y$ with $\partial u/\partial y = u_\tau/(\kappa y)$. Then ε can be determined as $u_\tau = k^{1/2} c_\mu^{1/4}$ so $\varepsilon = c_\mu^{3/4}/(\kappa y)$. In the end, u_τ or τ_w are determined, with the assumption $\mu = \mu_t$ made so that molecular viscosity is set to zero, from:

$$\begin{aligned} &\frac{u}{u_\tau}\frac{u_\tau}{u_\tau} = \frac{1}{\kappa}\ln\left(\frac{B_2 y u_\tau}{\nu}\right) \Rightarrow \frac{u\sqrt{k}c_\mu^{1/4}}{u_\tau^2} = \frac{1}{\kappa}\ln\left(B_2 y \frac{\sqrt{k}c_\mu^{1/4}}{\nu}\right) \\ &\Rightarrow u_\tau^2 = \frac{\tau_w}{\rho} = \frac{\sqrt{k}c_\mu^{1/4}\kappa}{\ln(B_2 y_A^+)}u \qquad \text{where } y_A^+ = \frac{c_\mu^{1/4}\sqrt{k}y_A}{\nu} \end{aligned} \tag{5.23}$$

The high Reynolds approach is not valid for flows with re-circulation as these flows come with a sign-change for u_τ. $|u_\tau|$ is used in the determination of y^+ but the condition $y^+ \in [30, 100]$ cannot be satisfied in the recirculation region (generally with lower velocities). Although the above algorithm does not cause problems for regions of recirculation (because u_τ is replaced by $c_\mu^{1/4}\sqrt{k}$ for the computation of y^+), blindly applying it corresponds to enforcing the log-law in a region where the laws of the viscous sub-layer should be used. In such a case, standard wall functions are inappropriate and are often replaced by a two-layer approach so that low Reynolds modelling does not have to be implemented. This approach consists in having two sets of equations and using one or the other depending on the local value of y_P^+ for each grid point in the boundary layer:

$$y_P^+ = \frac{c_\mu^{1/4}\sqrt{k}y_P}{\nu}$$

$y_P^+ > 11.3 \rightarrow$ log-law Standard Wall Treatment	$y_P^+ \leq 11.3 \rightarrow$ linear-law Enhanced Wall treatment
$\tau_w = \frac{\rho\sqrt{k_P}c_\mu^{1/4}\kappa}{\ln(B_2 y_P^+)}u_P$	$\tau_w = \frac{\mu}{y_P}u_P$
$u_\tau = \sqrt{\frac{\lvert\tau_w\rvert}{\rho}}\left(\frac{\tau_w}{\lvert\tau_w\rvert}\right)$	$u_\tau = \sqrt{\frac{\lvert\tau_w\rvert}{\rho}}\left(\frac{\tau_w}{\lvert\tau_w\rvert}\right)$
$u_y = \frac{u_\tau}{\kappa y}$	$u_y = \frac{\tau_w}{\mu}$
$P_k = \tau_w u_y$	$P_k = \tau_w u_y$
$\varepsilon = \frac{c_\mu^{3/4}k^{3/2}}{\kappa y}$	$\varepsilon = \frac{2\nu k_P}{y_P^2}$

5.2.3.3 Limiters and realizability

On top of correct near-wall behaviour, realizability is a physical and mathematical principle that should fundamentally be ensured by any turbulence model. It is defined as the non-negativity of the turbulent normal stresses together with the Schwarz-inequality between any fluctuation:

$$\begin{cases} \overline{u_i'^2} > 0 \\ \left(\overline{u_i' u_j'}\right)^2 < \overline{u_i'^2 u_j'^2} \end{cases} \tag{5.24}$$

As standard $k-\varepsilon$ and $k-\omega$ models are not realizable, realizability is enforced by replacing c_μ by a limited value. This corresponds to limiting the Reynolds stress

components for large values of the straining. More directly, the limiting can be done by writing the eddy viscosity as

$$\nu_t = c_\mu \frac{k^2}{\varepsilon} = c_\mu k T \qquad \text{with } T = \frac{k}{\varepsilon}$$

in which T is the time-scale of turbulence. Limiting the Reynolds stresses can then be introduced by a limiter of the form:

$$T = Min\left(\frac{k}{\varepsilon}, \frac{\alpha}{\sqrt{6}c_\mu S}\right) \text{ or } T = Min\left(\frac{k}{c_\mu \omega}, \frac{\alpha}{\sqrt{6}c_\mu S}\right) \text{ with } \begin{cases} S = \sqrt{2S_{ij}S_{ij}} \\ \alpha = 0.6 \end{cases}$$

α is chosen to avoid the overprediction of TKE at the leading edge that occurs with standard models. Limiters such as those are universally accepted; although they do not ensure realizability in all flows at least they limit the overprediction in stagnation flows.

5.2.3.4 k-ε realizable model with wall treatment

For the high-fidelity aerodynamic analysis, the realizable k-ε model [267] has been chosen for its robustness and ability to resolve boundary layers under strong adverse pressure gradients or in the presence of separation and recirculation. These phenomena are indeed likely to occur with sub-optimal highly-loaded candidate blades. Additionally, this model behaves adequately in the presence of rotation. These reasons justify why this model has been chosen above:

- the Spalart-Allmaras one-equation model [272], which is per se cheaper and has also been developed for wall-bounded flows but has difficulties in dealing with separation and possibly recirculation;
- the standard $k-\omega$ two-equation model mainly developed by Wilcox from 1988 onward [308], which has a more natural treatment of the near-wall region but usually performs better for low-Re flows;
- the $k-\omega$ SST model [200] that combines the $k-\omega$ model in wall vicinity with the $k-\varepsilon$ model in the free stream by the means of blending-functions; hence it is reliable for a wide class of flows including in the presence of adverse pressure gradients or shocks but at the price of the additional computational cost of solving the closure equations with additional terms (blending functions).

For transonic flows, compressibility affects turbulence through so-called "dilatation dissipation", which is neglected in section 5.2.3.1. Doing so, the observed decrease in spreading rate with increasing Mach number for free shear layers, would not be predicted. For this reason the dilatation dissipation term is included in Eqn. 5.11 according to [262].

As resolving the viscous and buffer sublayers does not yield, for the considered application characterized by a high Re, significant improvement on the overall performance values, the first cell centroid of the boundary layer mesh is placed within the log-layer ($y^+ \in [30, 300]$). Wall treatment is applied through non-equilibrium wall functions that account for the effect of a pressure gradient along the wall [168].

5.2.4 Discretization

The conservation equations (Eqs. 5.4-5.6), the closure equations (Eqn. 5.21) and all other complementary differential equations such as those for wall treatment, are discretized using the finite volumes scheme on the mesh described in section 4.3.1. For transport of a scalar quantity ϕ, the conservation equation over an arbitrary control volume V can be written as

$$\int_V \frac{\partial \rho\phi}{\partial t} dV + \oint \rho\phi \overline{U}.\overline{dA} = \oint \Gamma_\phi \nabla\phi.\overline{dA} + \int_V S_\phi dV \tag{5.25}$$

with $\overline{A}$ the surface area vector, Γ_ϕ the appropriate diffusion coefficient, $\nabla\phi$ the gradient and S_ϕ the source of ϕ per unit volume. For a cell, this equation is discretized in space as

$$\frac{\partial \rho\phi}{\partial t} V + \sum_f^{N_{faces}} \rho_f \overline{u}_f \phi_f . \overline{A}_f = \sum_f^{N_{faces}} \Gamma_\phi \nabla\phi_f . \overline{A}_f + S_\phi V \tag{5.26}$$

where N_{faces} is the number of faces enclosing the cell and the subscript $._f$ refers to the variables evaluated at the face f. Eqn. 5.26 contains the unknown scalar variable ϕ at the cell center as well as the unknown values ϕ_f on the surrounding faces. To compute the convection terms, these values are obtained by second-order upwinding though numerous other options exist. Hence ϕ_f is computed by a truncated Taylor series expansion about the cell centroid:

$$\phi_f = \phi + \nabla\phi.\overline{r} \tag{5.27}$$

in which ϕ and $\nabla\phi$ are the cell-centered values and $\overline{r}$ is the distance vector from the upstream cell centroid (relative to the velocity normal to the face) to the center of the considered face. The gradient $\nabla\phi$ is evaluated with the Green-Gauss cell-based technique with limiters to prevent divergence when needed.

Temporal discretization is achieved by implicit time integration so that:

$$\frac{\partial\phi}{\partial t} = \frac{\phi^{n+1} - \phi^n}{\Delta t} = F(\phi^{n+1}) \tag{5.28}$$

which implies that the solution in a cell at time step $n+1$ is related to the value at time n and the values in neighbouring cells at time $n+1$.

Fluent v12.0.16 solves the governing integral equations for the conservation of mass, momentum and energy and other scalars such as turbulent quantities by integration of the governing equations on the cells to obtain algebraic equations for the discrete dependent variables such as u_i $(i = 1, 2, 3)$, p, T and other conserved scalars. The discretized equations are then linearized and the solution of the resultant linear system yields updated values of the dependent variables. Two solvers are available albeit in both methods the velocity field is obtained from the momentum equations. On one hand, the continuity equation is used to obtain the density field while the pressure field is determined from the equation of state. This is the density-based solver. On the other hand, in the pressure-based solver, the pressure field is extracted by solving a pressure-velocity coupling equation.

5.2.4.1 Pressure-based solver

The pressure-based solver solves first the momentum equations, then the continuity equation before addressing the others and updating the fluid properties to start the loop again until convergence is reached. It is a co-located scheme whereby pressure and velocity are both stored at cell centers. To compute velocities at a face, momentum-weighted averaging [249] is used instead of linear averaging between cell centers as this would result in unphysical checker-boarding of pressure. Second-order upwinding is applied for density. The pressure-velocity coupling is realized with a Semi-Implicit Method for Pressure-Linked Equations (*SIMPLE*) scheme. Because the equations are solved in a segregated way (the momentum equation is solved independently of the continuity equation), the computed fluxes would not satisfy the continuity equation. The necessary fluxes and pressure correction terms are obtained by substituting the flux correction equations into the discrete continuity equation to obtain a discrete equation for the pressure correction. Doing so, the corrected face flux satisfies the discrete continuity equation during each iteration. For stability purposes, under-relaxation is applied onto variables and equations.

5.2.4.2 Density-based solver

The density-based solver solves the continuity, momentum and energy equations simultaneously as a vector of equations. Then the other equations (turbulence,...) are solved sequentially and the fluid properties updated before starting the loop again until convergence is reached. To solve the very stiff system resulting from the matrix representation of the NS-equations with the vectorized conserved variables, preconditioning is applied for steady computations [296]. It modifies the vector form of time-derivative terms in the NS-equations by pre-multiplying it with a preconditioning matrix to re-scale the acoustic speed, which is an eigenvalue of the system, with respect to the fluid velocity. Roe's flux splitting method is applied to the inviscid flux vector [254] and in its formulation, it boils down to 2^{nd} order central differencing with added matrix dissipation. The added matrix dissipation produces upwinding of the convected variables, as well as the pressure-velocity coupling required for stability and efficient convergence at low to moderate Mach numbers. Time discretization is realized with an implicit Euler scheme conjugated with Newton-type linearization of the fluxes. For steady flows time-marching is applied until a steady state is reached. The system of equations is solved with a symmetric point Gauss-Seidel method in conjunction with an algebraic multigrid method to accelerate the convergence of the solver by computing corrections on a series of coarse grid levels.

5.3 Implementation

In the present work, the time-dependency disappears if the equations are expressed in a non-inertial reference frame that rotates with the blades. This simplification comes at hand because the blades are placed periodically around the spinner but it implies that no non-moving part (such as the wing behind the propeller or an air intake) can be modelled. In the rotating reference frame, the flow may be considered as steady and the momentum equation contains two additional terms: the Coriolis and

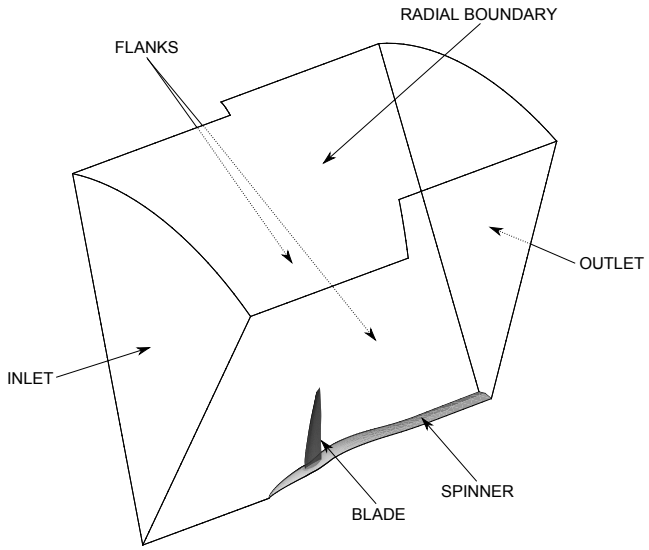

Figure 5.3: Boundary nomenclature.

centripetal accelerations. The steady hypothesis implies also that for what turbulence matters, only statistical averages are available.

The rotational velocity of the reference frame (ω or n) is calculated from the advance ratio J according to

$$J = \frac{u_\infty}{nD} = \frac{u_\infty}{\frac{\omega}{2\pi}D} \tag{5.29}$$

5.3.1 Boundary conditions and initialization

With the steady flow assumption, another simplification may be introduced. Indeed, because of periodicity considerations, it suffices to solve the flow in a single blade passage (as illustrated in Fig. 5.3) with appropriate boundary conditions on the flanks of the passage. These conditions are available in Fluent v12.0.16 in the form of periodic conditions that enforce strict equality for all flow variables between the two flanks.

The boundaries of the computational domain are named after Fig. 5.3; to these entities, the following boundary conditions are applied:

1. INLET: pressure-inlet with prescribed total pressure p_0 and total temperature T_0. The velocity obtained by the difference between the total pressure at the inlet and static pressure at the outlet is normal to the inlet and augmented at each radius r with the tangential component resulting from rotation ωr. The total pressure and temperature are computed from:

$$p_0 = p_\infty(1 + \frac{\gamma - 1}{2}{M_\infty}^2)^{(\frac{\gamma}{\gamma-1})} + p_{losses} \tag{5.30}$$

$$T_0 = T_\infty(1 + \frac{\gamma - 1}{2}{M_\infty}^2) \tag{5.31}$$

in which p_{losses} is a correction for the total pressure losses due to the propeller. In order to get the expected Mach number M_∞ at the inlet within a margin of 2.75%, fixed values of p_{losses} are applied for each advance ratio in disregard of the propeller geometry. Doing so, the computations are relaxed of having to iterate on p_{losses} to match perfectly M_∞ but are compared within a narrow range of M_∞. The influence of rotation is automatically accounted for by the Single Reference Frame model of Fluent v12.0.16. For turbulent computations, a turbulence intensity T_u of 1% and a turbulent length scale T_l of $0,05m$ are given. The turbulence parameters T_u and T_l are taken as safe approximates in order to be able to compare with wind-tunnel results despite the fact that those turbulent quantities for the wind-tunnels are not reported with the experimental results. However, these inputs do not significantly affect the overall performance estimates.

2. OUTLET: pressure-outlet with given static pressure p_∞ and static temperature T_∞ for any possible occurrence of reverse flow. The static conditions are given by those corresponding to the international standard atmosphere at flight level FL350 (10668m, 35000ft) for the cruise condition or FL000 (0m, 0ft) for the simulated take-off/landing condition.
3. FLANKS: periodic condition with no pressure jump. This particular boundary condition requires the grids on both flanks to be periodic.
4. SPINNER: adiabatic no-slip wall.
5. BLADE: adiabatic no-slip wall.
6. RADIAL BOUNDARY: pressure-far-field condition using the Riemann invariants theory to assign either no condition (on characteristics leaving the domain) or the irrotational free-stream total conditions of the axial free flow[1] (on characteristics entering the domain). This boundary condition emulates the effect of a free far-field at a prescribed pressure as would be the case in real flight.

Before the first iteration, the solution is initialized by applying the freestream quantities in all cells.

5.3.2 Solution strategy

A dedicated solution strategy had to be developed in order to achieve satisfactory convergence despite the delicate interaction between the rotating reference frame and the pressure-far-field condition or the early occurrence of massive flow separation on some blade designs. The strategy consists in starting the computations with a few iterations (typically 50) using the pressure-based solver with a laminar flow hypothesis at a lower Mach number and higher advance ratio (lower rpm than the expected one) before jumping to the density-based solver with laminar flow while increasing the Mach number and decreasing the advance ratio, this takes typically another 1000 iterations. Finally, the correct Mach number and rpm are set with the turbulent flow hypothesis. In this state, computations are ran for a fixed number of iterations yielding convergence within engineering accuracy (at least 2^{nd}-order reduction of the continuity residual and 3^{rd}-order reduction for velocity residuals). This is illustrated in Fig. 5.4 where the jumps at 2500 iterations pertain to the change in advance ratio.

[1] See Eqs. 5.30 and 5.31.

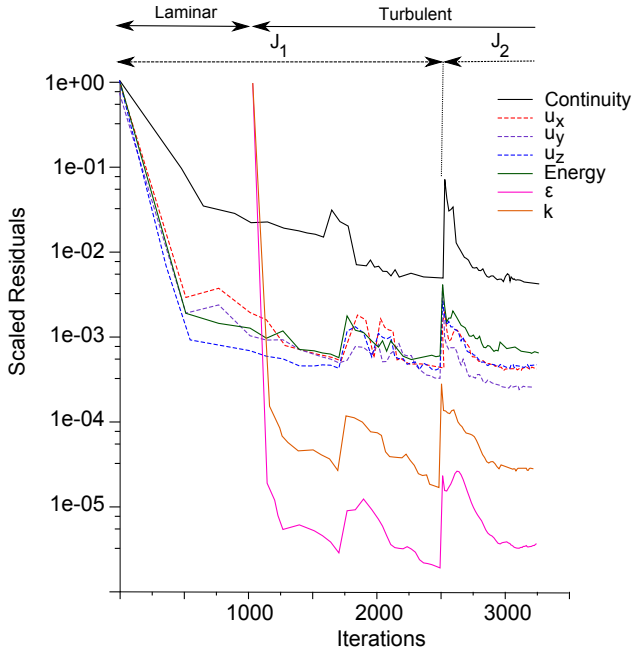

Figure 5.4: Typical convergence plot.

5.3.3 Post-processing

In the post-processing phase, the pressure and shear force distributions around the blade are integrated to compute the net thrust T_{blade} and the net power required to drive the blade P_{blade}. These quantities are multiplied by the number of blades before computing the non-dimensional thrust- and power-coefficients C_T and C_P:

$$C_T = \frac{T}{\rho_\infty n^2 D^4} \tag{5.32}$$

$$C_P = \frac{P}{\rho_\infty n^3 D^5} \tag{5.33}$$

These coefficients are used to compute the thrust and power of the unscaled propeller. Additional results are:

- the tip Mach number $M_{tip} = \sqrt{M_\infty^2 + (\omega R/c_\infty)^2}$,
- the moment coefficient around the pitch change axis for a single blade,

$$C_{Tq,z} = \frac{Tq_z}{\rho_\infty n^2 D^5} \tag{5.34}$$

- and of course the net efficiency

$$\eta = \frac{Tu_\infty}{P} = \frac{JC_T}{C_P} \tag{5.35}$$

5.4 Validation

Although Fluent v.12.0.16 and earlier versions have already been extensively validated on commonly accepted test cases, a broad campaign has been conducted to validate the chosen approach for the specific purpose of computing propeller flow. This campaign is reported in [188] and covers the NACA 4-(5)(05)-041 [246] and 4-(0)(03)-059 [90] straight propellers as well as the NASA SR-1 [30] and SR-3 [259] single rotation propfans whose blades feature 30° and 45° sweep respectively. More details about these propellers can be found in appendix A.Comparisons were made between computed thrust and power coefficients versus those obtained during wind-tunnel experiments for a simulated take-off/landing condition or transonic cruise conditions under various advance ratios so that moderate to high loadings are covered.

5.4.1 Take-off/Landing condition

Figures 5.5 and 5.6 compare the present results with experiments for both the thrust and power coefficients in the case of the NACA 4-(5)(05)-041 and NASA SR-1 propellers. The agreement is good in general though some punctual discrepancies exist. For the NACA 4-(5)(05)-041, a lower value of the power coefficient is predicted at the highest advance ratio despite accurate prediction of the thrust coefficient. Fortunately, this condition is not likely to occur with optimized blades as this propeller operates close to the brake state. In the case of the NASA SR-1, the discrepancy at lower advance ratio is related to strong blade deformations occurring at high rpm. These deformations are not accounted for in the present work. The overall agreement is slightly worse for this case but this could be related to a small error in blade setting angle or to blade untwist due to centrifugal and aerodynamic forces. In this condition, the propfan operates already at high rpm and is submitted to very strong loads while delivering the kind of thrust required for acceleration. On top of this, measuring the blade angle rigorously during experiments is a difficult task. A small change in blade angle (of less than $0,5°$) would make the computed and the experimental results match perfectly for this advance ratio. Nevertheless, the shape of the curves is accurately captured over normal operating conditions.

5.4.2 Cruise condition

Figures 5.7 to 5.11 show how the predicted performance values for propellers of diversified shapes, fall close of the measured values for Mach numbers ranging from 0.59 to 0.8. As apparent from Figs. 5.7 to 5.9, the highest discrepancies usually occur at low advance ratio. Once again, the most likely reasons for these differences are related to the blade angle β_{ref} as well as blade deflection due to high centrifugal and pressure loads during the experiments. These results also denote that satisfactory agreement is obtained from light to heavy loading (C_P ranging from -0.5 to 2.5) with flow fields exhibiting phenomena such as root blockage, transonic shocks or even flow separation [188].

Fig. 5.10 demonstrates that good agreement is maintained through various operating conditions. At high advance ratio, the propeller is windmilling; this condition is very well predicted over a wide range of advance ratios corresponding to emergency

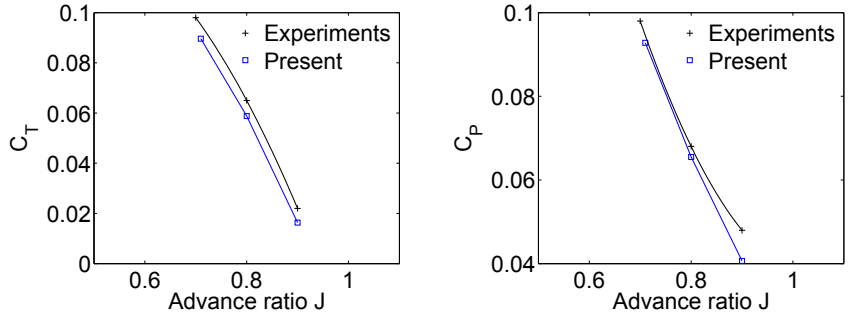

Figure 5.5: NACA 4-(5)(05)-041 propeller at $M_\infty = 0.2$ with $Re_{ref} = 5.2e05$ and $\beta_{ref} = 20°$. Experimental data taken from [248].

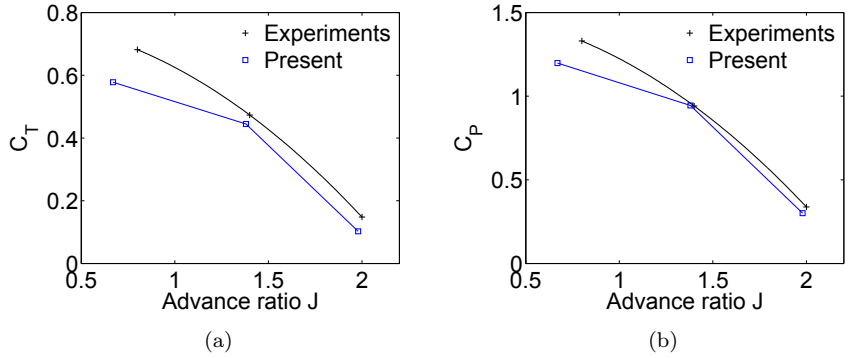

Figure 5.6: NASA SR-1 propeller at $M_\infty = 0.2$ with $Re_{ref} = 8.2e05$ and $\beta_{ref} = 43°$. Experimental data taken from [30].

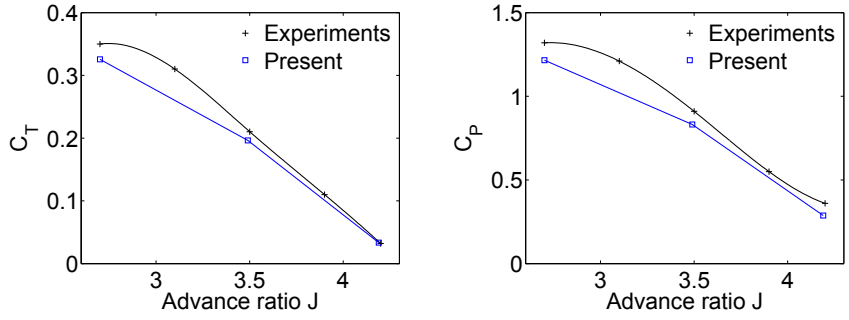

(a) (b)

Figure 5.7: NACA 4-(5)(05)-041 propeller at $M_\infty = 0.59$ with $Re_{ref} = 5.3e05$ and $\beta_{ref} = 60°$. Experimental data taken from [246].

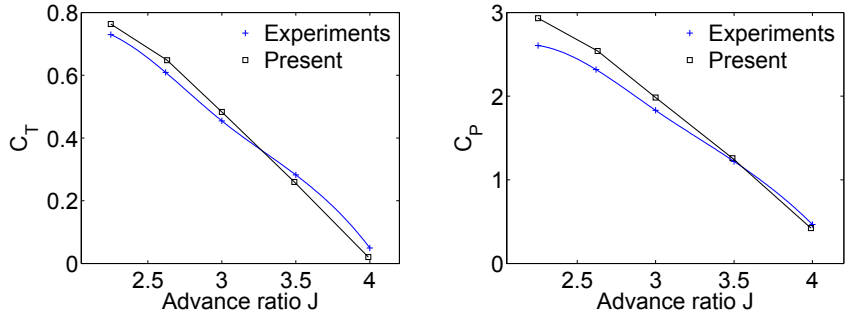

(a) (b)

Figure 5.8: NASA SR-3 propeller at $M_\infty = 0.6$ with $Re_{ref} = 4.3e05$ and $\beta_{ref} = 58°$. Experimental data taken from [259].

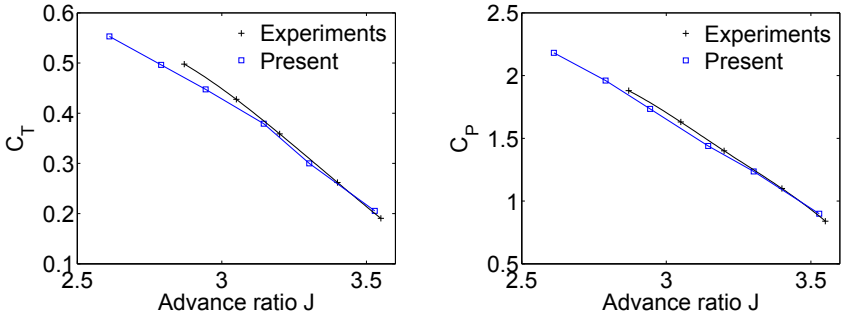

(a) (b)

Figure 5.9: NASA SR-1 propeller at $M_\infty = 0.75$ with $Re_{ref} = 3.8e05$ and $\beta_{ref} = 59°$. Experimental data taken from [30].

situations in real flight. The brake condition at moderate advance ratio is also predicted with a very good accuracy both for the thrust and power coefficients. As the rpm is increased, the computed results follow the experimental ones. Experimental data for $J < 2,9$ are not available due to rpm-limitations on the driving engine used for the wind-tunnel tests. Nevertheless, the computations were run with much lower advance ratios until $2,1$. At this advance ratio (and even at a slightly higher one), the shock spans over the entire blade passage from one blade to another and remains strong from blade root to tip. Each of the previous behaviours has its own streamlines pattern (see [124]). Having captured these different states without difficulties during the computations is highly valuable as it suggests that the high fidelity aerodynamic analysis tool can capture those different states without additional trimming during the computational process.

A comparison with predictions from other codes is shown in Fig. 5.11(b). Whitfield, et al. [307] obtained theirs with an Euler solution whereas Matsuo, et al. [194] obtained them with a Navier-Stokes computation. Srivastava, et al. [273] used an Euler computation with a 'hot-shape' (i.e. the blade is first deflected due to the centrifugal loading). As the blade is deflected during the experiments (due to both centrifugal and aerodynamic loading), it is common practice to apply a solid body rotation on the blade to match some coefficient (usually the power coefficient). This explains the excellent agreement for the results from [307] and [273] at $J = 3.7$ and $J = 3.51$ respectively. The agreement of the present results in terms of power coefficient C_P is good if compared both to experiments and other published results. This is especially true since the power coefficient is very sensitive to the blade angle and no correction of any kind is applied on the 'cold', undeflected, blade shape.

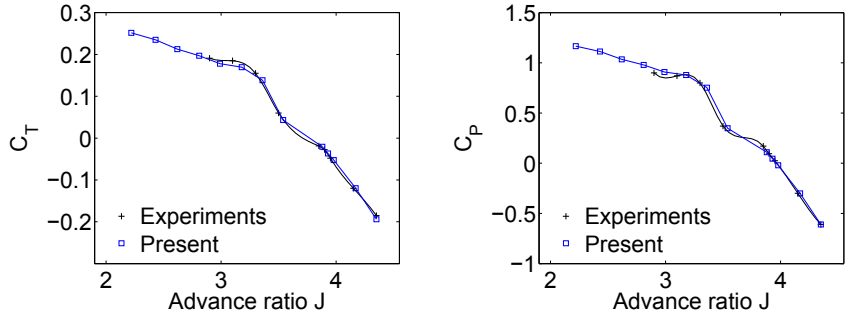

(a) (b)

Figure 5.10: NACA 4-(0)(03)-059 propeller at $M_\infty = 0.8$ with $Re_{ref} = 7.4e05$ and $\beta_{ref} = 60°$. Experimental data taken from [167].

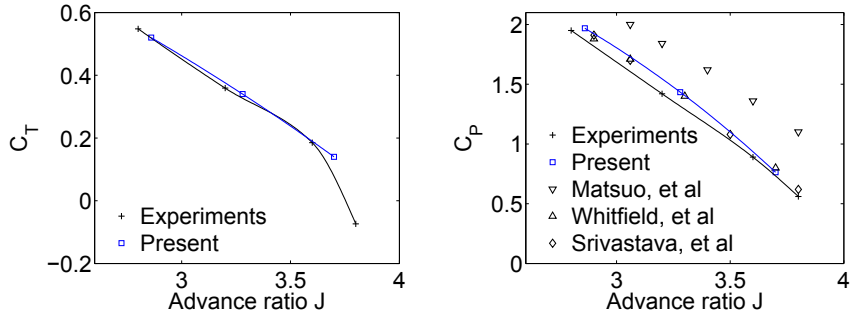

(a) (b)

Figure 5.11: NASA SR-3 propeller at $M_\infty = 0.8$ with $Re_{ref} = 5.7e05$ and $\beta_{ref} = 58°$. Experimental data taken from [259].

Chapter 6

Aeroacoustic solver

Knowledge of the pressure around the blade surface together with its kinematics, opens the path to computing the noise emitted by the propeller in operation. This is achieved by the Computational Hybrid Aeroacoustics solver that is available in the post-processing phase of the CFD-solver. This chapter begins with the fundamentals of the acoustic analogy before a short review of possible methods to compute the sound emitted by a propeller. As will be explained, only specific and dominant sources will be modelled out of all the sound sources enumerated in section 2.3. Then the fundamental assumptions of the present method will be discussed together with the associated mathematical formulation. Finally, the predictions are compared to published results for validation purposes.

Before going into the details of this high fidelity analysis tool, it is important to recall that the isolated propeller is considered completely free of installation effects and at zero angle of attack (i.e. the propeller plane is perpendicular to the forward velocity $\overline{u}_\infty$). The first assumption is quite important since it implies that no account is given for the scattering and refraction due to the presence of a fuselage and the boundary layer around it [81, 82, 177, 231] or for the additional noise that would be generated by the interaction of the highly turbulent and swirling slipstream with fixed surfaces such as the wing [286]. The zero angle of attack assumption implies that the cyclic or nearly cyclic effects due to inclination of the inflow with respect to the propeller disk, are neglected. This purely steady-state assumption is taken as it corresponds to the only intrinsic feature of a propeller design whereas cyclic variations depend on variable conditions. Indeed, these effects usually occur because of inflow distortions due to the upwash of a trailing wing or because of particular flight circumstances or installation features that deliberately put the propeller plane at an angle. For those particular cases, where the steady periodic assumption of section 5.3 breaks down, unsteady approaches are required and imply modelling of the full propeller disk such as in [52, 117, 231, 218, 313].

6.1 Overview of sound computing methods

From the 1919's on, attempts have been made to develop a method for noise prediction applied to propellers [202]. Yet the first successful attempt is usually attributed to L. Gutin [135] who focused on the level of harmonics due to rotating blade loads by a strip theory. The search for improved models continued until the publication of Ffowcs Williams - Hawkings' analogy [113] (FW-H) and counted numerous other works that are brilliantly put into perspective in [202] and [43]. Most current methods with a theoretical background, to distinguish them from the pleiad of empirical methods reported in [202], are derived from the acoustic analogy and are thus called *hybrid* because they essentially decouple the propagation of sound from its generation by the main flow. The sources are modeled from a CFD-solution whereas the propagation is modeled by a particular wave equation which is solved separately. As will be discussed in the next section, the main assumption is that this propagation does not bear any influence on the CFD-solution. Nevertheless, note that in some simple cases, the power of current computers allows for direct computation of both the sound and the flow, provided that the mesh satisfies specific criteria which make this approach prohibitive for a propeller in transonic flow.

6.1.1 The acoustic analogy

Sir James Lighthill [178] based his theory of jet noise, known as the *acoustic analogy*, on the separation of sound, regarded as weak propagating waves in a compressible fluid, from the aerodynamic flow responsible for convection. The propagation of weak sound waves is treated linearly by a wave equation that regards the global aerodynamic flow as a source term [40]. Hence the aeroacoustic problem (i.e. the sound field) is somehow conveniently decoupled from the aerodynamic problem (i.e. the calculation of acoustic sources). Within the framework of the analogy, the fundamental equation of aeroacoustics governs the propagation of small perturbations of the flow quantities in a quiescent medium away from the source region, with the assumption of complete knowledge of the flow field in this region [101]. This wave equation concerns the product of the perturbation density ρ' with the speed of sound squared c_∞^2 and is obtained by manipulation of the momentum conservation and continuity equations. The active flow region, responsible for the emission of sound by various mechanisms, is included in the propagation equation as a source term whose strength is given by a second order tensor known as Lighthill's stress tensor. This tensor is equivalent to quadrupole sources and vanishes outside the source region.

In 1969, Ffowcs Williams and Hawkings extended Lighthill's idea to the sound generated from surfaces in arbitrary motion [113]. They manipulated the Navier-Stokes equations by introducing the Dirac delta[1] (δ) and Heaviside[2] (H) generalized functions taking a function f as argument. The function f is essential in this development as it is exactly zero on the body of interest (see Fig. 6.1), positive in the fluid region and negative inside the body. Doing so, the modified fluid dynamics equations, that are originally applicable in the fluid region, are now valid everywhere and yielded

[1]The Dirac delta generalized function has the following properties: $\delta(f) = 1$ if and only if $f = 0$, $\delta(f) = 0$ if $f \neq 0$.

[2]The Heaviside generalized function is such that $H(f) = 0$ if $f < 0$ and $H(f) = 1$ if $f > 0$. Its generalized derivative is the Dirac delta generalized function.

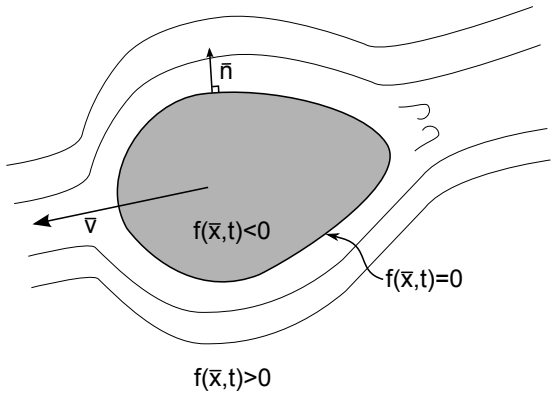

Figure 6.1: Body in arbitrary motion.

an inhomogeneous wave equation featuring quadrupole sources in the volume around the body of interest as well as dipole and monopole sources on its surface:

$$\frac{1}{c_\infty^2}\frac{\partial^2}{\partial t^2}p'(\mathbf{x},t) - \nabla^2 p'(\mathbf{x},t) = \frac{\partial}{\partial t}\big((\rho_\infty v_n)\delta(f)\big) - \frac{\partial}{\partial x_i}\big(l_i\delta(f)\big) + \frac{\partial^2}{\partial x_i \partial x_j}\big(T_{ij}H(f)\big) \tag{6.1}$$

where p' is the acoustic pressure equal to $c_\infty^2\rho'$ with ρ' the perturbation density, ρ_∞ and c_∞ are the density and speed of sound in the undisturbed medium, v_n is the normal velocity of the body surface given by the equation $f = 0$, l_i are the components of the force acting on the fluid and T_{ij} is Lighthill's stress tensor [129, 111, 43]. The first term of the right hand side of Eqn. 6.1 is the monopole or thickness source term, related to the kinematics of the body or the blade in the present case. The second term, also known as dipole or loading source term, is purely related to the distributed force acting on the fluid, such as the forces applied by the blade surface in the present case. The last term is known as the quadrupole source term and accounts for various non-linearities [44] such as non-linear wave propagation, variations in the local sound speed and noise emitted by shocks or other flow inhomogeneities.

The FW-H analogy is particularly convenient because the solution of Eqn. 6.1 can be written in such a way that the intrinsic features of the flow are expressed in a reference frame that is attached to the moving body and the Doppler effects (convective amplification and frequency shift) are entirely determined by the kinematics of the sources in the reference frame attached to the observer. These are also the reasons why the FW-H analogy is particularly suited for the noise generated by rotating bodies.

6.1.2 Tonal noise predictions

It is not realistic to sketch up here a reasonable overview of the 30 methods or so, reported in [202]; albeit the great majority of them is derived from one or another form of the Ffowcs Williams - Hawkings analogy. On top of analytical approaches ordinarily based on some form of strip-theory and linearized thin-airfoil theory, most authors

propose a method based on the knowledge of the local pressure and kinematics of small surface elements resulting from the spatial discretization of the blade (also called *panels*) and its immediate surroundings. Two authors stand out for the amount of publications they contributed to as well as for the general acceptance and applicability of their highly evolved models: F. Farassat and D.B. Hanson.

F. Farassat publishes his works since 1975 [93]. He uses a time-domain approach to solve Eqn. 6.1 with the use of a convolution of free-space Green's functions and a source distribution (see [255, 100] for the explanation of Green's functions applied to the wave equation) so that

$$\begin{aligned} 4\pi p'(\mathbf{x},t) =& \frac{\partial^2}{\partial x_i \partial x_j} \int_{\mathcal{V}} \left[\frac{T_{ij}}{r|1-M_r|} \right]_{\tau_e} d\mathbf{y} \\ & - \frac{\partial}{\partial x_i} \int_{f=0} \left[\frac{l_i}{r|1-M_r|} \right]_{\tau_e} dS \\ & + \frac{\partial}{\partial t} \int_{f=0} \left[\frac{\rho_\infty v_n}{r|1-M_r|} \right]_{\tau_e} dS \end{aligned} \tag{6.2}$$

where the quadrupole source term contribution is integrated over a finite volume $\mathcal{V}$ surrounding the blade whereas the monopole and dipole terms are integrated over the blade surface $f = 0$ as is illustrated on Fig. 6.2. Note that the free-space Green's function introduces in Eqn. 6.2 a Doppler factor depending on M_r the local Mach number of the blade surface, projected in the radiation direction $\mathbf{r} = \mathbf{x} - \mathbf{y}$ between the observer in $\mathbf{x}$ and the source in $\mathbf{y}$. This Mach number depends purely on the kinematics of the helical movement of the blade. Also note that the integrands are evaluated at the retarded time τ_e. It is the time when the sound received by an observer in position $\mathbf{x}$ at time t was actually emitted by the source in position $\mathbf{y}$ and it is computed from the knowledge of $\mathbf{x}$, thus also r the distance between source and observer[3], and t by solving

$$g(\mathbf{x},\mathbf{y},t) = \tau - t + r/c = 0 \tag{6.3}$$

for τ_e.

His work relies generally on generalized functions and their generalized derivatives [98,109]. The methodical derivation of all solutions is beyond the scope of this review; so the reader is referred to the individual papers or review papers such as [43, 100]. Farassat's work and the contributions of his collaborators, is so extensive that it is difficult to give a detailed account. It resulted in a series of formulations that are conveniently named:

- **Formulation 1** [93, 94, 100]: is a subsonic formulation from the point of view of a stationary observer though the sources are described in a reference frame that is attached to the blade. If the quadrupole term of Eqn. 6.1 is dropped[4], the formulation yields

[3] $r = |\mathbf{r}|$

[4] See section 6.2.1.1 for the implications of this drop.

$$4\pi p'(\mathbf{x},t) = \frac{1}{c}\frac{\partial}{\partial t}\int\limits_{f=0}\left[\frac{\rho_\infty c v_n + l_r}{r\,|1-M_r|}\right]_{\tau_e} dS + \int\limits_{f=0}\left[\frac{l_r}{r^2\,|1-M_r|}\right]_{\tau_e} dS \tag{6.4}$$

where the surface $f = 0$ is the actual blade surface and l_r are the components of the forces acting on the fluid, projected in the radiation direction.

This formulation holds for subsonic cases, in terms of the Mach number projected in the radiation direction M_r, so that the trouble arising with the singularity of the Doppler shift $|1 - M_r|$ is avoided. This formulation implies the numerical computation of the observer time derivative so it still is computationally quite demanding.

- **Formulation 1A** [111, 39]: is stated for a moving observer (i.e. the observer is assumed to translate forward at the same speed as the propeller). It is again a subsonic formulation though strictly speaking it is valid also for purely supersonic panels. Ignoring the volume integration of quadrupole sources, standard derivation then leads to

$$p'(\mathbf{x},t) = p'_T(\mathbf{x},t) + p'_L(\mathbf{x},t) \tag{6.5}$$

$$4\pi p'_T(\mathbf{x},t) = c_\infty \rho_\infty \int_{f=0}\left[\frac{M_n\left(r\dot{M}_i\hat{r}_i + c_\infty M_r - c_\infty M^2\right)}{r\,|1-M_r|^3} + \frac{\dot{M}_n}{r\,(1-M_r)^2}\right]_{\tau_e} dS \tag{6.6}$$

$$4\pi p'_L(\mathbf{x},t) = \frac{1}{c_\infty}\int_{f=0}\left[\frac{\dot{p}\cos\theta}{r\,(1-M_r)^2}\right]_{\tau_e} dS + \int_{f=0}\left[\frac{p\,(\cos\theta - M_n)}{r^2\,(1-M_r)^2}\right]_{\tau_e} dS + \frac{1}{c_\infty}\int_{f=0}\left[\frac{p\cos\theta\left(r\dot{M}_i\hat{r}_i + c_\infty M_r - c_\infty M^2\right)}{r^2\,|1-M_r|^3}\right]_{\tau_e} dS \tag{6.7}$$

which is formulation 1A expressed in a medium-fixed coordinate system [100, 117]. These equations involve θ, the angle between the radiation vector and the normal to the surface, projections of the kinematic Mach number of the blade surface in the normal and radiation directions, as well as time derivatives of it and of the local pressure. Equations 6.6 and 6.7 are for the thickness noise (subscript $_T$) and loading noise (subscript $_L$) respectively.

This formulation offers the advantage of being relatively easy to implement in computer codes because it does not require numerical differentiation of a time integral and is recommended by F. Farassat himself.

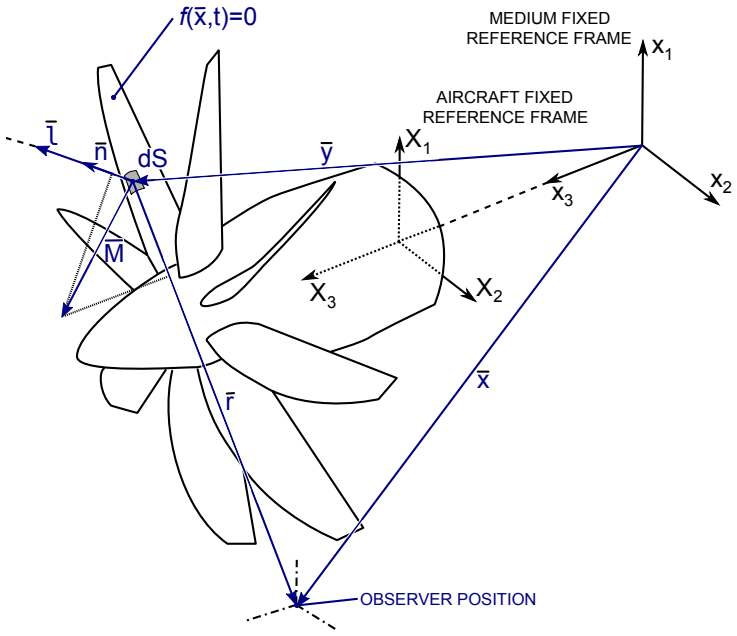

Figure 6.2: Reference frames and moving surface definition for formulation 1A.

- **Formulation 3** [95, 96]: is a formulation for a moving observer, valid for both supersonic and sonic panels but requires considerably more computational efforts than formulation 1A. This is why its use is often combined with formulation 1A by an adequate switching when M_r reaches unity [110, 84]. The equations are beyond the scope of this review but one possible implementation involves a collapsing sphere as illustrated in Fig. 6.3 and boils down to integrals over the open surface of the blade included in the sphere and the boundaries of that open surface [102, 96, 83, 84]. This sphere is the locus of all points satisfying $g = 0$ for a particular observer position $\overline{x}$ and a particular observer time t; thus it contains all the points that could potentially emit a signal at source time τ that could be received by the observer at time t. As τ approaches t, the radius of this sphere collapses. To compute the acoustic pressure p', the following steps should be followed [102, 43]:

  1. Determine the initial observer time t_i for which the sphere intersects the source surface.
  2. Choose the value of τ_j.
  3. Determine the intersection of the collapsing sphere $g = 0$ with the blade surface $f = 0$ (Γ-curve) and approximate the curve by straight segments.
  4. Compute the integrands at the ends of the segments and evaluate the line integral over Γ by the trapezoidal rule.
  5. Advance the source time τ_j and repeat steps 3 and 4 until no intersection is found between the sphere and the blade.
  6. Repeat these steps for each observer time required.

  But these steps, despite some helpful approximations, require typically two orders of magnitude more computer time than methods such as formulation 1A and are very challenging to code up because it involves the many determinations of the Γ-curve among other terms. Besides the collapsing sphere algorithms, alternative emission surface algorithms consider the integration over the locus of all points of the blade that do emit a sound that is received at time t by the observer (Σ-surface). The main difficulty with this approach is the construction of the Σ-surface which may be composed of several disjoint pieces in supersonic cases. The Σ-surface is constructed either from the location of source points at the retarded-time, or from the intersection of the collapsing sphere with the blade surface. Both the collapsing sphere and the emission surface algorithms are free of the Doppler singularity but mathematical singularities occur for some observer positions and under particular kinematic and geometric conditions. However, Farassat and Myers have shown in [108] that they vanish when specific contributions of the quadrupole source term are taken into account. This is an interesting point as the usual application of the FW-H analogy considers the monopole, dipole and quadrupole source terms as separate entities. But they are actually intricate, fully coupled parts of the same process. Discarding the quadrupoles is only justified when dimensional-analysis arguments state that dipoles are much more efficient; though the real-world case may be such that some physical phenomena decline themselves in both the dipole and quadrupole source terms.

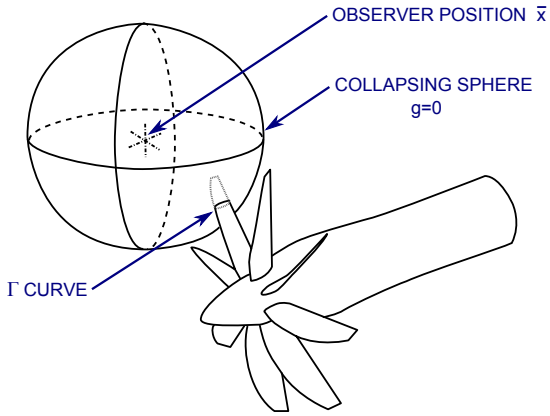

Figure 6.3: Collapsing sphere intersecting a blade.

D.B. Hanson developed theories in which the FW-H analogy is solved by integrals and summations in the frequency domain [138]. The rotating source distribution is replaced by a stationary set of radiation modes (i.e. components of the Fourier series). His methods are compiled in [139] but suffer from their limited validity either in the near- or in the far-field[5] and the difficulty to determine precise source location though they have the advantage that singularities associated with the sonic condition are not present [18]. This is a formal advantage of the frequency domain even though compactness[5] issues are still unresolved. Moreover, the peaks and abrupt slopes that are associated with singular behaviour require a huge set of frequency terms if comparable resolution with a time-domain approach is to be maintained [18].

Many other methods were proposed over the years. Among these, the author wishes to mention a few worth citing. First, the integration surface needs not necessarily be the blade surface. Indeed, the FW-H analogy may be written for the particular case of what is called a permeable data surface [74, 42, 104]. This surface encloses the sources and must be within the high-resolution CFD region. The problem with this formulation is the determination of the best location for the data surface; nevertheless, it is the preferred formulation nowadays if high-resolution CFD is available and it delivers interesting results [313]. Another theory using a permeable data surface is based on Kirchhoff's technique extended for moving surfaces [105, 99]. The common point between these approaches is that they require no volume integration provided the sources are enclosed within the surface and are accurately caught by the CFD solution, hence an additional computing cost. For Kirchhoff's approach, sensitivity to the location of the permeable surface is also reported [42]. It requires accurate knowledge of spatial gradients of pressure and does not have the convenient decomposition of noise based on physical grounds (thickness and loading). Finally, it should be noted that the use of Kirchhoff's formulation is strongly discouraged in [43] were it is shown that the input data obtained on the surface from the CFD is not suitable; it is not a solution to the wave equation so that non-wave fluctuations result

[5]See section 6.2.1.3.

in spurious and inaccurate sound predictions.

For supersonic problems, there exist asymptotic theories based either on asymptotic number of blades or harmonics [142, 284, 223]. These theories have limited industrial applicability though they bring insight into the supersonic source problem. Specific integration schemes, applied to FW-H or Kirchhoff formulations and which do not require the evaluation of the emission time, are also proposed by J. Prieur [237].

Finally, let us mention the advanced-time approach recently used by D. Casalino [55, 54] which is very close to the binning technique implemented in other codes [312, 174]. This approach does not require to solve the retarded time equation (Eqn. 6.3) since noise is computed in the source time-domain along with the time required to reach the observer (referred to as advanced-time). This travel-time is used to compute the observer's relative position; finally the signal is built up in the observer time-domain. Although such a formulation looks promising, the singularity problem is not yet assessed and the gain of not having to solve the retarded-time equation is limited by the necessity to store additional data for each cell on the blade surface and to order them properly when computing the signal at a given observer's time.

6.1.3 Broadband noise predictions

Broadband noise prediction methods are more scarce than tonal noise prediction methods. References [41] and [202] put these methods into historical perspective. Generally, one distinguishes four kinds of methods: empirical methods, analytical and semi-analytical methods, Computational AeroAcoustics (CAA) and those based on one or another analogy. Analytical and semi-analytical methods such as [258], are usually based on assumptions such as few lightly loaded blades composed of airfoils with small camber, thickness and angle of attack and subject to small fluctuations of the pressure field. For those reasons, they cannot be applied to highly loaded propellers modeled with a steady-state hypothesis. They usually come at hand in late design stages when more effort can be dedicated to specific geometries as in [315, 218]. CAA aims at the direct numerical simulation of the acoustic phenomena on the body of interest and would require prohibitive computational times. So the methods based on analogies such as the FW-H one are particularly popular for those situations where detailed surface pressure fluctuations are available. Farassat and Casper developed a time-domain approach based on the FW-H analogy and applied it on a permeable data surface for the computation of broadband noise with good accuracy [103].

6.2 CHA solver

Because the tonal noise of propellers usually falls within the range where the human ear is most sensitive, most metrics used for certification purposes include some form of penalty for tonal noise [314]. For this reason but also from computational cost considerations, tonal noise sources are assessed in this optimization whereas broadband noise sources are discarded.

This section will describe the time-domain formulation that is used in this work together with all the necessary assumptions. A time-domain approach has been chosen because it gives more insight into the physico-temporal relation between the physical noise sources (kinematics of a solid body, distribution of forces, shocks and other

non-linear phenomena) and the propagation to a receiver at some distance. This decomposition is less easily found with frequency-domain methods. Furthermore, it is easier to think about physical processes happening over time rather than in the somewhat more abstract frequency-domain. On top of this, time-based methods may be handily extended to account for non-moving surfaces or turbulence.

Because of its robustness and accuracy, as well as because of the availability of a large amount of publications about it, the foundations of the present CHA solver rely on formulation 1A of Farassat (Eqs. 6.6-6.7). The assumptions behind the chosen formulation will be discussed in the next section, with special attention to the issue of quadrupole sources, to the singularity appearing when M_r reaches unity and to compactness issues.

6.2.1 Assumptions

When dealing with the solution of the FW-H analogy by use of free-space Green's functions, fundamental assumptions are needed. These assumptions are commonly accepted in the community of propeller acoustics. First, the Reynolds number should be high and fluctuations small relative to the mean flow features. Second, the acoustic field is decoupled from the aerodynamic one and is not supposed to have back-coupling with it. So pressure fluctuations associated with sound should not influence the aerodynamic pressure distribution. Hence the acoustic contribution is removed from the l_i terms of Eqn. 6.2. This also implies that diffraction effects from one blade to the others are taken into account only if these are captured by the compressible CFD solution. Because the blade spacing to chord length ratio is large, capturing diffraction effects would imply a prohibitive computational cost. Moreover, no vibrations of the blades are taken into account and they behave as perfectly rigid bodies. Finally, no account is given for the reflection of sound by the spinner. The blades are considered as pure sound sources in a free space.

6.2.1.1 Quadrupole noise

Quadrupole sources account for non-linearities due to local variations of the speed of sound and the finite fluid velocity in the near vicinity of the blade. They essentially produce distortion of the acoustic waveform produced by the other sources [107, 44]. This term is usually decomposed in a pure quadrupole term requiring volume integration, blade and shock surface terms requiring surface integration and a trailing edge term requiring line integration [97, 106]. Except for the boundary layer and the wake, the pure quadrupole term is an inefficient noise generator because velocity gradients are small. The blade surface sources are in direct competition to loading noise but radiate in the disk plane. The shock surface term is believed to be the main contributor to the total quadrupole noise with a directivity which is equivalent to that of thickness noise. The line term contribution could be substantial and of monopole type. Farassat and Myers suggest that the contributions of the volume, blade surface and line terms are likely to be strongly reduced by destructive mutual interference [106, 107]. They also established that these contributions are well below the thickness and loading noise levels. So the wake term and the shock surface terms are proposed as the most potent noise generators.

As stated by Brentner and Holland [44], Taghaddosi and Argawal [283], and Peake and Crighton [223], the quadrupole term becomes significant only at blade tip Mach numbers well into the transonic regime. Choosing the design objective with a helical tip Mach number below 0.97, ensures that no portion of the blade reaches the sonic condition so that the major contribution to quadrupole sound, coming from the region of the blade close to the Mach radius [223], can be neglected at first order. Furthermore, Hanson [140] suggested and Brooks [45] showed that, provided the blades are thin and swept, the overall quadrupole noise is well below the thickness and loading terms taken together. Thus, the wake and shock terms are essential when dealing with thick airfoils at transonic speeds but may be neglected, at first, in the computation of noise for advanced propellers. Should the quadrupole term be accounted for in the present computations, it would come with an increased burden in numerical and computational treatment, involving complex and time consuming procedures, for only a marginal gain in accuracy for the estimation of the difference between two distinct blade designs. Furthermore, it may be reasonably assumed that the strength of the quadrupole sources will be similar for two distinct designs featuring resembling transonic flows, so that other terms indirectly accounted for in the objective function can effectively promote individuals which are potentially low producers of quadrupole noise. Hence reduction of the impact of quadrupole sources could be somehow achieved by emphasizing blade sweep to limit the transonic effects at the tip, by penalizing individuals with strong shocks along the blade, by favouring thin blades [202] and by keeping the helical tip Mach number of the optimized blade below 0.97.

Additionally, neglecting the quadrupole term, hence the volume integration around the blade surface, implies that if the blade surface is chosen as integration surface no account is given for refraction effects.

6.2.1.2 Sonic panels

Equation (6.2) is also revealing the main issue in the computation of propeller noise: the mathematical singularity for Mach numbers in the radiation direction close to unity ($M_r \approx 1$). It is essentially the occurrence of a Doppler singularity in the application of free-space Green's functions. This condition is discussed by C. Tam [284] or Myers and Farassat [210] who observed that the sum of the singular terms is less singular than the actual terms themselves. So they are either integrable or the finite part of the divergent integrals must be taken [101]. The consequent breakdown of the linear theory is discussed by H. Ardavan [20] who identifies it as a result of the mixed nature of the governing equations. Physically, this condition consists in the emission of a focused wave occurring at two coalescent emission times so it becomes a caustic in the solution. The main feature of this wave is a cylindrical decay like $1/\sqrt{r}$ instead of the $1/r$ decay of spherical waves [210, 21]. A common way around it, is to use Farassat's formulation 3. But even if for those parts of the blade which approach the sonic regime, the choice of the formulation is switched from 1A to 3; the increased computational cost might reveal himself to be prohibitory in the present optimization set-up. Fortunately, as only small parts of the blade are possibly affected by singular conditions, the present optimization method accommodates with approximations made only for those conditions close to singularity. These approximations must deliver acceptable values for the sound emitted around the singularity without resorting

to a time-consuming, yet more accurate, mathematical statement for the change of radiation properties. This approach is justified because the optimum is sought for propellers operating at subsonic tip speed.

Finally, it must be born in mind that individuals for which significant parts of the blade operate in the high transonic and/or low supersonic regimes, are created only as members of 'diversion' domains that must be left available for the EA to search in so that it has the potential to deliver better designs in the objective domain. The occurrence of supersonic tip speeds for some blade designs is thus accidental but the knowledge collected by assessing individuals in those unfavourable domains, is supposed to drive the search back into more favourable directions, essentially in the subsonic range, thanks to the prediction of poor performance.

6.2.1.3 Compactness criterion

The compactness criterion has briefly been introduced in section 4.3.1 for its implication on the size of mesh elements (sources) around the blade (source region). In the aeroacoustic theory, a source is said to be acoustically compact when a characteristic period of the source in the moving frame of reference is large with respect to retarded time variations over the source region. This translates in Eqn. 4.7:

$$L << \lambda_m(1 - M_r) \tag{4.7}$$

which states that the typical length scale of the source (here, its elongation L) should remain small with respect to the minimum acoustic wave-length to be resolved λ_m, modulated by the Doppler factor $(1 - M_r)$. These terms are illustrated in Fig. 6.4. Given the influence of the Doppler factor $(1 - M_r)$, a source is more compact when leaving the observer than when approaching. The largest dimension of mesh-elements on the blade surface is chosen such that the compactness criterion is verified typically up to the 7^{th} or 8^{th} harmonic of the BPF for nearly sonic Mach numbers in the radiation direction, yet with exclusion of the occurrence of the Doppler singularity.

Figure 6.4 is also useful to understand the concepts of near- and far-field. Indeed, the observer is in the acoustic far-field if $r >> \lambda_m$ so that wave-fronts are nearly planar at the observer's position.

6.2.2 Formulation

Recall Eqs. 6.5-6.7:

$$4\pi p'(\overline{x}, t) = 4\pi p'_T(\overline{x}, t) + 4\pi p'_L(\overline{x}, t) \tag{6.5}$$

$$4\pi p'_T(\overline{x}, t) = \\ c_\infty \rho_\infty \int_{f=0} \left[\frac{M_n \left(r\dot{M}_i \hat{r}_i + c_\infty M_r - c_\infty M^2 \right)}{r \left| 1 - M_r \right|^3} + \frac{\dot{M}_n}{r \left(1 - M_r \right)^2} \right]_{\tau_e} dS \tag{6.6}$$

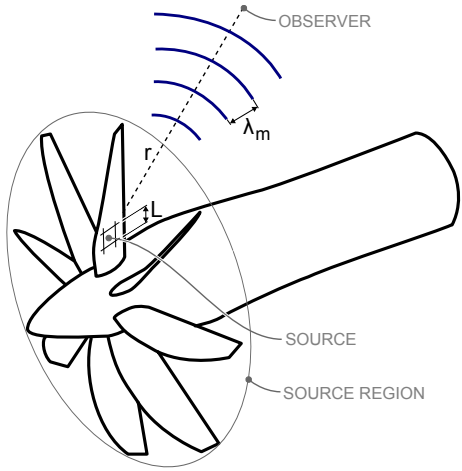

Figure 6.4: Characteristic dimensions and compactness.

$$
\begin{aligned}
4\pi p'_L(\overline{x},t) =& \frac{1}{c_\infty}\int_{f=0}\left[\frac{\dot{p}\cos\theta}{r\left(1-M_r\right)^2}\right]_{\tau_e} dS + \int_{f=0}\left[\frac{p\left(\cos\theta - M_n\right)}{r^2\left(1-M_r\right)^2}\right]_{\tau_e} dS \\
&+ \frac{1}{c_\infty}\int_{f=0}\left[\frac{p\cos\theta\left(r\dot{M}_i\hat{r}_i + c_\infty M_r - c_\infty M^2\right)}{r^2\left|1-M_r\right|^3}\right]_{\tau_e} dS
\end{aligned}
\tag{6.7}
$$

where the first term of the right-hand side of Eqn. 6.7 vanishes when working with steady computations of the pressure field around the blades, as is the case in the present study. This set of equations is particularly suited because the aerodynamic mesh can be used directly for the aeroacoustic calculations provided the compactness criterion is satisfied (Eqn. 4.7). A straightforward mid-panel quadrature is used to express the integrals of Eqs. 6.6 and 6.7 as

$$
4\pi\phi'(\overline{x},t) \approx \sum_{j=1}^{N}\sum_{m,k}\left[\frac{\mathcal{Q}_m(\overline{y_j}, t - r_j/c_\infty)}{r_j^k\left|1-M_r\right|_j^{(m+1)}}\right]_{\tau_e}\Delta S_j \tag{6.8}
$$

where ϕ' stands either for p'_T or p'_L and $\mathcal{Q}$ stands for the numerator representative of the far- ($k=1$) or near-field ($k=2$) terms of Eqs. 6.6 and 6.7[6]. Summation is done over the N cells forming the blade surface. As recently proposed by Farassat [100], the shorthand notation $\mathcal{Q}_m(\overline{y_j}, t - r_j/c)$ has been introduced for:

$$
\left[\frac{\mathcal{Q}_m(\overline{y_j}, t - r_j/c_\infty)}{r_j^k\left|1-M_r\right|_j^{(m+1)}}\right]_{\tau_e} \equiv \frac{\tilde{\mathcal{Q}}_m(\boldsymbol{\eta},\tau_e)}{r_j^k|_{\tau_e}.\left|1-M_r|_{\tau_e}\right|_j^{(m+1)}} \tag{6.9}
$$

[6]In this shorthand notation, k is appropriately chosen together with m to match the respective terms of Eqs. 6.6 and 6.7.

in which $\tilde{\mathcal{Q}}_m(\boldsymbol{\eta}, \tau_e)$ stands for $\tilde{\mathcal{Q}}_m(\overline{y}(\boldsymbol{\eta}, \tau_e), \tau_e)$ expressed in local blade coordinates.

To effectively compute Eqn. 6.8 for all cells, the retarded-time equation

$$|\overline{r}| \equiv |\overline{x}(t) - \overline{y}(\tau_e)| = c_\infty (t - \tau_e) \tag{6.10}$$

is solved for τ_e at each observer time t in the history of $p'(\overline{x}, t)$. It can be shown that this equation admits exactly one solution for subsonic motion between the source and the observer and up to three solutions in the case of supersonic motion. The retarded-time equation boils down to a transcendental implicit equation in $\psi = \omega(\tau - t)$ [84] of the type:

$$A\psi^2 + B\psi + C - \cos(\psi + D) + E\psi \sin(\psi + F) = 0 \tag{6.11}$$

where the constants A-F depend on known parameters such as the coordinates in the medium fixed and aircraft fixed reference frames, the speed of sound c_∞, the flight velocity u_∞ and the rotational velocity ω. Eqn. 6.11, given its type, cannot be solved analytically and classical root finding algorithms risk to fail in the presence of multiple roots. Fortunately, two additional conditions can be developed [84]:

1. A signal must be emitted before it can be observed. This causality condition applied on a solution ψ^* of Eqn. 6.11 translates into:

$$\text{sign}(\omega)\psi^* \leq 0 \tag{6.12}$$

   so that τ must be less or equal to t. This allows to reject spurious roots that would be found by solving Eqn. 6.11.

2. It can be shown that the roots of Eqn. 6.11, are bounded by the roots of

$$(A\psi^2 + B\psi + C)^2 = E_1^2\psi^2 + (1 + E_2\psi)^2 \tag{6.13}$$

   So if ψ^*_{max} and ψ^*_{min} are respectively the maximum and minimum roots of Eqn. 6.13 that satisfy Eqn. 6.12, then the roots ψ^* of Eqn. 6.11 should be searched in $[\psi^*_{min}, \psi^*_{max}]$.

So the Van Wijngaarden-Dekker-Brent method [235] is applied on the interval $[\psi^*_{min}, \psi^*_{max}]$. For a cell moving at subsonic speeds in the radiation direction, the search is stopped after one single root is found. In the case of cells moving at sonic or supersonic speeds, Eqn. 6.11 admits up to three roots. These are found by the recursive use of Van Wijngaarden-Dekker-Brent method triggered by a conditional logic switch based on the magnitude of the absolute helical Mach number of the considered cell.

As already discussed in the previous section, when the source Mach number projected in the radiation direction M_r approaches unity, the integrands of Eqs. 6.6 and 6.7 become singular. The truncation operator is then switched on over an interval 2κ centered around unity and it constrains the singularity through a truncated first order Taylor expansion of all terms of Eqs. 6.6 and 6.7 considered as functions of M_r solely. The lower and upper thresholds for the development are chosen as a high transonic value ($M_{r,0L} = 1 - \kappa = 0.96$) and a low supersonic value ($M_{r,0U} = 1 + \kappa = 1.04$) respectively. Then the integrands of Eqs. 6.6 and 6.7 are developed:

- For those cells with a Mach number in the radiation direction greater than that threshold ($M_{r,0L} < M_r \leq 1$), the corresponding terms of Eqn. 6.8 are

arbitrarily replaced by:

$$\frac{\check{\mathcal{Q}}_m(M_r)}{r_j^k\,(1-M_r)_j^{(m+1)}} \approx \frac{\check{\mathcal{Q}}_m(M_{r,0L})}{r_j^k\,(1-M_{r,0L})_j^{(m+1)}} + \varepsilon\left[\frac{\frac{\partial\check{\mathcal{Q}}_m(M_r)}{\partial M_r}\Big|_{M_{r,0L}}}{r_j^k\,(1-M_{r,0L})_j^{(m+1)}} + \frac{\check{\mathcal{Q}}_m(M_{r,0L})(m+1)}{r_j^k(1-M_{r,0L})^{m+2}}\right](M_r - M_{r,0L}) + \mathcal{O}^2(M_r - M_{r,0L}) \tag{6.14}$$

where the generic notation introduced for Eqn. 6.8 is used.

- Similarly, for cells having a Mach number in the radiation direction lower than the threshold ($1 < M_r < M_{r,0U}$), the corresponding terms of Eqn. 6.8 are replaced by:

$$\frac{\check{\mathcal{Q}}_m(M_r)}{r_j^k\,(M_r-1)_j^{(m+1)}} \approx \frac{\check{\mathcal{Q}}_m(M_{r,0U})}{r_j^k\,(M_{r,0U}-1)_j^{(m+1)}} + \varepsilon\left[\frac{\frac{\partial\check{\mathcal{Q}}_m(M_r)}{\partial M_r}\Big|_{M_{r,0U}}}{r_j^k\,(M_{r,0U}-1)_j^{(m+1)}} - \frac{\check{\mathcal{Q}}_m(M_{r,0U})(m+1)}{r_j^k(M_{r,0U}-1)^{m+2}}\right](M_r - M_{r,0U}) + \mathcal{O}^2(M_r - M_{r,0U}) \tag{6.15}$$

In Eqs. 6.14 and 6.15, $\check{\mathcal{Q}}_m(M_r)$ again refers to $\mathcal{Q}_m(\overline{y_j}, t - r_j/c)$ considered solely as a function of M_r (see Eqs. 6.6 and 6.7) whereas ε is a positive number between 0 and 1, chosen such that the left-hand side of Eqs. 6.14 and 6.15 remains bounded. Note that all terms of these equations are now regular in M_r and the second order terms in $(M_r - M_{r,0.})$ are dropped. In these equations, ε is a relaxation coefficient that controls how much of the first derivative is taken into account in the evaluation of the left-hand side. Interestingly, good results are obtained at an even lower cost by using the zero-th order development of $\check{\mathcal{Q}}_m(M_r)$ (with $\varepsilon = 0$). The computational time is then reduced by dropping terms in the summations for Eqs. 6.14 and 6.15. All results in the present implementation are obtained with this particular value ($\varepsilon = 0$) because the gain in accuracy is only marginal when ε differs from zero. But before generalizing this result, it should be assessed in the light of other experimental data sets. The process of truncation is schematically shown in Fig. 6.5 for $\varepsilon = 0$ together with the generic behaviour of the non-truncated terms.

As discussed in section 6.3, the choice of the truncation interval 2κ in Eqs. 6.14 and 6.15 has a significant influence on the results, but does not depend strongly on propeller shape nor operating conditions. A too narrow truncation interval ($\kappa \leq 0.35$) yields overpredictions or even failure of the computation. On the other hand, an abusively wide truncation interval ($\kappa \geq 0.45$) yields results that are systematically underpredicted.

A typical example of the spatial extent on the blade surface of the truncation operator is shown in Fig. 6.6. The pressure contribution from cells marked in blue, at an arbitrary observer time t, is computed through Eqs. 6.14 and 6.15, whereas all other

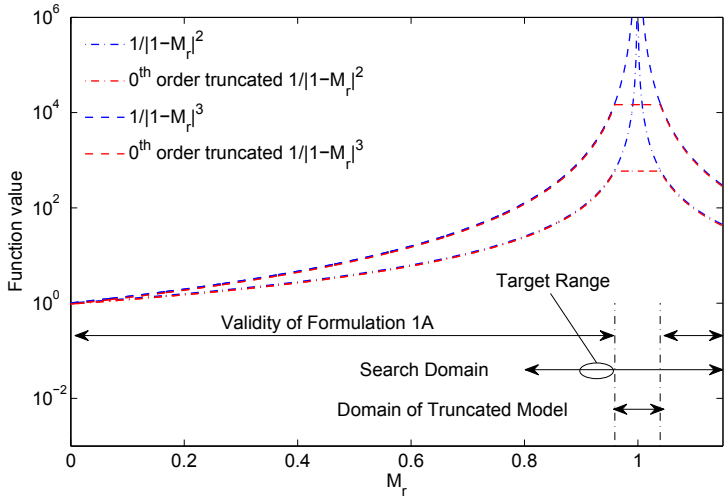

Figure 6.5: Singular behaviour and 0^{th}-order truncation ($\varepsilon = 0$) for the denominators of the terms of Eqn. 6.9. The validity domain of formulation 1A is represented and compared to the optimizer search domain. The oval highlights the target range within the search domain.

cells are computed through the accurate formulation 1A. This figure clearly shows the limited extent of cells that have a Mach number in the radiation direction that falls within the nearly singular domain. This region is known to be dominant for supersonic rotors both in the near and far fields [66, 222, 53] so the validity of the present method lies in its ability to deliver safe estimates at a low computational cost. For subsonic rotors, the near and far field noise is dominated by the tip region [221, 222, 53] and the truncation operator is active on a very restricted set of blade elements (i.e. those that have $M_r > 0.96$). In this case it affects a locally high, but globally not too substantial contribution to the total noise.

The method described above is implemented as a post-processing tool (User Defined Function) within Fluent v12.0.16. The thickness noise (Eqn. 6.6) and loading noise (Eqn. 6.7) are computed separately. As already explained, a single blade is processed through the CFD and the signal of the complete propeller is computed by a proper shifting in the observer-time domain of the signals emitted by different blades before summing them up. The tool then generates the time history of $p'(\overline{x}, t)$ for a sampling rate chosen high enough to satisfy the Nyquist criterion. This time history is further processed through a Fourier spectral analysis to retrieve the SPL associated with the BPF and its lower harmonics.

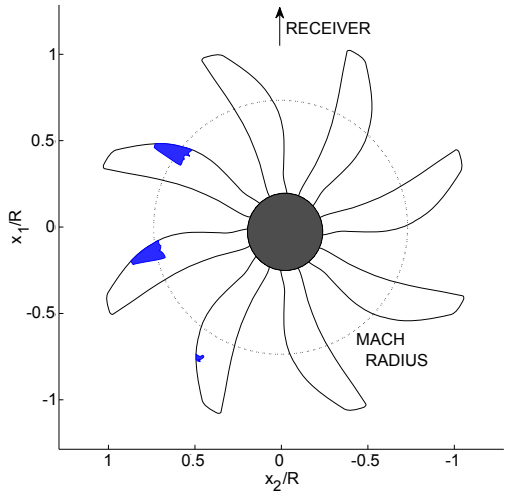

Figure 6.6: Spatial extent of the truncation operator ($\kappa = 0.04$). For a receiver located in the propeller plane at $2.64R_{tip}$ from the axis, the pressure contribution from cells marked in blue has been truncated. - NASA SR-3 at $M_\infty = 0.8$ and $J = 3.06$ ($M_{tip} = 1.14$). -

6.3 Validation

The validity of the high-fidelity CHA analysis, and in particular that of the truncated approximates, is rated by comparisons with experimental results and numerical results available in the literature. Diverse propeller geometries operating under various conditions, including the transonic and supersonic regimes where truncation becomes effective, are considered. More details about the reference propellers can be found in appendix A.

6.3.1 Take-off/Landing conditions

$\mathbf{M_\infty = 0.2}$

Figure 6.7 compares the measured and predicted SPL for a NASA SR-7 propfan operating at $M_\infty = 0.2$ and $J = 0.89$ with $\beta_{ref} = 37.8°$ [310]. This corresponds to a loading typical of the take-off/landing condition ($C_P = 0.85$). Good agreement is obtained at most receiver positions which are located according to [310]. The slight tilting of the main lobe in the downstream direction is nicely predicted.

Unfortunately, exploitable data under these conditions are scarce.

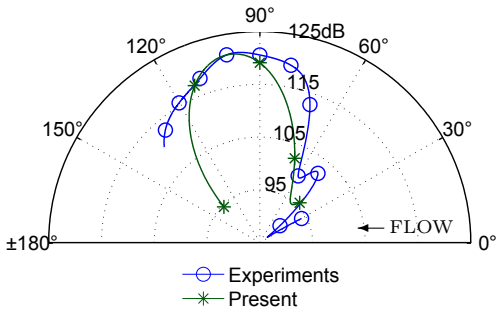

Figure 6.7: Comparison of measured and computed SPL at BPF for various receiver positions. NASA SR-7 propfan operating at $M_\infty = 0.2$ and $J = 0.89$ with $\beta_{ref} = 37.8°$ ($C_P = 0.85$) [310]. Experimental tones corrected to $1.68m$ sideline distance.

Very low speed comparison

An interesting comparison has been made with the work of S. Remmler [244] who used both a self-implemented Gutin-type single force model and the FW-H module of Fluent v6.3.26. The model is that of a car fan developed by Valeo. His computations account only for loading noise which is more important than the thickness one for this type of flow. The FW-H module of Fluent v6.3.26 accounts for the steady part of the pressure distribution as is the case of the present code. The unsteady part, which is a major contributor for these low speed applications is discarded in both approaches. So the purpose of Fig. 6.8, is not the accurate prediction of the SPL but the comparison between similar implementations of the same analogy and their assessment in the light of a less refined model. The agreement between both implementations is excellent for all observer's locations.

6.3.2 Cruise conditions

Although designing a propfan is not the purpose of this effort, the NASA SR-X series offers the advantage of being extensively documented. This is why the results obtained with the method described in section 6.2.2 are compared to experimental results collected by J. Dittmar and R. Joracki [78, 76, 77] on the SR-1 and SR-3 propfan blades. The present predictions are corrected to account for identified effects occurring during the experiments but not taken into account in the CHA-prediction. These corrections include:

- a correction for pressure losses in the wind tunnel according to [306] so that experiments and predictions are compared at the same free-stream static pressure,
- and a correction for the effect of pseudo-noise on the receivers during the experiments [281, 306].

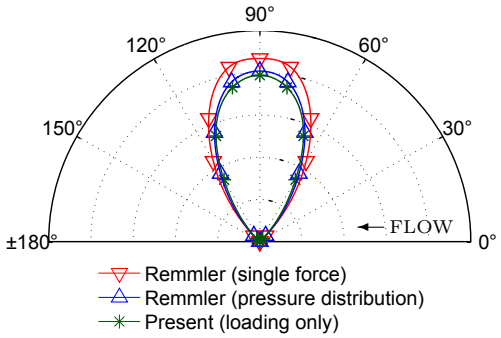

Figure 6.8: Comparison of directivity at BPF to S. Remmler's results for a Valeo car fan operating at $M_\infty = 0.12$ and $J = 1.63$. Solely the loading noise is considered.

As was shown by J. Dittmar and P. Lasagna [79], the wind tunnel data correlate well to in-flight measurements. Comparisons are made for each blade at three tip Mach numbers: one where the tip operates in purely transonic conditions, one where the tip reaches sonic conditions and one where the tip is in early supersonic conditions.

Figures 6.9(a) and 6.10(a) show a comparison of the computed and measured SPL for both propfans running at subsonic tip Mach numbers and under different loadings. The experimental data are collected by transducers that are flush mounted on the tunnel wall. They suffer from both refraction in the thick boundary layer along the wall and multiple reflections on the walls and the propeller rig, particularly aft of the propeller plane [131]. Additionally, this set-up is known to yield measurements lower than the free-field values for transducers placed upstream of the propeller plane and eventually higher for transducers downstream [91]. Transducers are located on a sideline at $3.92R$ distance to the propeller axis and the axial distance x is normalized by the tip radius and pointing downstream. For each transducer, the SPL for the Blade Passing Frequency (BPF) and, when available, the first harmonic (1^{st} Blade Passing Harmonic - 1^{st} BPH) are shown. The experimental data have also been corrected for the difference in operating conditions according to Dittmar and Lasagna [79].

A good agreement is found in the propeller plane where discrepancies are below $1dB$. In the case of the SR-3 computations, the accuracy of the computed SPL is more similar to the one obtained by Brooks and Mackall [46] with a non-singular formulation in the frequency domain accounting for quadrupole noise. The overall agreement up- and downstream of the propeller plane is within $3dB$ for x/R in the range $[-1, 1]$ and at least a part of it is related to the quadrupole noise that is neglected. This agreement is well within the discrepancy level of 3 to $15dB$ obtained in the same x/R range for similar conditions and blades by Dunn and Farassat [82], Carley [52], Frota et al. [117] and more recently by Polacsek et al. [231] or Gur and Rosen [133]. The same remark is true for higher harmonics.

If the tip Mach number is increased to reach sonic conditions close to the tip, the correctness of formulation 1A is relaxed and the truncation operator becomes effective. Results for different observers are shown on Figs. 6.9(b) and 6.10(b) where the agreement in the propeller plane is within $3dB$ both for the fundamental and the first harmonic. Upstream of the propeller plane at a distance x/R close to 1.0, the SPL is overpredicted by up to $6.5dB$ for highly loaded conditions ($C_P > 2$) whereas the agreement is good in the other cases. Downstream of the plane, the overprediction amounts up to $9dB$ at a similar distance and under very high loading ($C_P \approx 2,35$) but the agreement is good when moderate loadings, representative of modern propellers, are considered. Again, the results of the present code have an acceptable accuracy if compared to other works.

At supersonic tip speeds, the truncation operator becomes fully effective on more significant parts of the blades, located around the Mach radius, but this does not affect significantly the predictions, as shown in Figs. 6.9(c) and 6.10(c), despite the fact that the truncation affects the region believed to be dominant for this regime [53]. The agreement in and aft of the propeller plane is well within $4dB$ under realistic loading conditions with a clear trend to overprediction. This result compares well to the $2dB$ to $6dB$ accuracy obtained by Brooks and Mackall [46] or Farassat et al. [110], at this condition with non-singular formulations. The present result is also satisfactory when compared to [70] where a $1dB$ accuracy is obtained in similar conditions but with the use of a fixed $3dB$ correction, according to [186], to account for the quadrupoles that were neglected. Upstream of the propeller, the SPL is overpredicted to an even larger extent than in the rotational plane. But this discrepancy should be mitigated as the measurements in this part of the domain are known to significantly underestimate the real value.

Predicted tone spectra are shown on Figs. 6.11(a) and 6.12(a) for identical conditions to Fig. 6.9(a) and 6.10(a) respectively. Note that the harmonic content could not be measured at the first set of operating conditions as it fell below the tunnel background noise [78]. A good agreement is found up to the 4^{th} harmonic for both blades. From the 5^{th} harmonic, the agreement is excellent for the SR-1 whereas some discrepancies appear for the SR-3. But these are kept within $6.5dB$ and are probably related to the greater extent of local supersonic flow at this somewhat higher loading (the associated non-linear effects are not accounted for in the present method due to the neglect of quadrupole contribution). The spectral envelopes at the sonic condition exhibit similar features (Figs. 6.11(b) and 6.12(b)), except for the very high loading case on the SR-3 where the SPL is overpredicted for higher harmonics. Considering that this does not occur for lower loads, it can be concluded that extreme blade loading is mainly responsible for the discrepancies. The spectral content shown on Figs. 6.11(c) and 6.12(c), indicates the onset of the breakdown of the truncation method.

In principle, the loading-noise term includes the acoustic pressure associated with all sound scattering processes, typically the reflection or diffraction of the sound from one blade by adjacent blades. This effect is ignored in the present analysis and in similar previously published works found in the literature. It could partly explain some of the discrepancies found between predictions and measurements, at least at some radiation angles and for the higher frequencies. Additionally, Dunn and Farassat [82] showed that discrepancies of up to $5dB$ occur due to the neglect of blade deformation under centrifugal and aerodynamic loads as is the case in the

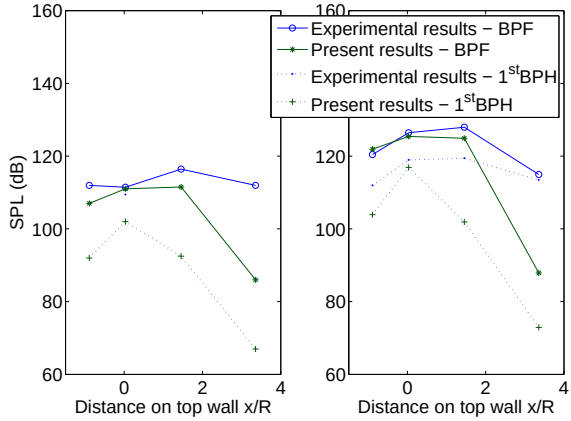

(a) SR-1 at subsonic tip speed.
left - $M_\infty = 0.6$, $\beta_{ref} = 60.0°$, $J = 3.08$, $C_P = 1.73$, $M_{tip} = 0.86$
right - $M_\infty = 0.7$, $\beta_{ref} = 58.5°$, $J = 3.26$, $C_P = 1.46$, $M_{tip} = 0.97$

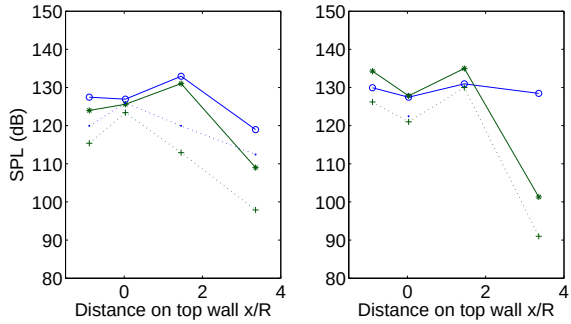

(b) SR-1 at sonic tip speed.
left - $M_\infty = 0.7$, $\beta_{ref} = 58.5°$, $J = 3.04$, $C_P = 1.77$, $M_{tip} = 1.01$
right - $M_\infty = 0.7$, $\beta_{ref} = 59.5°$, $J = 2.86$, $C_P = 2.12$, $M_{tip} = 1.04$

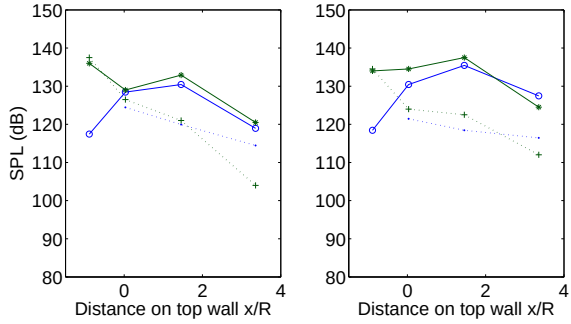

(c) SR-1 at supersonic tip speed.
left - $M_\infty = 0.8$, $\beta_{ref} = 58.5°$, $J = 3.25$, $C_P = 1.29$, $M_{tip} = 1.11$
right - $M_\infty = 0.8$, $\beta_{ref} = 58.5°$, $J = 3.06$, $C_P = 1.58$, $M_{tip} = 1.14$

Figure 6.9: Comparison of measured and computed SPL of the NASA SR-1 at various tip speeds for receivers on a sideline at $3.92R$.

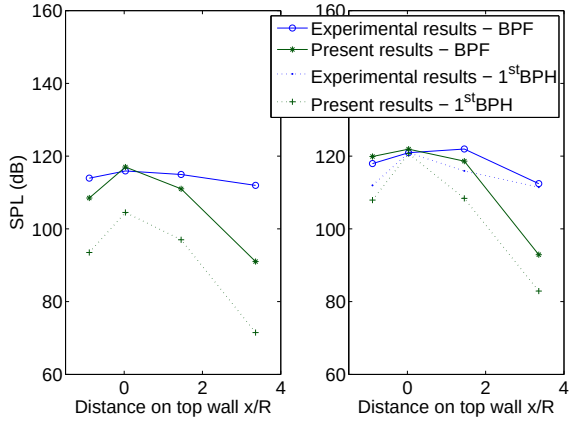

(a) SR-3 at subsonic tip speed.
left - $M_\infty = 0.6$, $\beta_{ref} = 60.0°$, $J = 3.00$, $C_P = 1.92$, $M_{tip} = 0.87$
right - $M_\infty = 0.7$, $\beta_{ref} = 59.5°$, $J = 3.26$, $C_P = 1.77$, $M_{tip} = 0.97$

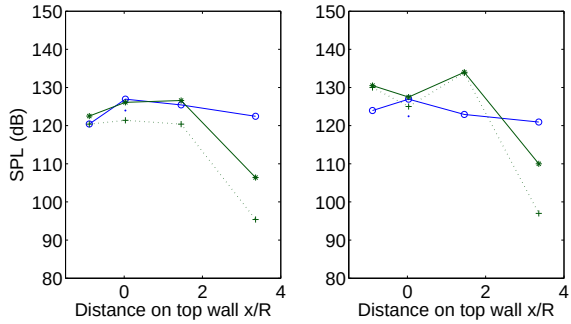

(b) SR-3 at sonic tip speed.
left - $M_\infty = 0.7$, $\beta_{ref} = 59.5°$, $J = 3.06$, $C_P = 2.02$, $M_{tip} = 1.00$
right - $M_\infty = 0.7$, $\beta_{ref} = 59.5°$, $J = 2.85$, $C_P = 2.35$, $M_{tip} = 1.04$

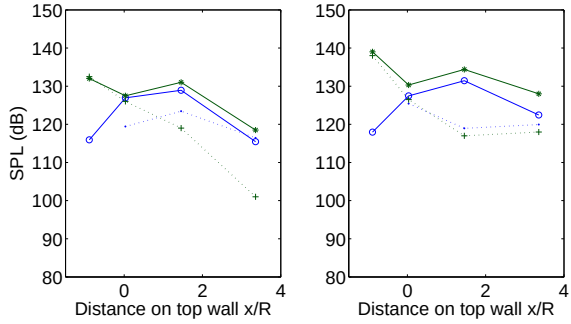

(c) SR-3 at supersonic tip speed.
left - $M_\infty = 0.8$, $\beta_{ref} = 58.5°$, $J = 3.26$, $C_P = 1.57$, $M_{tip} = 1.11$
right - $M_\infty = 0.8$, $\beta_{ref} = 58.5°$, $J = 3.08$, $C_P = 1.84$, $M_{tip} = 1.14$

Figure 6.10: Comparison of measured and computed SPL of the NASA SR-3 at various tip speeds for receivers on a sideline at $3.92R$.

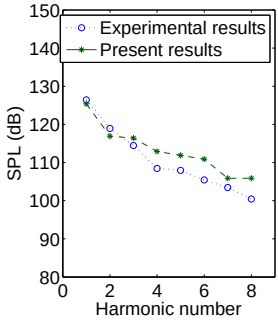

(a) SR-1 at subsonic tip speed.
$M_\infty = 0.7$, $\beta_{ref} = 58.5°$, $J = 3.26$, $C_P = 1.46$, $M_{tip} = 0.97$

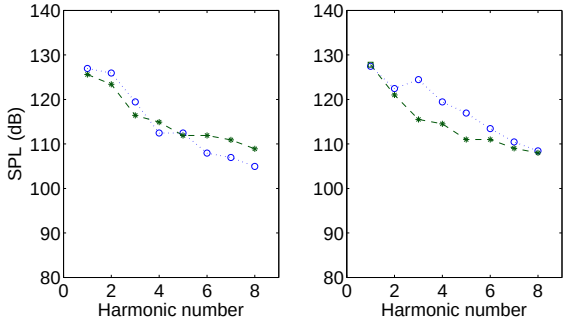

(b) SR-1 at sonic tip speed.
left - $M_\infty = 0.7$, $\beta_{ref} = 58.5°$, $J = 3.04$, $C_P = 1.77$, $M_{tip} = 1.01$
right - $M_\infty = 0.7$, $\beta_{ref} = 59.5°$, $J = 2.86$, $C_P = 2.12$, $M_{tip} = 1.04$

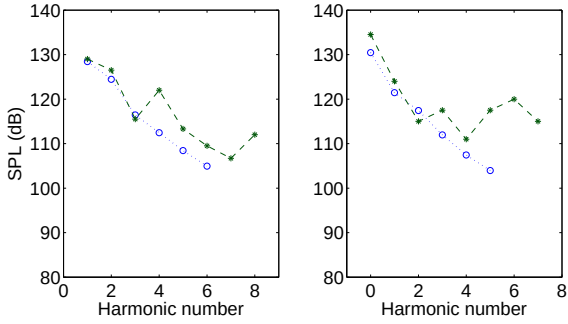

(c) SR-1 at supersonic tip speed.
left - $M_\infty = 0.8$, $\beta_{ref} = 58.5°$, $J = 3.25$, $C_P = 1.29$, $M_{tip} = 1.11$
right - $M_\infty = 0.8$, $\beta_{ref} = 58.5°$, $J = 3.06$, $C_P = 1.58$, $M_{tip} = 1.14$

Figure 6.11: Envelope of the BPF-harmonics in the propeller plane for the NASA SR-1 at various tip speeds for a receiver at $3.92R$.

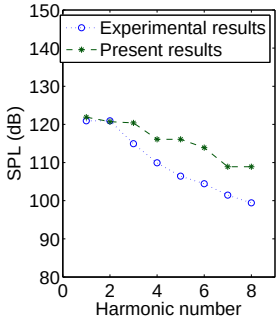

(a) SR-3 at subsonic tip speed.
$M_\infty = 0.7$, $\beta_{ref} = 59.5°$, $J = 3.26$, $C_P = 1.77$, $M_{tip} = 0.97$

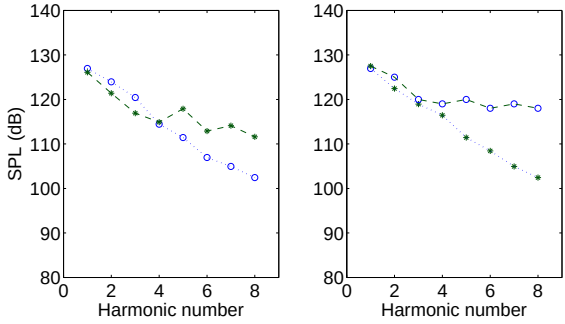

(b) SR-3 at sonic tip speed.
left - $M_\infty = 0.7$, $\beta_{ref} = 59.5°$, $J = 3.06$, $C_P = 2.02$, $M_{tip} = 1.00$
right - $M_\infty = 0.7$, $\beta_{ref} = 59.5°$, $J = 2.85$, $C_P = 2.35$, $M_{tip} = 1.04$

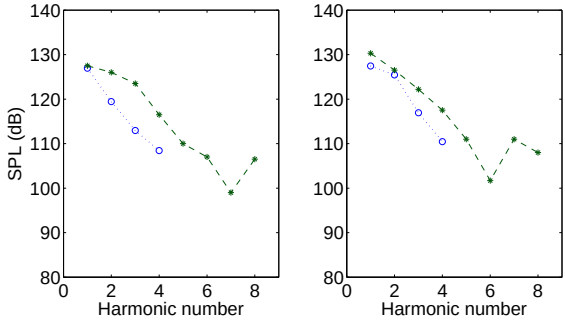

(c) SR-3 at supersonic tip speed.
left - $M_\infty = 0.8$, $\beta_{ref} = 58.5°$, $J = 3.26$, $C_P = 1.57$, $M_{tip} = 1.11$
right - $M_\infty = 0.8$, $\beta_{ref} = 58.5°$, $J = 3.08$, $C_P = 1.84$, $M_{tip} = 1.14$

Figure 6.12: Envelope of the BPF-harmonics in the propeller plane for the NASA SR-3 at various tip speeds for a receiver at $3.92R$.

present method, especially for higher harmonics.

6.3.2.1 Time-signal and truncation interval

To further investigate the effect of the truncation, the signal in the time domain is compared with the code written by Farassat, Padula and Dunn [110], later named DFP. This code switches, when needed, between Farassat's formulations 1A and 3, so that it ensures better accuracy. Note that the comparisons are made for a receiver at $2.64R$ from the axis and at a distance of $0.81R$ behind the propeller disk. Both codes do not include the quadrupole contribution. The effect of the truncation interval is shown in Figs. 6.13 and 6.14. For a narrow truncation interval, the thickness noise peak is slightly overpredicted, but the approximate solution fails completely for higher frequencies; resulting in a noisy time-signal. For a wider truncation interval, the thickness noise peak is completely underpredicted. As expected, thickness noise is dominant and is more significantly affected by the truncation than loading noise. Both for the time-signal and the discrete frequency spectrum (see Fig. 6.14), a κ-value of 0.4 proves to be the best compromise and yields acceptable results over a wide range of operating conditions, provided the helical tip Mach number is kept below 1.1 (see Figs. 6.11(b)-6.12(c)).

The truncated method is expected to deliver a reasonable approximate up- and downstream of the propeller plane in conditions considered to be on the far edge of the search domain for a viable modern propeller design ($M_\infty \approx 0.7 - 0.75$ and $M_{tip} \leq 1.0$).

6.3.2.2 Relative performance between geometries

Within the framework of an optimization routine, the ability of the code to correctly assess the variation of aeroacoustic performance between two blade designs is even more important than the prediction of absolute levels. Although in principle, the relative gap between individuals could be made questionable by the errors made on each prediction; this does not seem to occur with the present code. At low speeds, for a given condition and in complete disregard of the geometry, errors are systematic with the same trend toward underprediction of the SPL in and close to the propeller plane. So the correct assessment of aeroacoustic fitness is ensured in the subsonic domain by the accuracy of the results since formulation 1A is strictly applied without approximation.

In the high-transonic and low supersonic domains, where the truncation operator becomes effective, the present code performs with satisfaction in terms of relative fitness estimates. This is shown on Figs. 6.15 and 6.16 where the computed and experimental fitness of the NASA SR-1 and SR-3 blade designs are compared over the entire extent of the search domain. At $M_\infty = 0.8$ (Fig. 6.15), the relative difference between both individuals is nicely captured throughout different loading conditions even though non-linear effects are believed to affect the experimental results at high loading. Furthermore at constant advance ratio, over free stream Mach numbers ranging from 0.6 to 0.8 with the loading changing accordingly, the truncated method again captures the relative difference between both designs.

Note that the accuracy of the present sub-, trans- or supersonic results is not significantly improved when using a finer mesh whereas substantial degradation is

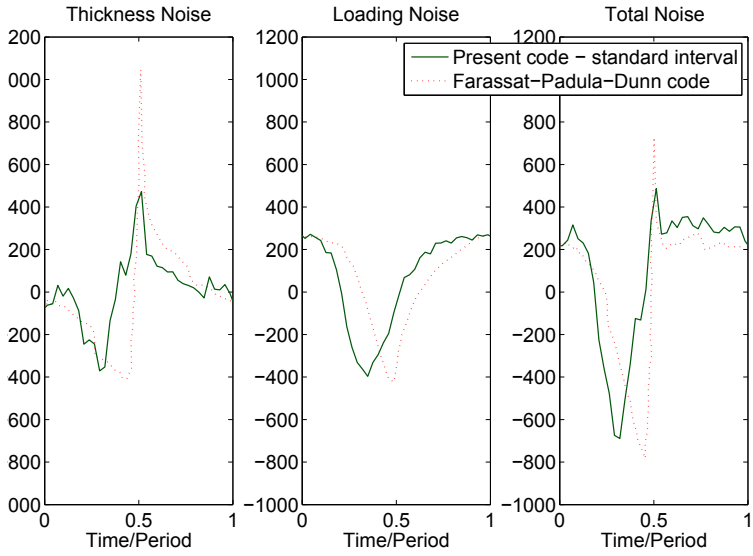

(a) Standard interval $\kappa = 0.04$.

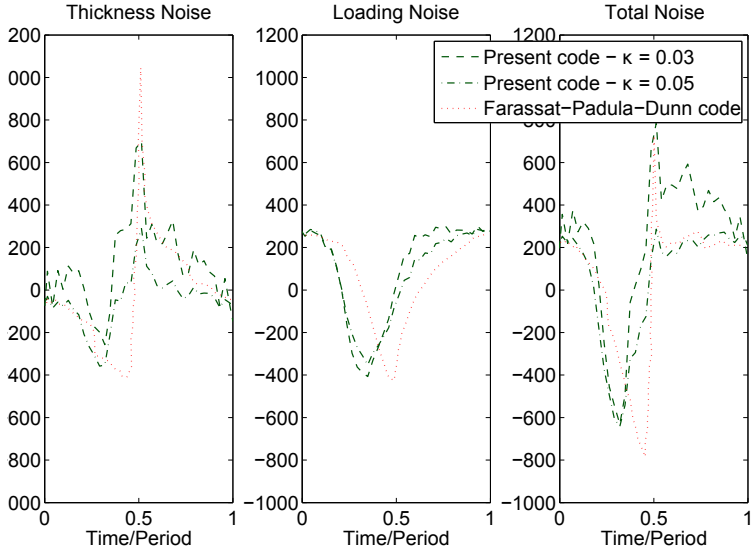

(b) Interval sensitivity.

Figure 6.13: Comparison of the time-signal obtained with the present code and DFP-code. NASA SR-3 propeller operating at $M_\infty = 0.8$ and $J = 3.06$ with $C_P = 1.83$ (results taken from [110] and corrected to match the operating conditions).

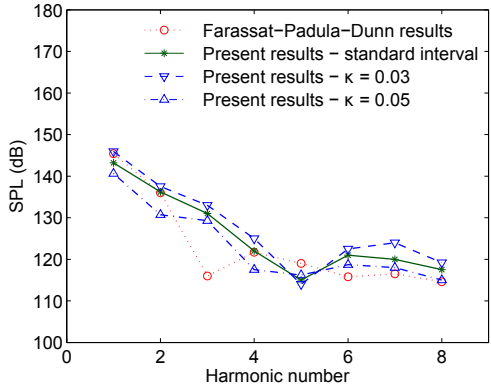

Figure 6.14: Frequency-domain comparison of the present code with the DFP-code under the same conditions as Fig. 6.13 for the NASA SR-3.

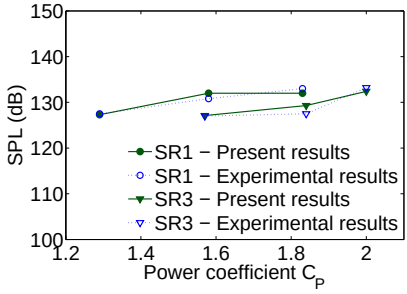

Figure 6.15: Comparison between fitness (SPL) as found experimentally and as computed by the present code at $M_\infty = 0.8$.

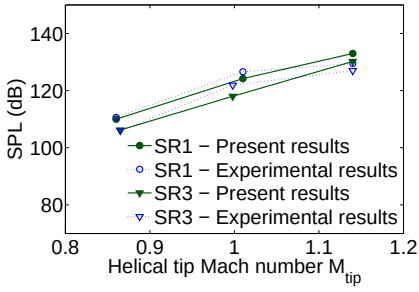

Figure 6.16: Comparison between fitness (SPL) as found experimentally and as computed by the present code at fixed advance ratio $J = 3.06$.

obtained if the mesh size is increased; hence, if the compactness requirement is not fulfilled.

6.3.2.3 Conclusion

In view of the present application for which the occurrence of the sonic or supersonic regimes are only the result of transient steps; a satisfying overall accuracy is obtained at both subsonic and high transonic tip speeds. For sonic and low supersonic cases, the SPL is satisfactorily predicted in and downstream of the propeller plane. Despite a shortcoming with respect to the high-frequency content at tip Mach numbers well above unity, the truncated method gives a reasonable approximate for the SPL with the exception of receivers located far upstream of the propeller plane; this is also reported elsewhere with other methods. In all cases, the discrepancies in and close to the propeller plane are typically below $5dB$, which is well within the margins observed with other codes. The approach is considered reliable for helical tip Mach numbers not exceeding 1.1. It keeps the computational effort within acceptable margins so that the search domain is not constrained by the occurrence of the singularity.

Chapter 7

Aeroelastic solver

A key point in the development of a propeller is to insure the structural integrity of the system. Though the integrity of the hub retention and of the other components associated with the pitch change mechanism are out of the scope of the present study, the integrity of the blade is included at this early stage because significant departures from conventional blade shapes are allowed.

Traditionally, the aerodynamic and aeroacoustic analyses are relying on the running position of the blade, also called the 'hot' position. It is common practice to leave it to the structural design team to define a posteriori the static, unloaded 'cold' shape to be manufactured such that at running conditions, the required hot shape is obtained. This step involves the iterative solution of the inverse aeroelastic problem. Unfortunately, the blade deformation at only one single operating condition can be closely matched [282]. Hence solving for the true coupling between aerodynamics and aeroelastics makes the design process computationally expensive and time consuming.

A way around the complexity of solving the inverse problem is to consider the shape determining distributions of chapter 4 as defining the cold rather than the hot shape. This is done for example in [47] but involves an iterative procedure between the aerodynamic and aeroelastic solver to converge step by step to the hot shape. On that account, this would be a computationally prohibitive approach for early design. Moreover, this approach would result in higher order interactions that would render accurate metamodelling of the aerodynamic, aeroacoustic and even aeroelastic responses extremely difficult.

For these reasons, it has been decided to account only for a partial coupling between the aerodynamics and the aeroelastics. The blade is defined in its hot shape and submitted to the aerodynamic solver. Later, a first estimate of the stress-state of the hot blade is obtained by computing the stresses resulting from the steady centrifugal and aerodynamic loadings. As the amplitude of local deformations is supposed to be negligible with respect to the overall blade dimensions, the computed stress state is supposed to be in the neighbourhood of the real state. In all likelihood, the reduction of stresses during the optimization process is anyway favourable for the real state. Dynamic effects due to periodic excitations are not considered at this stage. These effects range from vibrations of the blades themselves (blade flutter) [88, 199, 240] to vibration of the propeller disk and engine mount known as whirl

flutter [215,216]. These effects are important for successful propeller design but should be included in a later stage of the design phase by applying the proper analysis tools on the potential designs obtained with the present optimization.

In the current chapter, the aeroelastic solver, also referred to as Computational Structure Mechanics tool (CSM), will be briefly discussed together with the structural model of the blade and the imposed boundary conditions. Finally, the chosen criteria for the evaluation of complex stress states will be introduced. Along this chapter, the implications of specific choices will be mentioned.

7.1 A short review of blade stress computations

In the early ages of wooden propellers, structural blade design was mostly an art and relied greatly on practice and common sense. As reported in [213], new materials such as aluminium, steel and magnesium were quickly introduced together with empirical techniques to evaluate the stresses. It is worthwhile to mention that attempts to incorporate composite materials (micarta made of fabric impregnated with a synthetic resin) were made as early as 1922 by the Westinghouse Electric and Manufacturing Company but resulted in unsatisfactory characteristics [213]. Immediately, analytical techniques relying on strip analysis were developed and yielded more accurate predictions of the stress state. In these techniques, the blades are divided into segments at select radial stations while mass and stiffness are lumped at these stations [213, 136].

As long as blades were unswept, beam-models were used either in their analytical form or as finite elements [29]. But the advent of sweep made the beam-model obsolete and 3D methods based on finite elements were required. The efforts for the development of propfans in the 1980's coincide with the last bulk of useful publications on that topic. At first, the structural mesh consisted of a single layer of elements to which adequate properties were given to account for various materials in the composition of the blade [88, 147, 47]. Later, multiple layers were considered so that more accurate modelling of the blade structure could be realized [29, 282].

Today, 3D finite element models have become the standard. They use high-fidelity 3D meshes so that the properties of all elements composing the blade can be embraced.

7.2 Finite elements solver

7.2.1 Constitutive laws and hypotheses

7.2.1.1 Homogeneous, isotropic, linear elastic materials

Consider a solid body of volume V enclosed by a surface A and subject to surface forces $\bar{t}$ and body forces $\bar{b}$ as illustrated in Fig. 7.1. For static linear analysis, the governing differential equations are the static equilibrium equation (Eqn. 7.1), Hooke's law for elasticity (Eqn. 7.2) and the cinematic law (Eqn. 7.3) applied at a particular point P belonging to the volume V (i.e. $\forall \overline{x} \in V$):

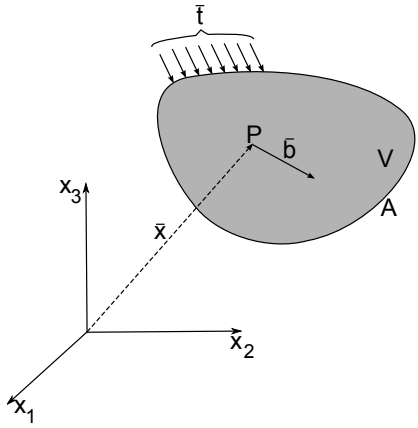

Figure 7.1: General elasticity problem for a solid body of volume V enclosed by a surface A and subject to surface forces $\bar{t}$ and body forces $\bar{b}$.

$$\sigma_{ij,i} = -b_j \tag{7.1}$$
$$\sigma_{ij} = D_{ijkl}\varepsilon_{kl} \tag{7.2}$$
$$\varepsilon_{ij} = \frac{1}{2}\left(u_{i,j} + u_{j,i}\right) \tag{7.3}$$

where

$$D_{ijkl} = G\frac{2\nu}{1-2\nu}\delta_{ij}\delta_{kl} + \frac{E}{2(1+\nu)}\left(\delta_{ik}\delta_{jl} + \delta_{il}\delta_{jk}\right) \tag{7.4}$$

In these equations, u_i refers to the displacement in the i^{th}-direction, σ_{ij} refers to the stress tensor, ε_{kl} refers to the strains and partial derivatives with respect to the j^{th}-direction are denoted $u_{i,j}$ for example. G is the shear modulus of the material and E is its Young's modulus. On top of these equations, adequate boundary conditions are applied so that displacements are compatible with supports (*essential* or *Dirichlet* boundary conditions) and so that stresses, derived from the displacement field, be compatible with the applied surface forces (*natural* or *Neumann* boundary conditions).

The strong form of Eqn. 7.1 is first multiplied by appropriate weighting functions ω_j $(j = 1, 2, 3)$ (Galerkin's method) before being integrated by parts over the domain V. After introduction of the natural boundary conditions, application of the Gauss divergence theorem and imposing $\omega_j = 0$ on the surface A where $\bar{t}$ is not known, one obtains the weak form of the problem:

$$\int_V \omega_{j,i}\sigma_{ij}dV = \int_V \omega_j b_j dV + \int_{A_t} \omega_j t_j dA \tag{7.5}$$

where A_t is the part of the surface A where surface loads $\bar{t}$ are applied. If the tensor $\omega_{j,i}$ is split in a symmetric part $\omega^S_{j,i}$ and an anti-symmetric part $\omega^A_{j,i}$, the last equation

can be written, by introduction of Hooke's law:

$$\int_V \omega^S_{j,i} D_{ijkl} u^S_{k,l} dV = \int_V \omega_j b_j dV + \int_{A_t} \omega_j t_j dA \tag{7.6}$$

If matrix notations are used, with

- $\overline{\varepsilon}^T \equiv [\varepsilon_{11}\ \varepsilon_{22}\ \varepsilon_{33}\ 2\varepsilon_{12}\ 2\varepsilon_{23}\ 2\varepsilon_{31}]$
- $\overline{\sigma}^T \equiv [\sigma_{11}\ \sigma_{22}\ \sigma_{33}\ \sigma_{12}\ \sigma_{23}\ \sigma_{31}]$
- $\overline{\sigma} = \mathbf{D}\overline{\varepsilon}$
- $\overline{u}^T \equiv [u_1\ u_2\ u_3]$
- $\overline{b}^T \equiv [b_1\ b_2\ b_3]$
- $\overline{t}^T \equiv [t_1\ t_2\ t_3]$
- $\overline{\omega}^T \equiv (\omega_1\ \omega_2\ \omega_3)$

and writing $\mathbf{S}$ the partial differentiation operator such that $\overline{\varepsilon} = \mathbf{S}\overline{u}$ and $\omega^S_{i,j} = \mathbf{S}\overline{\omega}$; the weak form becomes

$$\int_V \overline{\omega}^T \mathbf{S}^T \mathbf{D}\mathbf{S}\overline{u} dV = \int_V \overline{\omega}^T \overline{b} dV + \int_{A_t} \overline{\omega}^T \overline{t} dA \tag{7.7}$$

On this form, the finite elements theory is applied. It introduces shape functions N_e defined non-zero within each element e (i.e. they vanish at all nodes not belonging to element e as illustrated in Fig. 7.2). With these functions, here of the linear type because the nodes coincide with the intersections of the mesh, the continuous variables are expressed as continuous functions of the discrete nodal values so that $\overline{x} = \mathbf{N}\overline{x_e}$, $\overline{u} = \mathbf{N}\overline{u_e}$ and $\overline{\omega} = \mathbf{N}\overline{\omega_e}$, where $\overline{x_e}$, for example, refers to the vector formed by assembling the three components of $\overline{x}$ for all n_e nodes of an element in a single vector: $\overline{x_e}^T \equiv [x_1^1\, x_2^1\, x_3^1\, x_1^2\, x_2^2 \ldots x_1^{n_e}\, x_2^{n_e}\, x_3^{n_e}]$. Introducing $\mathbf{B} = \mathbf{S}\mathbf{N}$, Eqn. 7.7 becomes:

$$\sum_e \mathbf{K_e}\overline{u}_e = \sum_e \overline{f}_e \quad \text{with} \quad \begin{cases} \mathbf{K_e} = \int_{V_e} \mathbf{B}^T \mathbf{D}\mathbf{B} dV \\ \overline{f}_e = \int_{V_e} \mathbf{N}^T \overline{b} dV + \int_{A_{te}} \mathbf{N}^T \overline{t} dA \end{cases} \tag{7.8}$$

where V_e is the volume of element e and A_{te} the surface it shares with the exterior surface A_t. This is the algebraic elemental form of the problem with $\mathbf{K_e}$ the elementary rigidity matrix[1] and $\overline{f}_e$ the elementary force vector. Eqn. 7.8 exists over all elements so the next step is to globalize the system by taking continuity of certain unknowns between two adjacent elements into account and assembling all unknowns into one single vector $\overline{u}_g$ with N_{dof} components also called *degree of freedom*. This yields the global form of Eqn. 7.8 that needs to be solved:

$$\mathbf{K_g}\overline{u}_g = \overline{f}_g \tag{7.9}$$

7.2.1.2 Inhomogenous, anisotropic, bielastic materials

Composite materials are composed of high strength fibers continuous or not, embedded in a low density matrix resin. Thanks to their excellent specific properties and

[1] Also called stiffness matrix.

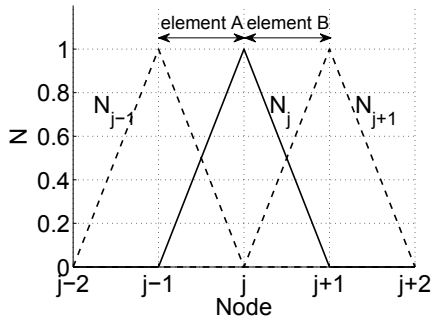

Figure 7.2: Global linear shape functions N_j for nodes $j-1$, j and $j+1$ defining the shape function for elements A and B in the case of 1D linear elements.

fatigue resistance, composite materials allow for substantial weight saving without altering the mechanical properties of the blade [197]. Their utmost advantage is the possibility to tailor them to the specific application by tuning the number of layers, their composition and their orientation so the principal-effort directions are suited.

These materials are well differentiated from homogeneous, isotropic, elastic materials such as metals. By nature, they are highly anisotropic because of the fibers orientation, highly non-homogeneous because of the presence of fibers and matrix resin, and they often have elastic properties depending upon the stress state (tensile or compressive). This makes the procedure to derive the global form of the constitutive equations (the equivalent of Eqn. 7.9) quite intricate. The detailed process is beyond the scope of the present work; it includes:

- homogenization to determine average macroscopic elastic properties of a periodic material from the individual properties at microscopic scale,
- lamination to possibly determine the average properties of a superimposition of a series of elementary layers depending upon the number of layers, their orientation, thickness, material characteristics and their stacking sequence,
- generalization of Hooke's law to provide appropriate constitutive equations.

For woven materials, preferential directions exist and orthotropic hypotheses can be applied to simplify the equations. Nevertheless, the process is even more complicated by the bi-elastic nature of the composites used for blade manufacture. Figure 7.3 illustrates this behaviour for one specific principal direction (i^{th}-direction).

7.2.1.3 Linear static analysis

The system behind Eqn. 7.9 is linear only under certain hypotheses. First, axial deformations ε_{ii} and angular deformations ε_{ij} (with $i \neq j$) should remain small with respect to unity; while displacements u_i should remain small with respect to the blade's size. Second, the material should stay within the linear elastic range where stresses σ_{ij} vary linearly with deformations ε_{ij}. In other words, the moduli of elasticity should be constants. This is the assumption taken for the present analysis

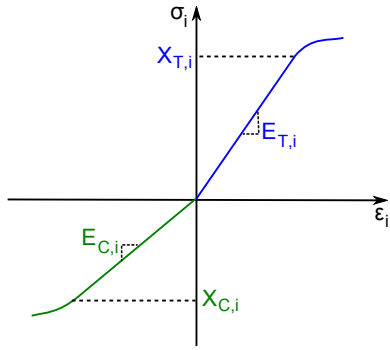

Figure 7.3: Bi-elastic behaviour in the i^{th} of the principal directions.

given the choice of deforming the hot shape. But when a structure is subjected to a tensile or compressive load, the resulting stress field modifies the bending behaviour. When needed, these effects can only be rigorously included by nonlinear analysis. Fortunately, some stiffness modifications due to loading can be allowed for, while still remaining within the linear range. Indeed, with the small displacement hypothesis, a linearized form of the nonlinear stiffness matrix can nevertheless be used.

For rotating structures such as blades, centrifugal forces act in the solid as is shown on Fig. 2.5 and are at any point proportional to the distance from the point to the axis of rotation. When a node moves away or moves closer to the axis, the centrifugal force varies. An allowance can be made for displacement-dependent forces by modifying the stiffness matrix. The global matrix $\mathbf{K_g}$ is then the sum of the linear stiffness matrix $\mathbf{K_{g,0}}$ and the centrifugal matrix $\mathbf{K_{g,\omega}}$.

7.2.2 Solution of the algebraic system

Samcef v-13.1-02 [10] is used as an integrated package for high-fidelity aeroelastic analysis. It is convenient for its ability to run in script mode so that it is easily integrated in an automatic procedure. Samcef v13.1-02 takes care of the spatial discretization in the BACON-module (see section 4.3.2), globalization and solution of the algebraic system in the ASEF-module and finally post-processing in the BACON-module again.

Eqn. 7.9 needs to be solved for the N_{dof} unknowns in $\overline{u}_g$. This huge algebraic system of linear equations is solved with Boeing's multi-frontal sparse matrix solver BCSLIB [22, 23, 228] which is recommended for medium to large problem size and provides very good performance. The solution is obtained by Cholesky decomposition of the rigidity matrix and simultaneous solution of multiple subsets of it. This solver offers a good balance between in- and out-of-core memory requirements. Other solvers available in Samcef v13.1-02 include the frontal solver (it requires more CPU-time to solve the system as only a single subset of the rigidity matrix is used), the conjugate gradient iterative solver which requires more out-of-core memory than the BCSLIB solver and the MUltifrontal Massively Parallel sparse direct Solver (MUMPS) which is fully parallelized but does not offer significant gains for the considered system size.

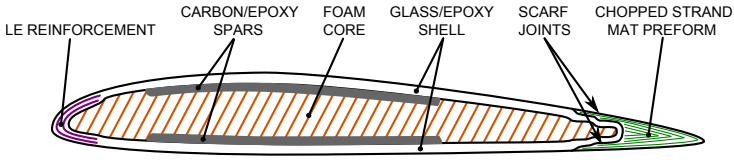

Figure 7.4: Modern braided blade construction [196].

7.3 Blade model and boundary conditions

7.3.1 Blade structure, materials and elements types

In opposition to traditional metal or wooden blades [213], modern blades for high speed aircraft are usually assembled from diverse forms of composite materials and possibly metal spars in some specific applications like propfans. A detailed account of possible blade structures with their pros and cons is given in [29] though some advanced techniques were not yet available at that time. Most of the available structural data, either from experiments or from CSM, are thence collected either from solid metal or from composite shell, foam core and metal spar blade assemblies [27, 282]. An interesting structure that is in use among the propeller industry and incorporates advanced use of composite materials, is that described by R. McCarthy in [196, 197]. This architecture relies on two carbon fiber spars running along the blade to carry the main loads (see Fig. 7.4). These spars are enclosed between a foam fill core and a glass fiber shell. The leading edge is reinforced by additional layers and the trailing edge is made of a preform so that the trailing part of the shell has sufficient radius to apply the braiding technique. This technique, illustrated in Fig. 7.5, is simple and versatile and results in structures with high conformability, torsional stability and damage resistance [171]. It feeds a mandrel at constant rate through the center of the machine and braids tows (*yarns*) from several moving carriers by intertwining them directly about the mandrel at controlled angle. Braiding differs from woven or knitted fabrics in how the yarns are interlaced [171]. The obvious advantage of this technique is to exclude junctions as those that would occur by wrapping of cross-ply laminates and to allow the designer to tailor the shear modulus G, essential for blade stiffness, by using hybrid braids of several materials (carbon and glass for example) and/or by adjusting the braid angle. Resin transfer molding is then used to bond the fibers while maintaining high fiber volume fractions.

Unfortunately, a blade structure such as the one of Fig. 7.4, testifies of a considerable amount of tailoring and would be extremely difficult to implement in an automated procedure where blades of highly changing geometry are assessed. This is especially true if one wants to preserve a lot of freedom at the level of the design variables. For this reason, only a simplified blade model is implemented such that it can reasonably be applied to any blade geometry. The simplified blade is a monocoque design as shown in Fig. 7.6. The shell is composed of stepped layers of braided composite (carbon/epoxy and E-glass/epoxy) that are directly braided on the foam core. The outer shell is composed of E-glass fiber because of its lower cost but also because a certain amount of glass fiber is desirable for the impact properties of the blade [196]. It runs from the edge of the shank assembly at 19.5% radius (see Fig. 7.9)

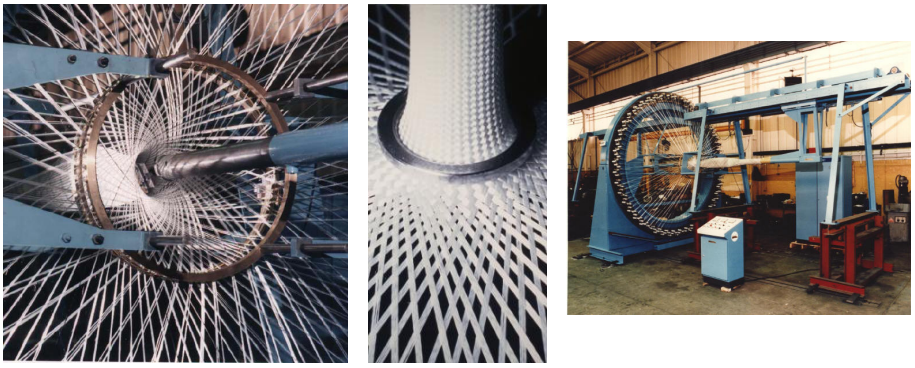

(a) (b) (c)

Figure 7.5: 3D braiding process of a propeller blade directly on the foam core mandrel (Fig. 7.5(a) and 7.5(c) from [15], Fig. 7.5(b) from [14]).

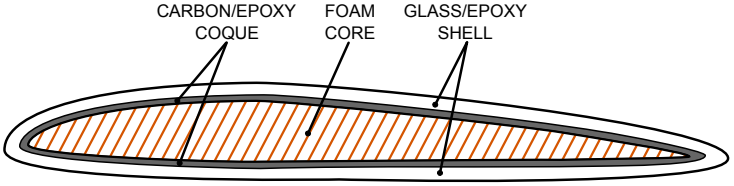

Figure 7.6: Monocoque blade construction.

to the tip. The inner most carbon fiber braid of Fig. 7.7, runs from the root to the tip whereas the other two braids are stepped and run from the root to 30.7% and 36.5% radius respectively. This stepping ensures the blade is properly supported in the transition region (see Fig. 7.8) where the outer shell blends from airfoil shape to cylinder and where critical stresses are likely to occur.

After the spatial discretization (see section 4.3.2), adequate hypotheses must be assigned to the mesh elements to model as accurately as possible the structure described in the previous paragraphs. The outer shell is modelled by draping of layers of composite laminate whose strength properties match those of the corresponding braids, into composite triangular shell elements (type 57 in Samcef v13.1-02) with a thickness. The principal direction for draping is the longitudinal direction. For the foam core, tetrahedral volume elements have been chosen (type 47). The junction between the core and the shell is done by perfect coupling of their respective degrees of freedom so that a perfect bonding is modelled. The strength properties of bi-elastic braids given in table 7.1, are taken from [120, 288] for the carbon/epoxy braid and from [288, 50] for E-glass/epoxy. The braider yarn angles are close to 50° with respect to the longitudinal direction in both cases. The foam core is made of rigid polyurethane foam of aeronautical quality [13] and its properties are given in

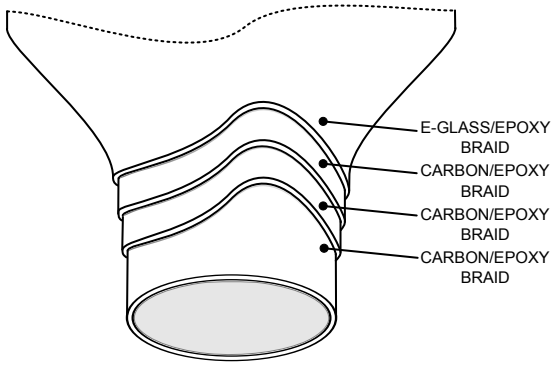

Figure 7.7: Braid layer arrangement. The E-Glass/Epoxy layer runs from 19.55% radius (see Fig. 7.9).

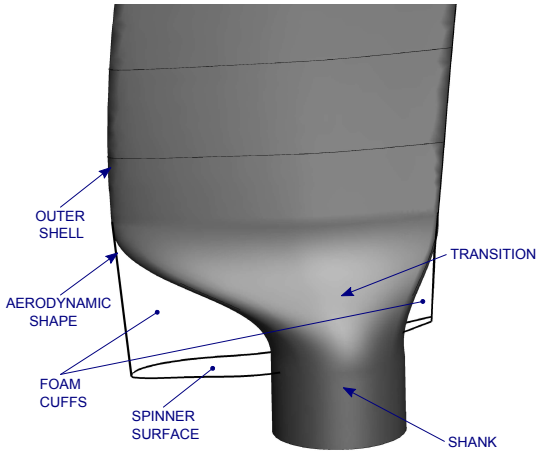

Figure 7.8: Transition of the blade structure from aerodynamic shape to root assembly..

			Carbon/Epoxy Braid	E-Glass/Epoxy Braid
Young's modulus	E_T	GPa	106.26 9.66	35.2 8
	E_C	GPa	93.15 9.0	23.1 6
Shear modulus	G	GPa	12.7 10	8 7
Poisson's ratio	N_T		0.81 0.04	0.31 0.06
	N_C			
Tensile strength	X_T,Y_T,Z_T	MPa	750.03 22.77	502 15
Compressive strength	X_C,Y_C,Z_C	MPa	473.34 22.77	418 12
Shear strength	R,S,T	MPa	70 70	71 60
Volumic mass	ρ	kg/m^3	1.870E+03	2.100E+03

Table 7.1: Material properties of the braided layers in the longitudinal (X,R) and transverse directions (Y,Z,S,T) with respect to the fibers.

			Polyurethane Foam
Young's modulus	E	GPa	0.94
Shear modulus	G	GPa	0.19
Poisson's ratio	N_T		0.35
	N_C		0.45
Tensile strength	X_T,Y_T,Z_T	MPa	16
Compressive strength	X_C,Y_C,Z_C	MPa	37
Shear strength	R,S,T	MPa	14.0
Volumic mass	ρ	kg/m^3	0.600E+03

Table 7.2: Material properties of the polyurethane foam core.

table 7.2.

7.3.2 Blade retention

At its root, the blade needs to be connected to the rotating hub in which the pitch change mechanism is enclosed. This connection is generally realized either by having the composite material to form a flange that is clipped or trapped by windings between two metal pieces [60,130], or by insertion of annular wedges to open out the material so that it stays clamped between two metal sleeves [69,293,196]. This kind of assembly is illustrated in Fig. 7.9 and has been chosen in the present case. As the focus lies in the analysis of the stress levels in the blade itself, especially if non-orthodox blade shapes are generated, only the composite portion of this assembly is modelled and subject to a clamping condition in all directions.

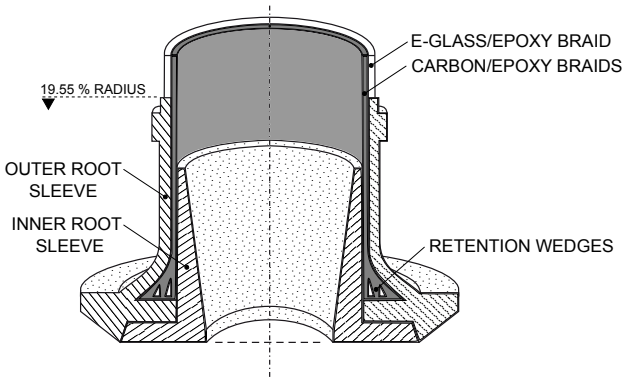

Figure 7.9: Blade root assembly.

7.3.3 Blade loads and pressure interpolation

7.3.3.1 Loads

Of the various loads applied on the blade in service, only the static loads are accounted for at this early design stage. The centrifugal loads are accounted for by modification of the stiffness matrix (see section 7.2.1.3). On top of these loads, the surface elements of the blade are subject to the pressure distribution resulting from the flow around the blade. These pressures are computed by the aerodynamic solver and are translated into loads normal to each element of the outer shell. This procedure is repeated for every operating condition so that the fundamental differences in pressure loading between the cruise and the take-off/landing conditions are taken into account.

7.3.3.2 Interpolation between aerodynamic and aeroelastic meshes

The disparity in the size and shape of the mesh elements between the aerodynamic and aeroelastic solvers (see sections 4.3.1 and 4.3.2), results not only in the nodes of the mesh being not collocated in regions of low curvature but also to local departures of both meshes in regions of high curvature. These situations are illustrated in Fig. 7.10. One solution to these departures would be to refine the mesh for the CSM-solver in those regions but this would increase CPU-usage significantly for marginal gains in accuracy.

The interpolation of pressure between both meshes is done with the interpolator developed at the VKI by F. Pinna in Matlab v7.4.0.287 [1]. Given a set of N data sites[2], this interpolator uses first the kd-tree method implemented by M. Kennel [166] to organize the data and find neighbouring data sites in an efficient way. Kennel's C++-implementation is wrapped in the Matlab code. The kd-tree method is a generalization of binary search trees to a k-dimensional space. It is very efficient since it requires $\mathcal{O}(\log N)$ time instead of the $\mathcal{O}(N)$ time required by brute-force [112]. Once

[2]A *data site* is a vector containing the coordinates of a point and other data at that point such as pressure, temperature, etc...

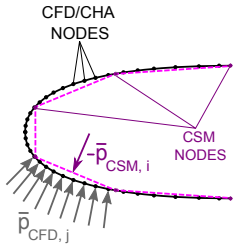

Figure 7.10: Disparities in node location between CFD/CHA meshes and CSM meshes. $\overline{p}_{CFD,j}$ is the aerodynamic pressure at node j of the CFD/CHA mesh whereas $\overline{p}_{CSM,i}$ is the interpolated pressure for element i of the CSM mesh.

the data are organized, the space is split in a relatively small number of subsets containing roughly the same number of data sites. This is done to avoid ill conditioning of the interpolation problem due to the presence of data sites at large distances of the point where the data needs to be interpolated. For that purpose, the partition of unity method is used [112]. It is a simple way to decompose the global interpolation problem over the domain into local interpolation problems over subsets while ensuring that the accuracy of the local fits is carried over to the global fit. In the present case, the aerodynamic domain is first split into non-overlapping 3D boxes containing each no more than 300 data sites. Then, the boxes are extended into each direction by 10% of their size in that particular dimension. This provides for the necessary overlap so that the accuracy of the global interpolation is preserved. Inside each box, an RBF interpolator is trained from the data sites (see section 3.3.4) with H. Wendland's C^2-function [301] instead of the Gaussian function. This function is illustrated for a 1D case in Fig. 7.11. Finally, the global interpolation at a particular point is the weighted sum of the local interpolations. The weighting is done according to [287]. For a point belonging to a single box, the weighting ensures the contributions of all other boxes are exactly zero so that the global interpolation is equal to the local interpolation within that box. For a point belonging to two or more boxes, the weighting is based on the distance to the boundaries of the boxes and ensures a fair contribution to the global interpolation from all local interpolations that are implied.

Appendix B gives comparisons of the initial and interpolated pressure fields for different geometries and conditions. These comparisons show the excellent accuracy that is preserved through the interpolation so that no spurious pressure loads are effected onto the blades.

7.4 Stress criteria

As commonly accepted for composite materials, global criteria are used instead of investigating the intricate situation of stresses in particular locations. These criteria have the advantage of being relatively easy to interpret and provide a direct answer to the question "Are the stresses within structurally acceptable limits?" The scalar values used in these criteria are computed straight from the stress tensor in each node. This step is performed in the post-processing phase of the CSM solver.

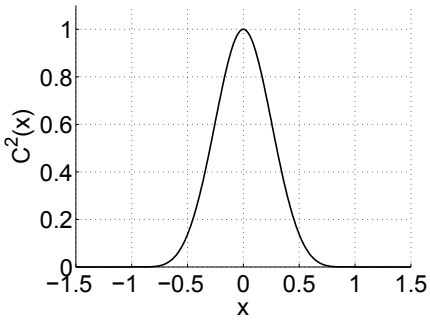

Figure 7.11: 1D Wendland's C^2 function.

7.4.1 Criteria for isotropic materials

For the foam core, assumed to be nearly isotropic, the von Mises equivalent stress criterion is used [299]. The equivalent tensile stress σ_{VM} is computed from the stress tensor by

$$\sigma_{VM} = \sqrt{\frac{1}{2}\left((\sigma_1 - \sigma_2)^2 + (\sigma_2 - \sigma_3)^2 + (\sigma_1 - \sigma_3)^2\right)} \tag{7.10}$$

where σ_i $(i = 1, 2, 3)$ refers to the components of the stresses in the structural axes[3]. This equivalent stress is then compared to the tensile yield strength to build the criterion value ζ_{VM} that should, strictly speaking, be inferior to 1:

$$\zeta_{VM} = \frac{\sigma_{VM}}{X_T} < 1 \tag{7.11}$$

The tensile strength is used as this is the most stringent form of the criteria. The criteria states that yielding begins when the elastic energy of distortion reaches a certain critical value. Of course, in real-world applications, values close to 1 are unsafe hence safety margins are applied. The particulars of the safety margin will be given in part III.

This criterion has been chosen for its acceptance and wide use for isotropic materials though other criteria exist such as the also widely used Tresca criterion [289] that is more related to the maximum shear stress but is usually more conservative than the von Mises criterion.

7.4.2 Criteria for orthotropic materials

Many different theories have been proposed to predict the load-carrying capacity of composite structures and provide safety margins while, whenever possible, taking the effects of geometrical non-linearity into account. These effects result into significant interactions between deformations in the longitudinal, transverse and shear directions. Four criteria are commonly used: the maximum strain, the maximum

[3]Principal axes are local orthogonal reference frame defined such that the three components of the stresses are aligned with the directions of the axes.

stress, the Tsai-Hill and the Tsai-Wu criteria. Whereas the first two criteria predict independent failure modes, the last two predict the onset of failure but not its mode and depend on more than one stress component. The Tsai-Hill criterion [145, 290] is a generalization of the maximum distortional energy criterion accounting for plane stress but involves either compressive or tensile strengths independently. The Tsai-Wu criterion [291], chosen in this work, is a simplification of Gol'denblat and Kapnov's generalized failure theory for anisotropic materials [128]. It requires both compressive and tensile strength data as inputs and leads to a polynomial form involving the components of the stress tensor in quadratic and interaction terms:

$$\begin{aligned}\zeta_{TW} = &\left(\frac{\sigma_1^2}{X_T X_C}\right) + \left(\frac{\sigma_2^2}{Y_T Y_C}\right) + \left(\frac{\sigma_3^2}{Z_T Z_C}\right) + \left(\frac{\tau_{12}}{R}\right)^2 + \left(\frac{\tau_{23}}{S}\right)^2 + \left(\frac{\tau_{13}}{T}\right)^2 \\ &+ \left(\frac{1}{X_T} - \frac{1}{X_C}\right)\sigma_1 + \left(\frac{1}{Y_T} - \frac{1}{Y_C}\right)\sigma_2 + \left(\frac{1}{Z_T} - \frac{1}{Z_C}\right)\sigma_3 \\ &+ 2F_{12}\sigma_1\sigma_2 + 2F_{23}\sigma_2\sigma_3 + 2F_{13}\sigma_1\sigma_3 < 1\end{aligned} \tag{7.12}$$

with

$$F_{12} = -\frac{1}{2}\sqrt{\frac{1}{X_T X_C}\frac{1}{Y_T Y_C}} \tag{7.13}$$

$$F_{23} = -\frac{1}{2}\sqrt{\frac{1}{Y_T Y_C}\frac{1}{Z_T Z_C}} \tag{7.14}$$

$$F_{13} = -\frac{1}{2}\sqrt{\frac{1}{X_T X_C}\frac{1}{Z_T Z_C}} \tag{7.15}$$

and where σ_i $(i = 1, 2, 3)$ are the components of the stresses in the element axes[4]. Eqn. 7.12 should strictly speaking deliver a value for ζ_{TW} below 1. With some stress tensors, negative values are obtained though this does not allow to conclude on the type of stresses (tensile or compressive). Given its origins, this criterion is a good matching for the von Mises criterion used for the foam core and is applied to advanced propellers in [47] for example. Again, the particulars of the safety margin will be discussed in part III.

More evolved criteria exist, such as the Hashin criteria [141] where distinct fiber and matrix failure modes are modelled, or the Grant-Sanders method [86] that also predicts the location of failure; but these involve additional complexity that is not required at this design stage.

[4]The element axes have the 3^{rd}-component normal to the shell and pointing outward, and the 1^{st}- and 2^{nd}-direction are defined in the plane of the element [10].

Part II

Aerodynamic and Aeroacoustic Optimization

Chapter 8

Optimization set-up

A coupled aerodynamic and aeroacoustic optimization without structural analysis, is presented in this part. This limited optimization mainly results from the need to integrate together as many tools as possible, in the present case two of the three high-fidelity analysis tools, as early as possible in the overall development of the method. Albeit limited to aerodynamics and aeroacoustics, it is not only helpful in the fine-tuning of the tools as well as of the design-variables; but also proves the potential of the method. Additionally, such an optimization could deliver some useful insight in the possible results of the true multidisciplinary optimization by the direction taken during the optimization process.

First, the detailed assembly of the optimization tools described in part I is described in the present chapter along with the parameters, the objectives and the constraints. Next, chapter 9 is dedicated to the analysis of the optimization process itself, from the composition of the DoE-database to the last population. In that chapter, the accuracy of the metamodel is assessed. Finally, a circumstantial analysis of the aerodynamic and aeroacoustic characteristics of some promising designs is given in chapter 10 before drawing the necessary conclusions and recommendations about this optimization run.

8.1 Design variables

Geometry parameters are summarized in table 8.1 together with the number of optimization variables dedicated to each of them. The value of a geometry parameter $x(r)$ at any radius r is determined through 3^{rd} order b-spline interpolation using the control points corresponding to that particular parameter. The ordinates x_i of those control points, effectively determining the shape of the geometry distribution $x(r)$, are used as variables and are allowed to fluctuate over specific intervals as shown in Fig. 8.1 for the blade geometry and in Fig. 8.2 for the airfoils. The width of the allowable intervals is chosen such that the optimization process bears a lot of freedom. This is especially true for the chord distribution which has 7 control points so that multiple inflexions are allowed. The drawback of the parameterization is that a radial distribution of a geometry parameter or a particular airfoil shape are not defined in

Variable		Number of Control Points	Number of Design Variables	
Chord length	$b(r)/D$	7	7	
Thickness ratio	$t(r)/b(r)$	4	3	
Sweep	$Sw(r)$	4	4	
Twist	$Tw(r)$	4	3	
Airfoil I thickness	t_A	6	5	[a]
Airfoil I camberline	y_A	4	2	
Airfoil II thickness	t_B	6	5	[b]
Airfoil II camberline	y_B	4	1	
Total			30	

[a] from blade root to 35% radius
[b] from 45% radius to blade tip

Table 8.1: Geometry parameters and design variables.

a unique way. Distinct sets of variables could result in the same distribution because of the non-uniqueness of b-spline parameterization. For the optimization itself, this is not a problem as such, but it confuses the metamodel and that could be potentially detrimental to the reliability of its approximations. Fortunately, given the low cardinality of the sets controlling the individual design variables, the probability of confusion is almost non-existing in the present work.

The diameter D of the scale-model propeller and the number of blades are fixed at $1.0m$ and 8 respectively while the blade angle (β_{ref}) is fixed at 63° for the cruise condition and 37° for the take-off/landing condition.

8.2 Optimizer architecture and set-up

The general lay-out of the optimization code is almost identical to the architecture described in section 3.4 though the CSM tool has been left aside as is apparent from Fig. 8.3. The DoE-database comprised 64 individuals chosen by fractional factorial sampling and augmented by the central individual (i.e. the individual having all design variables set at their respective mid-range positions). Moreover, a set of 16 random designs completes the database. The fractional sampling is based on full factorial sampling of six particular variables chosen because of their major influence both in aerodynamics and aeroacoustics. These are the last two variables controlling the geometrical sweep toward the tip, two controlling the thickness (at 30%- and 75%-radius) and two controlling the chord, one at the root and the other at 75%-radius.

For this optimization, one off-line trained ANN-metamodel (see section 3.3.3) is used for each performance parameter. It is trained with early stopping. The weighting factor F and the cross-over constant C of the MODE-optimizer (see section 3.2) are chosen as 0.6 and 0.8 respectively. This choice is a good compromise for convergence while maintaining high cross-over probability. The evolutionary process is spread over 1000 generations between two successive iterations. The population size is 50 of which between 10 and 5 individuals are submitted to the high-fidelity analysis at the

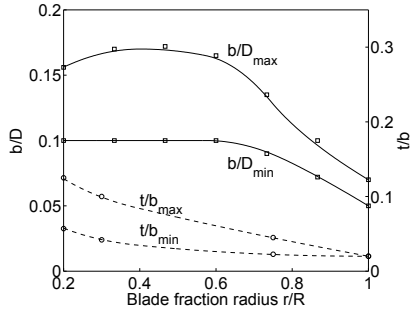

(a) Chord ($b(r)/D$ - □) and thickness ($t(r)/b(r)$ - ○).

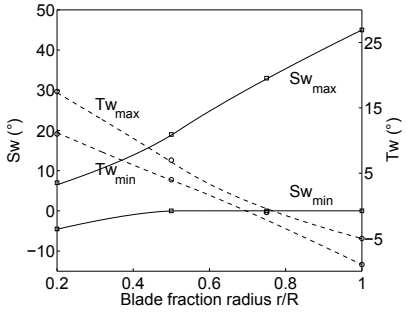

(b) Geometrical sweep ($Sw(r)$ - □) and twist ($Tw(r)$ - ○).

Figure 8.1: Minimum and maximum ordinates of the control points for the blade distributions together with the corresponding distributions.

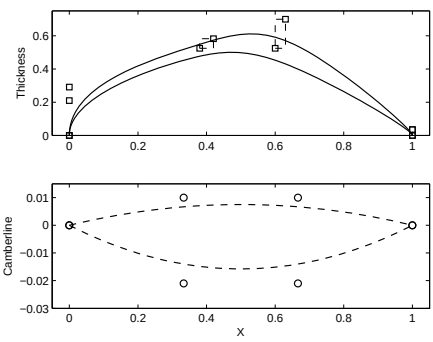

(a) Airfoil *I*.

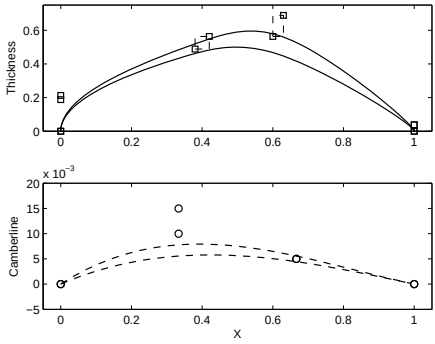

(b) Airfoil *II*.

Figure 8.2: Minimum and maximum ordinates of the control points for the airfoils together with the corresponding thickness-line and camberline.

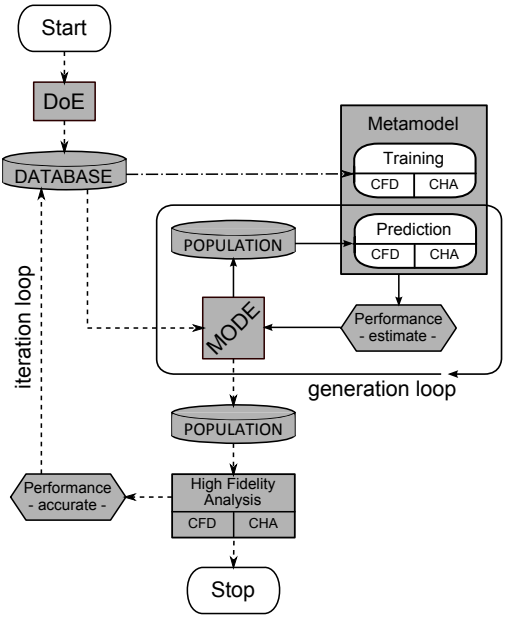

Figure 8.3: Layout of the optimization code used for the present optimization.

end of each iteration. These individuals are chosen for their excellent performance based on the metamodel approximation.

8.3 Operating conditions, objectives and constraints

The multi-objective and multipoint optimization is based on 2 operating conditions, comprising each 3 advance ratios. One set is representative of the cruise condition with three advance ratios $J_{CR,i}$ $(i = 1, 2, 3)$. $J_{CR,2}$ is adapted to match the constraint on minimum cruise thrust $T_{CR,2}$([1]) while $J_{CR,1}$ and $J_{CR,3}$ are at a fixed distance from $J_{CR,2}$ so that a glimpse of the performance curve is obtained (-0.5 and $+0.3$ respectively). The other set is representative of take-off and landing conditions at low Mach number and comprises also three advance ratios $J_{TO,i}$. $J_{TO,2}$ is adapted to match the constraint on minimum take-off thrust $T_{TO,2}$([1]) while $J_{TO,1}$ and $J_{TO,3}$ are again at a fixed distance from $J_{TO,2}$ (-0.2 and $+0.4$ respectively). The external operating conditions corresponding to cruise and take-off/landing are summarized in table 8.2.

In a multidisciplinary optimization, the objectives, together with the constraints, are the driving factors for the evolutionary process. The obvious advantage of a multi-objective approach with a Pareto-front and not a pseudo-objective, is that each

[1] See infra.

	Take-off/Landing	Cruise
ISA altitude (m)	0	10665
ρ_∞ (kg/m^3)	1.225	0.380
T_∞ (K)	288.15	218.81
M_∞	0.2	0.75
$Re_{b,ref}$	1.44e06	1.14e06

Table 8.2: Operating conditions. The Reynolds number $Re_{b,ref}$ is based on mean conditions at 75% radius.

discipline can be treated on its own, without the difficult necessity to assign weights between performance values stemming from different disciplines. On top of being a difficult task, the optimization outcome is often very sensitive to the choice of the weights [71]. In the current approach, both disciplines have their own objectives, but instead of having one objective for each operating point, some performance factors are aggregated in one single objective consisting of elements from either aeroacoustics or aerodynamics solely. For the aeroacoustic objectives, the receivers are located according to Fig. 8.4. The aggregated objectives consist of:

1. an aggregate of the propeller power at the three advance ratios both in the cruise and take-off/landing conditions (Ω_1),
2. an aggregate of the Sound Pressure Level (SPL) in the propeller plane (at receiver 3) both in the cruise and take-off/landing conditions (Ω_2),
3. and an aggregate of the SPL at three receiver locations (receivers 2, 3 and 4) both in the cruise and take-off/landing conditions (Ω_3).

This yields the system

$$\Omega_1 = w_{CR}\left(\sum_{i=1}^{3} w_{ai} P_{CR,i}\right) + w_{TO}\left(\sum_{i=1}^{3} w_{ai} P_{TO,i}\right) \tag{8.1}$$

$$\Omega_2 = w_{CR}\left(\sum_{i=1}^{3} w_{ai} SPL_{CR,i}^{rec\ 3}\right) + w_{TO}\left(\sum_{i=1}^{3} w_{ai} SPL_{TO,i}^{rec\ 3}\right) \tag{8.2}$$

$$\Omega_3 = w_{CR}\left(\sum_{j=2}^{4} w_b SPL_{CR,2}^{rec\ j}\right) + w_{TO}\left(\sum_{j=2}^{4} w_b SPL_{TO,2}^{rec\ j}\right) \tag{8.3}$$

in which the weights w_{CR} and w_{TO} are chosen arbitrarily as 0.75 and 0.25 respectively, to correspond to the relative time spent in these conditions during a standard flight. The weights w_{ai} are chosen to yield adequate off-design performance without endangering the design one ($w_{a2} = 0.7$ and $w_{ai} = 0.15 \quad \text{for} \quad i = 1, 3$) and the weights w_b are equal to 1/3 so that no receiver is favoured in this objective.

To elaborate a proper basis for comparisons, constraints are formulated in terms of propeller net thrust and advance ratio at cruise condition. The values for thrust and power are obtained for a $4.5m$ equivalent propeller from the non-dimensional thrust and power coefficients. The advance ratio $J_{CR,2}$ is constrained to more than

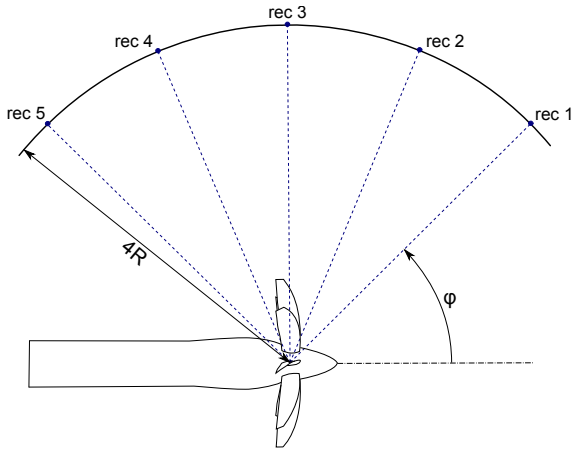

Figure 8.4: Location of the receivers ($\varphi = 45°$, $67.5°$, $90°$, $112.5°$ and $135°$).

	Take-off/Landing (kN)	Cruise (kN)
$T^{target}_{.,1}$	49.0	20.0
$T^{target}_{.,2}$	35.0	11.0
$T^{target}_{.,3}$	6.0	5.0

Table 8.3: Target thrusts $T^{target}_{.,j}$.

3.57 in order to limit the associated tip helical Mach number $M^{tip}_{CR,2}$ below 1.0 ($\Gamma^{J}_{CR,2}$-constraint):

$$\Gamma^{J}_{CR,2} = 3.57 - J_{CR,2} \tag{8.4}$$

Additionally, a thrust constraint is associated with each operating condition $J_{.,i}$ for both the cruise and take-off/landing sets with a tolerance Δ_T of $0.5kN$ for the cruise condition and of $1.5kN$ for the take-off/landing one. These constraints are formulated as

$$\Gamma^{T}_{.,j} = T^{target}_{.,j} - T_{.,j} - \Delta_T \tag{8.5}$$

so that negative values correspond to constraint satisfaction. The values $T^{target}_{.,j}$ are chosen so that a benchmark $4.5m$-propeller (see Fig. 8.5) is at least matched for any operating condition; these values are given in table 8.3. This benchmark propeller has no sweep, a semi-constant chord ($b/D = 0.15$ up to 75% radius) and is build with thin NACA 16 and 65 airfoil sections. It delivers $11kN$ thrust in cruise condition at $J_{CR,2} = 3.37$ ($M_{tip} = 1.03$) with an efficiency $\eta_{CR,2}$ of 0.68 and $35kN$ in take-off/landing condition at $J_{TO,2} = 0.95$ with an efficiency of 0.54. These thrusts and the corresponding power values are realistic for a medium-sized aircraft equipped with two or four propellers.

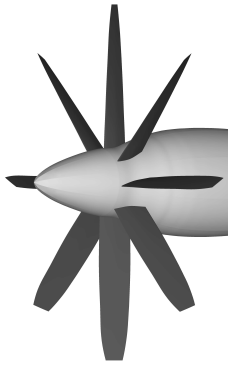

Figure 8.5: Benchmark propeller.

8.4 High-fidelity analysis workflow

Because the blade angles β_{ref} are fixed but different for the cruise and the take-off/landing conditions, and because the advance ratio $J_{.,2}$ is adapted separately as well, the high-fidelity analyses may be conducted concomitantly. The workflow for these analyses is illustrated in Fig. 8.6. At the end of each iteration, the 5 to 10 best individuals are submitted to the high-fidelity analysis; the number varies depending upon the distance between individuals and their location with respect to known individuals. For both conditions, the process starts by building the blade model from the design vector (see chapter 4) before generating a mesh. If the mesh does not satisfy basic quality measures (equi-size skew < 0.97, wrap $\neq 1$ and no left-handed faces), the mesh parameters are automatically adjusted. 18 adjusting sequences have been programmed. If no correct mesh is obtained despite those efforts, the process stops and the individual is considered as failed and is not registered to the database. If an acceptable mesh is obtained, the individual is passed to the CFD-solver. In the first run, $J_{CR,2}$ is chosen arbitrarily as the corresponding mean value of the DoE-database. To have a safe interval of the performance curve, which is necessary for precise adaption, $J_{CR,3}$ is taken as $J_{CR,2} + 0.3$ and $J_{CR,1}$ as $J_{CR,2} - 0.5$. At the end of the CFD-analysis, the non-dimensional performance values are computed. From these values, the thrust of an equivalent $4.5m$ propeller is calculated. If the thrust $T_{CR,2}$ does not match the target within the allowable interval $\pm\Delta_T$, a new advance ratio $J_{CR,2}$ is interpolated from the known performance. The CFD-analysis is then ran again with these new values though some computational time is saved by starting from the previous $J_{CR,3}$-solution. Once the CFD-solution is known for all advance ratios, the CHA-solver computes the SPL at all five receiver locations. A dedicated post-processor reads the data files written by both solvers and computes the desired non-dimensional performance values that are then written to a single performance file and registered in the database.

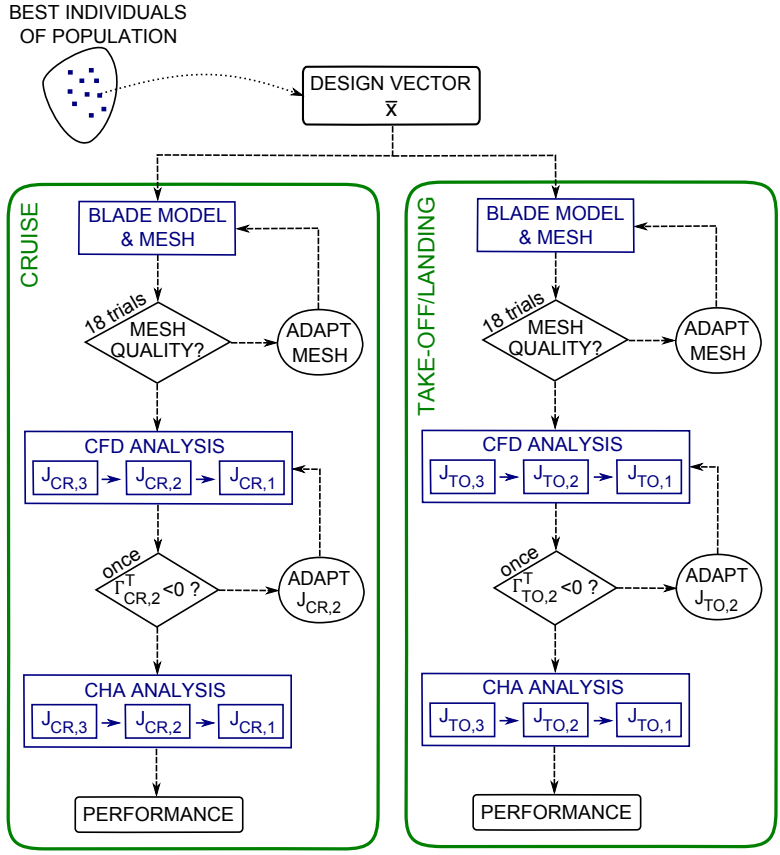

Figure 8.6: High-fidelity analysis workflow.

Chapter 9

Survey of the optimization process

9.1 DoE-database

As already described in section 8.2, the DoE-database comprised 81 individuals. The failure rate (i.e. the percentage of individuals for which no correct mesh could be generated or for which the CFD-analysis failed, either for the cruise or take-off/landing cases) is about 8.6%. Fig. 9.1 shows the radial distributions defining the geometry of the blades contained in the database. The non-dimensionalized objective values ($\hat{\Omega}$) of the individuals in the database, are shown in Fig. 9.2. The non-dimensionalization is achieved with respect to the respective maximum Ω-value among the DoE-database and the benchmark. As apparent from Figs. 9.1, 9.2(a) and 9.2(c), the database contains very diverse individuals in terms of geometry and Ω-values. The unswept benchmark, operating at a fairly low advance ratio $J_{CR,2}$ ($M_{tip} = 1.03$), is the most potent noise producer in the propeller plane. Interestingly, the 'band' distribution of Fig. 9.2(b) reveals some coupling between these two objectives.

Unfortunately, no individual from the database does satisfy all constraints simultaneously. The Γ-values for the database are shown in Fig. 9.3. For all constraints to be satisfied, an individual should have all its marks located in the lower left quadrant. From Fig. 9.3, it appears that the most stringent constraints are the first and second thrust constraints in the take-off/landing condition together with the constraint on the cruise advance ratio $\Gamma^{J}_{CR,2}$ (Eqn. 8.4).

9.2 Metamodel accuracy

The ANN-metamodels use non-dimensional values of each performance parameter. The performance values are non-dimensionalized and normalized with respect to a -10% offset from the lowest and a 10% offset from the highest values present among the database. For a performance parameter q, the normalized non-dimensional value

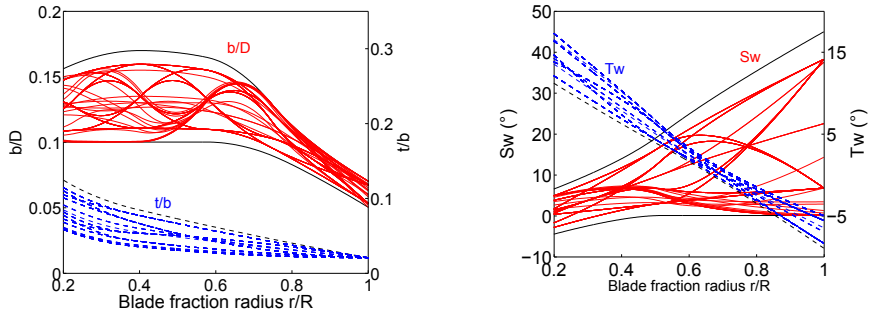

(a) Chord $(b(r)/D)$ and thickness $(t(r)/b(r))$.

(b) Geometrical sweep $(Sw(r))$ and twist $(Tw(r))$.

Figure 9.1: Planform definition of the individuals contained in the DoE-database.

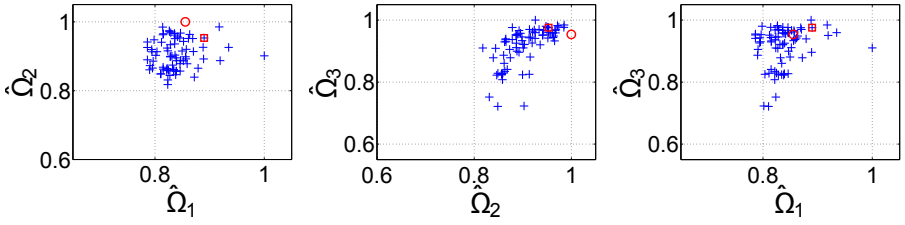

(a) (b) (c)

Figure 9.2: Normalized objective values in the DoE-database. ('+' for individuals - '□' for the central individual - '○' for the benchmark)

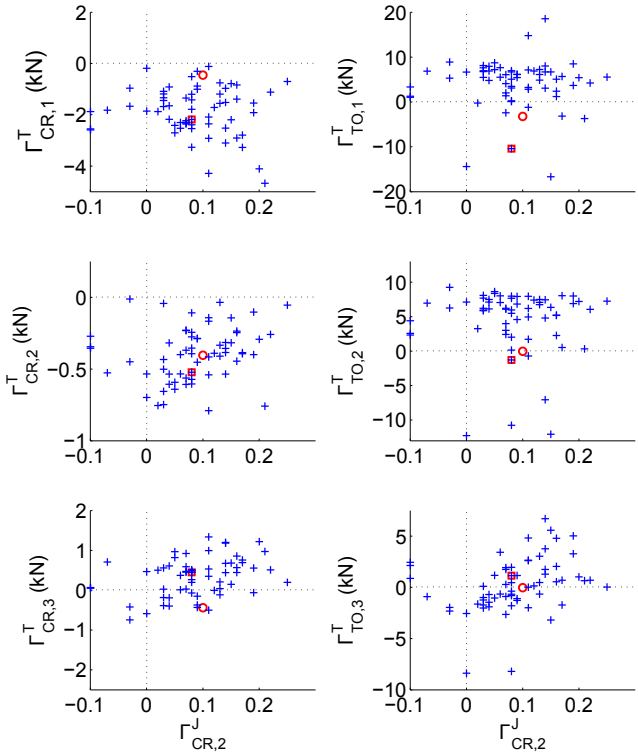

Figure 9.3: Constraint values in the DoE-database. ('+' for individuals - '□' for the central individual - '○' for the benchmark)

is written $\hat{q}$ if it is obtained by high-fidelity analysis and $\tilde{q}$ if it is the metamodel estimate. Figs. 9.4 and 9.5 present on the left-hand plots some normalized performance values versus their respective metamodel estimate. Ideally, all points should lie on the diagonal.

Interestingly, it is clear that the predictions of the cruise thrust $T_{CR,2}$ and SPL in the propeller plane $SPL^{rec3}_{CR,2}$ are more prone to errors. Though it should be born in mind that the scatter on $T_{CR,2}$ is on a narrow interval in terms of absolute values ($10.5kN$ to $11.3kN$). In the take-off/landing condition, the power $P_{TO,2}$ and the SPL in the propeller plane $SPL^{rec3}_{TO,2}$ are the most difficult performance parameters to estimate. For each parameter, the error on the metamodel prediction $\tilde{q} - \hat{q}$ obeys a normal distribution as is confirmed by the central normality plots[1] of Figs. 9.4 and 9.5. Superimposed on those plots is a line joining the first and third quartiles, it is extrapolated out to the ends of the sample to evaluate the linearity of the data because normally distributed data should lie on that line. Owing to the normality of the data, it is safe to compute the mean bias $\mu(\tilde{q} - \hat{q})$ and the standard deviation $\sigma(\tilde{q} - \hat{q})$ that are given in table 9.1 and shown on the left-hand plots of Figs. 9.4 and 9.5. The mean error is of the order of 3.5% to 9% except for the SPL. The standard deviation varies between 8 to 18% with the exception of the SPL. For the SPL, both the mean error and the standard deviation sky-rocket. Thence these values should be considered with greater care.

Given the 30 design variables and the strong interactions that exist between them when evaluating their influence on a performance parameter, most error values are satisfying. The ANNs clearly provide approximations that are safe to use to build an approximate image of the objective space, in which the search for optima occurs, but it is necessary to use the high-fidelity analysis tools to make major decisions. The disappointing values concerning the SPL corroborate an even higher level of interaction between distinct design variables. This is also confirmed by detailed analysis of the tonal sound [191].

	Take-off/Landing		Cruise	
	$\mu(\tilde{q} - \hat{q})$	$\sigma(\tilde{q} - \hat{q})$	$\mu(\tilde{q} - \hat{q})$	$\sigma(\tilde{q} - \hat{q})$
$J_{.,2}$	0.063	0.082	0.060	0.138
$T_{.,2}$	0.046	0.168	−0.035	0.092
$P_{.,2}$	−0.080	0.102	−0.091	0.176
$SPL^{rec3}_{.,2}$	−0.258	0.247	−0.134	0.266

Table 9.1: Mean bias μ and standard deviation σ of the error on normalized metamodel estimates.

[1] A normality plot displays the cumulative distribution function of the ordered values of $\tilde{q} - \hat{q}$ ('+') and that of a fitted normal distribution (straight line). Departures from the straight line indicate departures from normality.

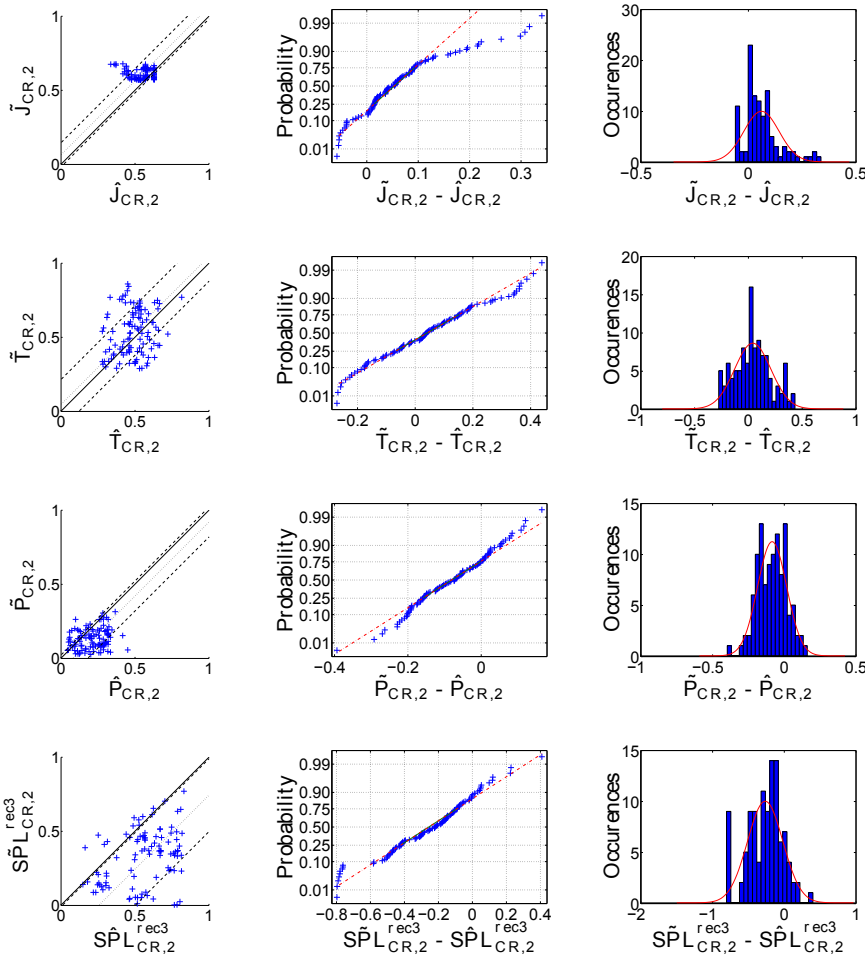

Figure 9.4: Metamodel accuracy, normality test and histogram with density for $\hat{J}_{CR,2}$, $\hat{T}_{CR,2}$, $\hat{P}_{CR,2}$ and $\hat{SPL}^{rec3}_{CR,2}$. For the metamodel accuracy, the mean error is shown by '...' and the standard deviation around the mean error by '---'.

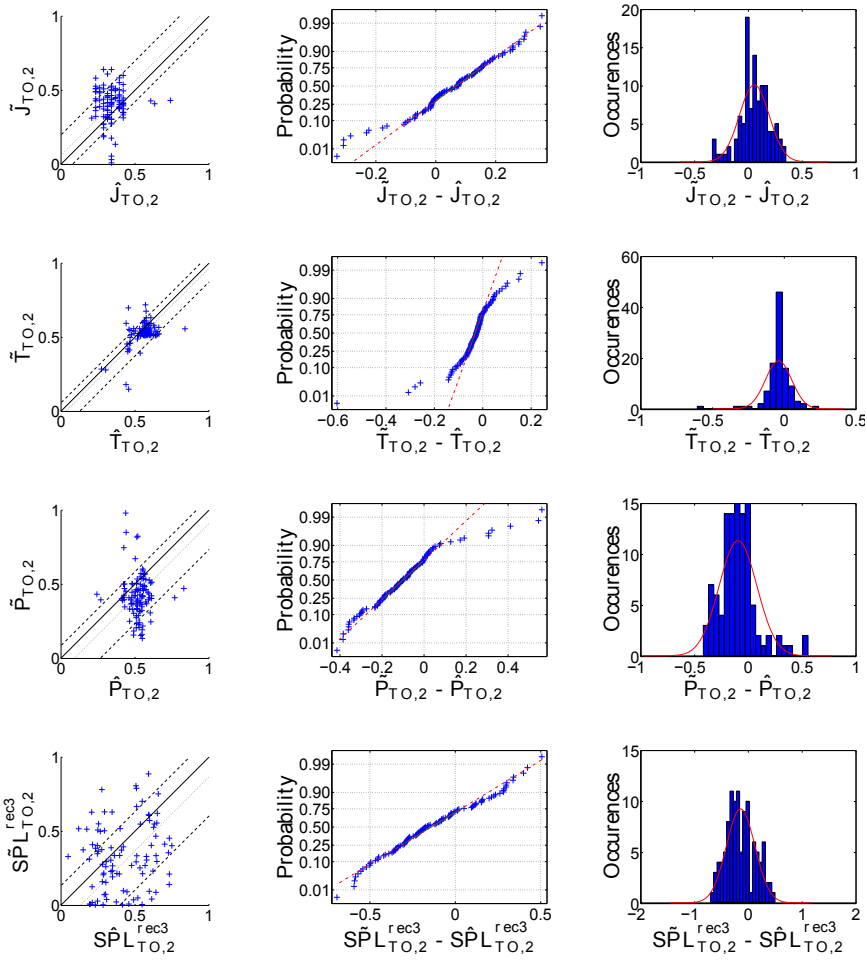

Figure 9.5: Metamodel accuracy, normality test and histogram with density for $\hat{J}_{TO,2}$, $\hat{T}_{TO,2}$, $\hat{P}_{TO,2}$ and $\hat{SPL}^{rec3}_{TO,2}$. For the metamodel accuracy, the mean error is shown by '...' and the standard deviation around the mean error by '---'.

9.3 Optimization results

The optimization process is spread over 36 iteration loops that resulted in a total of 1800 designs proposed at the end of the iterative loops. Of these, 252 were fed to the high-fidelity analysis. The limit on the number of iterations pertains mainly from cost and time constraints.

As is shown on Fig. 9.6, the optimization process effectively proceeded toward lower objective values in the three dimensions of the objective space built upon approximated values, in opposition to the real objective space resting upon the values obtained by high-fidelity analysis[2]. Of the 252 designs that were submitted to the high-fidelity analysis, only 119 were successfully processed through both the cruise and take-off/landing conditions. Their respective planform distributions are given in Fig. 9.7. The high failure rate (53%) is mostly the direct consequence of failures in the meshing step even though Fig. 9.7 suggests that the search space is not artificially restrained as the mesher is able to mesh very dissimilar geometries. This is nevertheless a serious limitation imposed by the mesher.

The fronts appearing on Fig. 9.6, correspond to the convergence within the generation loops toward the Pareto-front in the approximate objective space. A front is formed at each iteration because the training of the metamodels is done before each iteration loop, hence, each time, the optimum is sought after in a slightly different approximate objective space.

Despite the disappointing failure rate, the optimization resulted in 28 individuals that concomitantly satisfy all constraints; all of them were obtained in the last 10 iterations and are indicated on Fig. 9.6 to highlight the restrictions induced by the set of constraints. These individuals are located in the 3^{rd}-quadrant of the constraint values plots in Fig. 9.10. This figure clearly shows that the evolution proceeded from the DoE-individuals toward greater satisfaction of the constraints (negative Γ-values) along with higher advance ratios $J_{CR,2}$. The normalized objective values[3] of the 119 individuals are shown in Figs. 9.8 and 9.9 together with the original DoE-values. From both figures, the evolution toward lower Ω-values is apparent as well as the diversity present in the objective space. Regretfully, this rather limited set is probably not fully representative of the Pareto-front. But augmenting the cardinality of successfully analyzed individuals both by achieving a higher success rate and by conducting more iterations, would help in relieving this weakness. The comparison of Figs. 9.6 and 9.8 reveals also the influence of the metamodelling errors discussed in section 9.2. Indeed, the systematic underprediction of the power terms ($P_{.,i}$) and SPL terms ($SPL^{recj}_{.,i}$) leads to the corresponding objectives $\tilde{\Omega}$ being lower than $\hat{\Omega}$ so that the points in Fig. 9.8 are shifted in the positive direction along the three axes.

From Fig. 9.9(b), the Ω_2- and Ω_3-values appear to be strongly coupled. This is partly explained by the presence of the $SPL^{rec3}_{.,2}$ terms in Ω_3 though these account for only 1/3 of each summation (see Eqn. 8.3). Hence reducing the SPL in the propeller plane usually involves some reduction out of the plane as well.

The minimization of objective values led to a substantial improvement in cruise efficiency at $J_{CR,2}$ as is shown in Fig. 9.11(a). The 28 individuals satisfying all constraints are remarkably located in the upper-right region of the plot and are clearly

[2]If not mentioned, objectives and constraints are considered in their respective high-fidelity space.

[3]The same normalization factors as in section 9.1 are used.

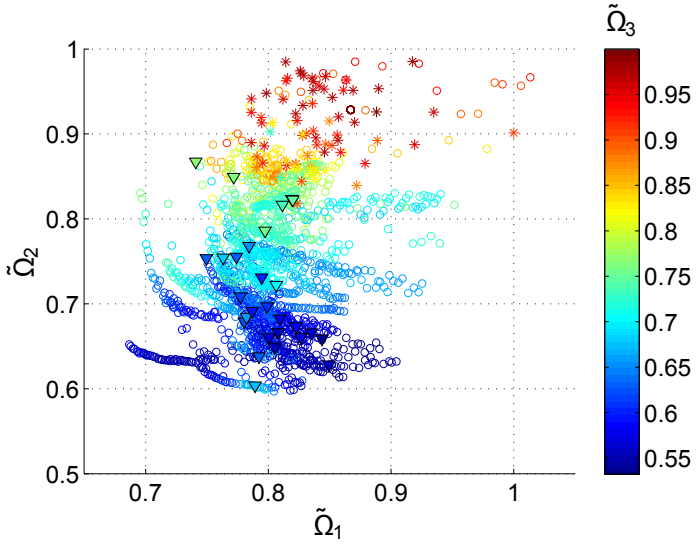

Figure 9.6: Pareto-front in the objective space built upon approximates. ('$\circ$' for individuals proposed by the optimizer after each iteration - '$*$' for the DoE-individuals - '$\triangledown$' for the individuals successfully evaluated by high-fidelity analysis and that satisfy all constraints concomitantly.)

at distance from the DoE-data. This is not the case for the take-off/landing condition which is not the driving factor behind the improvement in the Ω_1-value because of the relative weighting between the terms. This is the reason for the outlier of Fig. 9.11(b) (with $\eta_{TO,2} = 0.65$) to vanish among others in Fig. 9.9 as its cruise efficiency $\eta_{CR,2}$ is of the order of 0.7.

The planform definition of the 28 compliant individuals are given in Fig. 9.12. This figure shows that the diversity obtained in the objective space is stemming from the one present in the search space. This is certainly true for the chord and sweep distributions that exhibit varying and innovative features. As is visible in Fig. 9.12(b), a considerable subset of these individuals are relatively straight blades (i.e. they have no geometrical sweep at the tip). Remarkably, most blades are build upon thin airfoils and have strong twist toward the root while featuring minimal twist toward the tip. This is one of the numerous examples were the optimization procedure mimics the experience of designers. A detailed analysis of some of the best performing individuals will be given in the next chapter.

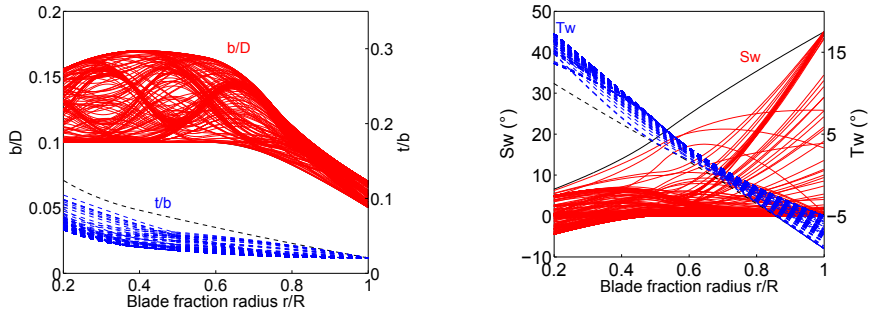

(a) Chord $(b(r)/D)$ and thickness $(t(r)/b(r))$.

(b) Geometrical sweep $(Sw(r))$ and twist $(Tw(r))$.

Figure 9.7: Planform definition of the 119 individuals processed through high-fidelity analysis (CFD and CHA solvers).

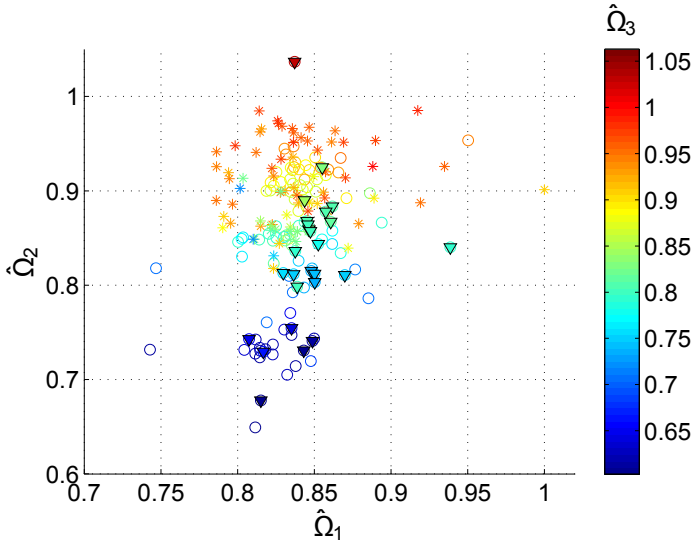

Figure 9.8: Pareto-front in the objective space built upon high-fidelity analysis. ('$\bigcirc$' for individuals successfully evaluated by high-fidelity analysis - '$\bigtriangledown$' for the individuals that satisfy all constraints concomitantly - '$*$' for the DoE-individuals.)

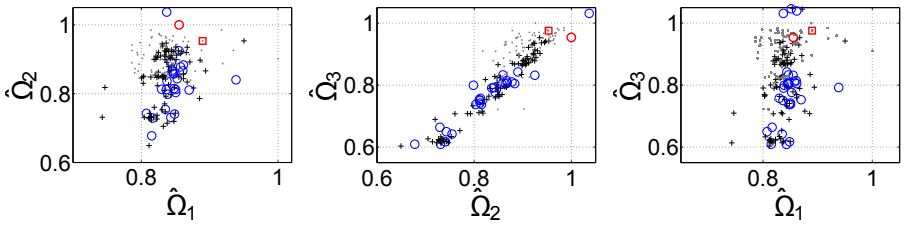

(a) (b) (c)

Figure 9.9: Normalized objective values of the individuals submitted to high-fidelity analysis. ('○' for individuals satisfying all constraints concomitantly - '+' for individuals that violate at least one constraint - '.' for the DoE-individuals - '□' for the central individual - '○' for the benchmark)

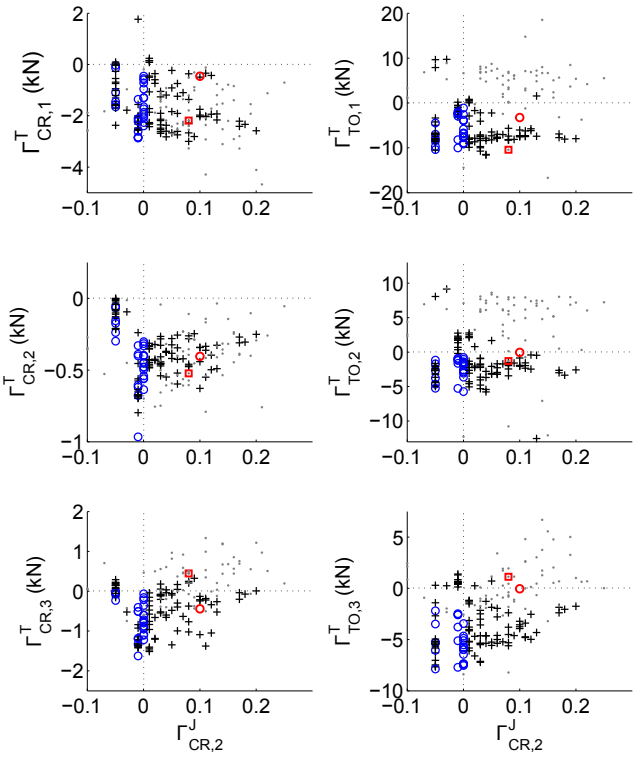

Figure 9.10: Constraint values of the individuals submitted to high-fidelity analysis. ('○' for individuals satisfying all constraints concomitantly - '+' for individuals that violate at least one constraint - '.' for the DoE-individuals - '□' for the central individual - '○' for the benchmark)

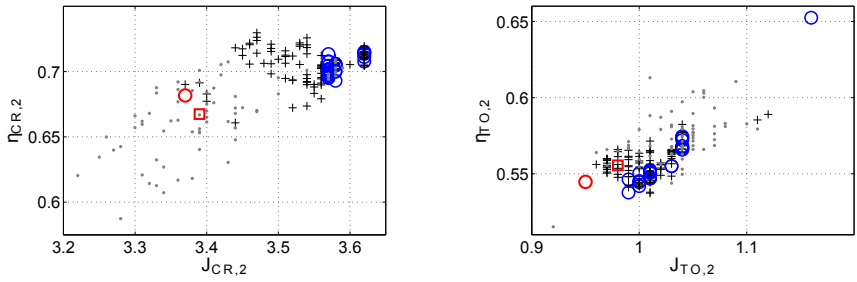

(a) Cruise efficiency $\eta_{CR,2}$.

(b) Take-off/landing efficiency $\eta_{TO,2}$.

Figure 9.11: Efficiency of the individuals submitted to high-fidelity analysis. ('○' for individuals satisfying all constraints concomitantly - '+' for individuals that violate at least one constraint - '.' for the DoE-individuals - '□' for the central individual - '○' for the benchmark)

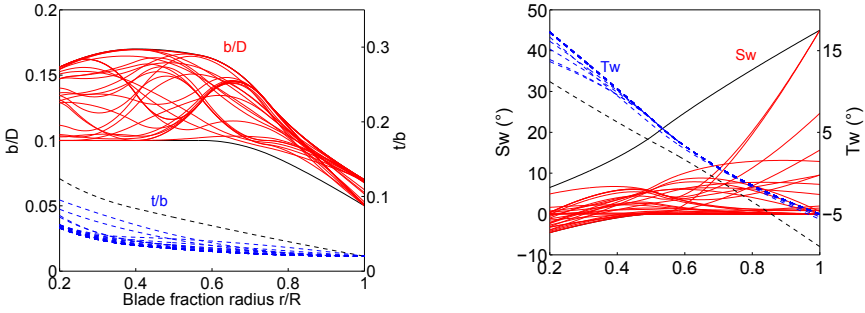

(a) Chord $(b(r)/D)$ and thickness $(t(r)/b(r))$.

(b) Geometrical sweep $(Sw(r))$ and twist $(Tw(r))$.

Figure 9.12: Planform definition of the 28 individuals that concomitantly satisfy all constraints.

Chapter 10

Analysis of specific individuals

The previous chapter was dedicated to the analysis of the optimization process itself and that of its gross results. In the present chapter, some promising blade designs will be analyzed in more details in order to assess the potential of the method and identify its likely downsides. In the end, conclusions about the present optimization are drawn.

10.1 Objective-values, constraint-values and geometries

Out of the individuals shown on Fig. 9.9 that satisfy all constraints , four are earmarked on Fig. 10.1 because of their low Ω-values:

1. individual A because it has the lowest $\hat{\Omega}_1$-value,
2. individual B because it has the lowest $\hat{\Omega}_2$-value,
3. individual C because it has the lowest $\hat{\Omega}_3$-value,
4. and individual D because it has also a low value for the $\hat{\Omega}_3$-objective.

Individuals A, B and C are of rank 0 whereas individual D is of rank 1. Their respective Γ-values are shown in Fig. 10.2 whereas their chord, thickness, twist and geometrical sweep distributions are given in Fig. 10.3. Individuals A and B have extremely low geometrical sweep combined with one or more humps consisting of strong spanwise variations of the chord. On the opposite, individuals C and D have high geometrical sweep combined with two distinct humps as clearly visible on Fig. 10.3. Noticeably, all four have thin airfoils and the highest possible twist distribution. The planform shape of those blades are visualized in Fig. 10.4.

It appears from table 10.1 that chord-variations toward the tip do not result in significant differences between leading-edge and geometrical sweep. Hence the tip of

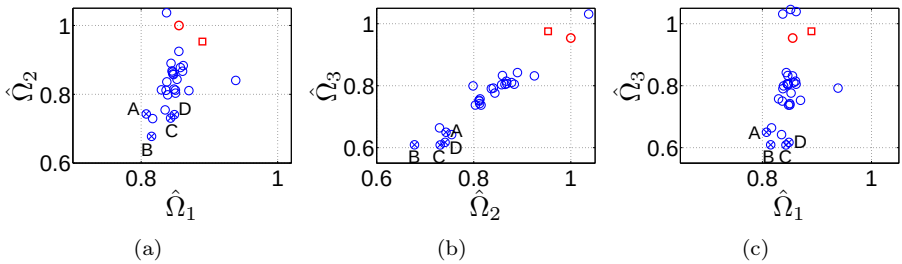

(a) (b) (c)

Figure 10.1: Normalized objective values of individuals A, B, C and D. ('○' for individuals satisfying all constraints concomitantly - '□' for the central individual - '○' for the benchmark)

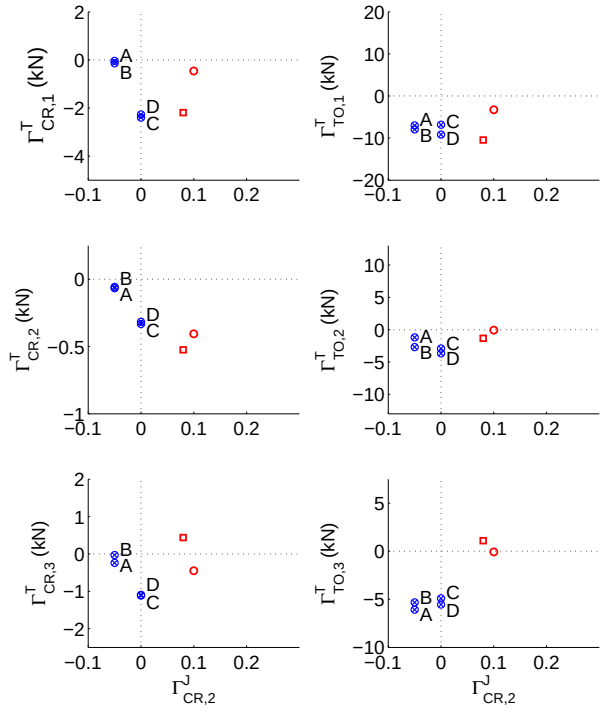

Figure 10.2: Constraint values of individuals A, B, C and D. ('○' for individuals satisfying all constraints concomitantly - '□' for the central individual - '○' for the benchmark)

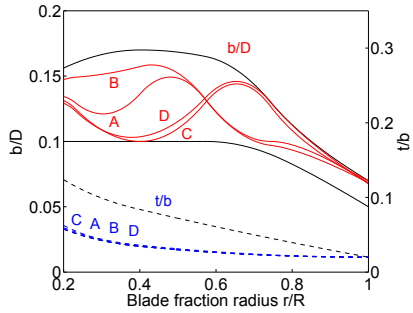

(a) Chord ($b(r)/D$) and thickness ($t(r)/b(r)$).

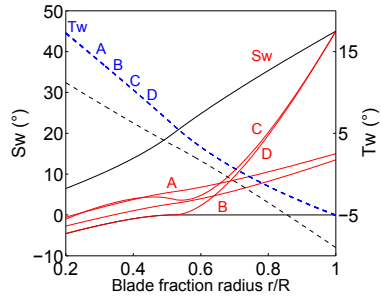

(b) Geometrical sweep ($Sw(r)$) and twist ($Tw(r)$).

Figure 10.3: Planform definition of individuals A, B, C and D.

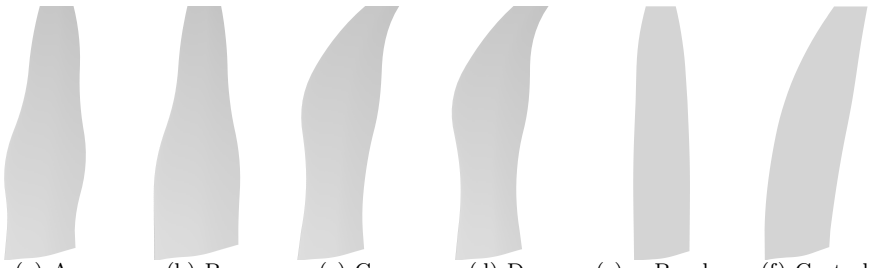

(a) A. (b) B. (c) C. (d) D. (e) Benchmark. (f) Central.

Figure 10.4: Blade geometry of individuals A, B, C and D with the benchmark and central individual.

Individual	A	B	C	D	Benchmark	Central
Sw_{LE}	13.8°	11.4°	45.6°	46.8°	17.0°	45.0°

Table 10.1: Leading-edge sweep (Sw_{LE}).

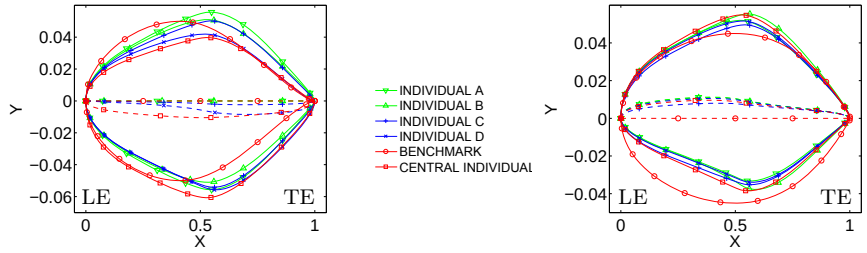

(a) Airfoil I used from blade root to 35% radius.

(c) Airfoil II used from 45% radius to blade tip.

Figure 10.5: Optimized airfoils. Note that airfoil I for the benchmark is a NACA 65-010CA and airfoil II is a NACA 16-009.

blades A and B is almost straight whereas blades C and D have a pronounced 'scimitar' shape which is mostly the consequence of their geometrical sweep distribution.

A comparison of the airfoils used for individuals A to D with the airfoils used for the central individual and the benchmark, is given in Fig. 10.5. The NACA 65-010CA and NACA 16-009 used respectively as airfoil I and airfoil II for the benchmark, have served in aircraft propellers for a long time. Indeed, these airfoils have sought after characteristics such as high lift-to-drag ratios over a wide range of lift coefficients, high critical Mach numbers and high maximum lift coefficients [67] on top of a considerable cross-sectional area near the trailing edge. The last feature is desirable for swept blades as it helps reducing the stresses in that critical region [303]. All optimized airfoils do have a nearly equal, for the inboard airfoil, or a smaller, for the outboard airfoil, cross-sectional area than these NACA-airfoils. As structural considerations are not considered in the present optimization, these airfoils might come with unacceptable stress-levels. Hence this is an argument to embed structural constraints in the optimization. Airfoils I tend to have thicknesses of the order of 10% to 12% against 10% for the NACA 65-010CA. The front part is usually thinner and the maximum thickness is moved aft. Except for individual D, there is almost no camber. Airfoils II have a maximum thickness of the order of 9%, like the NACA 16-009, and it is slightly moved aft. They have a noticeably flatter and more narrow front on the pressure side; a feature that is also reported in [189] for 2D airfoil optimization applied to propellers or in [175] for transonic airfoil optimization. It is a consequence of the increased camber with respect to the NACA 16-009.

	$\eta_{CR,1}$	Gain (%)	$\eta_{CR,2}$	Gain (%)	$\eta_{CR,3}$	Gain (%)
Benchmark	0.608	–	0.682	–	0.679	–
Central individual	0.607	0.0	0.667	−1.5	0.619	−6.0
Individual A	0.641	+3.7	0.715	+3.3	0.659	−2.0
Individual B	0.643	+3.9	0.714	+3.2	0.638	−4.1
Individual C	0.639	+3.1	0.702	+2.0	0.688	+0.9
Individual D	0.640	+3.2	0.704	+2.2	0.695	+1.6

Table 10.2: Propulsive efficiency η in cruise condition.

Individual	A	B	C	D	Benchmark	Central
$P_{CR,2}$ (kW)	3286	3287	3433	3415	3558	3674
Gain (%)	−7.6	−7.6	−3.5	−4.0	–	+3.3

Table 10.3: Power $P_{CR,2}$.

10.2 Aerodynamic characteristics

10.2.1 Overall performance

As is apparent from Fig. 9.11, the propulsive efficiency has globally increased in cruise and is maintained at take-off/landing. Gains of 2% to 3% (see table 10.2) are achieved at high Mach number for the optimized individuals. These are moderate gains and the obtained efficiencies are relatively low with respect to the achievable ones which are of the order of 0.75 for advanced conventional propellers operating at $M_\infty = 0.75$ (see Fig. 2.4). 1950's conventional propellers would deliver efficiencies just below 0.7 [247] in similar conditions. Advanced propfan concepts would achieve efficiencies of the order of 0.8 to 0.85, but they would operate at tip Mach numbers well above unity. The main reasons believed to be responsible for those moderate efficiencies are the limited number of iterations that were performed, the vast as well as raw search space and the high free stream Mach number. Fine tuning of the designs, essentially in terms of airfoil shape and twist distribution, might result into more significant gains.

The gains obtained at cruise are not matched at the design take-off/landing condition were they are much lower (table 10.4). Part of this can be explained by the weighting between both contributions in the Ω_1-objective. For off-design conditions, sweep is favourable when the rotational velocity is decreased (the advance ratio increased) at cruise but less in the take-off/landing case. On the other hand, no significant difference exists between swept and unswept individuals when the rotational velocity is increased in any condition. The central individual of the DoE-database is also given for reference purposes, despite the fact that it does not satisfy the $\Gamma^J_{CR,2}$- and both $\Gamma^T_{.,3}$-constraints.

Table 10.3 gives the power required at the design cruise condition ($P_{CR,2}$) for all individuals. Blades A and B offer the highest gains in terms of power. Nevertheless, the $3.5 - 4.0\%$ power decrease associated with blades C and D are quite significant.

The relative position of the optimized individuals with respect to the Ω_1-objective stems from the thrust and power coefficients (C_T and C_P) given in Fig. 10.6. The central individual has a higher C_P for nearly the same advance ratio as the benchmark both in the cruise and the take-off/landing conditions. This is the reason for its

	$\eta_{TO,1}$	Gain (%)	$\eta_{T0,2}$	Gain (%)	$\eta_{TO,3}$	Gain (%)
Benchmark	0.500	–	0.545	–	0.501	–
Central individual	0.511	+1.1	0.556	+1.1	0.406	−9.5
Individual A	0.503	+0.3	0.552	+0.7	0.616	+11.5
Individual B	0.509	+0.9	0.548	+0.3	0.622	+12.1
Individual C	0.510	+1.0	0.556	+1.1	0.597	+9.6
Individual D	0.500	+0.0	0.547	+0.2	0.600	+9.9

Table 10.4: Aerodynamic efficiency η in take-off/landing condition.

higher Ω_1-value resulting from a sub-optimal twist distribution with thicker airfoils. The optimized blades do not have significant differences at the design cruise condition ($J_{CR,2}$) in terms of C_T and C_P though they operate at different advance ratios than the benchmark. Globally, optimized blades operate at higher power coefficients as well as higher advance ratios hence higher efficiency. Swept blades (C & D) offer flatter efficiency curves resulting in better performance at off-design conditions. This is also the reason for their higher Ω_1 value. At take-off/landing, unswept blades (A & B) have lower C_P-values which explains their better Ω_1-value with the current weighting, albeit no substantial differences exist in terms of efficiency at $J_{TO,1}$ and $J_{TO,2}$.

10.2.2 Local features

The optimized airfoil shapes are presented in Fig. 10.5. The spanwise distributions of thrust and PTF are presented in Figs. 10.7 and 10.8. The elemental force coefficients in these figures are obtained by integrating the pressure and viscous forces acting on a spanwise blade element. The elemental thrust and the elemental PTF coefficients (C_{Tel} and C_{PTFel}) are defined as:

$$C_{Tel}(r) = \frac{T_{el}(r)}{1/2\rho_\infty u(r)^2 b_{ref}} \tag{10.1}$$

$$C_{PTFel}(r) = \frac{PTF_{el}(r)}{1/2\rho_\infty u(r)^2 b_{ref}} \tag{10.2}$$

where $u(r)$ refers to the local velocity (i.e. $u(r) = \sqrt{u_\infty^2 + (\omega r)^2}$) and b_{ref} is an arbitrarily chosen, constant, reference chord. Figures 10.9 and 10.10 give the respective pressure distributions at the cruise and take-off/landing design points ($J_{CR,2}$ and $J_{TO,2}$). The pressure coefficient C_p is computed as:

$$C_p = \frac{2}{\gamma M(r)^2}\left(p/p_\infty - 1\right) \tag{10.3}$$

where $M(r)$ refers to the local Mach number based on $u(r)$ and c_∞. These figures provide an explanation for some features found on the spanwise force distributions. Indeed, the poor pressure distributions for all individuals near the root explain the extremely low contribution from the root part of the blade (up to 50% radius) to the total thrust and suggest that additional efforts could be undertaken in this region.

Individuals A and B have similar traits, their respective airfoil II has a thinner front that leads, in cruise, to a moderate shock on the front part at 75% radius.

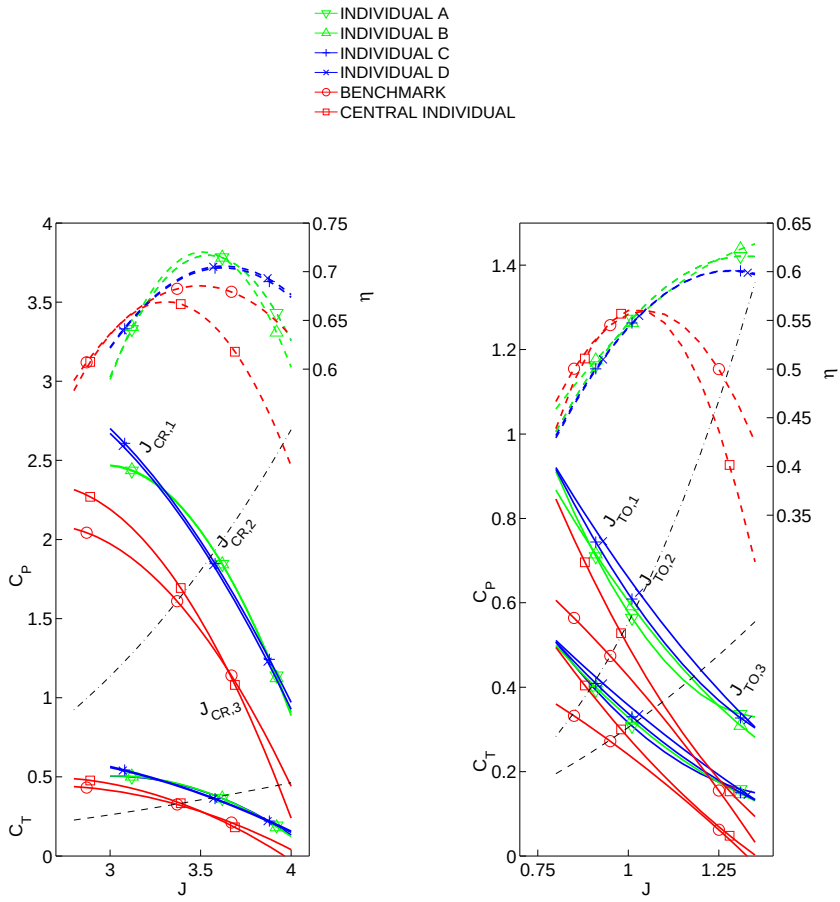

(a) Cruise condition ($M_\infty = 0.75$ and $\beta_{ref} = 63°$).

(b) Take-off/landing condition ($M_\infty = 0.2$ and $\beta_{ref} = 37°$).

Figure 10.6: Thrust and power coefficients (C_T and C_P) at design and off-design conditions with the corresponding efficiency η. The lines for constant thrust $T_{.,2}$ ('−−') and constant power $P_{.,2}$ ('−·') are based on the benchmark.

Then the flow accelerates before a second mild shock near the trailing edge. This is a different situation from the NACA 16-009 where a single shock is located on the aft part. At 99% radius, the shock is located close to the trailing edge and the flow gently accelerates upstream of it, leading to a favourable suction on the rear part. When comparing to the benchmark in cruise, the 99%-station has similar performance in therms of C_p and the 75%-station offers small improvement. At 25% (airfoil I) and 50% (airfoil II), very little thrust is generated. In take-off/landing conditions, the distribution of pressure at 25% radius results in virtually no thrust whereas thrust generation becomes effective at 50% radius. At 75% and 99% radius, the wavy character of the pressure distribution or the strong recompression for individual B, are related to the complex system of vortices as illustrated in Figs. 10.11(a) and 10.11(b). On these figures, the vortex system is visualized by the λ_2-criterion[1]. In particular, the spanwise vortex that is onset by the leading edge taper (which is due to the local change in chord $b(r)$), is responsible for strong spanwise currents that are characterized by locally high radial velocities. At 99%, the leading edge vortex connects to the blade tip vortex and that results in localized low pressures. The vortex system is also responsible for the perturbations in the spanwise thrust distributions of Fig. 10.8(a).

Individuals C and D have in contrast a pressure distribution at 50% radius both in cruise and at take-off/landing that results in a little more thrust for this portion. Most of the load is located near the leading-edge. Their somewhat poorer pressure distributions at 75% radius, is due to the presence of a rather strong shock on the forward section of the suction side in the cruise condition and an acute recompression in the take-off/landing condition. This results in poor thrust generation and is probably detrimental to efficiency. But the smooth pressure distributions at 99% radius in both conditions, translate into high local thrust. When comparing to the benchmark in cruise condition, the 75%-station has a worse pressure distribution whereas improvement is obtained at 99%-radius. In the take-off/landing condition, the recompression at 75% radius is obtained along a rather strong leading edge vortex that originates from the negative sweep obtained from the local changes in chord. This vortex, illustrated for both individuals in Figs. 10.11(c) and 10.11(d), remains attached to the leading edge unlike individuals A and B. In this condition, the section at 99% radius is fully immersed in the tip vortex flow so that a smooth pressure distribution is obtained in opposition to individuals A and B where the vortex system is responsible for recompressions. These results suggest that in all cases, additional efforts are required to yield better performance out of the root portion (airfoil I) whereas airfoil II is clearly a trade-off.

[1]The λ_2-method has been proposed by J. Jeong and F. Hussain [156]. Let $\nabla\overline{u}$ be the velocity gradient tensor of an incompressible fluid with its components $u_{i,j}$ (i.e. the i^{th}-velocity component differentiated with respect to the j^{th}-direction). The symmetric and antisymmetric parts of $\nabla\overline{u}$ may be written respectively as:

$$S_{ij} = \frac{1}{2}(u_{i,j} + u_{j,i}) \quad \text{and} \quad \Omega_{ij} = \frac{1}{2}(u_{i,j} - u_{j,i})$$

By neglecting viscous and unsteady effects, it can be shown that the tensor $S_{ij}^2 + \Omega_{ij}^2$ is proportional, with a negative factor, to the Hessian of the pressure p containing all second order spatial derivatives of p. Vortex cores are characterized by a local minimum in pressure so that its Hessian must be locally positive definite. Hence vortex cores are equivalent to a locally negative definite matrix $S_{ij}^2+\Omega_{ij}^2$. This last condition is met if two negative eigenvalues of $S_{ij}^2 + \Omega_{ij}^2$ occur thus if the second ordered eigenvalue (λ_2) is negative.

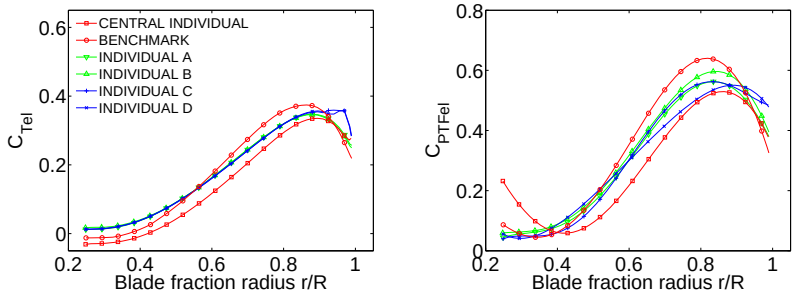

(a) Elemental thrust coefficient C_{Tel}. (b) Elemental PTF coefficient C_{PTFel}.

Figure 10.7: Spanwise elemental force coefficient distributions in cruise at $J_{CR,2}$.

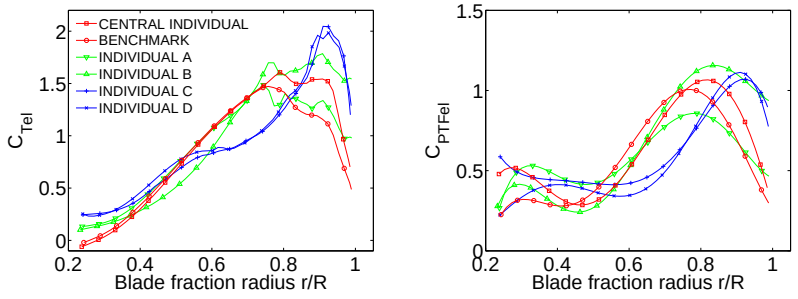

(a) Elemental thrust coefficient C_{Tel}. (b) Elemental PTF coefficient C_{PTFel}.

Figure 10.8: Spanwise elemental force coefficient distributions in take-off/landing at $J_{TO,2}$.

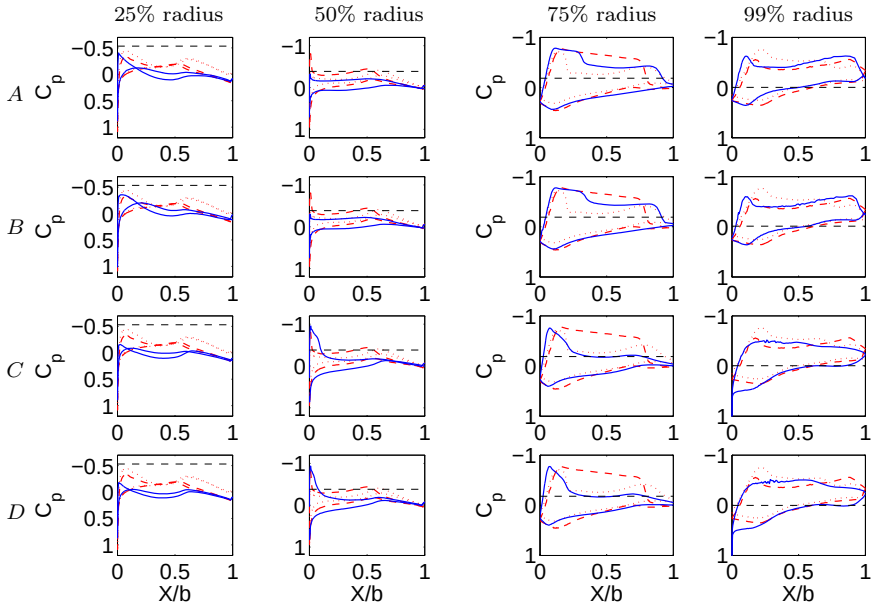

Figure 10.9: Pressure coefficients C_p at 25%, 50%, 75% and 99% radius for the cruise condition at $J_{CR,2}$ ('—' optimized individual, '– –' benchmark and '·····' central individual). The critical pressure coefficient $C_{p,crit}$ is indicated by '_ _'.

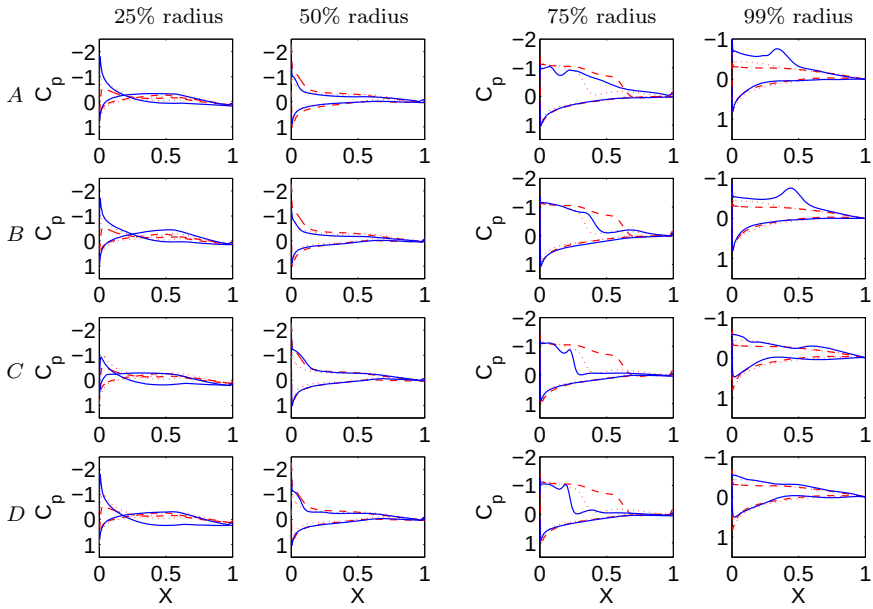

Figure 10.10: Pressure coefficients C_p at 25%, 50%, 75% and 99% radius for the take-off/landing condition at $J_{TO,2}$ ('—' optimized individual, '– –' benchmark and '·····' central individual).

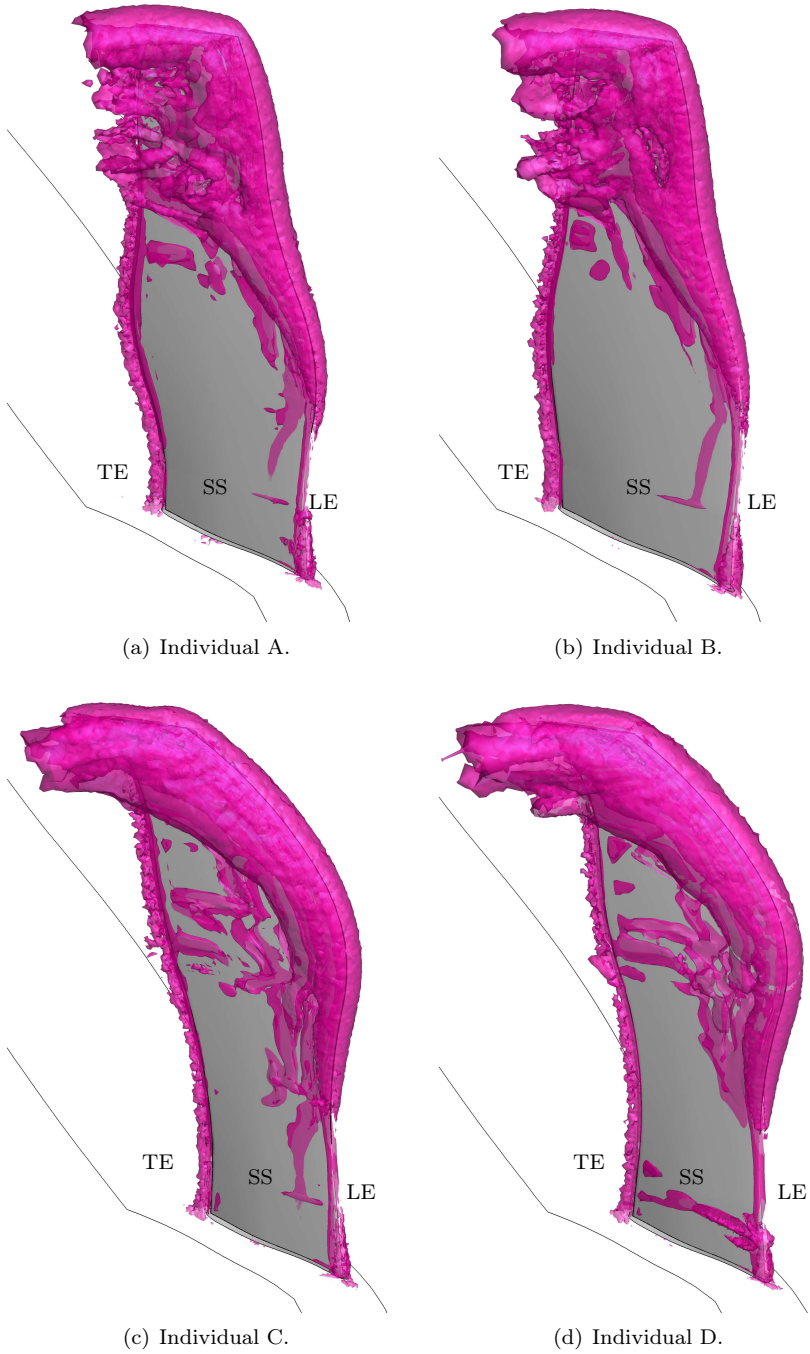

(a) Individual A.

(b) Individual B.

(c) Individual C.

(d) Individual D.

Figure 10.11: Vortex core visualization at $J_{TO,2}$ using iso-surfaces of λ_2 ($\lambda_2 < 0$).

10.3 Aeroacoustic characteristics

In terms of aeroacoustics, Fig. 10.12 shows the directivity plots at the Blade Passing Frequency (BPF) for all individuals at the design advance ratio of the cruise and take-off/landing design conditions ($J_{CR,2}$ and $J_{TO,2}$). As apparent from table 10.5 and Fig. 10.12, significant gains are achieved. Part of the gains of all individuals in the cruise condition are explained by higher advance ratios (hence lower helical tip Mach numbers)(from $J_{CR,2} = 3.37$ for the benchmark to values higher than 3.57 for the optimized individuals). This is the net result of the constraint on $J_{CR,2}$. This also implies that the truncation operator is only active for regions near the tip where M_r is likely to fall within the truncation range. It should be noted, however, that the results for the take-off/landing condition consider steady tonal sources only whereas unsteady sources might be significant contributors because of the low Mach number.

Fig. 10.12(a) also reveals major differences in terms of directivity in cruise condition: swept individuals (C and D) have a lower SPL in the propeller plane but radiate more effectively along the rotation axis. Additionally, they radiate more in the downstream direction than in the upstream one. These two features are also confirmed by the directivity pattern of the central individual (with 22.5° sweep).

Individuals A and B achieve important noise reduction too, although this result should be considered with some care as neglecting quadrupole noise for unswept blades operating in transonic flow could result in overprediction of the actual noise reductions [137, 106]. These individuals have a less loaded tip region (see Fig. 10.7) whilst the load is transferred to the 75% span where sound is less effectively radiated [137]. Similar beneficial effects of moving the load inboard have been found in [280, 75, 205]. Comparing to the benchmark and the central individual, the use of thinner airfoils also plays in favour of noise reduction.

The comparatively higher noise reduction obtained in the propeller plane for individuals C and D is the direct consequence of tip sweep which causes spanwise interferences known to be much more effective at high Mach numbers and close to the rotational plane [137]. Moreover, the more uniform pressure distribution at 99% radius, where sound is radiated more effectively, contributes to the reduction as well [137]. The negative sweep of individual D close to the blade root is believed to be the main reason for the difference in noise performance when compared to individual C. Indeed, except for the sweep at the root, the differences in geometry are minimal; nor do the spanwise loadings (see Fig. 10.7), airfoil shapes and pressure distributions exhibit significant dissimilarities. This sweep difference causes more noise at BPF in the upstream direction but less in the propeller plane for blade D.

Considering the take-off/landing condition, differences between individuals are much smaller (see table 10.5) and no substantial change in advance ratio is observed. Both swept propellers offer similar noise reductions in the rotational plane as do both unswept propellers. This agrees well with Hanson's conclusion that shape variations have less influence at low Mach numbers [137]. Moreover for this case, sweep does not lead to a significant advantage. Individuals C and D emit more noise because they are more heavily loaded near the tip (see Fig. 10.8). Despite the auspicious distribution with low tip loading, the benchmark emits more noise than the optimized individuals mainly because of the lower advance ratios, but also because of thicker airfoils and wider chord. The advance ratio is known as the most potent factor, together with the number of blades, influencing propeller noise [201]. Individuals A and B have

	Take-off/Landing		Cruise		
	SPL	Gain (dB)	SPL	Gain (dB)	M_{tip}
Benchmark	104.1	–	131.0	–	1.0253
Central individual	106.3	+2.2	120.7	−10.3	1.0225
Individual A	100.3	−3.8	120.3	−10.7	0.9930
Individual B	99.7	−4.4	119.2	−11.8	0.9930
Individual C	102.7	−1.4	117.3	−13.7	0.9990
Individual D	102.4	−1.7	114.3	−16.7	0.9990

Table 10.5: SPL at BPF for receiver 3 in the design condition ($J_{.,2}$) and helical tip Mach number in the design cruise condition ($J_{CR,2}$).

very low noise emissions at the take-off/landing condition, where quadrupole noise is likely negligible. As the chord distribution is the major difference (except for the airfoil shapes) between individuals A, B and the benchmark; the 'humpy' shape of individuals A and B explains at least partly their surprising performance in this condition. It is the author's belief that destructive interferences occur for the sound emitted at different spanwise locations thanks to the hump.

Analysis of Fig. 10.13 discloses another aspect of the sound emitted in the propeller plane. These results do not indicate any better noise reduction at higher harmonics neither by sweep nor by humps in cruise condition. In contrary, the reduction of SPL at the BPF and in some cases at the first BPH, comes with an increase at higher harmonics. At low Mach number, all optimized individuals exhibit a strong SPL at the BPF and the first harmonic. But they offer significant decrease for higher harmonics. As for this condition, no significant change in advance ratio is observed, the sweep and/or humps are most probably responsible for the differences with the benchmark.

The time signals for thickness, loading and total noise perceived at receiver 3 in the cruise condition at the design advance ratio $J_{CR,2}$ are given in Fig. 10.14. From that figure, it appears that loading noise is the dominant source in all cases. For the swept individuals, the characteristic leading edge spike in the thickness noise is faded; a feature known to be related to sweep [45, 18]. Additionally, strong interaction with loading noise results in efficient total noise reduction. This is the opposite situation to individual B for which thickness noise has constructive interference with the loading noise signal. As can be observed for the benchmark and the central individual, a higher tip Mach number essentially results in more amplitude for the thickness noise pulse.

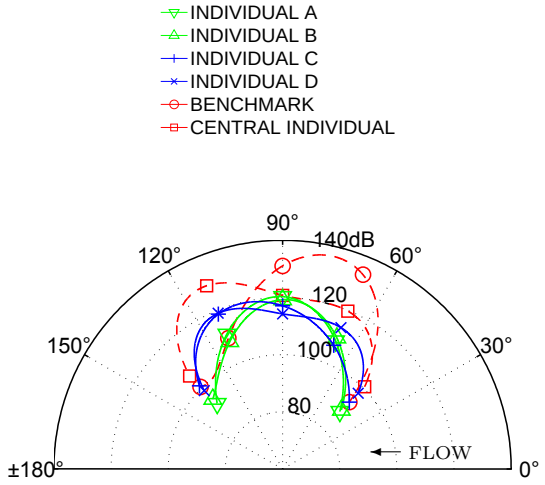

(a) Directivity in cruise condition at $J_{CR,2}$.

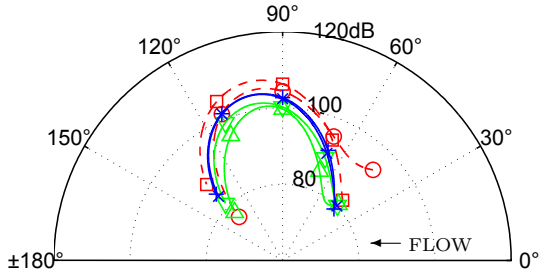

(b) Directivity in take-off/landing condition at $J_{TO,2}$.

Figure 10.12: Directivity plots based on the SPL at BPF.

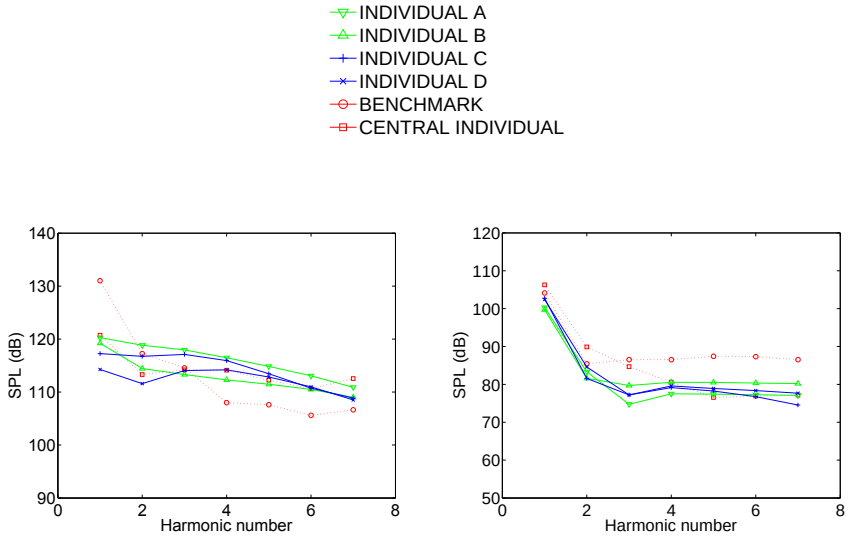

(a) Cruise condition at $J_{CR,2}$.

(b) Take-off/Landing condition at $J_{TO,2}$.

Figure 10.13: Envelope of the BPF-harmonics in the propeller plane (receiver 3).

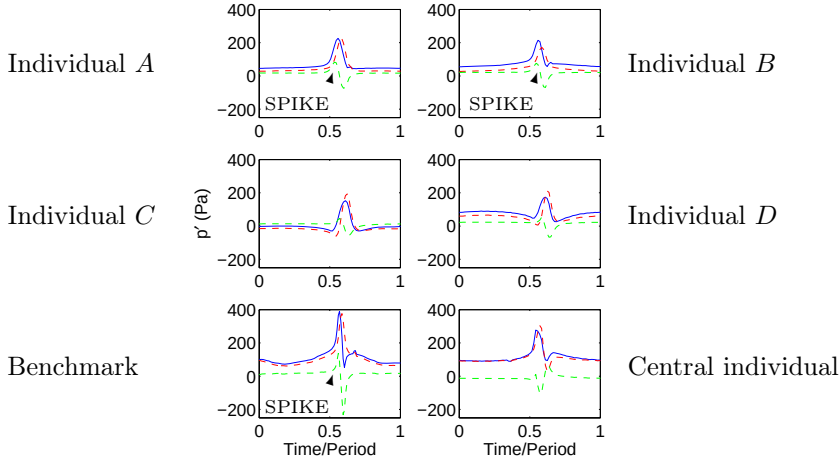

Figure 10.14: Time signal for receiver 3 in cruise condition with $J_{CR,2}$ ('——' Total noise - '– –' Thickness noise - '– –' Loading noise).

10.4 Conclusions

At this point, it is important to draw general conclusions about the bi-disciplinary optimization presented in the present part. The search resulted in successful designs that satisfy all constraints and offer some increase in efficiency as well as a considerable decrease in tonal noise. The obtained efficiencies are within the expected values for propellers operating at $M_\infty = 0.75$ were propeller efficiency traditionally drops (see Fig. 2.4). Through the optimization, innovative designs, in particular in terms of chord distribution, were trialled. It should be reminded that the optimization has been prematurely stopped mainly for time and cost considerations, and not because it was fully converged (i.e. if no additional improvement had been obtained for some iterations). So it is rather a proof of concept and served as preparatory work for building up experience before starting the true multidisciplinary optimization that will be presented in the next part.

In the end, the promising designs are shown on a comparative radar chart such as Fig. 10.15. This kind of chart represents the pros and cons of each design in a synthetic way, thereby allowing the design team to take the appropriate decisions. Figure 10.15 reveals how unswept designs came out of the evolutionary process thanks to better cruise efficiency, low out-of-plane SPL at cruise and low SPL in take-off/landing conditions. Swept individuals offer mainly the advantage of a low in-plane SPL at cruise.

- As far as the optimization process itself is concerned, the results validate the two-level approach discussed in section 3.4. The use of a metamodel, in this case an ANN, helps in driving the evolutionary process toward designs worth of interest, at a much lower cost than would have been the case if the performance was estimated for each individual of any population by a high-fidelity analysis solely. The recurrent use of an updated database is an efficient way to keep the error between a performance estimate by the metamodel and its value obtained by high-fidelity analysis, within acceptable margins. This recursive training is essential to augment the chances that an optimal design in the space of the approximate objectives is at least nearly optimal in the space of the real objectives. Unexpectedly, a high failure rate of the high-fidelity analysis was observed and is mostly related to meshing issues. So, additional logic has to be developed to cope with this situation.
- Given the 119 designs that were successively evaluated with the high-fidelity analysis tools, the fact that only 28 (23.5%) are compliant is the unpleasant consequence of the use of a metamodel. Its inability to deliver approximations that are extremely close to the real value means that a large amount of designs are either wrongly assessed (for 76.5% of the 119 individuals) or wrongly discarded during the evolutionary process.
- The examination of the objectives (defined in Eqns. 8.1-8.3), suggest that the Ω_3-objective is highly linked to its Ω_2-counterpart. Hence diminishing the noise in the propeller plane is an efficient way to diminish the sound out of that plane at the same time. Though the directivity of highly swept designs suggests that some consideration should best be given to out-of-plane points as well. For these reasons, both objectives could be blended into a single one without loss of information. It is also clear from the analysis that having a multi-point

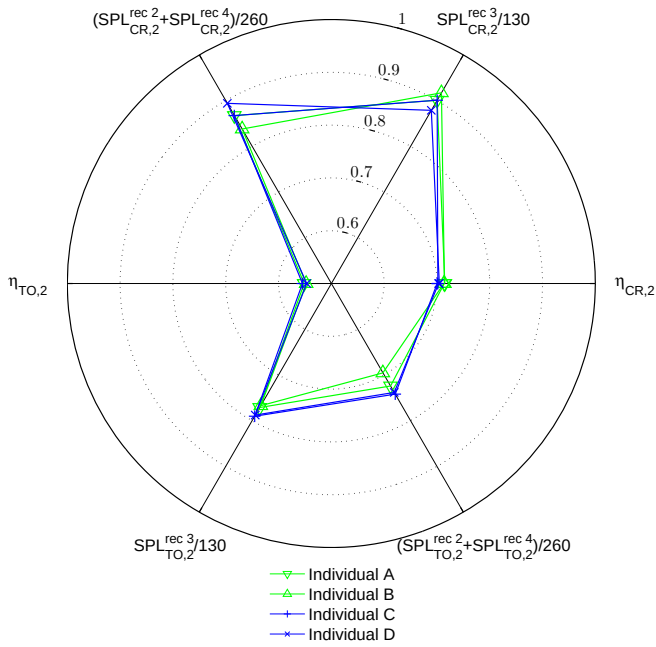

Figure 10.15: Decision chart.

optimization is essential as it guarantees the preservation of correct off-design performance and allows for a true matching of the desired thrust. This should be paramount over the increase in computational cost.

- The Ω_1-objective was formulated in terms of power P. A lower power P at fixed thrust T and free-stream velocity u_∞ implies a higher net efficiency η. The optimized designs all have a lower power requirement than the benchmark though the efficiencies are somewhat disappointing. Unfortunately, it has been found that the tolerance Δ_T on the target thrust plays an important role in this phenomenon. Indeed, all individuals have a lower power P but some generate a lower thrust T too (i.e. $T \in \left[T^{target} - \Delta_T, T^{target}\right[$). Hence the efficiency is not always substantially increased.

- One drawback of the workflow described in section 8.4 is that the design cruise and take-off/landing conditions do not correspond to the same RPM. This is because of the adaption on $J_{CR,2}$ and $J_{TO,2}$ under fixed blade angle β_{ref} to match the respective thrust $T_{.,2}^{target}$. In real-world applications, the RPM would be prescribed by cruise conditions and the blade angle $\beta_{ref,TO}$ adjusted, not the RPM, during the take-off/landing phase. The choice of a fixed β_{ref} at take-off was made for two reasons. First, changing the blade angle would imply the elaboration of a fresh mesh for that new case. This is a computationally more intensive process than just changing some simulation parameters in the CFD-solver. Moreover, this process might reveal to be tedious as a very high sensitivity to the blade angle was experienced during the development of the automated meshing scheme. Second, as an approximation of the performance curve is known, thanks to the three advance ratios, it is rather easy to estimate which advance ratio would deliver the proper thrust.

- Given the poor performance of the inboard portion of the blades, even though this is a traditional feature of propellers, the allowable margins for the twist and thickness distributions should be adjusted in accordance. Hence further optimizations should allow for thicker airfoils and more blade twist near the root.

- Four individuals were earmarked because of their attractive performance. Interestingly, two of them have high sweep toward the tip while the other two are straight blades. All of them feature rather abrupt changes in chord width that result in observable humps in the planform shape. These humps are associated with local leading edge sweep.

  From the aerodynamic point of view, these four individuals have better performance at the design cruise condition while delivering the required thrust at the off-design working points. Furthermore, the efficiency is increased at most operating conditions and the power is decreased. Straight-bladed individuals have lower power requirements than swept ones.

  From the aeroacoustic point of view, all four individuals achieve an overall noise reduction. This reduction stems from an increase in advance ratio combined with the beneficial effects of sweep for the swept designs or with an inboard shift of the load distribution for the straight designs. The unswept individuals also gained some advantage out of their radiation pattern that have lower lobes along the flight direction. Nevertheless, these individuals would be penalized

were quadrupole noise taken into account, because their straight tip does not help in relieving the transonic compressibility effects arising there.

It is somehow reassuring, to notice that the recipes that came out of the automated optimization procedure to decrease the total noise are all in perfect agreement with the parametric studies published in the literature. This is a striking observation and gives significant confidence in the possibilities of the present optimization method.

Part III

Aerodynamic, Aeroacoustic and Aeroelastic Optimization

Chapter 11

Optimization set-up

In this part, a multidisciplinary optimization is presented. As will be discussed later in this chapter, it includes objectives related to the aerodynamic, aeroacoustic as well as aeroelastic performance. This optimization takes into account the conclusions drawn from the bi-disciplinary optimization presented in the previous part.

For the purpose of clarity, this part shares the same organization as the previous one and the differences are highlighted. The optimization tools described in part I are again first assembled together. This is presented in the present chapter along with newly defined parameters, objectives and constraints. Next, chapter 12 focuses on the analysis of the optimization process itself, from the composition of the DoE-database to the last population. In that chapter, the accuracy of the metamodel is also discussed. In the end, a thorough analysis of the aerodynamic, aeroacoustic and aeroelastic characteristics of some promising designs is given in chapter 13.

11.1 Design variables

Table 11.1 gives an overview of the geometry parameters together with the number of design variables assigned to each of them. The set is identical with the one used in part II and 3^{rd} order b-spline interpolation is again used to compute $x(r)$ from the ordinates x_i of the control points. These points may fluctuate over respective intervals as shown in Fig. 11.1. In general, these intervals offer the same freedom as in the previous part but the inboard portions of the chord (b/D) and twist (Tw) distributions have been modified in accordance with the conclusion drawn in section 10.4. The hope is to gain more thrust from the inboard portion of the blades. Additionally, the allowance for zero sweep at the tip has been removed so that final designs have at least some sweep near the tip. The ranges concerning the airfoil shapes are given in Fig. 11.2. These ranges differ mainly from those of section 8.1 by:

- the reduced range for the 2^{nd} control point for the thickness of airfoil I,
- the allowance for more camber and the restriction on the possibility for negative camber for airfoil I,

Variable		Number of Control Points	Number of Design Variables	
Chord length	$b(r)/D$	7	7	
Thickness ratio	$t(r)/b(r)$	4	3	
Sweep	$Sw(r)$	4	4	
Twist	$Tw(r)$	4	3	
Airfoil I thickness	t_A	6	5	[a]
Airfoil I camberline	y_A	4	2	
Airfoil II thickness	t_B	6	5	[b]
Airfoil II camberline	y_B	4	1	
Total			30	

[a] from blade root to 35% radius
[b] from 45% radius to blade tip

Table 11.1: Geometry parameters and design variables.

- the allowance for more thickness at the leading edge and on the front part of airfoil II,
- the possibility for zero camber and the maximum camber for front part of airfoil II.

The eight-bladed, scaled propeller is $1m$ in diameter as well. The blade angle (β_{ref}) is kept at 63° for the cruise condition though this time, it is adapted for the take-off/landing condition (see section 11.3) so that the desired thrust is obtained at the same rotational velocity as in the cruise condition.

11.2 Optimizer architecture and set-up

The lay-out of the optimization code, shown in Fig. 11.3, is now completely identical to the architecture described in section 3.4 as all high-fidelity analysis tools are included. The DoE-database comprised again 64 individuals chosen by fractional factorial sampling augmented by the central individual and a set of 20 random designs. For this optimization, an off-line trained kriging-metamodel (see section 3.3.5) is used in the hope to reduce the metamodelling error. The weighting factor F and the cross-over constant C of the MODE-optimizer (see section 3.2) are both chosen as 0.8. This is another choice that is compliant with the recommendations in [278]. The evolutionary process is spread on 1000 generations between two successive iterations. The population size is 50 of which between 10 and 7 individuals are submitted to the high-fidelity analysis at the end of each iteration.

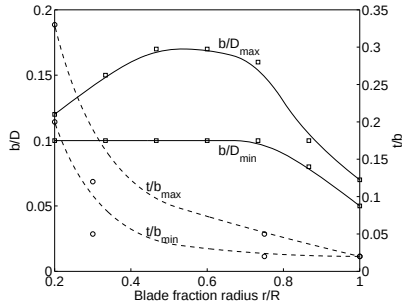

(a) Chord ($b(r)/D$ - □) and thickness ($t(r)/b(r)$ - ○).

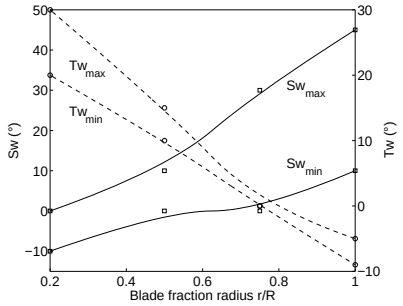

(b) Geometrical sweep ($Sw(r)$ - □) and twist ($Tw(r)$ - ○).

Figure 11.1: Minimum and maximum ordinates of the control points for the blade distributions together with the corresponding distributions.

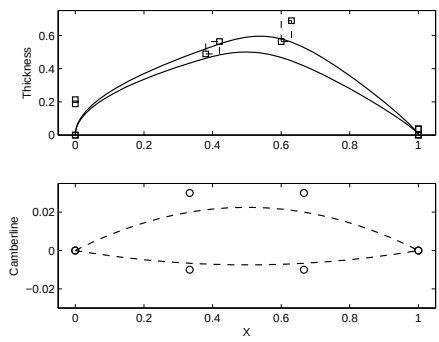

(a) Airfoil *I*.

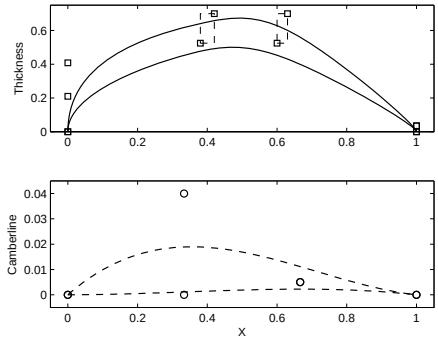

(b) Airfoil *II*.

Figure 11.2: Minimum and maximum ordinates of the control points for the airfoils together with the corresponding thickness-line and camberline.

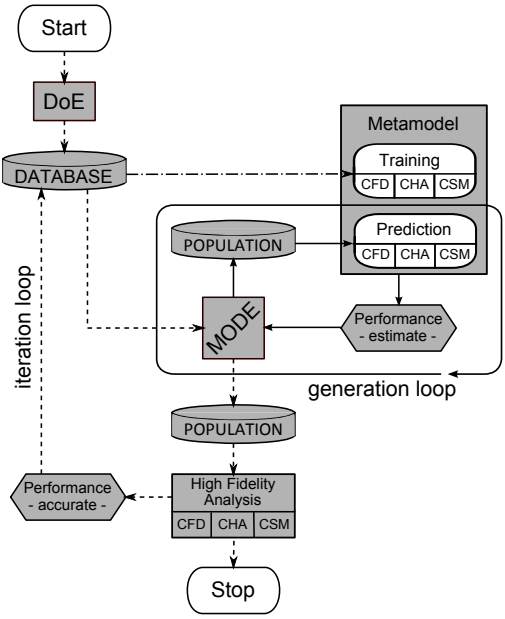

Figure 11.3: Layout of the optimization code used for the present optimization.

11.3 Operating conditions, objectives and constraints

Here again, 2 operating conditions with 3 advance ratios each, are used for this multi-objective and multi-point optimization. $J_{CR,2}$ is adapted to match the constraint on minimum cruise thrust $T_{CR,2}$ with β_{ref} fixed, while $J_{CR,1}$ and $J_{CR,3}$ are at a fixed distance from $J_{CR,2}$ ($J_{CR,1} = J_{CR,2} - 0.4$ and $J_{CR,3} = J_{CR,2} + 0.3$). This time for the take-off and landing condition at low Mach number, $J_{TO,2}$ is not adapted anymore to match the constraint on minimum take-off thrust $T_{TO,2}$ at fixed $\beta_{ref,TO}$. As proposed in section 10.4, the operating RPM (fixed by the engine-gearbox arrangement) is kept constant so that $J_{TO,2}$ is now computed from $J_{CR,2}$ by

$$J_{TO,2} = J_{CR,2} \frac{u_{\infty,TO}}{u_{\infty,CR}} \tag{11.1}$$

and the thrust $T_{TO,2}$ is matched by adjusting the blade angle $\beta_{ref,TO}$ (see section 11.4). $J_{TO,1}$ and $J_{TO,3}$ are again at a fixed distance from $J_{TO,2}$ (-0.2 and $+0.2$ respectively). These distances proved to be sufficient while avoiding the situation where some blades are in brake or windmill operation at $J_{TO,3}$. The external operating conditions corresponding to cruise are different from those used in part II in that the free-stream Mach number M_∞ has been reduced to 0.7 so that better efficiencies can be obtained whilst operating in the subsonic tip-speed domain. These conditions and the take-off/landing ones are summarized in table 11.2.

	Take-off/Landing	Cruise
ISA altitude (m)	0	10665
ρ_∞ (kg/m^3)	1.225	0.380
T_∞ (K)	288.15	218.81
M_∞	0.2	0.70
$Re_{b,ref}$	1.44e06	1.06e06

Table 11.2: Operating conditions. The Reynolds number $Re_{b,ref}$ is based on mean conditions at 75% radius.

Each discipline has its own objective in the present approach. It consists in a weighted sum of specific performance under various operating conditions. This time, the aerodynamic objective is built upon the efficiency instead of the power. This is to circumvent the possible effect of slight changes in thrust due to the tolerance Δ_T. The two objectives of section 8.3, concerning the SPL, respectively in and out of the rotational plane, are now blended into a single objective because they turned out to be highly correlated. For this aeroacoustic objective, the receivers are located at the same positions as in Fig. 8.4. Finally, an aeroelastic objective is incorporated. The system of objectives is now:

1. an aggregate of the propeller net efficiency at the three advance ratios both in the cruise and take-off/landing conditions (Ω_1),
2. an aggregate of the Sound Pressure Level (SPL) in and out of the propeller plane (at receivers 2, 3 and 4) both in the cruise and take-off/landing conditions (Ω_2),
3. and an aggregate of the blade total mass, maximum Tsai-Wu criterion value for the shell and maximum normalized von Mises equivalent stress value in the core, respectively at the three advance ratios both in the cruise and take-off/landing conditions (Ω_3).

This yields the system

$$\Omega_1 = w_{CR}\left(\sum_{i=1}^{3} w_{ai}\eta_{CR,i}^{-1}\right) + w_{TO}\left(\sum_{i=1}^{3} w_{ai}\eta_{TO,i}^{-1}\right) \tag{11.2}$$

$$\begin{aligned}\Omega_2 = {} & w_{CR}\left(\sum_{j=2}^{4}\sum_{i=1}^{3} w_{bij} SPL_{CR,i}^{rec\ j}\right) \\ & + w_{TO}\left(\sum_{j=2}^{4}\sum_{i=1}^{3} w_{bij} SPL_{TO,i}^{rec\ j}\right)\end{aligned} \tag{11.3}$$

$$\begin{aligned}\Omega_3 = {} & w_m m + \left[w_{CR}\left(\sum_{i=1}^{3} w_{ci}\zeta_{CR,i}^{TW}\right) + w_{TO}\left(\sum_{i=1}^{3} w_{ci}\zeta_{TO,i}^{TW}\right)\right] \\ & + \left[w_{CR}\left(\sum_{i=1}^{3} w_{ci}\zeta_{CR,i}^{VM}\right) + w_{TO}\left(\sum_{i=1}^{3} w_{ci}\zeta_{TO,i}^{VM}\right)\right]\end{aligned} \tag{11.4}$$

in which the weights w_{CR} and w_{TO} are chosen arbitrarily as 0.75 and 0.25 respectively to correspond to the relative time spent in these conditions during a standard

	Take-off/Landing (kN)	Cruise (kN)
$T^{target}_{.,1}$	48.0	18.5
$T^{target}_{.,2}$	35.0	11.0
$T^{target}_{.,3}$	12.5	5.0

Table 11.3: Target thrusts $T^{target}_{.,j}$.

flight. The weights w_{ai} are chosen to yield adequate off-design performance without endangering the design one ($w_{a2} = 0.7$ and $w_{ai} = 0.15 \quad \text{for} \quad i = 1, 3$). The weights w_{bij} are equal to 1/3 so that no receiver is favoured in this objective. The weights w_{ci} are also set to 1/3 as the blade must be structurally sound at all conditions while the purpose of w_m, which is based on the mass of the central individual, is to scale this term to values close to 1 so that its order of magnitude is similar to that of the other two terms of this objective.

Besides, constraints are now formulated in terms of either propeller net thrust and advance ratio at cruise condition or maximum acceptable stress criterion value in the shell and the core. This results in a set of 19 constraints. The value for thrust and power are obtained for a $4.5m$ equivalent propeller from the non-dimensional thrust and power coefficients. The advance ratio $J_{CR,2}$ is constrained to less than 3.08 in order to limit the associated tip helical Mach number $M^{tip}_{CR,2}$ below 1.0 ($\Gamma^{J}_{CR,2}$-constraint):

$$\Gamma^{J}_{CR,2} = 3.08 - J_{CR,2} \tag{11.5}$$

For each operating condition $J_{.,i}$ in cruise or take-off/landing, a constraint is put on thrust with a tolerance Δ_T of $0.5kN$ for the cruise condition and of $2.5kN$ for the take-off/landing one. These constraints are formulated in the same way as Eqn. 8.5. The values $T^{target}_{.,j}$ are chosen so that the same benchmark propeller as in section 8.3 is at least matched for any operating condition; these values are given in table 11.3. The benchmark delivers $11kN$ thrust in the cruise condition at $J = 3.26$ ($M_{tip} = 0.973$) with an efficiency η of 0.68 and $35kN$ in the take-off/landing condition at $J = 1.13$, thus the same RPM as the cruise condition, with an efficiency of 0.47 though this time the blade angle is of 43.5°. These thrust and the corresponding power values are realistic for a medium-haul aircraft equipped with four propellers.

Moreover, the structural constraints are considered for all operating points $J_{.,i}$. They concern the maximum value of the Tsai-Wu criterion $\zeta^{TW}_{.,j}$ (for the shell) and the maximum value of the von Mises equivalent stress normalized by the yield strength $\zeta^{VM}_{.,j}$ (for the foam core). At present, given the rudimentary blade architecture described in section 7.3, the values are arbitrarily constrained below 0.3 for the first criterion and below 0.5 for the second.

$$\Gamma^{TW}_{.,j} = \zeta^{TW}_{.,j} - 0.3 \leq 0 \tag{11.6}$$

$$\Gamma^{VM}_{.,j} = \zeta^{VM}_{.,j} - 0.5 \leq 0 \tag{11.7}$$

11.4 High-fidelity analysis workflow

Now the blade angle β_{ref} is fixed for the cruise condition but not for the take-off/landing one, and because the advance ratio $J_{TO,2}$ is now computed from Eqn. 11.1, the high-fidelity analyses may not be conducted concomitantly anymore. Hence the workflow for this optimization, presented in Fig. 11.4, is perceptibly different from the one shown in Fig. 8.6 in that the take-off/landing condition is now evaluated consecutively to the cruise one. The computational time for each individual is thus dramatically increased. The second difference lies in the introduction of the CSM solver at the end of each computational block. For practical reasons, it is kept in sequence with the CFD and CHA analyses though strictly speaking the pressure interpolation (see section 7.3.3.2) might start once the CFD solution is known.

Once again, the 10 to 7 best individuals are submitted to the high-fidelity analysis at the end of each iteration. The process starts by building the blade model for the cruise condition (with $\beta_{ref,CR} = 63°$) from the design vector (see chapter 4) before generating a mesh. If the mesh does not satisfy the quality measures listed in section 8.4, the mesh parameters are automatically adjusted. 18 adjusting sequences have been programmed. If no correct mesh is obtained despite those efforts, the process stops and no data is transfered to the training database. In case an acceptable mesh is obtained, the individual is passed to the CFD-solver. In the first run, $J_{CR,2}$ is chosen arbitrarily as the corresponding mean value of the DoE-database. To have a safe interval of the performance curve, which is necessary for precise adaption, $J_{CR,3}$ is taken as $J_{CR,2} + 0.3$ and $J_{CR,1}$ as $J_{CR,2} - 0.4$. At the end of the CFD-analysis, the non-dimensional performance values are computed. From these values, the thrust of an equivalent $4.5m$ propeller is calculated. If the thrust $T_{CR,2}$ does not match the target within the allowable interval $\pm\Delta_T$, a new advance ratio $J_{CR,2}$ is interpolated from the known performance curve. Polynomial interpolation of degree 2 is used for that purpose. The CFD-analysis is then run again with these new values though some computational time is saved by starting from the previous $J_{CR,3}$-solution. Once the CFD-solution is known for all advance ratios, the CHA-solver computes the SPL at all five receiver locations. The pressure interpolation is then performed concomitantly for the three advance ratios before starting the CSM-solver. A dedicated post-processor reads the data file written by the three solvers and computes the desired dimensional and non-dimensional performance values which, in the end, are written to a performance file.

The block for the evaluation of the performance at the take-off/landing condition is built in the same manner as the one for cruise but it is started in a parallel way once the CFD-solution is known and $J_{CR,2}$ is adapted according to Eqn. 11.1. The first blade model is built with a blade angle $\beta_{ref,TO}$ of 45°. If the mesh is not satisfactory, the meshing parameters are adjusted in accordance with the experience gained from part II. Up to 72 trials are done. A satisfactory mesh is immediately passed to the CFD-solver which computes sequentially the three advance ratios. At this stage, the obtained thrust $T_{TO,2}$ is compared to the target one. If the target value is not matched within the tolerance margins, the target thrust coefficient C_T^{target} is computed from $T_{TO,2}^{target}$ and $J_{TO,2}$ before computing the new value of $\beta_{ref,TO}^{new}$ by

$$\beta_{ref,TO}^{new} = \alpha_2 C_T^{target\,2} + \alpha_1 C_T^{target} + \alpha_0 \tag{11.8}$$

where the α_2- and α_1-coefficients are mean values computed from similar regressions

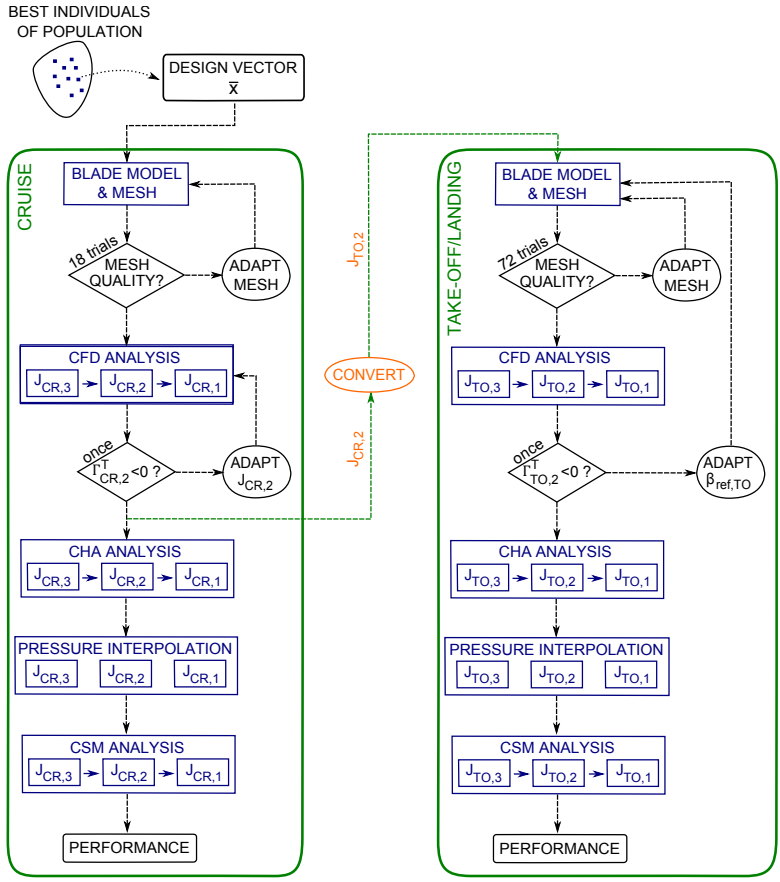

Figure 11.4: High-fidelity analysis workflow.

on a set of reference blades, and the α_0 is a fine-tuning coefficient computed individually for each blade from the thrust coefficient $C_{T;TO,2}$ obtained from $T_{TO,2}$ and $J_{TO,2}$:

$$\alpha_0 = \beta_{ref,TO} - \left(\alpha_2 {C_{T;TO,2}}^2 + \alpha_1 C_{T;TO,2}\right) \tag{11.9}$$

Once the new value $\beta^{new}_{ref,TO}$ is known, a new blade model is made and the meshing sequence initiated before launching the CFD-analysis. This adaption of the blade angle is performed only once. The remaining steps of the workflow are identical to those of the cruise condition.

Chapter 12

Survey of the optimization process

12.1 DoE-database

The DoE-database comprised 85 individuals (see section 11.2). The failure rate for this set is of 27.1%; mainly because of breakdown in the meshing. The higher percentage than in section 9.1 is the direct consequence of the necessity to develop two meshes for the take-off/landing condition because of the adaption on β_{ref}. The radial distributions defining the geometry of those blades are given in Fig. 12.1. The non-dimensionalized objective values ($\hat{\Omega}$) of the individuals in the database, are shown in Fig. 12.2 where non-dimensionalization is achieved with respect to the respective maximum Ω-value among the DoE-database or the benchmark. These two figures show the diversity of the individuals contained in the database both in terms of geometry as well as objective values. Thanks to the lower free-stream Mach number, the benchmark is now among the quietest designs despite its geometrical simplicity. Figure 12.2 clearly reveals that the objectives are now fully competing unlike the previous optimization.

In terms of constraints with respect to thrust, many individuals of the DoE-database satisfy them simultaneously even though the constraint on the design take-off/landing thrust ($\Gamma^T_{TO,2}$) appears to be the most difficult one to satisfy (see Fig. 12.3). The regressions for the $\beta_{ref,TO}$-adaption discussed in section 11.4, are partly responsible for this and the additional data gathered during the DoE-database development is used to update the α-coefficients of Eqn. 11.8. This time, the constraint on the cruise advance ratio $J_{CR,2}$ is immediately satisfied in all cases. For what concerns the structural constraints Γ^{TW} and Γ^{VM}, Figs. 12.4 and 12.5 show that many individuals from the database are structurally sound for the considered operating conditions. It is also evident from those figures that the increased centrifugal load at $J_{.,1}$ is responsible for more individuals to fail on these constraints. The central individual is characterized mainly by unacceptable solicitation of the foam core as is apparent from Fig. 12.5.

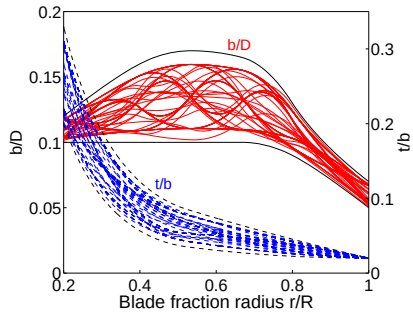

(a) Chord $(b(r)/D)$ and thickness $(t(r)/b(r))$.

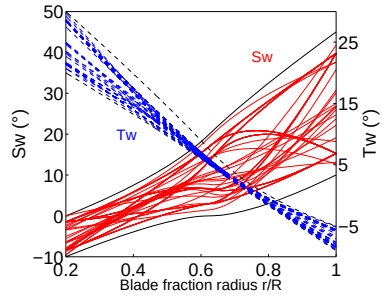

(b) Geometrical sweep $(Sw(r))$ and twist $(Tw(r))$.

Figure 12.1: Planform definition of the individuals contained in the DoE-database.

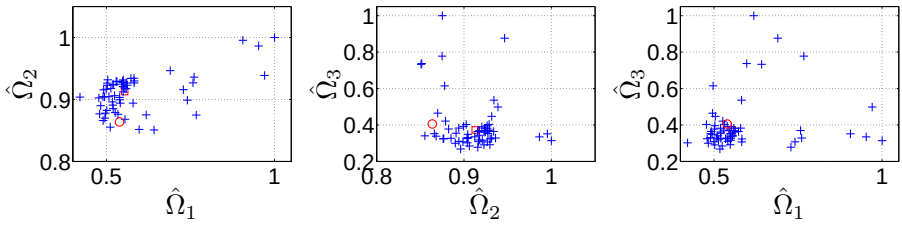

(a) (b) (c)

Figure 12.2: Normalized objective values in the DoE-database. ('+' for individuals - '□' for the central individual - '○' for the benchmark)

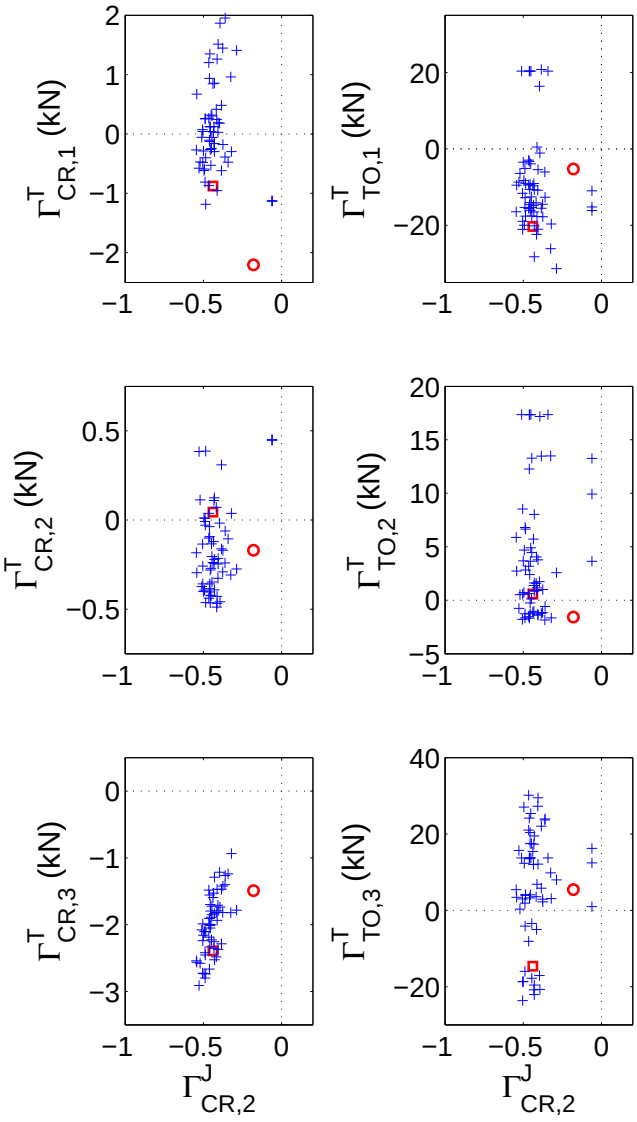

Figure 12.3: Constraint values for thrust in the DoE-database. ('+' for individuals - '□' for the central individual - '○' for the benchmark)

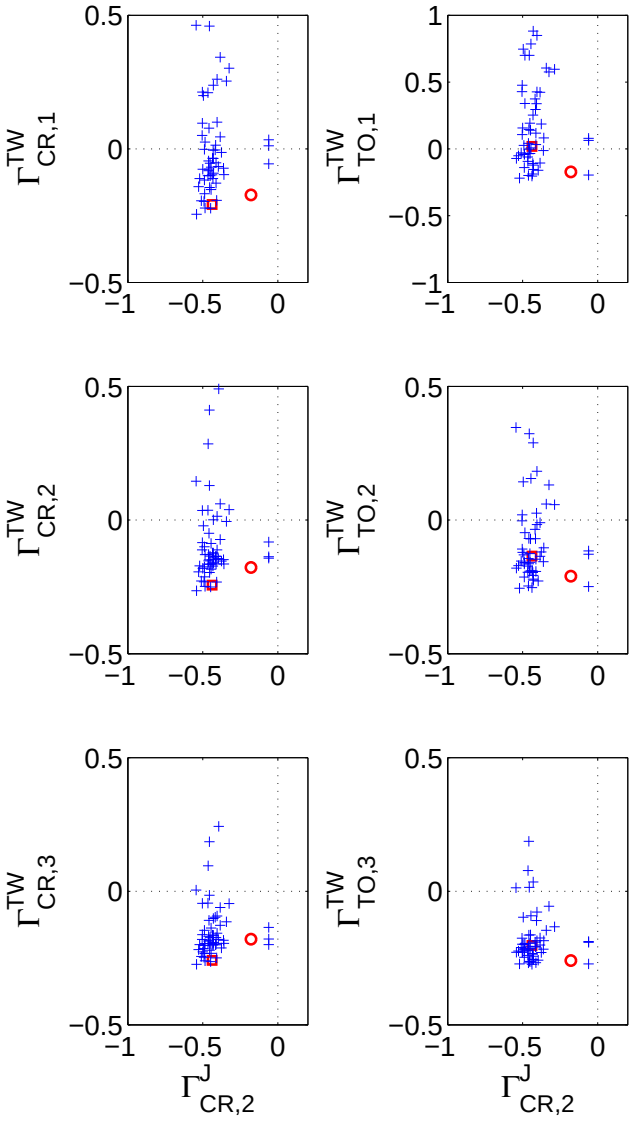

Figure 12.4: Constraint values for the Tsai-Wu criterion in the DoE-database. ('+' for individuals - '□' for the central individual - '○' for the benchmark)

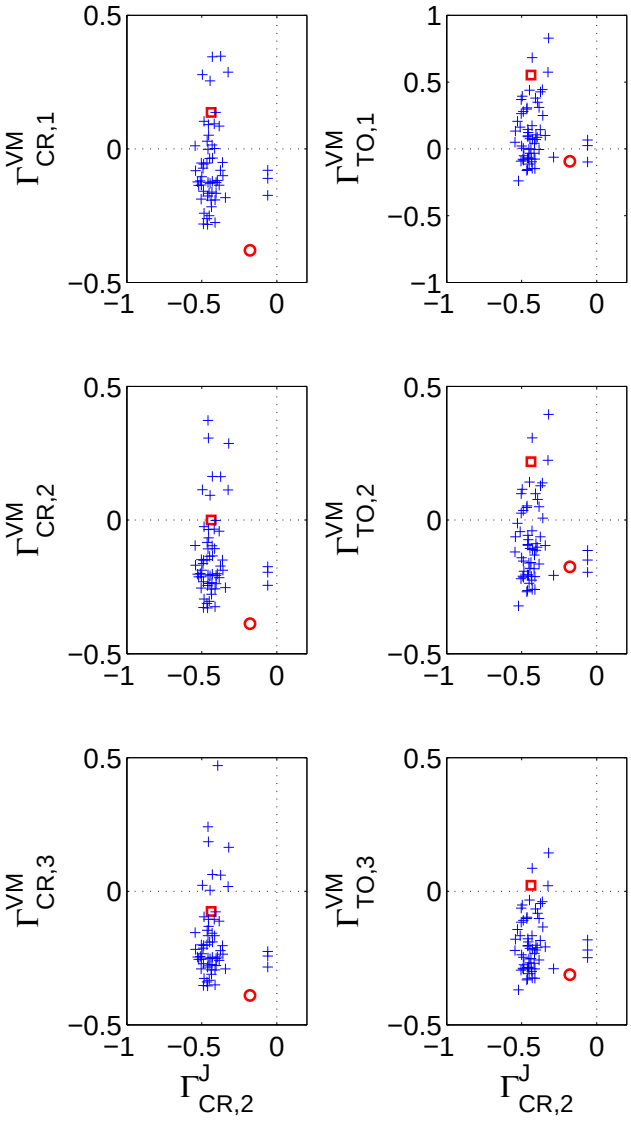

Figure 12.5: Constraint values for the von Mises criterion in the DoE-database. ('+' for individuals - '□' for the central individual - '○' for the benchmark)

12.2 Metamodel accuracy

The kriging-metamodels used in the present optimization, rest upon non-dimensional values of each performance parameter. Non-dimensionalization and normalization occur with respect to a -10% offset from the lowest and a 10% offset from the highest values present among the database. Figure 12.6 shows the accuracy of the respective metamodels for some normalized performance values in the cruise condition.

For $J_{CR,2}$, $T_{CR,2}$ and $SPL^{rec3}_{CR,2}$, the kriging metamodel is a much better estimator than was the ANN-metamodel of the previous optimization. As is confirmed by table 12.1, both the mean error and the standard deviation are much smaller than previously. This is especially true for $SPL^{rec3}_{CR,2}$ which was the worst estimate in the previous run. Unexpectedly, it is now $P_{CR,2}$ that is badly estimated and in the present case the metamodel is quasi systematically overestimating it. This translates in a high mean error and standard deviation though these quantities should be treated with care as the corresponding central plot from Fig. 12.6 suggests that these data are not normally distributed.

Both ζ-values in cruise reveal the difficulty for the metamodel to correctly capture all relationships between the design variables and the value of stress criteria. Indeed, in both cases, some individuals were estimated in the low ζ-range whereas they had in fact high ζ-values, hence the spreading of points close and along the abscissa in the corresponding left-side plots. The mean error on ζ^{TW} is less than 10% and artificially high because of a few "accidents" with huge discrepancies between the estimate and the actual value. The mean error on ζ^{VM} is much lower because less mis-estimations happened.

Interestingly, the picture is globally better for the performance values estimated in the take-off/landing condition (see Fig. 12.7). All mean errors are reduced and the standard deviation is kept within reasonable limits (see table 12.1). This is surprisingly true for $P_{TO,2}$ which is estimated in a much more accurate way than in cruise though in a similar manner as the optimization from the previous part.

The kriging-metamodels are globally much more proficient than the ANN-metamodels used in part II. Despite their attractive accuracy and robustness, this short analysis reveals the benefits of maintaining high-fidelity analysis tools embedded in the optimization loop to safeguard the relevancy of the decisions. The safe estimates concerning the SPL despite an even higher level of interaction, and the overall better accuracy underline the capacity of kriging-models to predict very complex systems.

	Take-off/Landing		Cruise	
	$\mu(\tilde{q}-\hat{q})$	$\sigma(\tilde{q}-\hat{q})$	$\mu(\tilde{q}-\hat{q})$	$\sigma(\tilde{q}-\hat{q})$
$J_{.,2}$	–	–	-0.037	0.075
$T_{.,2}$	0.000	0.101	0.018	0.061
$P_{.,2}$	0.000	0.132	0.195	0.209
$SPL^{rec3}_{.,2}$	-0.006	0.061	0.006	0.053
$\zeta^{TW}_{.,2}$	-0.030	0.094	-0.096	0.165
$\zeta^{VM}_{.,2}$	-0.020	0.117	-0.026	0.105

Table 12.1: Mean bias μ and standard deviation σ of the error on normalized metamodel estimates.

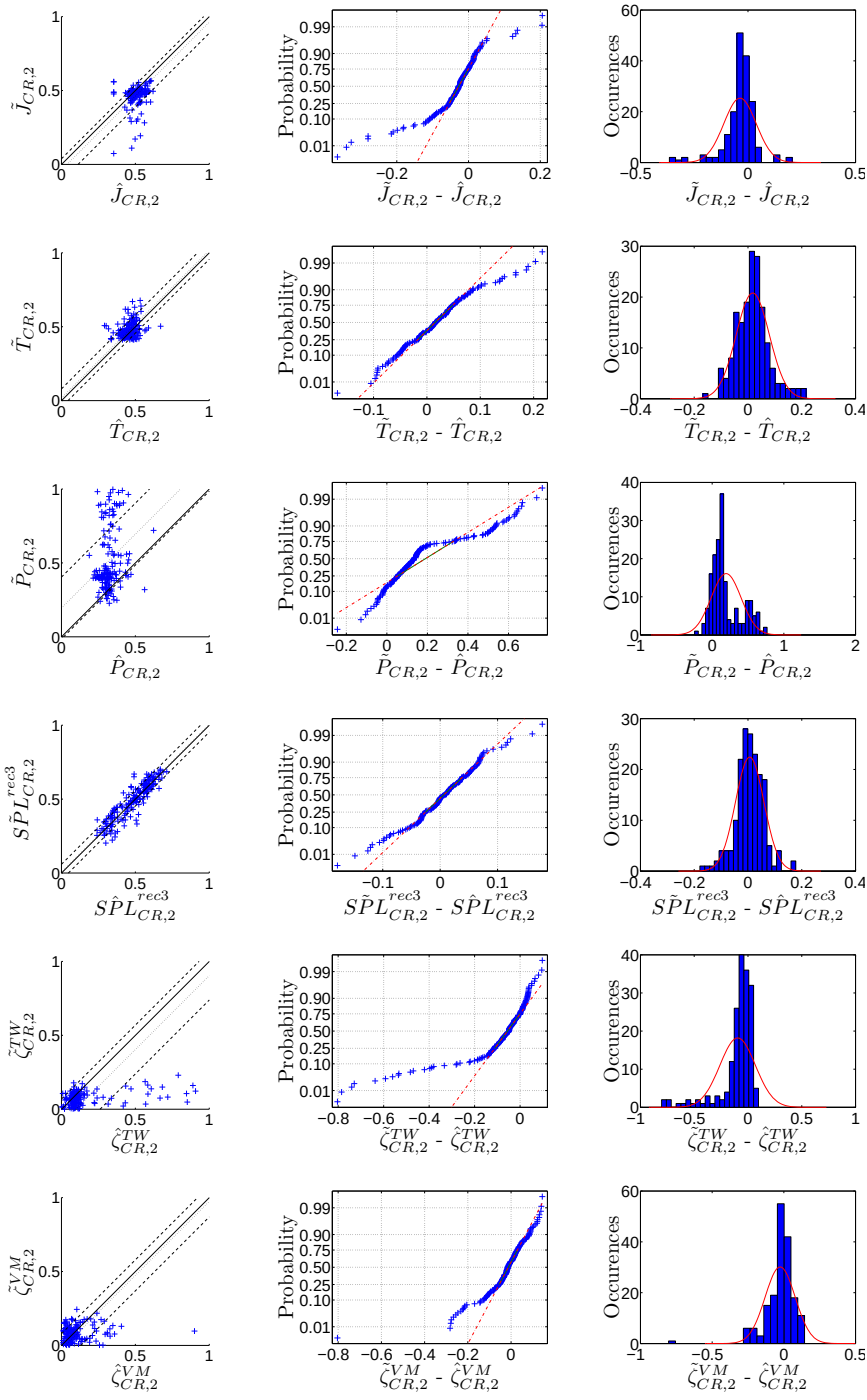

Figure 12.6: Metamodel accuracy, normality test and histogram with density for $\hat{J}_{CR,2}$, $\hat{T}_{CR,2}$, $\hat{P}_{CR,2}$, $S\hat{P}L^{rec3}_{CR,2}$, $\zeta^{TW}_{.,2}$ and $\zeta^{VM}_{.,2}$. For the metamodel accuracy, the mean error is shown by '...' and the standard deviation around the mean error by '---'.

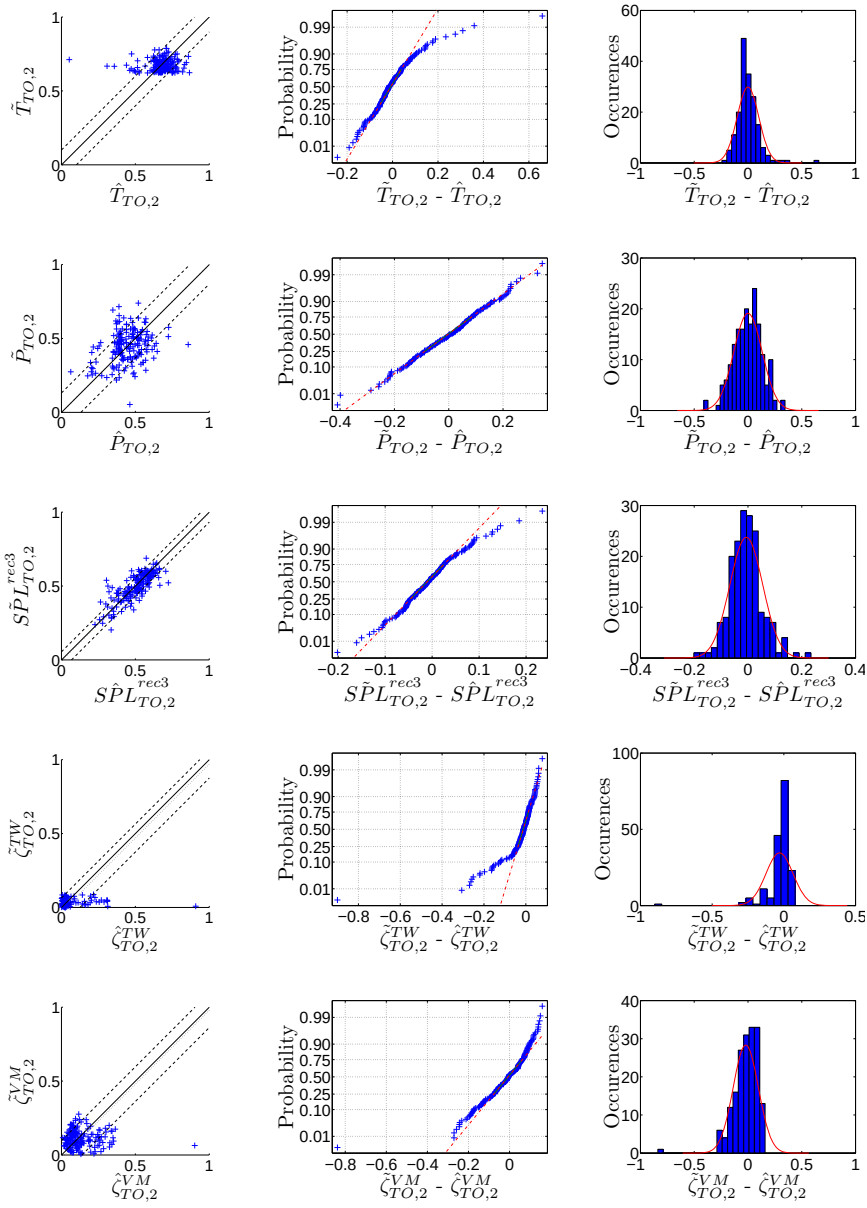

Figure 12.7: Metamodel accuracy, normality test and histogram with density for $\hat{T}_{TO,2}$, $\hat{P}_{TO,2}$, $\hat{SPL}^{rec3}_{TO,2}$, $\zeta^{TW}_{.,2}$ and $\zeta^{VM}_{.,2}$. For the metamodel accuracy, the mean error is shown by '. . .' and the standard deviation around the mean error by '- - -'.

12.3 Optimization results

The optimization process is spread over 42 iteration loops that resulted in total in 2100 designs proposed at the end of the iterative loops. 446 of them were fed through the high-fidelity analysis. For the last 10 iterations, no improvement for any of the objectives was witnessed notwithstanding the fact that new blade shapes were proposed. This was the reason to stop the process and keep the cost within reasonable margins.

In the approximate objective space ($\tilde{\Omega}_i$ for $i = 1, 2, 3$) shown in Fig. 12.8, the optimization evolved toward minimization of the objectives albeit apparently, in a less striking manner as for Fig. 9.6. The individuals proposed by the optimizer are much more clustered around those of the DoE-database than in the previous part. Another feature is that no visible fronts are present on Fig. 12.8 whereas some were on Fig 9.6. It is unclear whether this is a consequence from the fact that the Pareto-front is now a true 3-D surface (the objectives are now fully competing unlike in the previous run; hence fronts are less obvious) or because there is poorer convergence within the generation loops toward the Pareto-front corresponding to each single iteration.

Of the 446 designs that were submitted to the high-fidelity analysis, only 176 successfully processed through it. Their respective planform distributions are given in Fig. 12.9. The high failure rate (60.5%) is mostly the direct consequence of difficulties to obtain an acceptable mesh but Fig. 12.9 suggests that the search space is not artificially restrained by these faults.

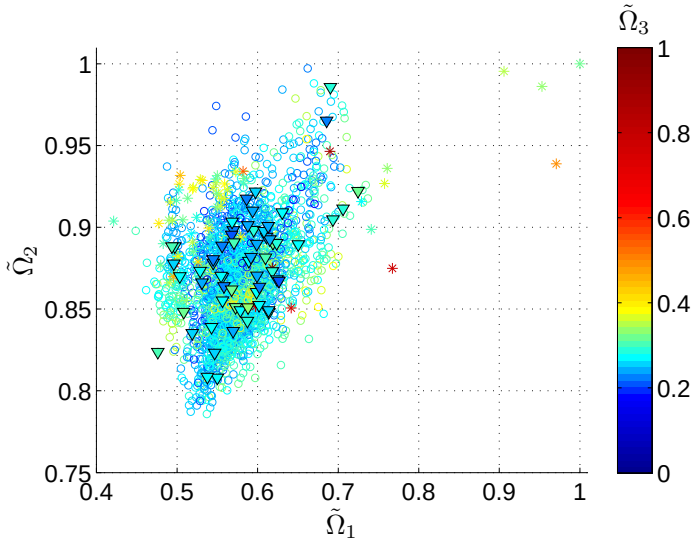

Figure 12.8: Pareto-front in the objective space built upon approximates. ('$\circ$' for individuals proposed by the optimizer at the end of each iteration - '$*$' for the DoE-individuals - '$\triangledown$' for the individuals successfully evaluated by high-fidelity analysis and that satisfy all constraints concomitantly.)

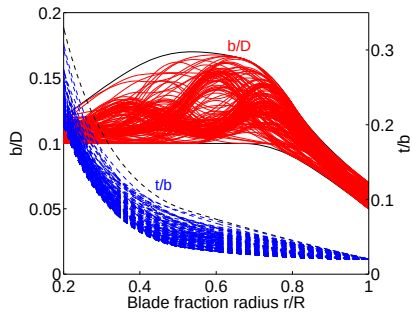

(a) Chord ($b(r)/D$) and thickness ($t(r)/b(r)$).

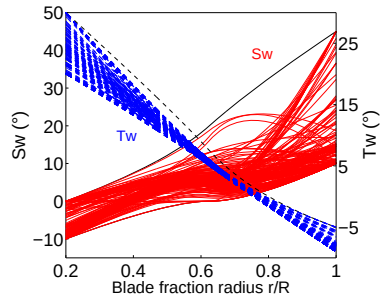

(b) Geometrical sweep ($Sw(r)$) and twist ($Tw(r)$).

Figure 12.9: Planform definition of the 176 individuals processed through high-fidelity analysis (CFD and CHA solvers).

Nevertheless, 61 individuals that concomitantly satisfy all constraints were obtained. This is a substantial improvement with respect to the previous optimization. These individuals are indicated on Fig. 12.8 and are located in the 3^{rd}-quadrant of the constraint values plots in Figs. 12.12-12.14. The evolution toward better satisfaction of the constraints appears clearly from those figures, certainly in terms of structural constraints but also in terms of thrust constraints at the take-off/landing condition. The normalized objective values in the high-fidelity space of the 176 individuals are shown in Figs. 12.10 and 12.11 together with the original DoE-values. From both figures, the evolution toward minimal Ω-values is apparent; especially in terms of the Ω_2- and Ω_3-values that show the biggest relative reduction from the DoE-database. The band distribution on Fig. 12.10 suggests less decrease could be obtained in terms of the Ω_1-objective. The comparison of Figs. 12.8 and 12.10 is indicative of the better quality of the metamodels as discussed in section 12.2.

Figure 12.15(a) shows the striking increase in cruise efficiency for the optimized individuals eventhough the efficiency in take-off/landing condition does not benefit from a similar development (Fig. 12.15(b)). Hence the other terms than $\eta_{CR,2}$ in Eqn. 11.2 are essentially responsible for the stagnating Ω_1-values.

The planform definition of the 61 individuals that comply with all constraints, are given in Fig. 12.16. As is visible on Fig. 12.16(b), a considerable subset of these individuals have small geometrical sweep toward the tip. Remarkably, most blades feature one or more humps in the chord distribution and are built upon thin airfoils. A detailed analysis of some of the best performing individuals will be given in the next chapter.

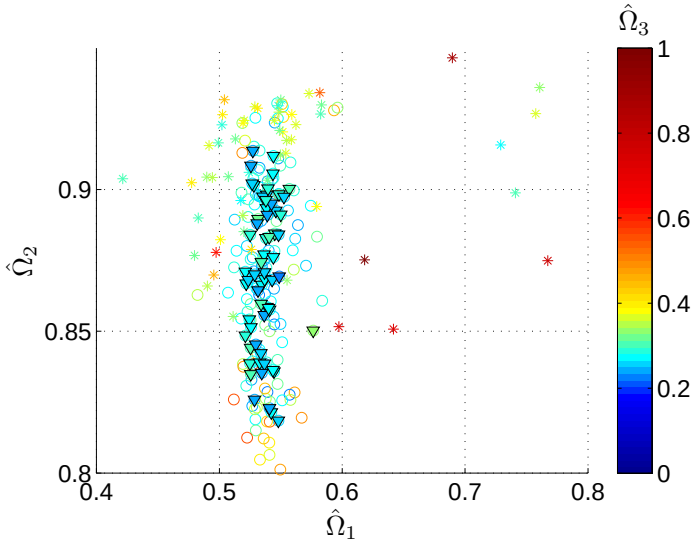

Figure 12.10: Pareto-front in the objective space built upon high-fidelity analysis. ('○' for individuals successfully evaluated by high-fidelity analysis - '▽' for the individuals that satisfy all constraints concomitantly - '∗' for the DoE-individuals.)

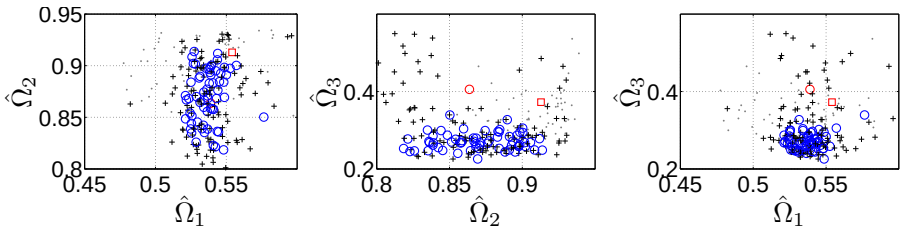

Figure 12.11: Normalized objective values of the individuals submitted to high-fidelity analysis. ('○' for individuals satisfying all constraints concomitantly - '+' for individuals that violate at least one constraint - '.' for the DoE-individuals - '□' for the central individual - '○' for the benchmark)

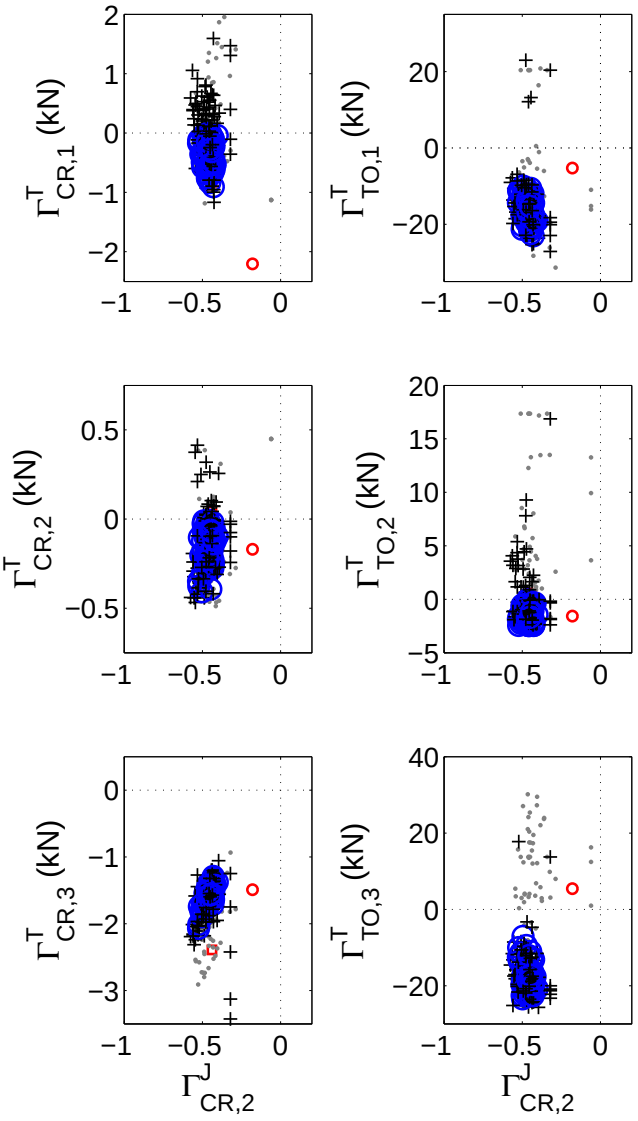

Figure 12.12: Constraint values for thrust of the individuals submitted to high-fidelity analysis. ('+' for individuals - '□' for the central individual - '○' for the benchmark)

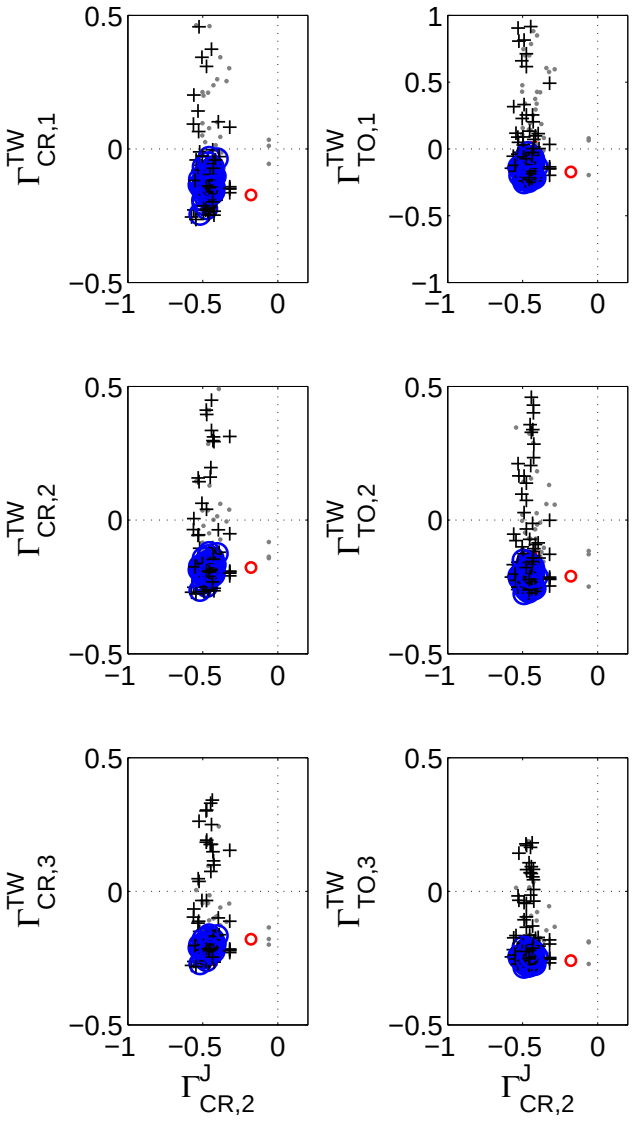

Figure 12.13: Constraint values for the Tsai-Wu criterion of the individuals submitted to high-fidelity analysis. ('+' for individuals - '□' for the central individual - '○' for the benchmark)

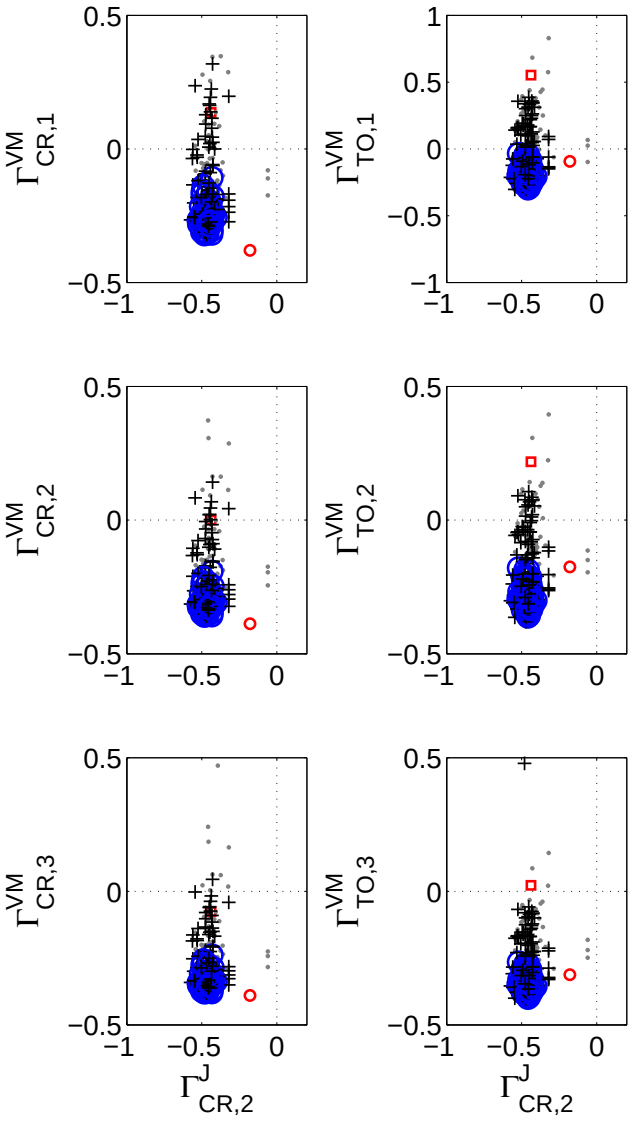

Figure 12.14: Constraint values for the von Mises criterion of the individuals submitted to high-fidelity analysis. ('+' for individuals - '□' for the central individual - '○' for the benchmark)

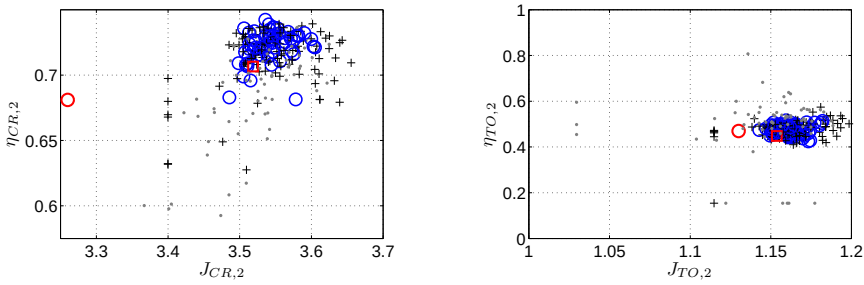

(a) Cruise efficiency $\eta_{CR,2}$.

(b) Take-off/landing efficiency $\eta_{TO,2}$.

Figure 12.15: Efficiency of the individuals submitted to high-fidelity analysis. ('○' for individuals satisfying all constraints concomitantly - '+' for individuals that violate at least one constraint - '.' for the DoE-individuals - '□' for the central individual - '○' for the benchmark)

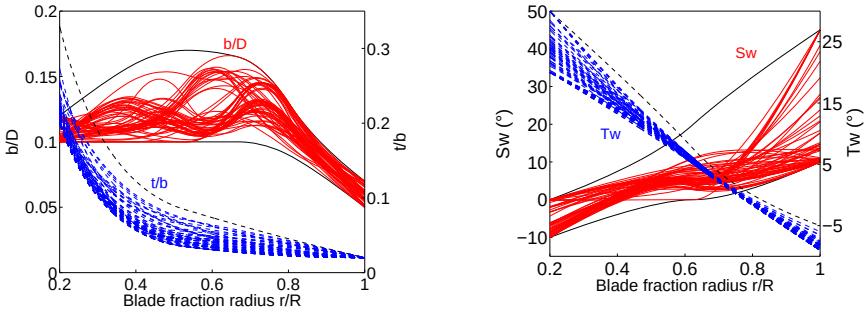

(a) Chord $(b(r)/D)$ and thickness $(t(r)/b(r))$.

(b) Geometrical sweep $(Sw(r))$ and twist $(Tw(r))$.

Figure 12.16: Planform definition of the 61 individuals that concomitantly satisfy all constraints.

Chapter 13

Analysis of specific individuals

In the present chapter, four peculiar blade designs from the 61 discussed in section 12.3, are presented with more details about their aerodynamic, aeroacoustic and aeroelastic performance. Finally, conclusions pertaining to the present optimization and its results, are drawn.

13.1 Objective-values, constraint-values and geometries

Out of the set of individuals that satisfy all constraints, 4 have been earmarked for their performance (see Fig. 13.1):

1. individual A because it has the lowest $\hat{\Omega}_1$-value,
2. individual B because it has the lowest $\hat{\Omega}_2$-value,
3. individual C because it has the lowest $\hat{\Omega}_3$-value,
4. and individual D because it has the highest cruise efficiency $\eta_{CR,2}$.

Individuals A, B and C are of rank 0 whereas individual D is of rank 2. Figures 13.2, 13.3 and 13.4 show the constraint satisfaction values for those four individuals. All of them are within the compliant domain in terms of thrust and benefit from a comfortable margin in terms of stress criteria. The central individual of the DOE-database is also given for reference purposes despite the fact that it does not satisfy the constraint on thrust at $J_{.,2}$, the $\Gamma^{TW}_{TO,1}$-constraint and some $\Gamma^{VM}_{.,j}$-constraints.

The distributions defining the geometry of individuals A-D are given in Fig. 13.5 and the resulting planforms are shown in Fig. 13.6. All individuals exhibit a wavy chord distribution that translates into noticeable humps in the planform shape, and have rather thin sections. The hump is located between 60%- and 80%-radius. Individual D has a twist distribution that is different from the others in that it has less

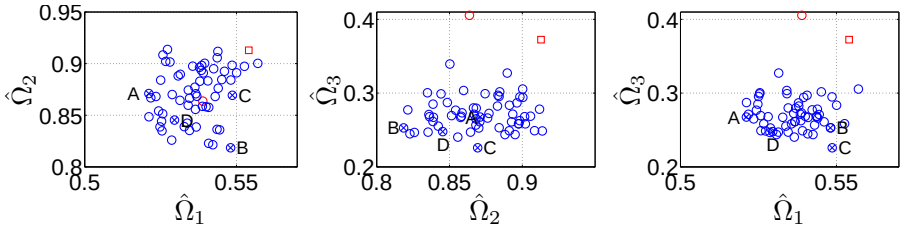

(a) (b) (c)

Figure 13.1: Normalized objective values of individuals A, B, C and D. ('○' for individuals satisfying all constraints concomitantly - '□' for the central individual - '○' for the benchmark)

Individual	A	B	C	D	Benchmark	Central
Sw_{LE}	36.8°	41.5°	33.0°	36.5°	17.0°	45.0°

Table 13.1: Leading-edge sweep (Sw_{LE}).

twist near the root. In terms of geometrical sweep, the 4 blades feature low geometrical tip sweep. As such, this is a surprising feature for high-speed blades but the planforms reveal that leading-edge sweep is obtained anyway by the combined effect of the geometrical sweep and the taper induced by the diminishing chord toward the tip. The values of Sw_{LE} for individuals A-D, given in table 13.1, suggest that all of them have moderate to high leading-edge sweep toward the tip.

The optimized airfoil shapes are shown in Fig. 13.7. The main characteristics of the optimized airfoils are:

- the increased camber of airfoil I for all individuals,
- the more narrow and flatter front of airfoil II in all cases, with the crest on the suction side located around 60%-chord and the thicker rear part. This is a similar trend to the results of transonic airfoil optimization [175].

The first item was not present in the previous optimization as this possibility was very limited by the allowable ranges. The position of the crest and the flatter front on the suction side were already present in section 10.1 though the crest was less pronounced. The shape of the front part of the pressure side of airfoil II is significantly different with this optimization in that more thickness is present. This is mainly due to the camber in the front part.

13.2 Aerodynamic performance

13.2.1 Overall performance

The aerodynamic performance of individuals A-D in terms of C_T, C_P and η are given in Fig. 13.8. In cruise, at $J_{CR,2}$, these blades deliver the required thrust within

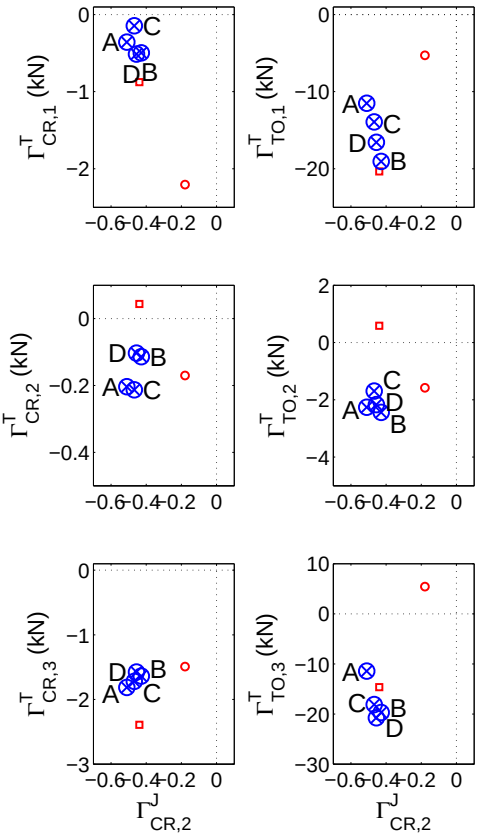

Figure 13.2: Constraint values for thrust in the DoE-database. ('+' for individuals - '□' for the central individual - '○' for the benchmark)

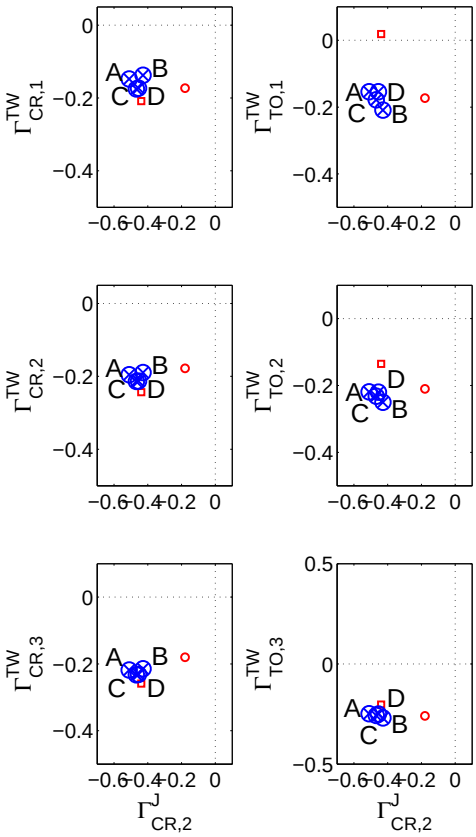

Figure 13.3: Constraint values for the Tsai-Wu criterion in the DoE-database. ('+' for individuals - '□' for the central individual - '○' for the benchmark)

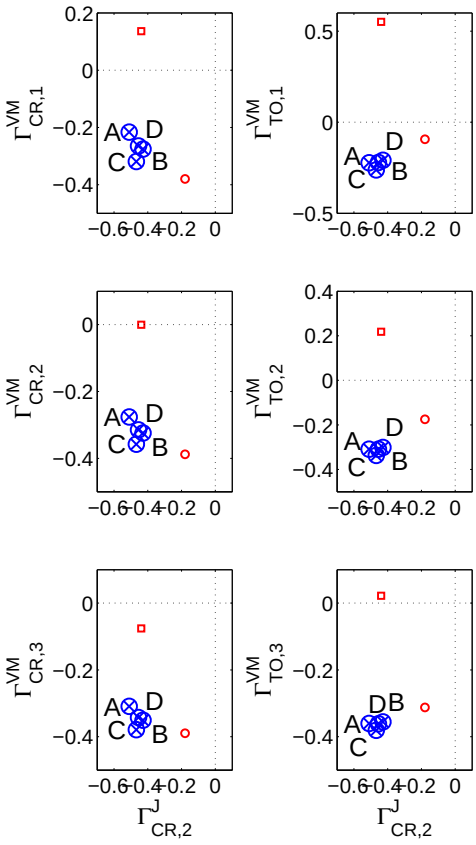

Figure 13.4: Constraint values for the von Mises criterion in the DoE-database. ('+' for individuals - '□' for the central individual - '○' for the benchmark)

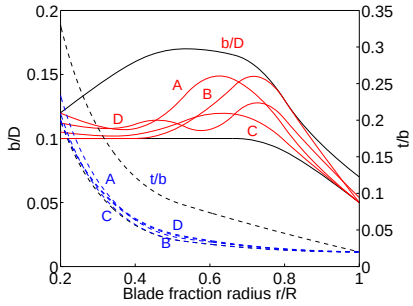

(a) Chord ($b(r)/D$) and thickness ($t(r)/b(r)$).

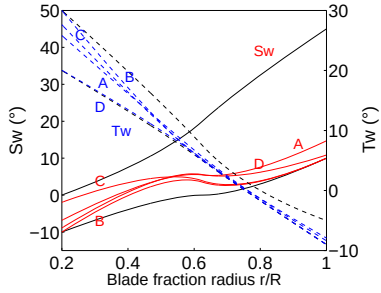

(b) Geometrical sweep ($Sw(r)$) and twist ($Tw(r)$).

Figure 13.5: Planform definition individuals A, B, C and D.

(a) A. (b) B. (c) C. (d) D. (e) Benchmark. (f) Central.

Figure 13.6: Blade geometry of individuals A, B, C, D, the benchmark and the central individual.

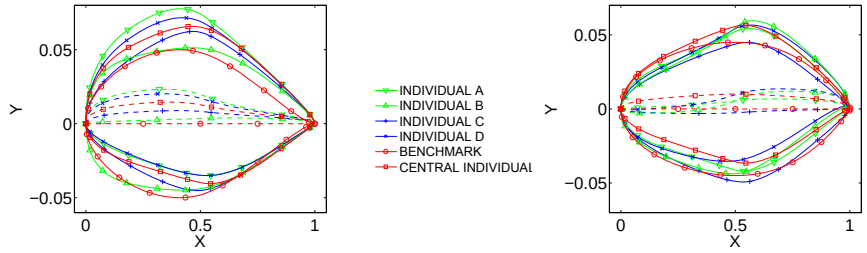

(a) Airfoil I used from blade root to 35% radius.

(c) Airfoil II used from 45% radius to blade tip.

Figure 13.7: Optimized airfoils. Note that airfoil I for the benchmark is a NACA 65-010CA and airfoil II is a NACA 16-009.

	$\eta_{CR,1}$	Gain (%)	$\eta_{CR,2}$	Gain (%)	$\eta_{CR,3}$	Gain (%)
Benchmark	0.602	–	0.684	–	0.693	–
Central individual	0.500	−10.2.0	0.545	−13.9	0.501	−19.2
Individual A	0.674	+7.2	0.732	+4.8	0.728	+3.5
Individual B	0.649	+4.7	0.708	+2.4	0.707	+1.4
Individual C	0.662	+6.0	0.722	+3.8	0.735	+4.2
Individual D	0.678	+7.6	0.739	+5.5	0.749	+5.6

Table 13.2: Aerodynamic efficiency η in cruise condition.

a margin of 2.2%. They all operate at a much higher advance ratio, hence a lower RPM, than the benchmark. In terms of thrust-coefficient, differences are small except for the lowest advance ratio $J_{CR,1}$ where individuals C and D deliver an additional $3kN$-thrust when compared to the others. Differences are more pronounced in terms of power-coefficient and result in significant differences in required power and efficiency as is apparent from tables 13.2 and 13.3. Efficiency gains in the design cruise condition range between +2.4% and +5.5% depending on the individual. The direct consequence of these achievements are benefits in power at the design cruise condition (see Fig. 13.8(a)) of the order of 8% to 13% (table 13.3). Improvements are achieved in off-design conditions as well with acceptable performance.

In the take-off/landing conditions, individuals A and D, chosen for their aerodynamic performance, come with an increase in efficiency (see table 13.4 and Fig. 13.8(b)) though only individual A offers a real decrease in required power (see Fig. 13.8(b)). In this condition, the individuals operate at a slightly higher advance ratio than the benchmark as well. The adaption process on β_{ref} described in section 11.4, results in blade angles ranging from 45° to 47.5° depending on the individual.

13.2.2 Local features

Figure 13.9 shows the distribution of elemental thrust (T_{el}) and elemental PTF (PTF_{el}) in the design cruise condition. Comparing to the benchmark, this figure reveals that all individuals benefit from an increased contribution from the inboard

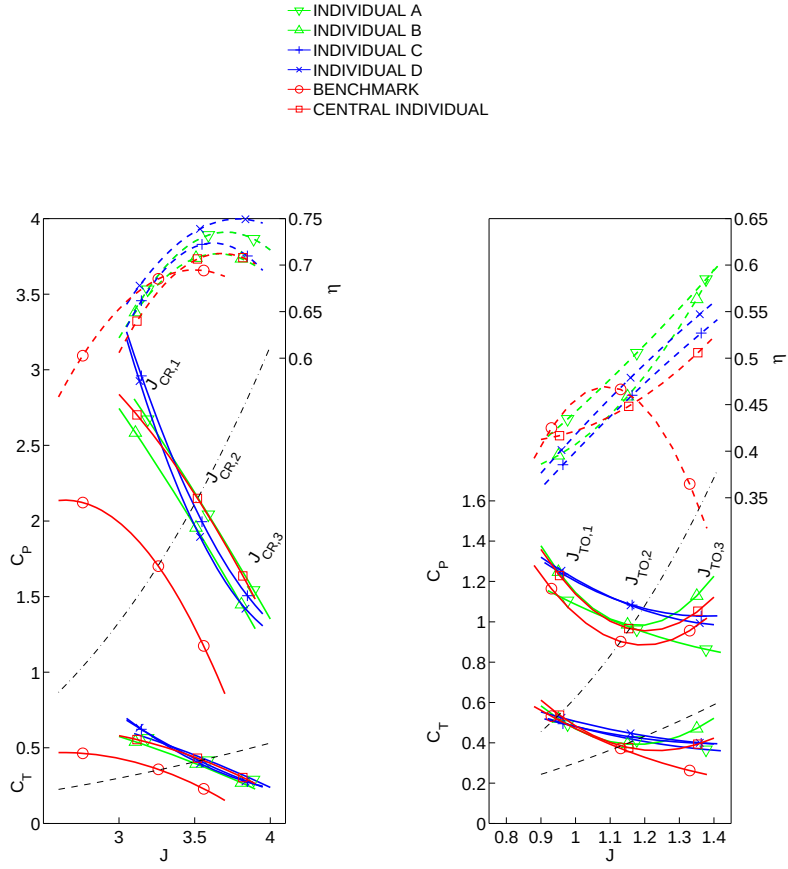

(a) Cruise condition ($M_\infty = 0.70$ and $\beta_{ref} = 63°$).

(b) Take-off/landing condition ($M_\infty = 0.2$ and adapted β_{ref}).

Figure 13.8: Thrust and power coefficients (C_T and C_P) at design and off-design conditions with the corresponding efficiency η. The lines for constant thrust $T_{.,2}$ ('−−') and constant power $P_{.,2}$ ('−·') are based on the benchmark.

Individual	A	B	C	D	Benchmark	Central
$P_{CR,2}$ (kW)	3034	3112	3071	2947	3388	3391
Gain (%)	−10.4	−8.1	−9.3	−13.0	–	0.0

Table 13.3: Power $P_{CR,2}$.

	$\eta_{TO,1}$	Gain (%)	$\eta_{T0,2}$	Gain (%)	$\eta_{TO,3}$	Gain (%)
Benchmark	0.425	–	0.466	–	0.365	–
Central individual	0.417	−0.8	0.448	+1.8	0.506	+14.1
Individual A	0.435	+1.0	0.506	+4.0	0.585	+22.0
Individual B	0.395	−3.0	0.459	−0.7	0.563	+19.8
Individual C	0.385	−4.0	0.460	−0.6	0.527	+16.2
Individual D	0.401	−2.4	0.479	+1.3	0.547	+18.2

Table 13.4: Aerodynamic efficiency η in take-off/landing condition.

part of the blade in the total thrust. The corresponding load is taken from the outboard part so that the tips are more lightly loaded. The PTF is more uniformly distributed than the benchmark or the central individual. Both for the thrust and the PTF, the major contribution comes from the blade region between 60%- and 90%-radius. These curves are relevantly different from those of Fig. 10.7 in that the load is more effectively removed from the tip region and transferred to the inboard part.

The corresponding local distributions of the pressure coefficient C_p are given in Fig. 13.10 for different radii at the design cruise condition. At 25%-radius, all pressure distributions are more favourable when compared to the benchmark or the central individual. Individual B features a strong shock located immediately after the abrupt change in curvature on the suction side at 20%-chord (see Fig. 13.7(a)). This shock spans practically the whole blade in the radial direction and partly explains its lower efficiency. In any case, the results at low radii are in contrast with those presented in section 10.2.2 where thrust production from the inboard part was virtually non-existent due to the inadequate pressure distribution. The driving factor behind this improvement is the allowance for increased camber for airfoil I. At 50%-radius, both individuals B and C feature a shock but of different strength. Overall, the pressure distributions are again more favourable than the benchmark or the central individual, and constitute a substantial improvement from section 10.2.2. The portion around 75%-radius contributes significantly to the thrust and PTF when compared to the other parts of the blade. At this radius, individuals B-D feature a shock of similar strength yet it is stronger than the one present on individual A. This station is more lightly loaded than the corresponding one on the benchmark and the existing load is clearly located toward the leading-edge because of the shock located on the forward part of the airfoil. Near the tip, the load is also concentrated toward the leading-edge but shocks tend to be rather weak. The pressure distributions at 75%- and 99%-radius also confirm that less load is present in those regions when compared to the benchmark. The last is true for the present blades to a larger extent than for those of section 10.2.2.

For all individuals, the optimization of the airfoils resulted in shapes that cause the load to be located on the forward part of the airfoil, especially at high radii. Except for the tip region, the more narrow front part of airfoil II combined with its thicker rear part, results in a shock location on the first half of the airfoil. This location is known to produce less wave drag than aft locations but comes with less loading when compared to the results of Li et al. [175].

The distributions of thrust and PTF in the design take-off/landing condition are given in Fig. 13.11. When compared to individuals A and B, the higher contribution

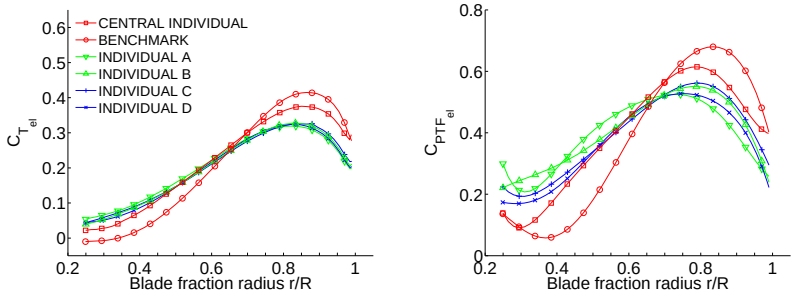

(a) Elemental thrust coefficient C_{Tel}. (b) Elemental PTF coefficient C_{PTFel}.

Figure 13.9: Spanwise elemental force coefficient distributions in cruise at $J_{CR,2}$.

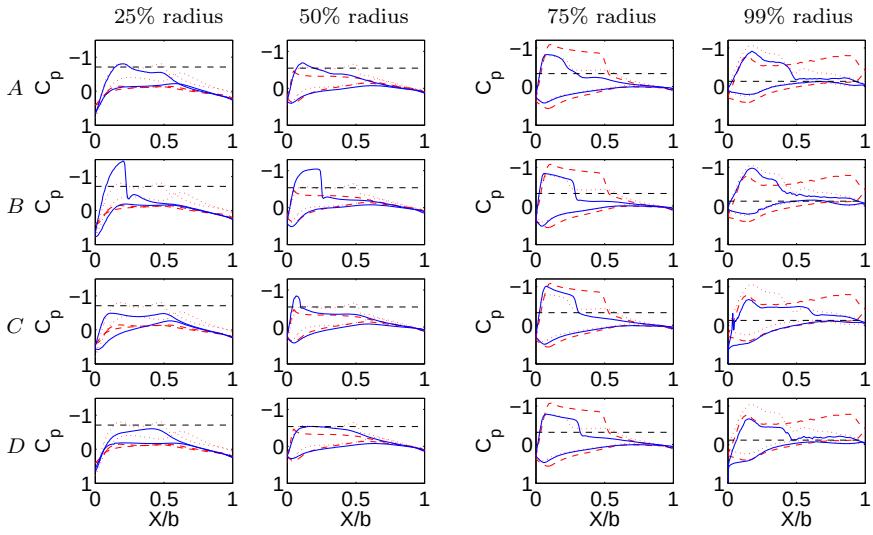

Figure 13.10: Pressure coefficients C_p at 25%, 50%, 75% and 99% radius for the cruise condition at $J_{CR,2}$ ('—' optimized individual, '– –' benchmark and '·····' central individual). The critical pressure coefficient $C_{p,crit}$ is indicated by '_ _'.

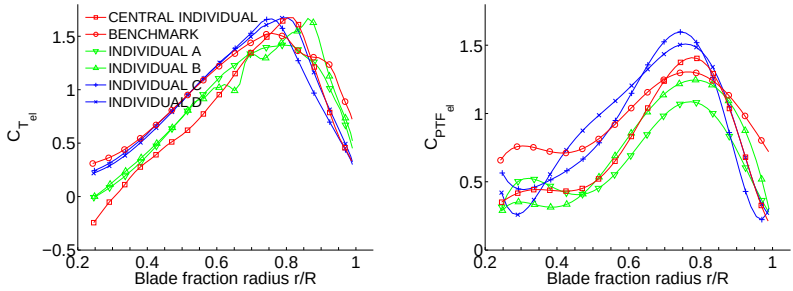

(a) Elemental thrust coefficient C_{Tel}. (b) Elemental PTF coefficient C_{PTFel}.

Figure 13.11: Spanwise elemental force coefficient distributions in take-off/landing at $J_{TO,2}$.

from the inboard part of individuals C and D to thrust, is the consequence of the airfoil shape and blade twist. They result in more favourable pressure distributions with less suction on the pressure side (see Fig. 13.12). Unfortunately, this comes with higher PTF for most stations; thence a higher required power (see table 13.4). At 50%-radius, the pressure distributions of all individuals are more favourable than the benchmark and part of the pressure-load is moved aft when compared to the cruise condition. Both at 25% and 50%, the pressure distributions are better than those obtained during the previous optimization. At 75%-radius, individuals A and B are leading-edge loaded and feature a strong suction that is immediately followed by a strong recompression which is associated with the leading-edge vortex system (see Fig. 13.13). Individuals B and C have their pressure-load reparted over most of the chord because the vortex system is significantly different at this station. This station is located anyway in the part of the blade that contributes the most to the overall forces and from there on to the tip, the load is rapidly decreasing. The tip region, in contrast to the 75%-region, does not contribute as significantly and, for all individuals, it is much less loaded than the corresponding one on the benchmark. For individuals C and D, the last two stations have nice pressure distributions.

13.3 Aeroacoustic performance

Figure 13.14 shows the directivity plots at the BPF of all individuals for the design advance ratio in the cruise ($J_{CR,2}$) and take-off/landing conditions ($J_{TO,2}$). It should be once more reminded that the results in take-off/landing conditions do not take the influence of unsteady tonal sources, though they might be significant contributors because of the low Mach number. As apparent from that figure and table 13.5, significant gains are achieved for individual B with respect to the benchmark. Gains are moderate for individual D whereas individuals A and C come with a small SPL decrease. Additionally, it appears that the gains obtained in the cruise condition are of similar magnitude as those obtained in the take-off/landing condition, except for blades A and C. Noticeably, all optimized blades emit more sound than the

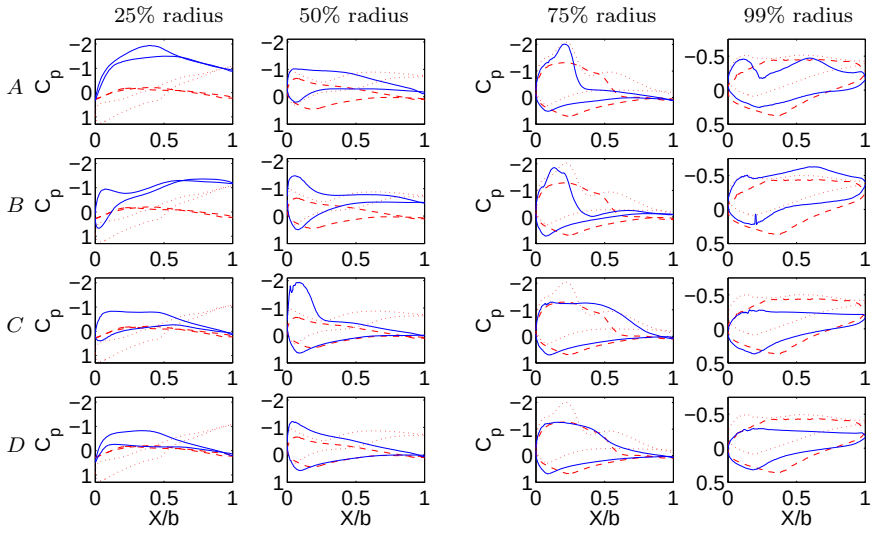

Figure 13.12: Pressure coefficients C_p at 25%, 50%, 75% and 99% radius for the take-off/landing condition at $J_{TO,2}$ ('—' optimized individual, '– –' benchmark and '·····' central individual).

benchmark at the back of the rotational plane but this is offset upstream of it. In all cases, the tip operates well into the subsonic domain for the cruise condition as is apparent from table 13.5. Interestingly, the optimization at a lower Mach number (0.7 versus 0.75 in part II) did result in lower tip speed also. Despite the possibility for nearly sonic tip speeds (as $J_{CR,2}$ is not fixed), it is left unused even though higher tip speed are usually associated with higher efficiencies. On the other hand, this implies that the truncation operator is totally inactive for blades $A - D$.

The results suggest that the optimization effectively processed toward lower SPL values with all individuals emitting much less noise than the central individual which is representative for the SPLs present in the DOE-database. They all have a directivity pattern comparable to the ones obtained in section 10.3 for blades A and B. The differences are mainly concerning the SPL upstream of the rotational plane in cruise condition (around $100dB$ now against $110dB$ in section 10.3 for $\varphi = 67.5°$) and a higher SPL for receiver 3 in take-off/landing except for individual B.

Figure 13.15 shows the acoustic signals in the time domain at receiver 3 in the design cruise condition ($J_{CR,2}$). The loading noise is the dominant source in all cases. The optimized shapes result in an effective suppression of the characteristic spike in the thickness noise that is associated with the leading edge. From the comparison of tables 10.5 and 13.5, it is worth noticing that despite the reduction in tip speed, no decrease of the SPL is witnessed because the loading noise is dominant in all cases.

In terms of blade passing harmonics (see Fig. 13.16), the optimized shapes result in a decrease of the SPL at the higher harmonics in the cruise condition even though this was not an objective as such. The decrease is relatively independent of the

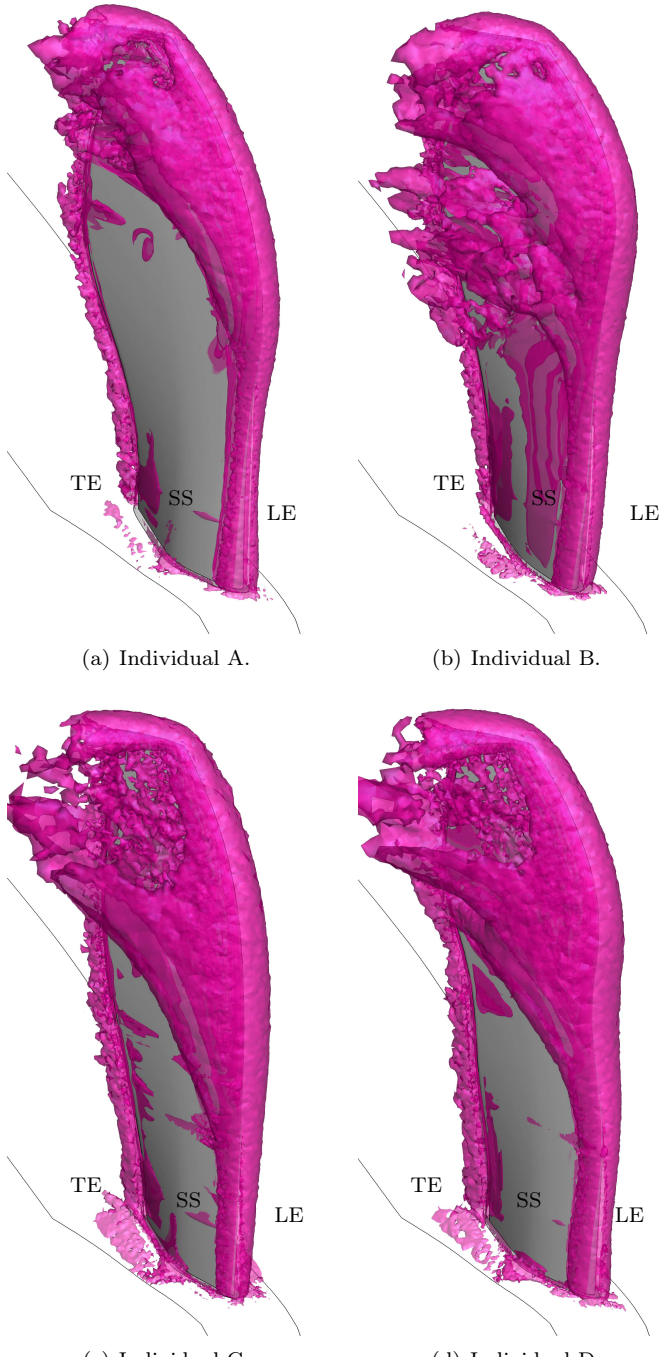

(a) Individual A.

(b) Individual B.

(c) Individual C.

(d) Individual D.

Figure 13.13: Vortex core visualization at $J_{TO,2}$ using iso-surfaces of λ_2 ($\lambda_2 < 0$).

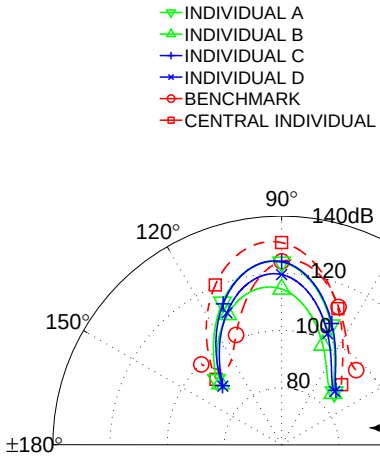

(b) Directivity in cruise condition at $J_{CR,2}$.

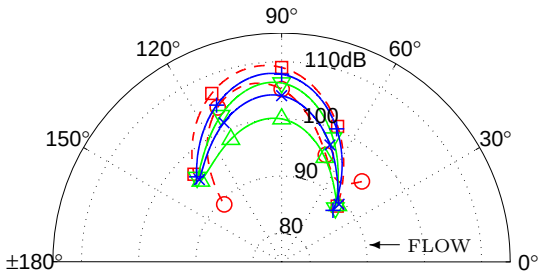

(c) Directivity in take-off/landing condition at $J_{TO,2}$.

Figure 13.14: Directivity plots based on the SPL at BPF.

	Take-off/Landing		Cruise		
	SPL	Gain (dB)	SPL	Gain (dB)	M_{tip}
Benchmark	105.2	–	124.2	–	0.9728
Central individual	109.0	+3.8	130.8	+6.6	0.9384
Individual A	106.3	+1.1	123.9	−0.3	0.9302
Individual B	100.0	−5.2	114.5	−9.7	0.9396
Individual C	107.8	+2.6	124.1	−0.1	0.9349
Individual D	104.0	−1.2	119.6	−4.6	0.9364

Table 13.5: SPL at BPF for receiver 3 in the design condition ($J_{.,2}$) and helical tip Mach number in the design cruise condition ($J_{CR,2}$).

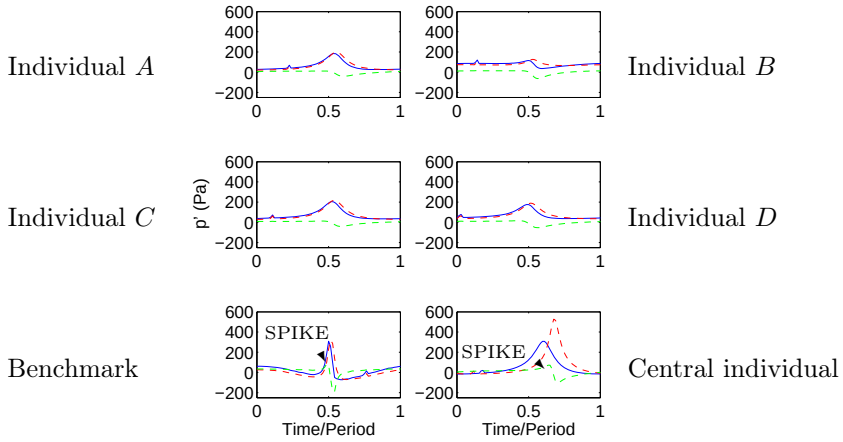

Figure 13.15: Time signal for receiver 3 in cruise condition with $J_{CR,2}$ ('—' Total noise - '– –' Thickness noise - '– –' Loading noise).

harmonic number. This is a very different situation than in section 10.3 where higher tip speeds brought higher tones at high frequency. At low Mach number, all optimized individuals exhibit a strong SPL at the BPF and a lower one for the higher harmonics. All of them radiate more sound than the benchmark at higher frequencies for that flight condition.

13.4 Aeroelastic performance

Table 13.6 gives an overview of the blade mass (m), the Tsai-Wu criterion value (ζ^{TW}) in the shell and the von Mises equivalent stress value normalized by the yield strength (ζ^{TW}) in the core, for the design cruise condition. Given the inefficient use of the blade material in a monocoque design, these results are promising. Despite the presence of humps, all individuals come with relatively low ζ-values. The inclusion of the Ω_3-objective, taking structural considerations into account is primarily responsible for this achievement. Such results would not have been achieved with 'go-no go' criteria solely, such as the Γ^{TW}- and Γ^{VM}-constraints. Such constraints are indeed only able to fence the compliant domain within the search space and are not able to drive the search to minima.

Figures 13.17 to 13.20, show ζ^{TW} and ζ^{VM} for individuals A to D respectively. In all cases, the maximum stresses in the shell occur on the ridges of the transition region, which is clearly the most critical part of those blades. This is a reassuring fact as a better structural design with a tailored use of the materials will undoubtedly lead to a reduction of the stresses in this region. On all blades, the hump causes higher, though not significantly high, stresses in the shell along the leading- and trailing-edge region

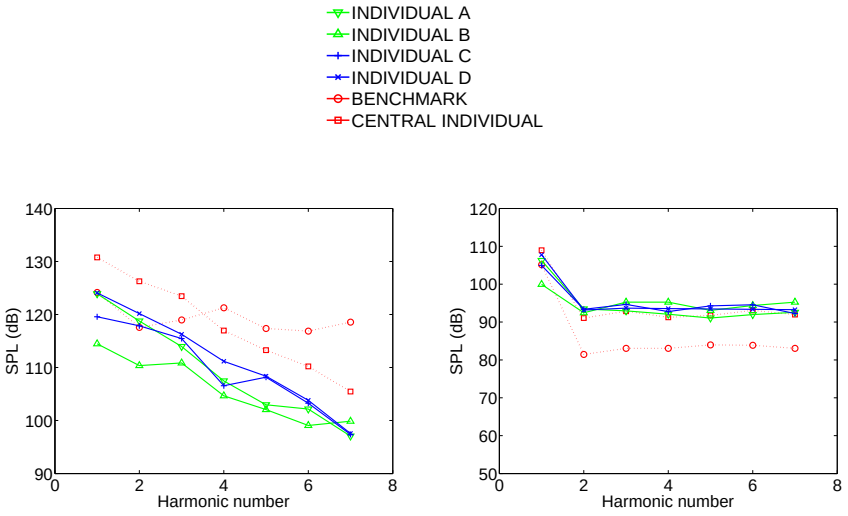

(b) Cruise condition at $J_{CR,2}$.

(c) Take-off/Landing condition at $J_{TO,2}$.

Figure 13.16: Envelope of the BPF-harmonics in the propeller plane (receiver 3).

Individual	A	B	C	D	Benchmark	Central
m (kg)	44.87	43.32	39.54	42.45	35.78	53.19
$\zeta^{TW}_{CR,2}$	0.104	0.110	0.086	0.087	0.069	0.0566
$\zeta^{VM}_{CR,2}$	0.224	0.176	0.142	0.185	0.266	0.499

Table 13.6: Stress criteria at $J_{CR,2}$.

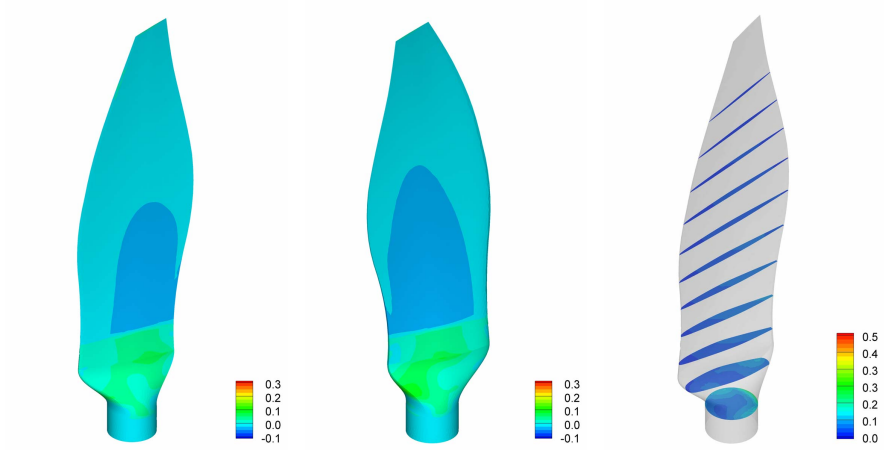

(a) $\zeta^{TW}_{CR,2}$ on the pressure side. (b) $\zeta^{TW}_{CR,2}$ on the suction side. (c) $\zeta^{VM}_{CR,2}$ in the foam core.

Figure 13.17: Stress criteria for individual A in cruise ($J_{CR,2}$).

located inboard of the hump. Except for individual B, the stressed region extends far inboard for up to 3 or 4 maximum chord from the hump. These stresses result from the lumped mass associated with the hump but, given their low values, they do not constitute a structural challenge as such. In the core, the hump does not lead to significant stresses either. The core is the most solicited at the root underneath the trailing-edge. Again, this situation might improve greatly with a more refined structural design. The lower ζ^{TW}- and ζ^{VM}-values for individual C are mainly the consequence of the low blade mass thanks to thinner sections.

In the take-off/landing condition, the centrifugal load is similar to the one in cruise because the RPM is equal between both conditions (see section 11.4). The only change comes from the different blade angle β_{ref} that results in a slight difference in centrifugal twisting moment. Hence it is essentially the change in pressure-load that is responsible for a decrease of the stresses in the shell and an increase in the core for individuals B, C and D when compared to the design cruise condition (see tables 13.6 and 13.7). Only individual A benefits from a decrease of the stresses in the core as well. The analysis of Figs. 13.21 to 13.24 reveals that the maximum solicitation of the shell has moved from the edge of the transition region with the root, to the edge of the transition region with the aerodynamic shape. Individual B is the only exception to this as the highest criterion values still occur on the ridges. Another feature is that the shell on the pressure side of the outboard part (from the end of the transition up to the tip) is less solicited than in the cruise condition whereas the suction side is more solicited with the high stress region extending much more in the chordwise and spanwise directions from the leading- and trailing-edge.

The core has the maximum solicitation kept within the root as was the case in cruise. At other stations, the stresses in the core have the same order of magnitude as in cruise though they have a slimly different pattern.

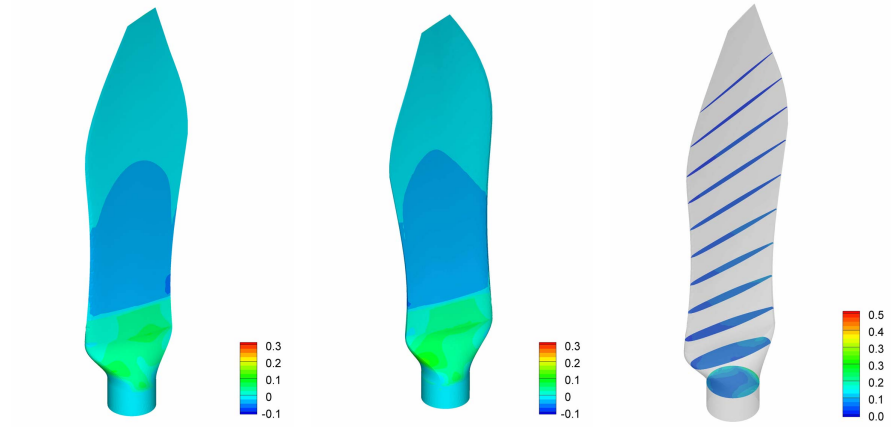

(a) $\zeta_{CR,2}^{TW}$ on the pressure side. (b) $\zeta_{CR,2}^{TW}$ on the suction side. (c) $\zeta_{CR,2}^{VM}$ in the foam core.

Figure 13.18: Stress criteria for individual B in cruise ($J_{CR,2}$).

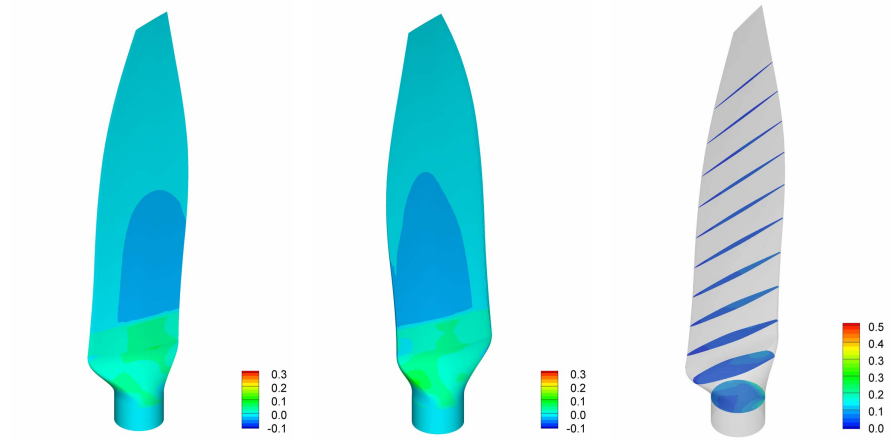

(a) $\zeta_{CR,2}^{TW}$ on the pressure side. (b) $\zeta_{CR,2}^{TW}$ on the suction side. (c) $\zeta_{CR,2}^{VM}$ in the foam core.

Figure 13.19: Stress criteria for individual C in cruise ($J_{CR,2}$).

Individual	A	B	C	D	Benchmark	Central
$\zeta_{TO,2}^{TW}$	0.081	0.050	0.068	0.080	0.090	0.165
$\zeta_{TO,2}^{VM}$	0.191	0.199	0.163	0.191	0.325	0.718

Table 13.7: Stress criteria at $J_{TO,2}$.

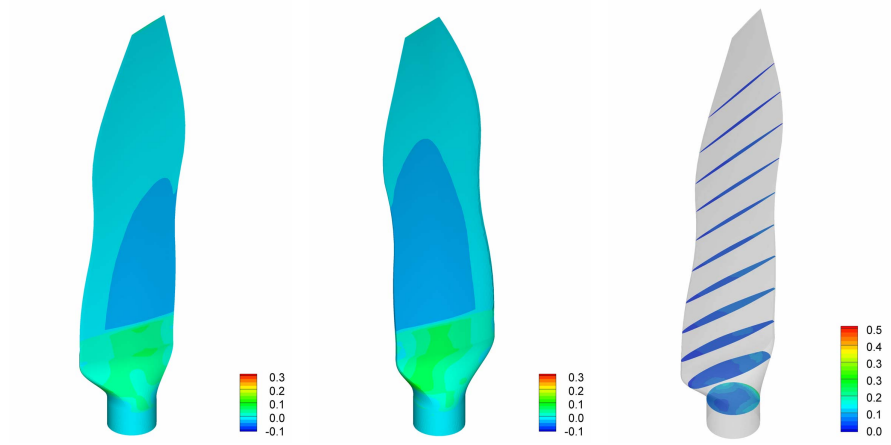

(a) $\zeta_{CR,2}^{TW}$ on the pressure side. (b) $\zeta_{CR,2}^{TW}$ on the suction side. (c) $\zeta_{CR,2}^{VM}$ in the foam core.

Figure 13.20: Stress criteria for individual D in cruise ($J_{CR,2}$).

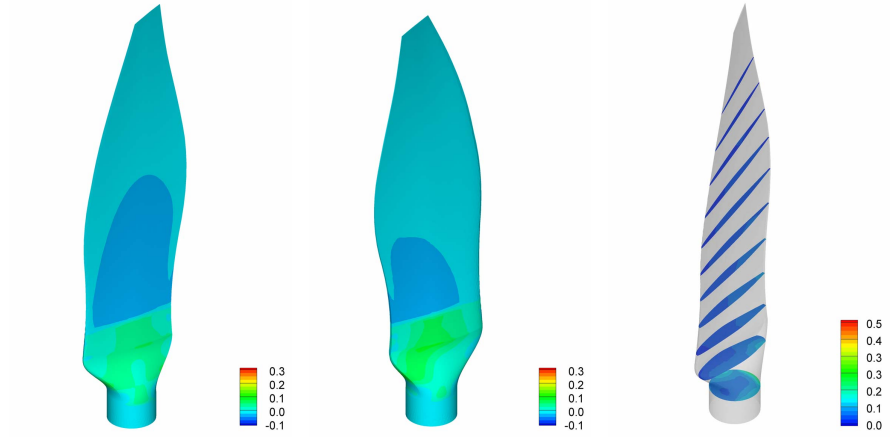

(a) $\zeta_{TO,2}^{TW}$ on the pressure side. (b) $\zeta_{TO,2}^{TW}$ on the suction side. (c) $\zeta_{TO,2}^{VM}$ in the foam core.

Figure 13.21: Stress criteria for individual A in take-off landing condition ($J_{TO,2}$).

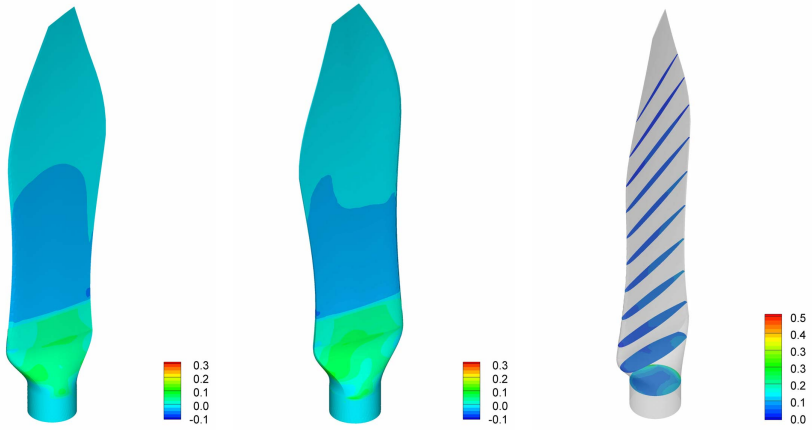

(a) $\zeta_{TO,2}^{TW}$ on the pressure side. (b) $\zeta_{TO,2}^{TW}$ on the suction side. (c) $\zeta_{TO,2}^{VM}$ in the foam core.

Figure 13.22: Stress criteria for individual B in take-off landing condition ($J_{TO,2}$).

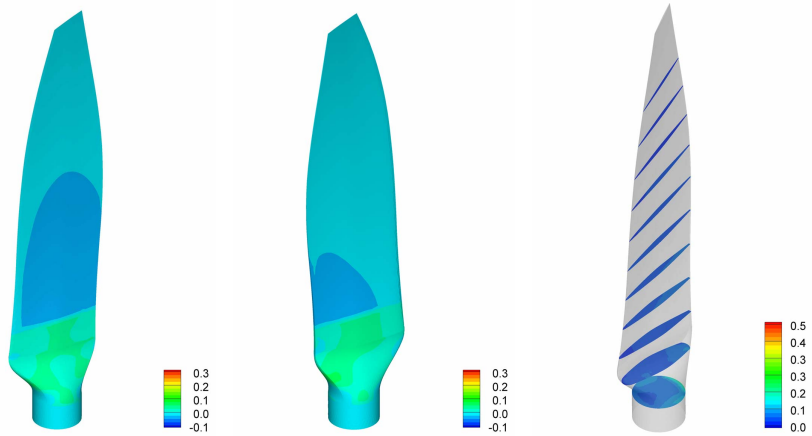

(a) $\zeta_{TO,2}^{TW}$ on the pressure side. (b) $\zeta_{TO,2}^{TW}$ on the suction side. (c) $\zeta_{TO,2}^{VM}$ in the foam core.

Figure 13.23: Stress criteria for individual C in take-off landing condition ($J_{TO,2}$).

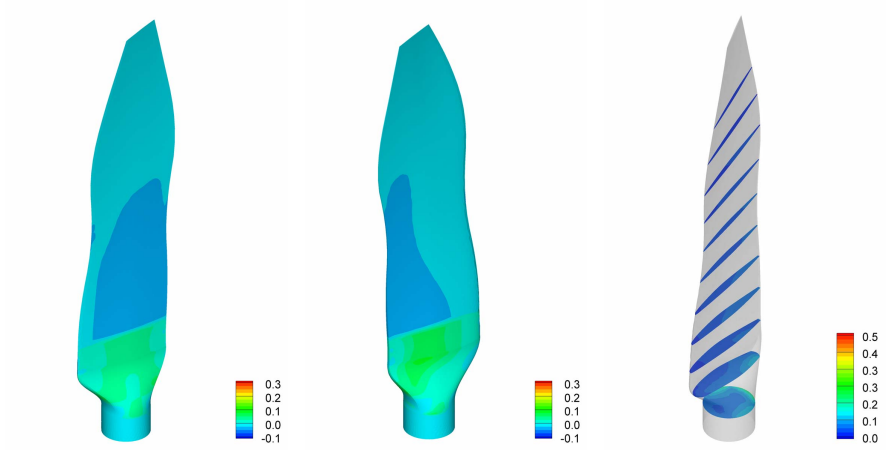

(a) $\zeta_{TO,2}^{TW}$ on the pressure side. (b) $\zeta_{TO,2}^{TW}$ on the suction side. (c) $\zeta_{TO,2}^{VM}$ in the foam core.

Figure 13.24: Stress criteria for individual D in take-off landing condition ($J_{TO,2}$).

13.5 Conclusions

The multi-point and multidisciplinary optimization procedure presented in the current part, includes aerodynamics coupled with aeroacoustics and basic aeroelasticity. It led to a series of blade designs that are compliant with all constraints and offer interesting efficiencies as well as acceptable tonal noise emissions. Here again, the designs feature innovative chord distributions. Moreover, the final designs tend to have low geometrical tip sweep but leading-edge sweep is obtained through the taper induced by the decreasing chord toward the tip. Both peculiarities are the result of the optimization process itself and not an artefact of the parameterization or a limitation of the design space.

The comparative radar chart in Fig. 13.25 illustrates the complexity of the decision to be taken at the end of the optimization process. The four designs that were discussed in more details in this chapter have cruise efficiencies that are close to each other and differ mainly in the tones emitted in the propeller plane as well as the level of stresses during cruise or take-off/landing. The design team is indeed left with a bunch of designs (in the end many of the designs obtained in section 12.3 could be presented on such a chart) with their respective pros and cons but the author purposely leaves this discussion to more appropriate instances.

- Once more, the two-level approach (see section 3.4) proves to be a convenient way to perform optimization. It is efficient, safer than an optimization relying solely on metamodelling, and cost-effective in terms of computational power. The quality of the metamodel is of course crucial in safeguarding the process from inappropriate decisions in the selection step of the evolutionary process. In the present case, the kriging technique is used and offers reliable estimates

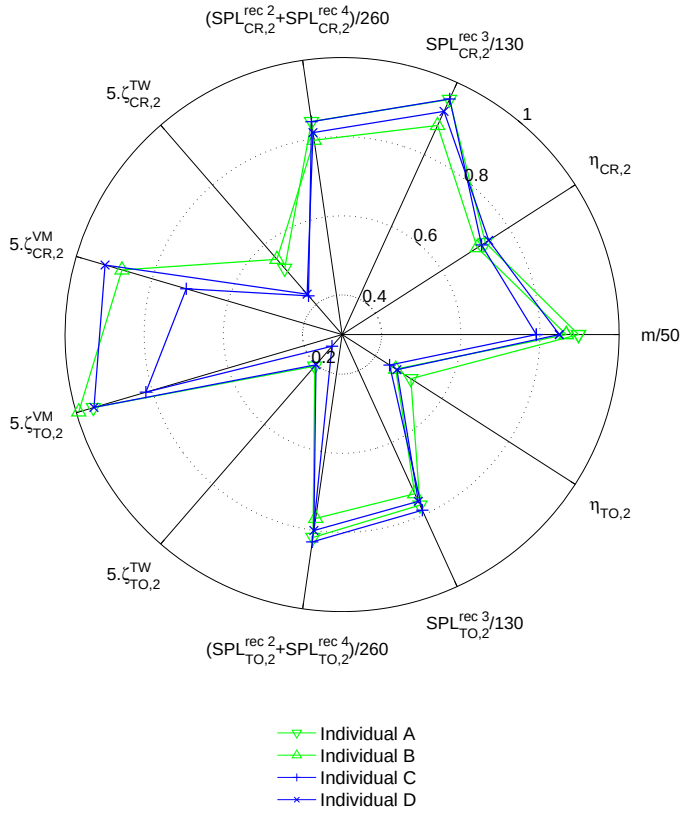

Figure 13.25: Decision chart.

for most performance parameters.

- Despite the efforts undertaken to avoid failure of the high-fidelity analysis due to ill-structured meshes, a high failure rate is still experienced. This somehow raises concerns as it implies that some regions of the search space have been mistakenly deemed as inconvenient and are left unexplored. But this is the price to pay for complete automation of the process with the current mesh-generation software.
- The higher accuracy of the metamodels translates directly in a higher level of compliant individuals (61 among 176 individuals successively analyzed with high-fidelity, representing 34.7%).
- The fact that the objectives (Eqns. 11.2-11.4) respectively stem from a single discipline is the right way to ensure that they truly compete with each other. Their number has been deliberately kept to 3 in order to facilitate the interpretation of the results without the need for complex visualization techniques. The drawback of this choice is of course the necessity to introduce weights in Eqns. 11.2-11.4 and the dependency that comes with them. Once again, the multi-point character is essential not only to guarantee the off-design performance but also in the adaption process so that all individuals are assessed in the correct conditions.
- This time Ω_1-objective was formulated directly in terms of propeller net efficiency η. This efficiently removed the negative influence of the tolerance Δ_T that was found in section 10.4.
- The decision to let the take-off/landing design RPM be the same as the one in the design cruise condition (see section 11.4), gives better correspondence between the optimization process and real-world applications. The drawback of this decision is the increased computational effort that is necessary to generate a mesh once the blade angle β_{ref} has been adjusted to match the desired thrust. This particular step is strongly correlated to the high-failure rate mentioned here before.
- The modifications of the search space by changing the allowable intervals for twist, chord and airfoils resulted in a significant increase of the contribution from the inboard part of the blade to the net thrust. These changes were initiated by the findings of section 10.4.
- Four of the optimized designs were presented with more detail because of their performance in terms of aerodynamics, aeroacoustics or aeroelastics. The four feature a distinct hump in the chord distribution that contributes to a shift of the aerodynamic load from the tip to the inboard part. Interestingly, none of them has high geometrical sweep near the tip even though leading-edge sweep is present in substantial amounts. This sweep is obtained by tapering the chord near the tip.

  From the aerodynamic point of view, these four individuals have enhanced efficiencies in the design and off-design cruise conditions while delivering the required thrust at the all operating points. This leads to a substantial decrease of the required power.

  From the aeroacoustic point of view, all four individuals emit less noise than the initial designs, especially at the higher harmonics in cruise. The thin airfoil

sections and the leading-edge sweep make the loading noise dominant over the thickness noise. As the load is kept constant, this explains why no decrease of the SPL is witnessed between the present optimization and the previous one despite the reduction of the tip speed. The radiation pattern is consistent with blades that feature low geometrical sweep. The four designs have most of the attributes listed at the end of section 6.2.1.1 as beneficial in terms of quadrupole noise. The only exception for this is blade B that exhibits a strong shock along the blade span in cruise. It is therefore suspicious that blade B has also the lowest objective value with respect to the SPL (Ω_2-objective). This shortcoming illustrates the necessity of at least one of the three following solutions:

- either the implementation of quadrupole noise sources and volume integration in the CHA-solver or the use of a permeable integration surface surrounding the blade so that the contribution from quadrupoles is taken into account by the integration on the permeable surface provided the CFD is accurate enough in the domain enclosed by that surface (it is the most accurate solution but with an increased computational cost in both cases);
- either the inclusion of terms in one of the objectives to penalize those individuals that have local flow features that are known to be potent quadrupole noise producers such as shocks (this is a less accurate solution but it comes with a low impact on the computational cost);
- or the use of engineering good sense in the post-processing of the optimization results (this is the most arbitrary but also the least expensive solution).

From an aeroelastic point of view, the four designs have stress-criteria levels that are acceptable at this stage but require additional tailoring and trimming of the whole structure to exploit the full potential of composite materials and reduce blade weight, thence stresses consecutively, to a further extent. The lumped mass associated with the hump does not result in dramatic stress situations.

Part IV

Conclusions

Conclusions

The present multidisciplinary optimization procedure, incorporating the VKI optimization code, is particularly suited for early design stages. Its purpose is to generate, analyze and compare as many blade designs as possible before proposing a limited set of geometries with promising performance. Hence it carries out a comprehensive and efficient search in the design space.

The optimizer based on MODE performs with satisfaction and is able to cope with the discontinuities in the mapping between the search and objective space. Such discontinuities occur because some geometries of a population could not be meshed for example or from the occurrence of non-linear phenomena like shocks. The fact that evolutionary algorithms are population based gives them their good behaviour in this context: they do not rely on the analysis of a single blade design. It is also good practice to combine such an optimizer with a two-level (or more) approach. This is especially true when the computational effort of each single analysis is demanding in time and resources. Metamodels are an interesting option for that purpose. They provide fast estimates and require moderate efforts for their training. With them, generations of individuals can be assessed in a few seconds so that the search toward optima in the objective space is fast when based upon the estimates. Hence the search is conducted in the approximate objective space which is supposed to be in close resemblance with the true objective space. But their accuracy is precisely the major concern. The present results showed how different metamodels lead to different levels of accuracy, depending on the performance parameter that is modelled. Kriging-based models performed significantly better, with one exception, than ANN-metamodels. This suggests the need for a priori investigations about the quality of the proposed metamodel for the particular variable it is intended to predict. In this matter, objectives do not necessarily suffer from moderate inaccuracies but constraints do. They act as go - no go criteria and therefore a small inaccuracy might force a perfectly sound and even promising individual to be withdrawn from the evolutionary process. The second-level consists of more accurate, thus also more demanding, high-fidelity analysis tools. The precious information they deliver is then used to recursively train the metamodel. Doing so, the validity of the metamodel is maintained even in the new regions of the design space that are being searched in. This helps to ensure the overall accuracy, hence relevancy, of the optimization method. It is then evident that final decisions concerning the optima, should rely on the high-fidelity values.

Concerning the elaboration of a computerized blade model, the use of radial distributions as a basis for the description of the blade geometry is effective because they offer a direct translation between a design variable and the blade shape. Major trou-

ble arises when it come to generating a mesh for CFD-analysis. Despite the efforts that were undertaken to circumvent the observed deficiencies, this is still the major cause of failure, at the high-fidelity level. Unfortunately, this implies that many blade designs could not be passed through the CFD-analysis and have therefore been left aside during the evolutionary process. Some of them could have had very interesting performance while other just had an infeasible shape. Fortunately, all that information is not completely lost for the search is conducted in the approximate objective space. If the metamodel is sufficiently accurate in that region, interesting designs should still provide information.

The CFD-tool uses a proven approach to compute the aerodynamic performance. Its results are accurate. For relevant optimization, some output, such as propeller thrust, should be kept constant. This also means that the CFD-tool has to incorporate a mechanism to assure that proposed blade designs are analyzed under that condition. This justifies the use of a multi-point approach where the performance of a design is assessed at different working points. It implies a higher computational cost than a single point solution but the glimpse of the performance curve that is obtained in this way, is crucial in the correct adaptation of the working points so that the required thrust is matched. Moreover, take-off or landing performance of propellers is also quite important so that at least two operating conditions have to be modelled. The cost of such analysis is effectively reduced by modelling an isolated propeller with cyclic boundary conditions so that only a single blade is analyzed. This simplified model delivers performance values that are in close agreement with the experimental ones.

The CHA-tool that was developed and used, is also resting upon a well proven theoretical basis. As long as the assumptions behind formulation 1A of Farassat hold, the results delivered by the present implementation are within the margins set by other codes. One should raise concern when the conditions for the logarithmic singularity occur, i.e. when the projection of the velocity of a point of the blade surface, along the radiation direction, is close to the speed of sound in the surrounding air. But given the finite character of acoustic pressure and energy, the author proposed a truncated approach in which only the first term of a Taylor's series expansion of the singular integrands is considered. This term is finite since it is evaluated at a nearly sonic, but not exactly, condition. This approach is not far from the proposition of R.K. Amiet [18] to obtain a first-hand calculation by just dropping singular terms from the integration. Comparisons have shown that the approximates computed with the present code for singular cases, are within acceptable margins from the more accurate results obtained by more complete codes. The strong point of the present one is its computational cheapness which is more than welcome given the large amounts of blade designs that have to be evaluated under different conditions.

The CSM-tool rests upon a finite elements solver to compute the total mass of the blade as well the stresses resulting from the centrifugal and aerodynamic forces. Only a simplified blade model is implemented and the aeroelastic problem is decoupled from the aerodynamic one. Hence the CSM computations provide a convenient, yet rudimentary, sanity check from a structural point of view. This tool lacks validation because experimental data are not documented on relevant materials.

The first optimization delivered a small amount of optimized blades (28) with respect to aerodynamics and aeroacoustics. All of them satisfy an extensive set of operational constraints. Moreover, this first optimization pointed out the weaknesses

of the way the optimization method and high-fidelity tools were implemented, particularly in terms of ranges for the design variables and of mesh generation. The formulation of the aerodynamic objective in terms of power coefficient also turned out to be rather a weak way to improve the propulsive efficiency because of the necessary tolerances on the required thrust. The detailed analysis of some designs with particular performance revealed also interesting geometrical features. All blades feature some kind of hump, i.e. a rather abrupt change in chord, and a few have even low geometrical sweep. Nevertheless, they offer small improvement in terms of efficiency but a substantial one in terms of noise.

The second optimization is performed with complete integration of the CFD, CHA and CSM tools. It provided a set of 61 optimized designs that are fully compliant with operational as well as structural constraints. Designs with low geometrical sweep and humps emerged and come with a substantial increase in efficiency this time, but a moderate decrease of the emitted noise. Fortunately, the hump does not cause unacceptable levels of stresses. Even though this optimization performed better than the previous one, it still suffers from a high failure rate due to the difficulty to obtain a correct mesh and the difficulty to predict the correct blade angle $\beta_{ref,TO}$ for a blade whose performance is yet completely unknown.

An efficient procedure for multidisciplinary optimization is developed and successfully tested. Both optimizations highlight the feasibility and the capabilities of multidisciplinary optimization when applied to propeller blades for high-speed aircraft. It is proficient in exploring the search space for a moderate cost and in delivering designs with features that are worth further consideration. Detailed analysis should investigate first whether no additional improvement could be yielded with minor changes to the design. The precious knowledge of an experienced design team should be used for that purpose. Then, in a second phase, the design should be submitted to all analyses required in the development of a new blade, with inclusion of coupling between disciplines.

Recommendations for future work

In the perspective of optimization, other mesh generation packages on the market seem to offer enhanced capabilities for propeller blade meshing because they where developed with long, highly twisted, swept blades in mind. Provided it can work autonomously, such a mesher could help increase the success rate of the high-fidelity analysis. This would not only directly increase the number of optimized designs, it would also increase the accuracy of the metamodel, thereby enhancing the search.

It is the author's belief that there are probably too many high-level interactions between the design variables. One such example is the one between the variables affecting the airfoil shape and those controlling twist. The elemental lift, for example, is mainly controlled by the shape of the front part of the airfoil, but also by its angle of attack with respect to the local flow. Hence a excellent airfoil shape that would be evaluated at a wrong angle, would lead to poor performance and the information concerning that good shape would be lost. It is the author's belief that airfoil shapes should ideally be optimized in a separate procedure that is embedded in the global optimization. The purpose of the sub-optimization should be to deliver the best possible airfoil shape for each given blade design. This would circumvent and even

overcome the interactions at the expense of the complexity of the procedure and its global cost but would maintain the freedom of design because the airfoil shape would still influence all disciplines. Another workaround would be to use a single set of airfoil shapes resulting from a $2D$ or pseudo-$3D$ optimization in transonic conditions similar the those expected from the intended propeller. This option is much cheaper in terms of computational cost but it decreases the potential of the design space because the airfoil shape would not influence the aeroacoustic and aeroelastic results anymore. So it is a difficult choice. Another such example is the spinner. It is known to have a significant influence on the flow, with differences by up to 3 efficiency points [203]. So it is probably safer, in terms of optimization, to obtain first an optimized shape and then gather additional efficiency points by refining the spinner shape.

The emergence of humps on all of the optimized shapes raises the question of their true influence on both flow and noise, as a first step. These humps are a true result of the optimization as shapes with a flatter chord distribution existed in the populations but were outperformed. A comparative study should be carried out to systematically investigate, with highly-detailed numerical simulations, the effect of humps when combined with blades having low, moderate and high geometrical sweep toward the tip. Such a study should of course consider these blades both at constant thrust and constant RPM.

Appendices

Appendix A

Propellers used for validation

This appendix presents the propellers used for validation purposes and their main geometrical features. The driving factor behind the choice of these propellers in particular is the availability of geometrical and performance data as well as their relevance in terms of advanced features such as sweep and planform shape. Among the NASA SR-X series, the SR-1 and SR-3 profans were chosen because acoustic data are available at various operating conditions.

A.1 NACA 4-(5)(05)-041

Number of blades	4
Geometrical sweep at tip	unswept
Blade sections	NACA 16-series
at 75%-radius	
Chord ratio b/D	0.087
Lift coefficient C_{ld}	0.49
Thickness ratio t/b	0.045
Design conditions	
M_∞	0.8
β_{ref}	60°
J	3.2
C_P	1.4
C_T	0.245
η	0.56
M_{tip}	1.12

Table A.1: Main propeller characteristics (at design condition) from [246].

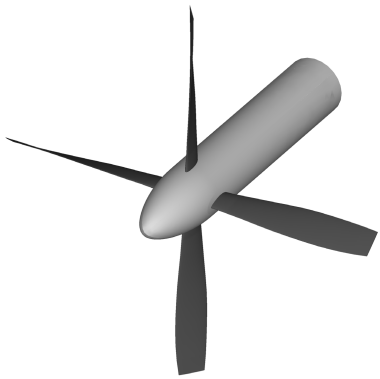

Figure A.1: NACA 4-(5)(05)-041 propeller.

A.2 NACA 4-(0)(03)-059

Number of blades	3
Geometrical sweep at tip	unswept
Blade sections	NACA 16-series
at 75%-radius	
Chord ratio b/D	0.12
Lift coefficient C_{ld}	0.0
Thickness ratio t/b	0.035
Design conditions	
M_∞	0.95
β_{ref}	NA
J	2.2
C_P	NA
C_T	NA
η	NA
M_{tip}	NA

Table A.2: Main propeller characteristics (at design condition) from [90].

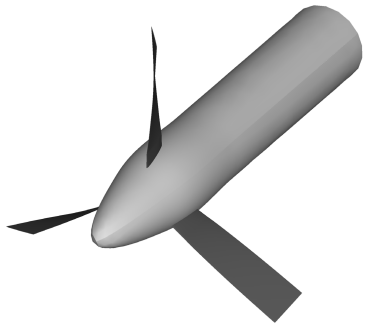

Figure A.2: NACA 4-(0)(03)-059 propeller.

A.3 NASA SR-1

Number of blades	8
Geometrical sweep at tip	27°
Blade sections	NACA 16- and 65-series
at 75%-radius	
Chord ratio b/D	0.144
Lift coefficient C_{ld}	0.125
Thickness ratio t/b	0.024
Design conditions	
M_∞	0.8
β_{ref}	55°
J	3.06
C_P	1.7
C_T	0.44
η	0.79
M_{tip}	1.17

Table A.3: Main propeller characteristics (at design condition) from [30].

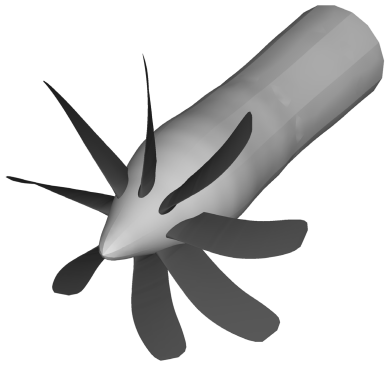

Figure A.3: NASA SR-1 propfan.

A.4 NASA SR-3

Number of blades	8
Geometrical sweep at tip	45°
Blade sections	NACA 16- and 65-series
at 75%-radius	
Chord ratio b/D	0.182
Lift coefficient C_{ld}	0.23
Thickness ratio t/b	0.024
Design conditions	
M_∞	0.8
β_{ref}	60.5°
J	3.06
C_P	1.695
C_T	0.43
η	0.782
M_{tip}	1.14

Table A.4: Main propeller characteristics (at design condition) from [259].

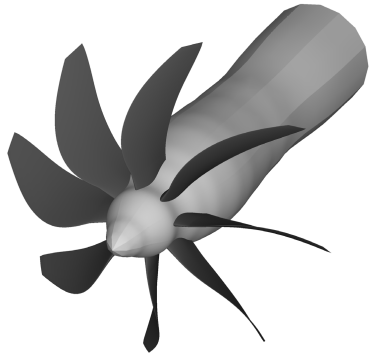

Figure A.4: NASA SR-3 propfan.

Appendix B

Interpolation of pressure

The accuracy of the pressure interpolation described in section 7.3.3.2 is assessed by comparison of the pressure coefficient (C_p) distributions obtained by the CFD-solver with those obtained after interpolation. These are shown for various radii (from 35% to 95% by increments of 10%). Note that in this chapter, the Mach number used to compute C_p at a radius r is $M(r) = \sqrt{M_\infty^2 + (\omega r/c_\infty)^2}$. The benchmark as well as the central individual and individuals A and D of part II, are considered at different advance ratios in the take-off/landing and cruise conditions.

B.1 Take-off/Landing condition

Figs. B.1-B.4 show the C_p-contours in take-off/landing conditions at $M_\infty = 0.2$. This particular condition is responsible for the highest pressure loads on the blades. These figures reveal the excellent agreement that is obtained whether the pressure gradient is positive, negative or non-existing. The results are of particularly good quality even in the region close to the leading edge where geometrical curvature is strong and poor interpolation could have occurred because of data sites from the suction side influencing the interpolation on the pressure side and vice-versa.

Isobars on the pressure and suction sides of the blade are plotted in Fig. B.1 for individual D as a matter of example. The match is excellent despite some slight differences on the pressure side in the region between 75% and 85% radius. These small discrepancies should not result in significantly different stress states. Note that the interpolated isobars stop at lower radius at the edge of the outer structural shell of the blade as explained in section 7.3.1.

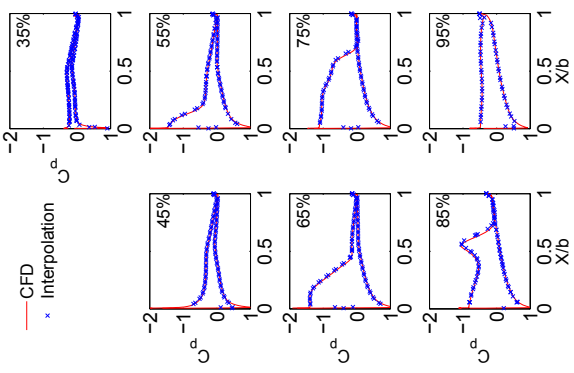

Figure B.1: Benchmark at $J_{TO,2}$.

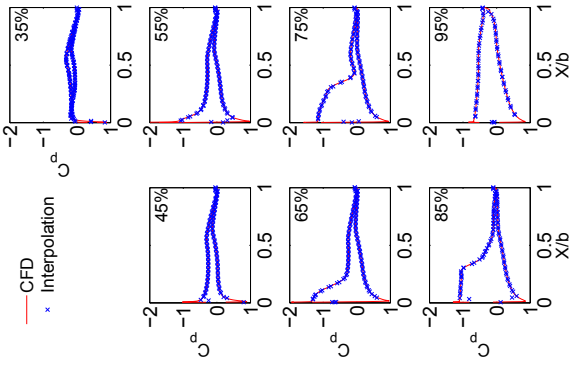

Figure B.2: Central Individual at $J_{TO,2}$.

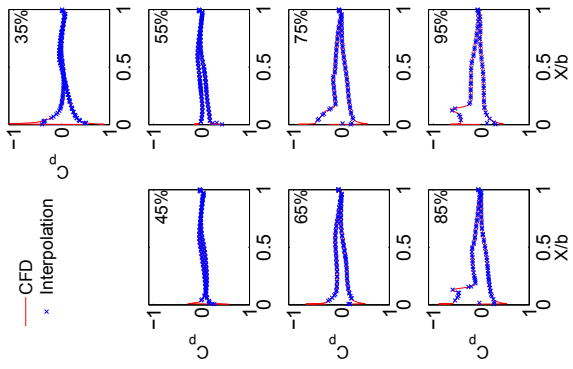

Figure B.3: Propeller A at $J_{TO,3}$.

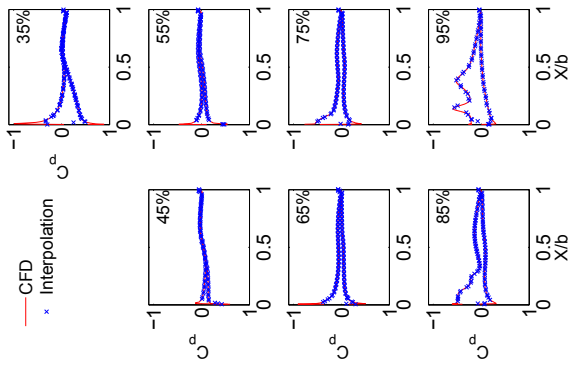

Figure B.4: Propeller D at $J_{TO,3}$.

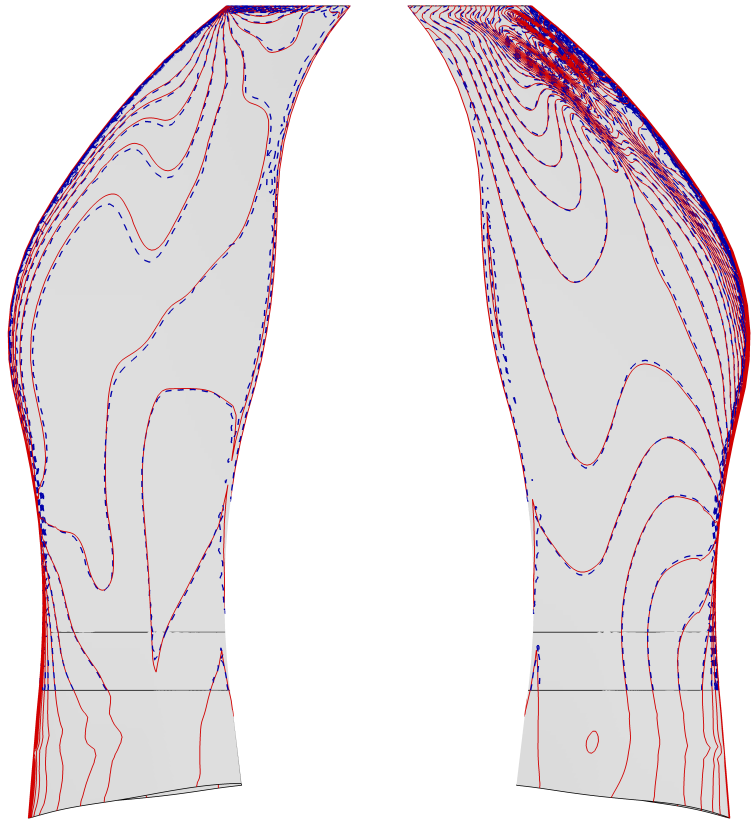

(a) Pressure side. (b) Suction side.

Figure B.5: Isobars on propeller D at $J_{TO,3}$. (— for CFD isobars, – – for interpolated isobars)

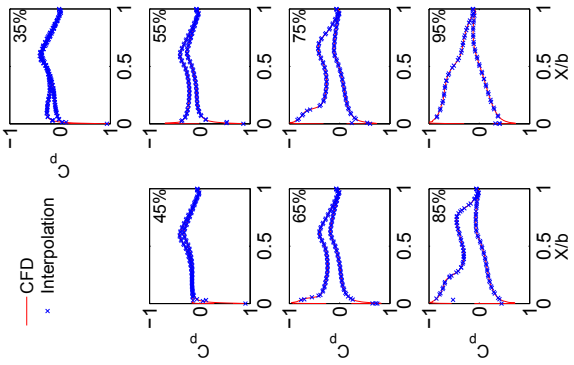

Figure B.6: Benchmark at $J_{CR,2}$.

B.2 Cruise condition

For the cruise condition at $M_\infty = 0.75$, the same comparisons between C_p-contours are given in Figs. B.6-B.9. For individuals A and D, the lowest advance ratio ($J_{CR,1}$) is used so that the accuracy of the interpolator is tested on pressure distributions with the highest non-linearities. For individual A (Fig. B.8), the shock present at 55%, 65% and 85% is nicely preserved through the interpolation.

In example, the isobars on the suction and pressure sides of individual D are shown in Fig. B.2. The correspondence is again excellent.

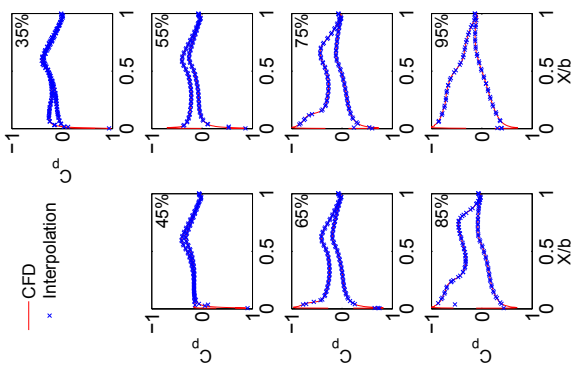

Figure B.7: Central Individual at $J_{CR,2}$.

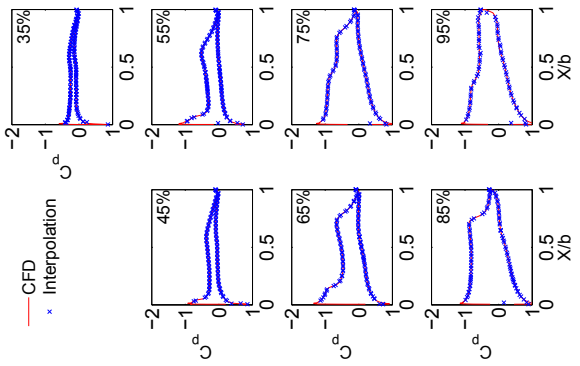

Figure B.8: Propeller A at $J_{CR,1}$.

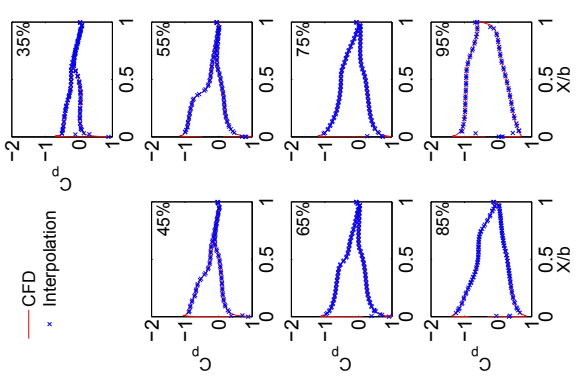

Figure B.9: Propeller D at $J_{CR,1}$.

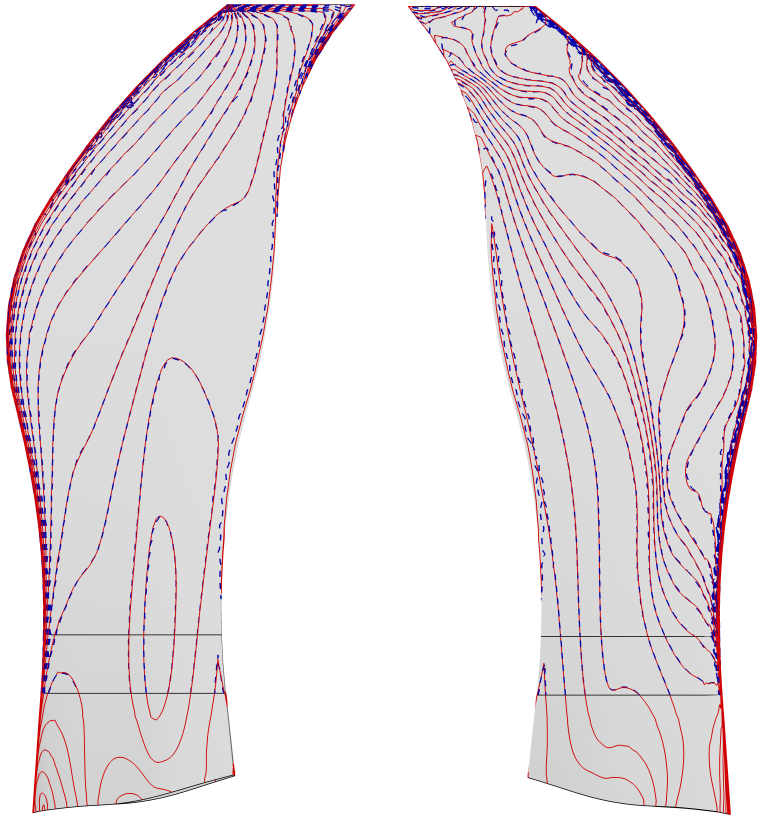

(a) Pressure side. (b) Suction side.

Figure B.10: Isobars on propeller D at $J_{CR,1}$. (— for CFD isobars, – – for interpolated isobars)

List of Figures

List of Tables

LIST OF TABLES

Bibliography

[1] Matlab v7.4.0.287 (r2007a). www.mathworks.com, 2007. The MathWorks Inc.

[2] Regional turboprop resurgence continues; jet demand shifts upward. www.asd-network.com, December 2007.

[3] Aviation gas turbine forecast. www.forecastinternational.com, Newton (USA), 2008.

[4] Bombardier's greener turboprop. http://findarticles.com, April 2008.

[5] Gambit 2.4.6. www.ansys.com, 2008. Ansys Inc.

[6] Prince of Wales cuts carbon footprint with cleaner turboprops. VLM booklet, July 1 2008. www.flyvlm.com.

[7] Tgrid 5.0.6. www.ansys.com, 2008. Ansys Inc.

[8] Differential Evolution Homepage. www.icsi.berkeley.edu/∼storn/code.html, April 2009.

[9] Fluent 12.0.16. www.ansys.com, 2009. Ansys Inc.

[10] Samcef v13.1-02. www.samtech.com, 2009. Samtech s.a.

[11] Turboprops considered for US Army ACS (Aerial Common Sensor). Air Forces monthly Nr. 257, August 2009.

[12] Light Combat Aircraft. Aerospace America, February 2010. pp 10-11.

[13] Material property data (Sawbones solid rigid polyurethane foam). www.matweb.com, August 2010.

[14] A&P Technology. http://www.braider.com, Cincinnati (USA), January 2011.

[15] B&F Carter. http://www.bfcarter.co.uk, Bolton (United Kingdom), January 2011.

[16] Abbas, H. A., Sarker, R., and Newton, C. PDE: A Pareto-frontier differential evolution approach for multi-objective optimization problems. In *IEEE Congress on Evolutionary Computation* (Piscataway (USA), May 27-30 2001), vol. 2, IEEE, pp. 971–978.

[17] Abbott, I., von Doenhoff, A., and Stivers Jr, L. Summary of airfoil data. Report R-824, NACA, NACA-Langley aeronautical laboratory (USA), 1945.

[18] Amiet, R. Thickness noise of a propeller and its relation to blade sweep. *Journal of Fluid Mechanics 192* (July 1988), 535–560.

[19] Anderson Jr, J. *Fundamentals of aerodynamics*, 3rd ed. McGraw-Hill, New York (USA), 2001.

[20] Ardavan, H. The breakdown of the linearized theory and the role of quadrupole sources in transonic rotor acoustics. *Journal of Fluid Mechanics 226* (1991), 591–624.

[21] Ardavan, H. Asymptotic analysis of the radiation by volume sources in supersonic rotor acoustics. *Journal of Fluid Mechanics 266* (1994), 33–68.

[22] Ashcraft, C., Grimes, R., and Lewis, J. Accurate symmetric indefinite linear equation solvers. *SIAM Journal on Matrix Analysis and Applications 20*, 2 (1998), 513–561.

[23] Ashcraft, C., Grimes, R., Lewis, J., Peyton, B., and Simon, H. Progress in sparse matrix methods for large linear systems on vector supercomputers. *International Journal of Supercomputer Applications 1*, 4 (1987), 10–30.

[24] Babu, B. *Advances in Computational Optimization and its Applications*. Universities Press, Hyderabad (India), 2007, ch. Improved differential evolution for single- and multi-objective optimization: MDE, MODE, NSDE & MNSDE, pp. 24–30.

[25] Babu, B., Mubeen, J., and Chakole, P. Multiobjective optimization using Differential Evolution. *TechGenesis-The Journal of Information Technology 2*, 2 (2005), 4–12.

[26] Banke, J. Beauty of future airplanes is more than skin deep. www.nasa.gov, May 2010.

[27] Bansal, P., Arseneaux, P., Smith, A., Turnberg, J., and Brooks, B. Analysis and test evaluation of the dynamic response and stability of three advanced turboprop models. Contractor Report CR 174814, NASA, NASA Lewis Research Center, August 1987.

[28] Bellman, R. *Adaptive control processes: A guided tour*. Princeton University Press, New York (USA), 1961.

[29] Billman, L., Ladden, R., Turnberg, J., Gruska, C., and Leishman, D. Large scale prop-fan structural design study - volume i: Initial concepts. Contractor Report CR 174992, National Aeronautics and Space Administration, NASA Lewis research center (USA), 1989.

[30] Black, D., Menthe, R., and Wainauski, H. Aerodynamic design and performance testing of an advanced 30° swept, eight bladed propeller at mach numbers from 0,2 to 0,85. Contractor Report CR 3047, National Aeronautics and Space Administration, NASA Lewis research center (USA), 1978.

[31] Bonnassies, O. Atr poised for production ramp-up, September 21 2010.

[32] Borst, H. Summary of propeller design procedure and data. volume i: aerodynamic design and installation. Technical Report 73-34A, Army Air Mobility Research and Development Laboratory, Rosemont (USA), November 1973.

[33] Bousquet, J. Méthodes aérodynamiques utilisées en France pour l'étude des hélices pour avions rapides. In *Aerodynamics and Acoustics of propellers* (Toronto (Canada), October 1984), no. AGARD CP-366, Advisory Group for Aerospace Research and Development.

[34] Bousquet, J., and Gardarein, P. Recent improvements in propeller aerodynamic computations. In *18th AIAA Applied Aerodynamics Conference and Exhibit* (Denver (USA), August 14-17 2000).

[35] Boyle, F. An efficient procedure for viscous propeller flow field calculations. In *38th AIAA/ASME/SAE/ASEE Joint propulsion conference and exhibit* (Indianapolis (USA), July 2002), AIAA.

[36] Boyle, F., O'Flaherty, M., and Eaton, J. Three-dimensional Euler solutions for axisymmetric and non-axisymmetric advanced propeller flows. In *35th AIAA/ASME/SAE/ASEE Joint Propulsion Conference and Exhibit* (Los Angeles (USA), June 20-24 1999), no. AIAA 99-31187, AIAA.

[37] Boyle, F., O'Flaherty, M., and Eaton, J. Validation of efficient Euler algorithms for advanced propellers under transonic and subsonic conditions. In *17th Applied Aerodynamics Conference* (Norfolk (USA), June 28 - July 1 1999), no. AIAA 99-3228, AIAA.

[38] Braybrook, R. The propeller revival. *Armada International 22* (August-September 1998), 12–20.

[39] Brentner, K. Prediction of helicopter rotor discrete frequency noise: A computer program incorporating realistic blade motions and advanced acoustic formulation. Technical Memorandum TM-87721, NASA, NASA Langley Research Center (USA), October 1 1986.

[40] Brentner, K. Using finite volume methods for aeroacoustics. In *Computational Acoustics: scattering, Gaussian beams and aeroacoustics* (Amsterdam (Netherlands), 1990), D. Lee, A. Cakmak, and R. Vichnevetsky, Eds., vol. 2 of *Proceedings of the 2nd IMACS Symposium on Computational Acoustics*, IMACS, Elsevier Science Publishers, pp. 269–282.

[41] Brentner, K., and Farassat, F. Helicopter noise prediction: the current status and future direction. *Journal of Sound and Vibration 170*, 5 (1994), 79–96.

[42] Brentner, K., and Farassat, F. Analytical comparison of the acoustic analogy and Kirchhoff formulation for moving surfaces. *AIAA Journal 36*, 8 (August 1998), 1379–1386.

[43] Brentner, K., and Farassat, F. Modeling aerodynamically generated sound of helicopter rotors. *Progress in Aerospace Sciences 39* (2003), 83–120.

[44] Brentner, K., and Holland, P. An efficient and robust method for computing quadrupole noise. *Journal of the American Helicopter Society 42*, 2 (April 1997), 172–181.

[45] Brooks, B. Acoustic measurement of three prop-fan models. In *6th AIAA Aeroacoustics conference* (Hartford (USA), June 1980), no. AIAA 80-0995, AIAA.

[46] Brooks, B., and Mackall, K. Measurement and analysis of acoustic flight test data for two advanced design high speed propeller models. In *22nd Aerospace Sciences Meeting* (Reno (USA), January 9-12 1984), no. AIAA 84-0250.

[47] Brown, K., Harvey, P., and Chamis, C. Structural tailorlng of advanced turboprops. In *28th Structures, Structural Dynamlcs and Materlals Conference,* (Monteray, April 6-8 1987), no. AIAA 87-0753, AIAA, pp. 827–837.

[48] Brès, G., Pérot, F., and Freed, D. A Ffowcs Williams – Hawkings solver for Lattice- Boltzmann based computational aeroacoustics. In *16th AIAA/CEAS Aeroacoustics Conference* (Stockholm (SWEDEN), June 7-9 2010), no. AIAA 2010-3711, AIAA.

[49] Burger, C. *Propeller performance analysis and multidisciplinary optimization using a genetic algorithm.* PhD thesis, Auburn University, Auburn (USA), December 17 2007.

[50] Byun, J.-H., and Chou, T.-W. *Stress-strain behavior of 3-D braided composites*, vol. MD-Vol 29. ASME, New York (USA), 1991.

[51] Campbell, R. An approach to constrained aerodynamic design with application to airfoils. Technical Paper TP-3260, NASA, November 1992.

[52] Carley, M. *Time domain calculation of noise generated by a propeller in a flow.* Ph. d. thesis, Trinity College - Department of Mechanical Engineering, Dublin (Ireland), October 1996.

[53] Carley, M. Propeller noise fields. *Journal of Sound and Vibration 233*, 2 (2000), 255–277.

[54] Casalino, D. *Analytical and numerical methods in vortex-body aeroacoustics.* PhD thesis, Politechnico di Torino and Ecole Centrale de Lyon, 2002. 2002-13.

[55] Casalino, D. An advanced time approach for acoustic analogy predictions. *Journal of Sound and Vibration 261* (2003), 583–612.

[56] Celik, I., Ghia, U., Roache, P., Freitas, C., Coleman, H., and Raad, P. Procedure for estimation and reporting of uncertainty due to discretization in CFD applications. *Journal of Fluids Engineering 130*, 7 (July 2008), 1–4.

[57] Chang, I., Torres, F., and Tung, C. Geometric analysis of wing sections. Technical Memorandum TM-110346, NASA, NASA Ames Research Center, April 1995.

[58] Chase, M., and DeLong, M. The move-up market: Entry-level market movers - turboprops to VLJs, August 2007.

[59] Chattopadhyay, A., Wells, V., McCarthy, T., and Han, A. An integrated optimum design approach for high speed prop-rotors including acoustic constraints. Contractor Report CR 193222, NASA, June 1993.

[60] Cheeseman, I., Lawrence, C., Woolford, C., and Holmes, T. Reinforced plastic blades, January 1971.

[61] Cho, J., and Lee, S.-C. Propeller blade shape optimization for efficiency improvement. *Computers and Fluids 27*, 3 (1998), 407–419.

[62] Cichocki, A., and Unbehauen, R. *Neural networks for optimization and signal processing.* Wiley & sons, New York (USA), 1994.

[63] Coello, C., and Veldhuyzen, D. V. *Evolutionary algorithms for solving multi-objective problems.* Kluwer Academic Publishers, New York (USA), 2002.

[64] Conway, J. Analytical solutions for the actuator disk with variable radial distribution of load. *Journal of Fluid Mechanics 297* (1995), 327–355.

[65] Conway, J. Exact actuator disk solutions for non-uniform heavy loading and slipstream contraction. *Journal of Fluid Mechanics 365* (1998), 235–267.

[66] Crighton, D., and Parry, A. Asymptotic theory of propeller noise - part ii: Supersonic single-rotation propeller. *AIAA Journal 29*, 12 (1991), 2031–2037.

[67] Daigneault, R., and Hall, D. Advanced propeller technology for new commuter aircraft. *Society of Automotive Engineers* - (1983), 2454–2464. Art. Nb. 820720.

[68] Dasgupta, D., and Michalewicz, Z. *Evolutionary Algorithms - An overview*. Springer-Verlag, Berlin (Germany), 1997.

[69] Davies, S., McCarthy, R., and Watts, R. Devices of fibrous-reinforced plastic material, May 1972.

[70] De Gennaro, M., Caridi, D., and Pourkashanian, M. Ffowcs williams-hawkings acoustic analogy for simulation of NASA SR-2 propeller noise in transonic cruise condition. In *V^th European Conference on Computational Fluid Dynamics* (Lisbon (Portugal), June 14-17 2010), ECCOMAS.

[71] Deb, K. *Multi-objective optimization using evolutionary algorithms*. John Wiley & Sons, United Kingdom, 2004.

[72] Deb, K., Agrawal, S., Pratap, A., and Meyarivan, T. A fast ellitist non-dominated sorting genetic algorithm for multi-objective optimization: NSGA-II. In *6th International Conference on Parallel Problem Solving from Nature* (Paris (France), September 16-20 2000), M. Schoenauer, K. Deb, G. Rudolph, X. Yao, E. Lutton, J. J. Merelo, and H.-P. Schwefel, Eds., Springer Verlag, pp. 849–858.

[73] Demay, D. Strong european bizav growth predicted through 2015, August 2008.

[74] di Francescantonio, P. A new boundary integral formulation for the prediction of sound radiation. *Journal os Sound and Vibration 202*, 4 (1997), 491–509.

[75] Dittmar, J. Observations from varying the lift and drag inputs to a noise prediction method for supersonic helical tip speed propellers. Technical Memorandum TM-83797, NASA, 1984.

[76] Dittmar, J., and Joracki, R. Additional noise data on the SR-3 propeller. Technical Memorandum TM-81736, NASA, NASA Lewis Research Center (USA), May 1981.

[77] Dittmar, J., and Joracki, R. Noise of the SR-3 propeller model at 2° and 4° angle of attack. Technical Memorandum TM-82738, NASA, NASA Lewis Research Center (USA), December 1981.

[78] Dittmar, J., Joracki, R., and Blaha, B. Tone noise of three supersonic helical tip speed propellers in a wind tunnel. Technical Memorandum TM-79167, NASA, NASA Lewis Research Center (USA), June 1979.

[79] Dittmar, J., and Lasagna, P. A preliminary comparison between the SR-3 propeller noise in flight and in a wind tunnel. Technical Memorandum TM-82805, NASA, NASA Lewis Research Center and Dryden Flight Research Center (USA), April 1982.

[80] Drela, M., and Giles, M. Viscous-inviscid analysis of transonic and low Reynolds number airfoils. *AIAA Journal 25*, 10 (October 1987), 1347–1355.

[81] Dunn, M., and Farassat, F. State-of-the-art of high-speed propeller noise prediction - A multidisciplinary approach and comparison with measured data. In *13th AIAA Aeroacoustics Conference* (Tallahassee (USA), October 22-24 1990), no. AIAA 90-3934, AIAA.

[82] Dunn, M., and Farassat, F. High speed propeller noise prediction - A multidisciplinary approach. *AIAA Journal 30*, 7 (July 1992), 1716–1723.

[83] Dunn, M., and Tarkenton, G. User's manual for the Langley high speed propeller noise prediction program (dfp-atp). Contractor Report CR 4208, NASA, NASA Langley Research Center (USA), 1989.

[84] Dunn, M., and Tarkenton, G. Computational methods in the prediction of advanced subsonic and supersonic propeller induced noise - ASSPIN user's manual. Contractor Report CR 4434, NASA, NASA Langley Research Center (USA), April 1992.

[85] Dyn, N., Levin, D., and Rippa, S. Numerical procedures for surface fitting of scattered data by radial functions. *SIAM Journal on Scientific and Statistical Computing (Society for Industrial and Applied Mathematics) 7*, 2 (April 1986), 639–659.

[86] Edge, E. Stress-based Grant-Sanders method for predicting failure of composite laminates. *Composites Science and Technology 58* (1998), 1033–1041.

[87] Edgerton, D. *The shock of the old: technology and global history since 1900.* Oxford University Press, New York (USA), 2007.

[88] Elchuri, V., and Smith, G. Flutter analysis of advanced turbopropellers. *AIAA Journal 22*, 6 (June 1984), 801–802.

[89] Epstein, B., Peigin, S., and Tsach, S. A new efficient technology of aerodynamic design based on CFD driven optimization. *Aerospace Science and Technology 10* (2006), 100–110.

[90] Evans, A., and Liner, G. A wind-tunnel investigation of the aerodynamic characteristics of a full-scale supersonic-type three-blade propeller at Mach numbers to 0,96. Report R-1375, NACA, NACA-Langley aeronautical laboratory (USA), 1953.

[91] Eversman, W. The effect of the wind tunnel wall boundary layer on the acoustic testing of propellers. In *12th Aeroacoustics Conference* (San Antonio (USA), April 10-12 1989), no. AIAA 89-1097, AIAA.

[92] Falkner, V. The calculation of aerodynamic loading on surfaces of any shape. Reports & Memoranda 1910, Aeronautical Research Committee, Great Britain, 1943.

[93] Farassat, F. Theory of noise generation from moving bodies with an application to helicopter rotors. Technical Report R-451, NASA, 1975.

[94] Farassat, F. Linear acoustic formulas for calculation of rotating blade noise. *AIAA Journal 19*, 9 (September 1981), 1122–1130.

[95] Farassat, F. Theoretical analysis of linearized acoustics and aerodynamics of advanced supersonic propellers. In *Aerodynamics and Acoustics of Propellers* (Toronto (Canada), October 1-4 1984), no. AGARD CP-366 (10), AGARD, pp. 1–15.

[96] Farassat, F. Prediction of advanced propeller noise in the time domain. *AIAA Journal 24*, 4 (April 1986), 578–584.

[97] Farassat, F. Quadrupole source in prediction of the noise of rotating blades - A new source description. In *11th AIAA Aeroacoustics Conference* (Sunnyvale (USA), October 19-21 1987), no. AIAA 87-2675, AIAA.

[98] Farassat, F. Introduction to generalized functions with applications in aerodynamics and acoustics. Technical Paper TP-3428, NASA, 1994.

[99] Farassat, F. The kirchhoff formulas for moving surfaces in aeroacoustics - the subsonic and supersonic cases. Technical Memorandum TM-110285, NASA, September 1996.

[100] Farassat, F. Derivation of formulations 1 and 1a of Farassat. Technical Memorandum TM-2007-214853, NASA, NASA Langley Research Center (USA), March 2007.

[101] Farassat, F., and Brentner, K. The acoustic analogy and the prediction of the noise of rotating blades. *Theoretical and Computational Fluid Dynamics 10* (1998), 155–170.

[102] Farassat, F., and Brown, T. A new capability for predicting helicopter rotor and propeller noise including the effect of forward motion. Technical Memorandum TM X-74037, NASA, June 1977.

[103] Farassat, F., and Casper, J. Some analytic results for the study of broadband noise radiation from wings, propellers and jets in uniform motion. *Journal of Aeroacoustics 2*, 3 & 4 (2003), 335–350.

[104] Farassat, F., Dunn, M., Tinetti, A., and Nark, D. Open rotor noise prediction methods at NASA Langley - A technology review. In *15th AIAA/CEAS Aeroacoustics Conference* (Miami (USA), May 11-13 2009), no. AIAA 2009-3133, AIAA.

[105] Farassat, F., and Myers, M. Extension of Kirchhoff's formula to radiation from moving sources. *Journal of Sound and Vibration 123*, 3 (1988), 451–460.

[106] Farassat, F., and Myers, M. An analysis of the quadrupoles noise source of high speed rotating blades. In *Computational Acoustics: scattering, Gaussian beams and aeroacoustics* (Amsterdam (Netherlands), 1990), D. Lee, A. Cakmak, and R. Vichnevetsky, Eds., vol. 2 of *Proceedings of the 2nd IMACS Symposium on Computational Acoustics*, IMACS, Elsevier Science Publishers, pp. 227–240.

[107] Farassat, F., and Myers, M. Aeroacoustics of high speed rotating blades: the mathematical aspects. In *Computational Acoustics: Acoustic Propagation* (Amsterdam (Netherlands), 1993), D. Lee, A. Robinson, and R. Vichnevetsky, Eds., vol. 2 of *Proceedings of the 3rd IMACS Symposium on Computational Acoustics*, IMACS, Elsevier Science Publishers, pp. 117–148.

[108] Farassat, F., and Myers, M. Line source singularity in the wave equation and its removal by quadrupole sources - A supersonic propeller noise problem. In *International Conference on Theoretical and Computational Acoustics* (Mystic (USA), July 5-9 1993), J. F. Williams, D. Lee, and A. Pierce, Eds., vol. 1 of *Structural acoustics, scattering and propagation*, World Scientific Publishing Co., pp. 29–43.

[109] Farassat, F., and Myers, M. Multidimensional generalized functions in aeroacoustics and fluid mechanics - part i: basic concepts and operations. *International Journal of Aeroacoustics 10*, 2&3 (2011), 161–200.

[110] Farassat, F., Padula, S., and Dunn, M. Advanced turboprop noise prediction based on recent theoretical results. *Journal of Sound and Vibration 119*, 1 (1987), 53–79.

[111] Farassat, F., and Succi, G. The prediction of helicopter rotor discrete frequency noise. *Vertica 7*, 4 (1983), 309–320.

[112] Fasshauer, G. *Meshfree approximation methods with Matlab*, vol. 6 of *Interdisciplinary Mathematical Sciences*. World Scientific, Singapore, 2007.

[113] Ffowcs Williams, J., and Hawkings, D. Sound generated by turbulence and surfaces in arbitrary motion. In *Philosophical transactions of the Royal Society* (1969), vol. A264, pp. 321–342.

[114] Flinn, E. Futuristic aircraft: old-fashioned look is only skin deep. Aerospace America, November 2010. pp. 14-15.

[115] Forrester, A., Sobester, A., and Keane, A. *Engineering design via surrogate modelling*. John Wiley & sons, Chippenham (UK), 2008.

[116] Frisch, U., Hasslacher, B., and Pomeau, Y. Lattice-gas automata for the Navier-Stokes equation. *Physical Review Letters 56* (1986), 1505–1508.

[117] Frota, J., Lempereur, P., and Roger, M. Computation of the noise of a subsonic propeller at an angle of attack. In *4th AIAA/CEAS Aeroacoustics conference* (Toulouse (France), June 1998), no. AIAA 1998-2282, AIAA.

[118] Froude, R. On the elementary relation between pitch, slip and propulsive efficiency. *Transactions of the Institute of Naval Architects 19* (1878), 47–57.

[119] Froude, R. On the part played in propulsion by difference in fluid pressure. *Transactions of the Institute of Naval Architects 30* (1889), 390–405.

[120] Gause, L., and Alper, J. Structural properties of braided graphite/epoxy composites. *Journal of Composites technology and Research 9*, 4 (Winter 1987), 141–150.

[121] George, P. L., Hecht, F., and Saltel, E. Automatic mesh generator with specified boundary. *Computer Methods in Applied Mechanics and Engineering 92*, 3 (November 1991), 269–288.

[122] Giannakoglou, K., and Karakasis, M. Hierarchical and distributed metamodel-assisted Evolutionary Algorithms. In *Lecture Series on Introduction to Optimization and Multidisciplinary Design* (Sint-Genesius-Rhode, 2006), no. LS 2006-04, von Karman Institute.

[123] Glauert, H. An aerodynamic theory of the airscrew. Reports & Memoranda 786, Aeronautical Research Committee, Great Britain, 1922.

[124] Glauert, H. *Aerodynamic theory*, vol. 4L. California Institute of Technology, Berlin (Germany), 1935, ch. Airplane propellers, pp. 169–360.

[125] Goble, B., and Hooker, J. Validation of an unstructured grid Euler/Navier-Stokes code on a full aircraft with propellers. In *39th AIAA Aerospace Sciences Meeting and Exhibit* (Reno (USA), January 8-11 2001), no. AIAA 2001-16797, AIAA.

[126] Goldberg, D. *Genetic algorithms in search, optimization and machine learning*. Addison-Wesley, Stuttgart (Germany), 1989.

[127] Goldberg, D., and Deb, K. *Foundations of Genetic Algorithms 1 (FOGA-1)*. Morgan Kaufmann, San Mateo (USA), 1991, ch. A comparison of selection schemes used in genetic algorithms, pp. 69–93.

[128] Gol'denblat, I., and Kopnov, V. *Strength of glass-reinforced plastics in the complex stress state*, vol. I of *Polymer Mechanics*. Faraday Press, 1966.

[129] Goldstein, M. *Aeroacoustics*. McGraw-Hill, (USA), 1976.

[130] Grimes, R., Harlamert, W., and Thompson, D. Aircraft propeller assembly with composite blades, October 1983.

[131] Groeneweg, J. Aeroacoustics of advanced propellers. In *17th ICAS Congress* (Stockholm (Sweden), September 9-14 1990), AIAA, pp. 108–126.

[132] Groeneweg, J., and Bober, L. NASA Advanced propeller research. Technical memorandum TM-101361, NASA, NASA Lewis research center (USA), 1988.

[133] Gur, O., and Rosen, A. Multidisciplinary design optimization of a quiet propeller. In *14th AIAA/CEAS Aeroacoustics conference* (Vancouver (Canada), May 2008), no. AIAA 2008-3073, AIAA.

[134] Gur, O., and Rosen, A. Optimization of propeller based propulsion system. In *49th AIAA/ASME/ASCE/AHS/ASC Structures, Structural Dynamics, and Materials Conference* (Schaumburg (USA), April 7-10 2008), no. AIAA 2008-1977, AIAA.

[135] Gutin, L. On the sound field of a rotating airscrew. *Zhurnal Technicheskoi Fiziki 6* (1936), 889–909. translated as NACA TM-1192 in 1948.

[136] Hammack, J. The aerodynamic design of supersonic propellers from structural considerations. Technical Note TN-2851, NACA, Langley Aeronautical Laboratory, December 1952.

[137] Hanson, D. Influence of propeller design parameters on far-field harmonic noise in forward flight. *AIAA Journal 18*, 11 (November 1980), 1313–1319.

[138] Hanson, D. Near field frequency-domain theory for propeller noise. *AIAA Journal 23*, 4 (April 1985), 499–504.

[139] Hanson, D. Unified aeroacoustics analysis for high speed turboprop aerodynamics and noise: Vol. I - Development of theory for blade loading, wakes and noise. Contractor Report CR 4329, NASA, NASA Lewis Research Center (USA), March 1991.

[140] Hanson, D., and Fink, M. The importance of quadrupole sources in prediction of transonic tip speed propeller noise. *Journal of Sound and Vibration 62*, 1 (1979), 19–38.

[141] Hashin, Z. Failure criteria for unidirectional fiber composites. *Journal of Applied Mechanics 47* (1980), 329–334.

[142] Hawkings, D., and Lowson, M. Theory of open supersonic rotor noise. *Journal of Sound and Vibration 36*, 1 (1974), 1–20.

[143] Hecht-Nielsen, R. Theory of the backpropagation neural network. In *IEEE International Joint Conference on Neural Networks* (Washington DC (USA), June 18-22 1989), vol. I, IEEE, pp. 593–605.

[144] Hicks, R., and Henne, P. Wing design by numerical optimization. *Journal of Aircraft 15*, 7 (July 1978), 407–413.

[145] Hill, R. *The mathematical theory of plasticity.* Oxford University Press, London (United Kingdom), 1950.

[146] Hinton, C. GE set to challenge Pratt & Whitney with turboprop engine, July 29 2008.

[147] Hirschbein, M., Kielb, R., Aiello, R., Nall, M., and Lawrence, C. Structural and aeroelastic analysis of the SR-7L propfan. Technical Memorandum TM-86877, NASA, NASA Lewis Research Center, March 1985.

[148] Hoeveler, P. Turboprops in for a comeback? *Flug Revue 07/2003* (July 2003), –.

[149] Holland, J. *Adaption in natural and artificial systems.* University of Michigan Press, Ann Arbor (USA), 1975.

[150] Huyse, L., and Lewis, R. Aerodynamic shape optimization of two-dimensional airfoils under uncertain conditions. Contractor Report CR 2001-210648, NASA - ICASE, NASA Langley Research Center (USA), January 2001.

[151] Jameson, A. Aerodynamic design via control theory. *Journal of Scientific Computing 3* (September 1989), Journal of Scientific Computing.

[152] Jameson, A. Optimum aerodynamic design via boundary control. In *AGARD-VKI Lecture Series on Optimum Design Methods in Aerodynamics* (1994), von Karman Institute for Fluid Dynamics.

[153] Jameson, A. *Computational Fluid Dynamics Review.* Wiley, New York (USA), 1995, ch. Optimum aerodynamic design using control theory, pp. 495–528.

[154] Jameson, A., and Vassberg, J. CFD for aerodynamic design: its current and future impact. In *39th AIAA Aerospace Sciences Meeting. & Exhibit* (Reno (USA), January 8-11 2001), no. AIAA 2001-0538.

[155] Janic, M. *The sustainability of air transportation.* Ashgate, Aldershot (UK), 2007.

[156] Jeong, J., and Hussain, F. On the identification of a vortex. *Journal of Fluid Mechanics 285* (1995), 69–94.

[157] Jeong, S., Murayama, M., and Yamamoto, K. Efficient optimization design method using Kriging model. *Journal of Aircraft 42*, 2 (2005), 413–420.

[158] Jeracki, R., and Mitchell, G. Low and high speed propellers for general aviation - performance potential and recent wind tunnel test results. Technical Memorandum TM-81745, NASA, Lewis Research Center, April 1981.

[159] Johnston, R., and Sullivan, J. Propeller tip vortex interactions. In *28th Aerospace Sciences Meeting* (Reno (USA), January 8-11 1990), no. AIAA 90-0437, AIAA.

[160] Joines, X., and Houck, C. On the use of non-stationary penalty functions to solve nonlinear constrained optimization problems with GA's. In *Proceedings of the 1st IEEE International Conference on Evolutionary Computations* (Orlando (USA), 1994), IEEE, p. 579–584.

[161] Jones, R., and Marsh, S. Airshow - turboprops on the comeback trail, July 17 2008.

[162] Jones, W., and Launder, B. Prediction of laminarization with a two-equation model of turbulence. *International Journal of Heat and Mass Transfer 15* (1972), 301–314.

[163] Karakasis, M., Giannakoglou, K., and Koubogiannis, D. Aerodynamic design of compressor airfoils using Hierarchical, Distributed, Metamodel-Assisted Evolutionary Algorithms. In *7th European Conference on Turbomachinery, Fluid Dynamics and Thermodynamics* (Athens (Greece), March 5-8 2007).

[164] Keane, A., and Nair, P. *Computational approaches for aerospace design.* John Wiley & Sons, Chichester (United Kingdom), 2005.

[165] Kennedy, J., and Eberhart, R. Particle swarm optimization. In *IEEE International Conference on Neural Networks* (Perth (Australia), November 27 - December 01 1995), vol. 4, IEEE, pp. 1942–1948.

[166] Kennel, M. KDTREE 2: Fortran 95 and C++ software to efficiently search for near neighbors in a multi-dimensional Euclidean space. Tech. rep., University of California, San Diego (USA), August 2004. http://arxiv.org/abs/physics/0408067.

[167] Kenyon, G., and Reynolds, R. Investigation of a three-blade propeller in combination with two different spinners and an NACA D-type cowl at Mach numbers up to 0.80. Research Memorandum RM A54B18a, NACA, Ames Aeronautical Laboratory, April 21 1954.

[168] Kim, S.-E., and Choudhury, D. A near-wall treatment using wall functions sensitized to pressure gradient. In *Separated and Complex Flows* (1995), vol. ASME FED Vol. 217, ASME.

[169] Kingsley-Jones, M. Turning a cycle. *Flight International 168*, 5006 (October 11-17 2005), 38–43.

[170] Kingsley-Jones, M. Regional sales continue their slide, December 16 2008.

[171] Ko, F. *ASM Handbook : Volume 21 - Composites.* ASM International, (USA), 2001, ch. Braiding, pp. 69–77.

[172] Koehler, J., and Owen, A. *Handbook of statistics.* Elsevier Science, New York (USA), 1996, ch. Computer experiments, pp. 261–308.

[173] Krige, D. *A statistical approach to some mine valuations and allied problems at the Witwaterstrand.* PhD thesis, University of Witwaterstrand, 1951.

[174] Leishman, J. Aeroacoustics of 2D and 3D blade-vortex interaction using the indicial method. In *Proceedings of the 52nd Annual Forum of the American Helicopter Society* (June 1996).

[175] Li, W., Huyse, L., and Padula, S. Robust airfoil optimization to achieve consistent drag reduction over a Mach range. Contractor Report CR 2001-211042, NASA - ICASE, NASA Langley Research Center (USA), August 2001.

[176] Li, W., and Padula, S. Performance trades study for robust airfoil shape optimization. In *21st AIAA Applied Aerodynamics Conference* (Orlando (USA), June 23-26 2003), no. AIAA 2003-3790, AIAA.

[177] Li, X., and Sun, X. Effects of fuselage on propeller noise. In *15th AIAA Aeroacoustics Conference* (Long Beach (USA), October 25-27 1993), no. AIAA 93-4442, AIAA.

[178] Lighthill, M. On sound generated aerodynamically. In *Proceedings of the Royal Society* (1952), vol. 211, pp. 564–587. Series A.

[179] Lippmann, R. P. An introduction to computing with neural nets. *IEEE ASSP Magazine 3*, 2 (April 1987), 4–22.

[180] Lockard, D., Luo, L.-S., and Singer, B. Evaluation of the Lattice-Boltzmann equation solver PowerFLOW for aerodynamic applications. Contractor Report CR 2000-210550, NASA-ICASE, Langley Research Center, October 2000.

[181] Lopez, D., Angulo, C., and Macareno, L. An improved meshing method for shape optimization of aerodynamic profiles using genetic algorithms. *International Journal for Numerical Methods in Fluids 56* (2008), 1383–1389.

[182] Lynch III, D., Blake, W., and Mueller, T. Turbulent flow downstream of a propeller, part 1: wake turbulence. *AIAA Journal 43*, 6 (June 2005), 1198–1210.

[183] Lynch III, D., Blake, W., and Mueller, T. Turbulent flow downstream of a propeller, part 2: ingested, propeller-modified turbulence. *AIAA Journal 43*, 6 (June 2005), 1211–1220.

[184] Mackenzie, C. Back to the turboprop? a solution on pollution and cost. *International Herald Tribune 18* (May 2 2006), –.

[185] Madavan, N. Multiobjective optimization using a Pareto Differential Evolution Approach. In *Proceedings of the Congress on Evolutionary Computation* (Honolulu (USA), 2002), vol. 2, pp. 1145–1150.

[186] Magliozzi, B., Hanson, D., and Amiet, R. *Aeroacoustics of Flight Vehicles: theory and practice*, vol. I. NASA, Langley Research Center, August 1991, reference publication Propeller and Propfan Noise, pp. 1–61.

[187] Maillard, E., and Gueriot, D. RBF neural network, basis functions and genetic algorithm. In *International Conference on Neural Networks* (Houston (USA), June 9-12 1997), vol. 4, pp. 2187 – 2192.

[188] Marinus, B. Multidisciplinary evaluation of known propeller configurations. Project Report 2007-15, von Karman Institute for Fluid Dynamics, Rhode-Saint-Genèse (Belgium), June 2007.

[189] Marinus, B. Influence of parameterization and optimization method on the optimum airfoil. In *27th Congress of the International Council of the Aeronautical Sciences* (Nice (FRANCE), September 19-24 2010), no. 124, ICAS.

[190] Marinus, B., Bosschaerts, W., and Roger, M. Aerodynamic study of a 'humpy' propeller. In *46th Symposium of Applied Aerodynamics organized by 3AF* (Orléans (France), March 28-30 2011), Association Aéronautique et Aérospatiale de France.

[191] Marinus, B., Roger, M., and Van den Braembussche, R. Aeroacoustic and aerodynamic optimization of aircraft propeller blades. In *16th AIAA/CEAS Aeroacoustics Conference* (Stockholm (SWEDEN), June 7-9 2010), no. AIAA 2010-3850, AIAA.

[192] Martin, J., and Simpson, T. A Monte Carlo Simulation of the Kriging Model. In *10th AIAA/ISSMO Multidisciplinary Analysis and Optimization Conference* (Albany (USA), August 30 - September 1 2004), no. AIAA 2004-4483.

[193] Martin, J. D., and Simpson, T. W. Use of Kriging models to approximate deterministic computer models. *AIAA Journal 43*, 4 (2005), 853–863.

[194] Matsuo, Y. Navier-Stokes computations for flowfield of an advanced turboprop. In *24th ASME/SAE/ASEE Joint Propulsion Conference* (Boston (USA), July 1988), no. 88-3094, AIAA.

[195] Mayer, S. ATR press conference, January 23 2009.

[196] McCarthy, R. *Plastics, Metals, Ceramics, 11th Int. Chapter Conf. of the SAMPE*. SAMPE European Chapter, Basel (Switzerland), May 29-31 1990, ch. Braiding of hybrid composite propeller blades, pp. 127–142.

[197] McCarthy, R., Haines, G., and Newley, R. Polymer composite applications to aerospace equipment. *Composites Manufacturing 5*, 2 (1994), 83–93.

[198] McClellan, J. Best used turboprops: Demand is growing for these fuel-efficient turbines, September 2007.

[199] Mehmed, O., and Kaza, K. Experimental classical flutter results of a composite advanced turboprop model. Technical memorandum TM-88792, NASA, NASA Lewis research Center (USA), July 1986.

[200] Menter, F. Zonal two equation k-ω turbulence models for aerodynamic flows. In *23rd Fluid Dynamics, Plasmadynamics, and Lasers Conference* (Orlando (USA), July 6-9 1993), no. AIAA 1993-2906, AIAA.

[201] Metzger, F. An assessment of propeller aircraft noise reduction technology. Contractor Report CR 198237, NASA, NASA Langley Research Center (USA), August 1995.

[202] Metzger, F. A review of propeller noise prediction methodology 1919-1994. Contractor Report CR 198156, NASA, NASA Langley Research Center (USA), June 1995.

[203] Metzger, F., and Rohrbach, C. Benefits of blade sweep for advanced turboprops. *Journal of Propulsion 2*, 6 (June 1986), 534–540.

[204] Michalewicz, Z., and Janikow, C. Z. Handling constraints in Genetic Algorithms. In *4th International Conference in GAs* (Los Altos (USA), July 1991), pp. 151–157.

[205] Miller, C., and Sullivan, J. Noise constraints affecting optimal propeller designs. In *Society of Automotive Engineers* (1985), no. SAE 850871, Society of Automotive Engineers.

[206] Mäkinen, R., Periaux, J., and Toivanen, J. Multidisciplinary shape optimization in aerodynamics and electromagnetics using genetic algorithms. *International Journal for Numerical Methods in Fluids 30* (1999), 149–159.

[207] Mohammadi, B., and Pironneau, O. Shape optimization in fluid mechanics. *Annual Review of Fluid Mechanics 36* (2004), 255–279.

[208] Morris, A., Allen, C., and Rendall, T. CFD-based optimization of aerofoils using radial basis functions for domain element parametrization and mesh deformation. *International Journal for Numerical Methods in Fluids 58* (March 2008), 827–860.

[209] Morrow, D. Twilight of turboprops? Passengers go out of their way to catch jets, February 18 2000.

[210] Myers, M., and Farassat, F. Structure and propagation of supersonic singularities from helicoidal sources. In *11th AIAA Aeroacoustics Conference* (Sunnyvale (USA), October 19-21 1987), no. AIAA 87-2676, AIAA.

[211] Myers, R., and Montgomery, D. *Response Surface Methodology: process and product optimization using designed experiments*. Wiley & sons, New York (USA), 1995.

[212] Nallasamy, M., Clarck, B., and Groeneweg, J. Euler analysis of the three dimensional flow field of a high-speed propeller: boundary condition effects. Technical Memorandum TM-88955, NASA, NASA Lewis Research Center (USA), June 1987.

[213] Nelson, W. *Airplane propeller principles*. John Wiley & sons, London (England), 1947.

[214] Nemec, M., and Zingg, D. Multipoint and multi-objective aerodynamic shape optimization. *AIAA Journal 42*, 6 (June 2004), 1057–1065.

[215] Nitzsche, F. Whirl-flutter investigation on an advanced turboprop configuration. *Journal of Aircraft 26*, 10 (October 1989), 939–946.

[216] Nitzsche, F. Whirl-flutter suppression in advanced turboprops and propfans by active control techniques. *Journal of Aircraft 31*, 3 (May-June 1994), 713–719.

[217] Obayashi, S. Airfoil shape parameterization for evolutionary computation. In *Lecture Series on Genetic Algorithms for Optimisation in Aeronautics and Turbomachinery* (Sint-Genesius-Rode (Belgium), 2000), no. LS 2000-07, von Karman Institute for Fluid Dynamics.

[218] Pagano, A., Barbarino, M., Casalino, D., and Frederico, L. Tonal and broadband noise calculations for aeroacoustic optimization of propeller blades in a pusher configuration. In *15th AIAA/CEAS Aeroacoustics Conference* (Miami (USA), May 11-13 2009), no. AIAA 2009-3138.

[219] Pagano, A., Frederico, L., Barbarino, M., and Aversano, M. Multi-objective aeroacoustic optimization of an aircraft propeller. In *12th AIAA/ISSMO Multidisciplinary Analysis and Optimization Conference* (Victoria (Canada), September 10-12 2008), no. AIAA 2008-6059, AIAA.

[220] Papadimitriou, D., and Giannakoglou, K. A continuous adjoint method with objective function derivatives based on boundary integrals for inviscid

and viscous flow. In *44th AIAA Aerospace Sciences Meeting and Exhibit* (Reno (USA), January 9-11 2006), no. AIAA 2006-0116.

[221] Parry, A., and Crighton, D. Asymptotic theory of propeller noise - part i: Subsonic single-rotation propeller. *AIAA Journal 27*, 9 (1989), 1184–1190. Presented at the 10th AIAA Aeroacoustics Conference, July 9-11, Seattle (USA).

[222] Peake, N., and Crighton, D. An asymptotic theory of near-field propeller acoustics. *Journal of Fluid Mechanics 232* (1991), 231–285.

[223] Peake, N., and Crighton, D. Lighthill quadrupole radiation in supersonic propeller acoustics. *Journal of Fluid Mechanics 223* (1991), 363–382.

[224] Peigin, S., and Epstein, B. Robust handling of non-linear constraints for GA optimization of aerodynamic shapes. *International Journal for Numerical Methods in Fluids 45* (2004), 1339–1362.

[225] Peigin, S., and Epstein, B. Robust optimization of 2D airfoils driven by full Navier-Stokes computations. *Journal of Computer and Fluids 33* (February 2004), 1175–1200.

[226] Perrier, P. Multi-disciplinary constraints in aerodynamic design. In *RTO-AVT Symposium on "Aerodynamic design and optimisation of flight vehicles in a concurrent multi-disciplinary environment"* (Ottawa (Canada), October 18-21 1999), no. RTO MP-35.

[227] Phillips, E. Fighting it out, May 19 2008.

[228] Pierce, D., and Lewis, J. Sparse multifrontal rank revealing QR factorization. *SIAM Journal on Matrix Analysis and Applications 18*, 1 (1997), 159–180.

[229] Pierret, S. *Designing turbomachinery blades by means of the function approximation concept based on artificial neural network, genetic algorithm, and the Navier-Stokes equations.* Phd thesis, Faculté polytechnique de Mons - von Karman Institute for Fluid Dynamics, Mons (Belgium), December 1999.

[230] Pironneau, O. *Optimal shape design for elliptic systems.* Springer-Verlag, New York (USA), 1984.

[231] Polacsek, C., Spiegel, P., Boyle, F., Eaton, J., Brouwer, H., and Nijboer, R. Noise computation of high speed propeller driven aircraft. In *6th AIAA/CEAS Aeroacoustics conference* (Lahaina (USA), June 2000), AIAA.

[232] Poloni, C. *Notes on numerical fluid mechanics*, vol. 68. Vieweg, Wiesbaden (Germany), 1999, ch. Multi-objective aerodynamic optimisation by means of robust and efficient genetic algorithm, pp. 1–24.

[233] Porto, V., Fogel, D., and Fogel, L. Alternative neural network training methods, June 1995.

[234] Prandtl, L. Tragflügeltheorie; I und II Mitteilung. Nachrichten S.151 - S.107, Königlichen Gesellschaft der Wissenschaften Math.-Phys., 1918-1919.

[235] Press, W., Teukolsky, S., Vetterling, W., and Flannery, B. *Numerical recipes.* Cambridge University Press, New York (USA), 2007.

[236] Price, K., and Storn, R. Differential evolution. *Dr Dobb's Journal* (April 1 1997), 18–24.

[237] Prieur, J. Analysis and capability of a non-compact integration method for rotor noise prediction. In *Forum Acusticum* (Berlin (Germany), March 14-19 1999), no. ONERA TP 1999-145.

[238] Pringle, R. Aircraft trainers on the fly, October 13 2006.

[239] Rai, M. Robust optimal design with differential evolution. In *10th AIAA/ISSMO Multidisciplinary Analysis and Optimization Conference* (Albany (USA), August 30 - September 1 2004), no. AIAA 2005-4588, AIAA.

[240] Ramsey, J., and Kaza, K. Concentrated mass effects on the flutter of a composite advanced turboprop model. Technical Memorandum TM-88854, NASA, NASA Lewis Research Center, October 1986.

[241] Rankine, W. On the mechanical principles of the action of propellers. *Transactions of the Institute of Naval Architects 6* (1865), 13–39.

[242] Ray, T., and Tsai, H. *Numerical Grid Generation in Computational Field Simulations*. The International Society of Grid Generation, Mississippi (USA), June 2002, ch. Some issues in NURBS representation of airfoil shapes for optimization, pp. 815–825.

[243] Rechenberg, I. *Evolutionsstrategie - Optimierung technischer systeme nach prinzipen der biologischen evolution*. Fommann-Holzboog, Stuttgart (Germany), 1973.

[244] Remmler, S. Aeroacoustic noise computation of an axial flow fan. Project Report 2008-13, von Karman Institute for Fluid Dynamics, Rhode-Saint-Genèse (Belgium), February 2008.

[245] Reuther, J., Jameson, A., Alonso, J., Rimlinger, M., and Saunders, D. Constrained multipoint aerodynamic shape optimization using an adjoint formulation and parallel computers: parts 1 & 2. *Journal of Aircraft 36* (1999), 51–74.

[246] Reynolds, R., Buell, D., and Walker, J. Investigation of an NACA 4-(5)(05)-041 four-blade propeller with several spinners at Mach numbers up to 0,9. Research memorandum RM A52I19a, NACA, NACA-Ames aeronautical laboratory (USA), 1952.

[247] Reynolds, R., Sammonds, R., and Kenyon, G. An investigation of a four-blade single-rotation propeller in combination with an NACA 1-series D-type cowling at Mach numbers up to 0.83. Research Memorandum RM A53B06, NACA, Ames Aeronautical Laboratory, April 13 1953.

[248] Reynolds, R., Sammonds, R., and Walker, J. Investigation of single- and dual-rotation propellers at positive and negative thrust, and in combination with an NACA 1-series D-type cowling at Mach numbers up to 0,84. Technical Report TR-1336, NACA, NACA-Ames aeronautical laboratory (USA), 1957.

[249] Rhie, C., and Chow, W. Numerical study of the turbulent flow past an airfoil with trailing edge separation. *AIAA Journal 21*, 11 (November 1983), 1525–1532.

[250] Riabouchinsky, D. Contribution à l'étude des hélices. Publication Scientifique 118, Ministère de l'Air, Paris (France), 1938.

[251] Richardson, J., Palmer, M., Liepins, G., and Hilliard, M. Some guidelines for genetic algorithms with penalty functions. In *Proceedings of the 3rd International Conference on Genetic Algorithms* (1989), pp. 191–197.

[252] Richter, H., and Menczykalski, S. Innovative configurations and advanced concepts for future civil aircraft. In *Lectures Series on Civil Propulsion of the future* (Sint-Genesius-Rhode (Belgium), June 6-10 2005), no. LS 2005-06, von Karman Institute for Fluid Dynamics.

[253] Robinson, G., and Keane, A. Concise orthogonal representation of supercritical airfoils. *Journal of Aircraft 38*, 3 (2001), 580–583.

[254] Roe, P. Characteristic based schemes for the Euler equations. *Annual Review of Fluid Mechanics 18* (1986), 337–365.

[255] Roger, M. Aeroacoustics - some theoretical background / the acoustic analogy. In *Lecture Series 2006-05: Computational aeroacoustics* (Brussels (Belgium), April 2006), von Karman Institute for fluid dynamics.

[256] Roger, M. Noise from moving surfaces. In *Lecture Series 2006-05: Computational aeroacoustics* (Brussels (Belgium), April 2006), von Karman Institute for fluid dynamics.

[257] Roger, M. On the noise from open rotors. In *Lecture Series 2006-05: Computational aeroacoustics* (Brussels (Belgium), April 2006), von Karman Institute for fluid dynamics.

[258] Roger, M., and Moreau, S. Extension and limitations of analytical airfoil broadband noise models. In *12th CEAS-ASC / 3rd X3-Noise Workshop : "Turbomachinery broadband noise"* (Bilbao (Spain), October 23-24 2008), Council of European Aerospace Societies.

[259] Rohrbach, C., Metzger, F., Black, D., and Ladden, R. Evaluation of wind tunnel performance testings of an advanced 45° swept, eight bladed propeller at Mach numbers from 0.45 to 0.85. Contractor Report CR 3505, National Aeronautics and Space Administration, NASA Lewis research center (USA), 1982.

[260] Sacks, J., Welch, W., Mitchell, T., and Wynn, H. Design and analysis of computer experiments. *Statistical Sciences 4*, 4 (1989), 409–423.

[261] Samareh, J. Survey of parameterization techniques for high-fidelity multidisciplinary shape optimization. *AIAA Journal 39*, 5 (May 2001), 877–884.

[262] Sarkar, S., and Balakrishnan, L. Application of a Reynolds-stress turbulence model to the compressible shear layer. Contractor Report CR 182002, NASA-ICASE, 1990.

[263] Schulten, J. Advanced propeller performance calculation by a lifting surface method. *Journal of Propulsion and Power 12*, 3 (May-June 1996), 477–485.

[264] Sefrioui, M., and Périaux, J. *Parallel problem solving from nature - PPSN VI.* Springer-Verlag, Heidelberg (Germany), 2000, ch. A Hierachical Genetic Algorithm using multiple models for optimization, pp. 879–888.

[265] Shene, C.-K. Introduction to computing with geometry, July 2009.

[266] Shi, Y., and Eberhart, R. A modified particle swarm optimizer. In *IEEE International Conference on Evolutionary Computation* (May 4-9 1998), IEEE, pp. 69–73.

[267] Shih, T.-H., Liou, W. W., Shabbir, A., Yang, Z., and Zhu., J. A new k-ε Eddy-viscosity model for high Reynolds number turbulent flows - model development and validation. *Computers & Fluids 24*, 3 (1995), 227–238.

[268] Simpson, T., Poplinski, J., Koch, P. N., and Allen, J. Metamodels for computer-based engineering design: Survey and recommendations. *Engineering with Computers 17*, 2 (July 2001), 129–150.

[269] Smirti, M., and Hansen, M. The potential of turboprops to reduce aviation fuel consumption. Tech. rep., University of California Transportation Center, Berkeley (USA), January 09 2009.

[270] Sobieczky, H. *Notes on Numerical Fluid Mechanics*, vol. 68. Vieweg & Sohn Verlag, 1998, ch. Parametric airfoils and wings, pp. 71–88.

[271] Song, W., and Keane, A. A study of shape parameterisation methods for airfoils optimisation. In *10th AIAA/ISSMO Multidisciplinary Analysis and Optimization Conference* (Albany (USA), August 30 - September 1 2004), no. AIAA 2004-4482, AIAA.

[272] Spalart, P., and Allmaras, S. A one-equation turbulence model for aerodynamic flows. In *30th Aerospace Sciences Meeting and Exhibit* (Reno (USA), January 6-9 1992), no. AIAA 92-0439, AIAA.

[273] Srivastava, R., and et al. Application of an efficient hybrid scheme for aeroelastic analysis of advanced propellers. *Propulsion and Power 7*, 5 (September 1991), 767–775.

[274] Stefko, G., Bober, L., and Neumann, H. New test techniques and analytical procedures for understanding the behavior of advanced propellers. *Society of Automotive Engineers* -, SAE 830729 (1984), 3.43–3.58.

[275] Stefko, G., and Jeracki, R. Wind-tunnel results of advanced high-speed propellers at takeoff, climb, and landing mach numbers. Technical Memorandum TM-87030, NASA, NASA Lewis Research Center, November 1 1985.

[276] Stein, M. L. *Interpolation of Spatial Data: Some theory of Kriging.* Springer-Verlag, New York (USA), 1999.

[277] Storn, R., and Price, K. Differential Evolution: a simple and efficient adaptive scheme for global optimization over continuous spaces. Technical Report TR-95-012, International Computer Science Institute, Berkeley (USA), 1995.

[278] Storn, R., and Price, K. Differential Evolution - A simple and efficient heuristic for global optimization over continuous spaces. *Journal of Global Optimization 11* (November 1997), 341–359.

[279] Stuermer, A. Unsteady CFD simulations of propeller installation effects. In *42nd AIAA/ASME/SAE/ASEE Joint Propulsion Conference and Exhibit* (Sacramento (USA), July 9-12 2006), no. AIAA 2006-4969, AIAA.

[280] Succi, G. Noise and performance of propellers for light aircraft. MIT Report 154, Massachusetts Institute of Technology, Cambridge (USA), 1980.

[281] Sulc, J., Hofr, J., and Benda, L. Exterior noise on the fuselage of light propeller driven aircraft in flight. *Journal of Sound and Vibration 84* (September 1982), 105–120.

[282] Sullivan, W., Turnberg, J., and Violette, J. Large-scale advanced prop-fan (LAP) blade design. Contractor Report CR 174790, NASA, Lewis Research Center, 1988.

[283] Taghaddosi, F., and Agarwal, R. Quadrupole modeling for prediction of high-speed impulsive noise of propellers. In *6th AIAA/CEAS Aeroacoustics conference* (Lahaina (USA), June 2000), AIAA.

[284] Tam, C. On linear acoustic solutions of high speed helicopter impulsive noise problems. *Journal of Sound and Vibration 89*, 1 (1983), 119–134.

[285] Tang, Z., and Désidéri, J.-A. Towards self-adaptive parametrization of Bézier curves for airfoil aerodynamic design. Research Report INRIA 4572, Institut National de Recherche en Informatique et en Automatique, Sophia Antipolis, September 2002.

[286] Tanna, H., Burrin, R., and Jr., H. P. Installation effects on propeller noise. *Journal of Aircraft 18*, 4 (April 1981), 303–309.

[287] Tobor, I., Reuter, P., and Schlick, C. Efficient reconstruction of large scattered geometric datasets using the Partition of Unity and Radial Basis Functions. *Journal of WSCG 12*, 1-3 (February 2004), –.

[288] Tong, L., Mouritz, A., and Bannister, M. *3D fibre reinforced polymer composites*. Elsevier Science, Oxford (United Kingdom), 2002.

[289] Tresca, H. Mémoire sur l'écoulement des corps solides soumis à de fortes pressions. *Compte rendu de l'Académie des Sciences de Paris 59* (1864), 754.

[290] Tsai, S., and Azzi, V. Strength of laminated composite materials. *AIAA Journal 4*, 2 (February 1966), 296–301.

[291] Tsai, S., and Wu, E. A general theory of strength for anisotropic materials. *Journal of Composite Materials 5*, 1 (January 1971), 58–80.

[292] Tsai, T., de Jong, F., and Levy, R. Computation of the tip vortex flowfield for advanced aircraft propellers. Contractor Report CR 182179, NASA, NASA Lewis Research Center (USA), 1988.

[293] Unknown. Composite materials in propellers (Dowty Rotol Limited). *Aircraft Engineering and Aerospace Technology 61*, 11 (1989), 10–15.

[294] Vanderplaats, G. *Numerical optimization techniques for engineering design*. McGraw-Hill, New York (USA), 1984.

[295] Veldhuis, L., and Luursema, G. Comparison of an actuator disk and a blade modeling approach in Navier-Stokes calculations on the SR-3 propfan. In *18th AIAA Applied Aerodynamics Conference* (Denver (USA), August 14-17 2000), no. AIAA 2000-4528, AIAA.

[296] Venkateswaran, S., Weiss, J., and Merkle, C. Propulsion related flowfields using the preconditioned Navier-Stokes equations. In *AIAA/ASME/SAE/ASEE 28th Joint Propulsion Conference* (Nashville (USA), July 1992), no. AIAA-92-3437.

[297] Verstraete, T. *Multidisciplinary turbomachinery component optimization considering performance, stress and internal heat transfer*. Phd thesis, von Karman Institute for Fluid Dynamics - Universiteit Gent, Rhode-Saint-Genèse - Gent (Belgium), June 2008.

[298] Vogeley, A. Axial momentum theory for propellers in compressible flows. Technical Note TN 2164, NACA, August 1950.

[299] von Mises, R. Mechanik der Festen Korper im plastisch deformablen Zustand. *Göttin. Nachr. Math. Phys. 1* (1913), 582–592.

[300] Weinberger, S. Lockheed debuts concept for a stealthy drone. www.wired.com.

[301] Wendland, H. Piecewise polynomial, positive defnite and compactly supported radial functions of minimal degree. *Advances in Computer Mathematics 4* (October 1995), 389–396.

[302] Westmoreland, W., Tramel, R., and Barber, J. Modeling propeller flow-fields using CFD. In *46th AIAA Aerospace Sciences Meeting and Exhibit* (Reno (USA), January 7-10 2008), no. AIAA 2008-402, AIAA.

[303] Whitcomb, R. A discussion of the design of highly swept propeller blades. Research Memorandum RM L50A23, NACA, Langley Aeronautical Research Laboratory, May 4 1950.

[304] White, H. *Artificial Neural Networks*. Blackwell, Guildford (United Kingdom), 1992, ch. Neural Network Learning and statistics, pp. 81–89.

[305] White, H., Hornik, K., and Stinchcombe, M. *Artificial Neural Networks*. Blackwell, Guildford (United Kingdom), 1992, ch. Multilayer feedforward networks are universal approximators, pp. 12–28.

[306] Whitfield, C., Gliebe, P., Mani, R., and Mungur, P. High speed turboprop aeroacoustic study (single-rotation). Contractor Report 182257, NASA, NASA Langley Reseacrh Center, May 1989.

[307] Whitfield, D. Three-dimensional unsteady Euler solutions for propfans and counter-rotating propfans in transonic flow. In *19th Conference on Fluid Dynamics, Plasma Dynamics, and Lasers* (Honolulu (USA), June 1987), no. 87-1197, AIAA.

[308] Wilcox, D. Reassessment of the scale-determining equation for advanced turbulence models. *AIAA Journal 26*, 11 (November 1988), 1299–1310.

[309] Wolfram, S. Cellular automaton fluids 1: Basic theory. *Journal of Statistical Physics 45* (1986), 471–526.

[310] Woodward, R. Measured noise of a scale model high speed propeller at simulated takeoff/approach conditions. In *25th Aerospace Sciences Meeting* (Reno (USA), January 12-15 1987), no. AIAA 87-0526, AIAA.

[311] Wu, H.-Y., Yang, S., Liu, F., and Tsai, H.-M. Comparison of three geometric representations of airfoils for aerodynamic optimization. In *16th AIAA Computational Fluid Dynamics Conference* (Orlando (USA), June 23-26 2003), no. AIAA 2003-4095, AIAA.

[312] Xue, Y., and Lyrintzis, S. Rotating Kirchhoff method for three-dimensional transonic blade-vortex interaction hover noise. *AIAA Journal 32*, 7 (1994), 1350–1359.

[313] Yin, J., and Stuermer, A. Coupled uRANS and FW-H analysis of installed pusher propeller aircraft configurations. In *15th AIAA/CEAS Aeroacoustics Conference* (Miami (USA), May 11-13 2009), no. AIAA 2009-3137, AIAA.

[314] Young, R., Tai, J., Havrilesko, B., and Mavris, D. A comparison of community noise metrics for open rotor engine architectures. In *16th AIAA/CEAS Aeroacoustics Conference* (Stockholm (Sweden), June 7-9 2010), no. AIAA 2010-4002, AIAA.

[315] Zhou, Q., and Joseph, P. A frequency domain method for the prediction of broadband noise from an open rotor. In *10th AIAA/CEAS Aeroacoustics Conference* (Manchester (United Kingdom), May 10-12 2004).